Experimental Benchmarking of Spin Tracking Algorithms for Electric Dipole Moment Searches at the Cooler Synchrotron COSY

Der Fakultät für Mathematik, Informatik und Naturwissenschaften der RWTH Aachen University vorgelegte Dissertation zur Erlangung des akademischen Grades eines Doktors der Naturwissenschaften

von

Master of Science

Marcel Stephan Rosenthal

aus Aachen (Nordrhein-Westfalen)

Experimental Benchmarking of Spin Tracking Algorithms for Electric Dipole Moment Searches at the Cooler Synchrotron COSY

Known CP violating sources in the Standard Model of Particle Physics are not sufficient to explain the predominance of the observed matter in the Universe. Additional sources beyond the Standard Model are required. These sources can manifest in permanent electric dipole moments (EDMs) of elementary particles. Searches for neutral particles already started decades ago, but no value significantly different from zero has been observed. The current upper limit for the neutron amounts to $2.9 \cdot 10^{-26}\,e\,\mathrm{cm}$ (90 % C. L.). New measurement methods for protons and deuterons in dedicated electrostatic storage rings are proposed. As an intermediate step, essential requirements and limitations are studied by the JEDI (Jülich Electric Dipole moments Investigations) collaboration at the existing magnetic storage ring, the Cooler Synchrotron COSY. A first direct measurement of the deuteron EDM is planned, which employs a radiofrequency (RF) Wien filter to create an EDM related spin polarization signal. In the scope of this thesis a new framework providing a convenient environment for simulation and analysis was created to model this new method. It interfaces with the existing simulation code COSY INFINITY to calculate transfer maps for the particle beam and spin coordinates. These maps are used to perform repetitive tracking. New transfer map based algorithms have been implemented to extend the functionality for time-varying electromagnetic fields.

One of the major requirements for storage ring based EDM searches is a long spin coherence time, which limits the available time to conduct the measurement. Important contributions to spin decoherence arising from path-lengthening of individual particles and from intrinsic spin resonances have been discussed and verified by simulation studies. To cancel those contributions, storage ring parameters like betatron tunes, chromaticities and momentum compaction factors require precise adjustment. The measured locations of longest spin coherence times confirmed the model predictions for different betatron tunes. Based on a conservative definition, spin coherence times of about 750 s have been achieved during these studies at COSY. The long spin coherence time allowed for the benchmarking of the new algorithms for time-varying fields. An existing RF solenoid running on an artificial spin resonance was used to introduce vertical polarization oscillations. Theoretical calculations predict a dependence of the oscillation amplitude on the solenoid frequency. These calculations were successfully verified by simulations and measurements. Also analytical estimates of the EDM related polarization could be confirmed by the new algorithms. Systematic contributions mimicking this signal arise from misalignments and field imperfections of the RF Wien filter or the storage ring magnets. Calculations predicted that an RF Wien filter rotation about the longitudinal axis by 0.1 mrad produces a similar signal as an EDM of $d_d \approx 5 \cdot 10^{-19}\,e\,\mathrm{cm}$. The same order of magnitude was obtained by randomly shifting the quadrupole magnets in vertical direction assuming a Gaussian distribution with a width of $\sigma_y = 0.1\,\mathrm{mm}$. Finally, orbit correction methods to suppress these systematic contributions were applied in simulations. These partially compensated the false EDM signal contributions from misalignments of the static storage ring elements.

Experimentelles Benchmarking von Spin Tracking Algorithmen zur Suche nach elektrischen Dipolmomenten am Kühlersynchrotron COSY

Bekannte Quellen von CP Verletzung im Standardmodell der Teilchenphysik reichen nicht aus, um den Materieüberschuss im bekannten Teil des Universums zu erklären, sodass weitere Quellen jenseits des Standardmodells nötig werden. Diese Quellen können zu messbaren elektrischen Dipolmomenten (EDMs) beitragen. In den seit mehreren Dekaden durchgeführten Messungen mit neutralen Teilchen konnte bisher kein von Null verschiedenes EDM beobachtet werden. Die derzeit präziseste Messung für das Neutron EDM lieferte ein oberes Limit von $2{,}9 \cdot 10^{-26}\,e\,\mathrm{cm}$ (90 % C. L.). Die Nutzung von dedizierten elektrischen Speicherringen für Messungen mit Protonen, Deuteronen und leichten Kernen wurde vorgeschlagen. Die Voraussetzungen und Limitierungen werden derzeit von der JEDI (Jülich Electric Dipole moments Investigations) Kollaboration am bestehenden magnetischen Speicherring, dem Kühlersynchrotron COSY, untersucht. Ebenfalls ist eine erste direkte Messung des Deuteron EDMs unter Verwendung eines hochfrequenten (HF) Wien Filters geplant, die ein EDM bezogenes Spin-Polarisationssignal erzeugt. Im Rahmen dieser Arbeit wurde ein neues Framework entwickelt, welches eine komfortable Umgebung zur Simulation und Analyse bereitstellt, um diese Messmethode zu überprüfen. Dieses Framework ist mit dem bestehenden Simulationscode COSY INFINITY verknüpft, der es ermöglicht Transferabbildungen für die Koordinaten der Teilchen und deren Spins zu berechnen. Die iterative Anwendung dieser Abbildungen ermöglicht die zeitliche Entwicklung der Koordinaten zu simulieren (Tracking). Eine Hauptvoraussetzung für die EDM Experimente in Speicherringen ist eine lange Spinkohärenzzeit, da diese die verfügbare Messzeit limitiert. Wichtige Beiträge zur Spindekohärenz, die einerseits aus einer Weglängenänderung von einzelnen Teilchen resultieren und andererseits durch intrinsische Spinresonanzen hervorgerufen werden, wurden diskutiert und in Simulationen überprüft. Um diese Beiträge zu minimieren, müssen Parameter des Speicherrings, u. a. Arbeitspunkte, Chromatizitäten und „momentum compaction"-Faktor präzise eingestellt werden. Die Modellvorhersagen zur Maximierung der Spinkohärenzzeit wurden durch Messungen bei verschiedenen Arbeitspunkten bestätigt. Unter Verwendung einer konservativen Definition wurden Spinkohärenzzeiten von etwa 750 s erreicht. Dies ermöglichte eine Validierung der neuen Algorithmen die zur Simulation von HF Feldern implementiert wurden. Ein existierender HF Solenoid wurde verwendet, um Oszillationen der vertikalen Polarisation hervorzurufen und zu untersuchen. Theoretische Berechnungen, die eine Abhängigkeit der Oszillationsamplitude von der Solenoidfrequenz vorhersagen, wurden erfolgreich in Simulationen und Messungen reproduziert. Ebenfalls wurden analytische Schätzungen des EDM-abhängigen Polarisationsaufbaus durch auf den neuen Algorithmen basierenden Simulationsrechnungen bestätigt. Systematische Beiträge, die einen ähnlichen Polarisationsaufbau produzieren, entstehen durch Fehlaufstellungen und Feldfehler des HF Wien Filters bzw. der Elemente des Speicherrings. Hier haben Berechnungen gezeigt, dass eine Rotation des HF Wien Filters von 0,1 mrad um die longitudinale Achse einen ähnlichen Aufbau wie ein Deuteron EDM von $d_d \approx 5 \cdot 10^{-19}\,e\,\mathrm{cm}$ ergeben. Die gleiche Größenordnung wurde auch durch zufällige, vertikale Verschiebungen der Quadrupole unter Annahme einer Normalverteilung mit einer Breite von $\sigma_y = 0{,}1\,\mathrm{mm}$ erreicht. Zur Unterdrückung dieser systematischen Beiträge wurden Orbitkorrekturmethoden untersucht. Mit diesen war eine anteilige Kompensation des nicht EDM bezogenen Polarisationsaufbaus, der durch Fehlaufstellungen der Speicherringelemente hervorgerufen wird, möglich.

Contents

Chapter 1

Introduction

Physics aims for a description of nature in mathematical models. Fundamental symmetries play an important role in these models. A prominent example is the Standard Model of Particle Physics (SM), which describes the smallest constituents of matter, the elementary particles, and their interactions. Although it was verified by many experimental observations, it currently lacks for an explanation of the observed matter over antimatter dominance in the known part of the Universe [1]. A disappearance of antimatter during the evolution of the Universe requires a violation of certain fundamental symmetries. This violation can manifest in permanent electric dipole moments (EDMs) of elementary particles. Their existence is strongly suppressed in the SM. However, significantly larger EDMs are predicted by models, which incorporate physics beyond the Standard Model (BSM). Hence, experimental searches for EDMs bear the potential to reveal their various sources [2], but require a high statistical and systematical sensitivity. Although the search for permanent EDMs in neutral systems like neutrons already started decades ago, a non-vanishing value could not be observed up to now [1]. In general, the applied measurement methods aim for a detection of a spin polarization signal arising from the interaction of a potential EDM with electric fields. Since charged particles are accelerated by electric fields, experimental methods avoiding particle evasion from the experimental area are mandatory. For that reason, particle storage rings seem to be an ideal choice satisfying this requirement. EDM measurements for muons have already been performed in storage rings [3], while the current experimental EDM limit for protons is deduced from theoretical considerations applied to the results of atomic EDM measurements [4]. Future direct measurements for proton and deuteron are proposed in dedicated storage rings utilizing pure electric or a combination of electric and magnetic fields [5, 6]. Feasibility studies are conducted within the JEDI (Jülich Electric Dipole moment Investigations) collaboration at the existing storage ring [7], the Cooler Synchrotron COSY [8, 9]. The magnetic ring COSY accelerates and stores polarized protons and deuterons with a momentum up to 3.8 GeV/c. A first direct measurement of the deuteron EDM is foreseen. The experimental requirements are investigated by measurements and theoretical considerations, which demand a precise model of the storage ring. One of the existing models is based on the software framework COSY INFINITY [10]. Within the scope of this thesis a comprehensive extension and benchmarking of this model has been performed. Experimental efforts have been carried out and accompanied to validate the new algorithms implemented to this model. The structure of this thesis is designed as follows.

Chapter 2 gives a general definition of EDMs, an overview of theoretical sources and their connection to a matter antimatter asymmetry in the Universe. Furthermore the current experimental results for neutral and charged particles, i.e. proton and electron are discussed.

Chapter 3 illustrates the beam and spin dynamics in particle storage rings. Relevant storage ring parameters characterizing the particle motion like tunes, chromaticities and momentum compaction factor are described. Important spin resonances and their connection to EDM measurement methods in storage rings are pointed out.

Chapter 4 depicts the Cooler Synchrotron COSY and its magnetic lattice setup. Additionally, the experimental setup and data acquisition of the polarization experiments are discussed.

In Chapter 5 the associated simulation framework used for accelerator and storage ring modeling is illustrated. The development of new algorithms, i.e. for the simulation of radiofrequency (RF) fields in the simulation framework, is presented. Finally, the benchmarking results of the calculated storage ring parameters compared to measurement results is shown.

In Chapter 6 the benchmarking process of the static storage ring is continued and an important quantity for EDM measurements in storage rings, the spin coherence time, is discussed. The connection of storage ring parameters to the spin coherence time is pointed out. Required conditions of the lattice setup to achieve long spin coherence times are evaluated and verified by measurements.

In Chapter 7 the implementation of RF fields is tested. Oscillations of the spin polarization induced by an RF solenoid are investigated and compared to particle tracking simulations and analytical estimates.

Chapter 8 makes use of the validated algorithms to depict the EDM measurement method and the expected polarization signal. Systematic contributions mimicking an EDM like signal are examined by introducing misalignments of the storage ring elements. The prospects of orbit correction routines to reduce this contributions are explored.

In Chapter 9 the results are summarized and an outlook is given.

Chapter 2

Motivation

This thesis is written in the context of the recently founded JARA-section: FAME[1]. One task of this section is the search for mechanisms, which are responsible for the matter-antimatter asymmetry in the Universe. The focus of this thesis is the investigation of electric dipole moment (EDM) measurements in storage rings. Permanent EDMs of particles are generated by processes and interactions that violate parity and time reversal transformations. The latter are connected to CP violation, as mentioned in Section 2.2.3. These processes are a postulated requirement for the creation of the matter-antimatter asymmetry in Universe. Details about the asymmetry, the fundamental discrete symmetries in physics as well as EDMs are discussed in this chapter.

2.1 Matter-Antimatter Asymmetry

The matter-antimatter asymmetry is one of the big, unsolved puzzles of cosmology. Astrophysical observations show, that at least the known part of the Universe is matter dominated and there is no evidence for primordial antimatter [11, 12]. This excess of matter can be expressed by the baryon-to-photon density ratio, also known as baryon asymmetry, η_{BAU}. This quantity is used as parameter for cosmological models and can be measured in two independent ways [13]. From Big-Bang-Nucleosynthesis (BBN) and from the angular distribution of the cosmic microwave background (CMB). Both approaches have been investigated and result in [14, 15]:

$$\eta_{\mathrm{BAU}} = \frac{n_B - n_{\bar{B}}}{n_\gamma} = (6.047 \pm 0.074) \cdot 10^{-10} (\mathrm{CMB}) \ , \tag{2.1}$$

$$5.7 \cdot 10^{-10} \leq \eta_{\mathrm{BAU}} \leq 6.7 \cdot 10^{-10} (\mathrm{BBN}, 95\,\%\ \mathrm{C.\ L.}) \ . \tag{2.2}$$

Here, n_B ($n_{\bar{B}}$) denotes the baryon (anti-baryon) density, and n_γ the photon density. In fact, the anti-baryon density is zero. But, according to theory, an equal amount of matter and antimatter produced in the big bang is predicted. Two explanations could resolve the reason for the measured asymmetry:

1. Separated regions of matter and antimatter could have been formed during the evolution of the Universe and the milky-way is part of a matter dominated region.

2. Asymmetric annihilation processes of matter and antimatter result in the measured excess of matter.

[1] Jülich Aachen Research Alliance - Forces and Matter Experiments

The former case could be identified by the measurement of a single heavy nuclei in primary cosmic rays. Since the production of secondary anti-nuclei is strongly suppressed, a single anti-nucleus of ^{3}He or preferably carbon would be enough for an indication of anti-stars and anti-galaxies in the Universe [16]. The search is currently performed experimentally by the AMS experiment [17], which is also part of the JARA-FAME section.

For the latter case (asymmetric annihilation), the following three conditions formulated by Sakharov [18] need to be fulfilled:

1. **Baryon number violation**: Obviously, there must be processes, which violate the baryon number conservation, otherwise no asymmetry between baryons and anti-baryons could be generated.

2. **Violation of C and CP symmetries**: Processes must violate charge conjugation symmetry (C) and charge conjugation plus parity transformation symmetry (CP). This is required to produce an imbalance in the production of baryons and anti-baryons.

3. **The Universe is out of thermal equilibrium**: In thermal equilibrium each process occurs as often as its reverse process and there would be no net change of baryon numbers.

CP violating processes can manifest in EDMs. This will be discussed in the following sections.

2.2 Discrete Symmetries and Their Violation

The conservation of fundamental symmetries plays an important role in physics [13]. The search for violations has been of particular interest in the 20$^{\text{th}}$ century [19]. Especially the three discrete symmetries: Parity transformation, charge conjugation transformation and time reversal transformation symmetry have been tested.

2.2.1 Parity Transformation

Parity transformation symmetry implies that a physical process will perform exactly equal as its mirror image (i.e. under the transformation $\vec{x} \rightarrow -\vec{x}$). In 1956, Lee and Yang recognized that there is no experimental confirmation of this symmetry in weak processes yet, while there is strong evidence for this symmetry in the strong and electromagnetic interactions [20]. They suggested to investigate parity violation in beta decays. Only one year later, Wu et al. performed an experiment observing the beta decay of polarized ^{60}Co [21]:

$$^{60}\mathrm{Co} \rightarrow {}^{60}\mathrm{Ni} + e^- + \bar{\nu}_e \ . \tag{2.3}$$

In this process, the electron is emitted in the direction opposite to the nuclear spin. Since the velocity flips sign under parity transformation, this result was the first proof of parity violation. A further important milestone was achieved by the observation of charged pion decays [22, 23, 24]:

$$\pi^- \to \mu^- + \bar{\nu}_\mu \ , \tag{2.4}$$
$$\pi^+ \to \mu^+ + \nu_\mu \ . \tag{2.5}$$

By measuring the spin of the emitted muon, it was observed that the neutrino spin is always anti-aligned to the flight direction, while it is aligned in case of an anti-neutrino. If one assumes massless neutrinos, this result is Lorentz-invariant and fixes the helicity of the neutrino. Thus, there are only left-handed neutrinos and right-handed anti-neutrinos [11].

2.2.2 Charge Conjugation Transformation

The second discrete symmetry is the charge conjugation transformation symmetry. A charge conjugation transformation converts each particle into its antiparticle. The process in Equation 2.5 is transformed as follows:

$$\begin{aligned} &\pi^+ \to \mu_L^+ + \nu_{\mu,L} \\ \xrightarrow{C}\ &\pi^- \to \mu_L^- + \bar{\nu}_{\mu,L} \ . \end{aligned} \tag{2.6}$$

As shown previously, a left-handed anti-neutrino does not occur. Thus, pion decay processes are a perfect example of the C symmetry violation in the weak sector.

2.2.3 Time Reversal Transformation

The third discrete symmetry is the time reversal transformation symmetry. It implies that the rates of any physical process are equal, if it runs reverse in time ($t \to -t$). Tests of this symmetry in strong and electromagnetic interactions showed no evidence of violation. The first direct observation of T violation in the weak sector was measured in the decay of neutral kaons [25]. In general, direct measurements of T violation in the weak sector are hard to perform, since strong and electromagnetic processes are naturally stronger [11]. A suitable different approach is to take the CPT theorem into account [26]. According to this theorem, the application of C, P and T transformation, taken in any order, results in a symmetric process for any "quantum field theory based on a Hermitian, local (no action at a distance), normal-ordered Lagrangian which is invariant under Lorentz transformations, and for which the usual field commutation or anti-commutation rules hold" [13]. Therefore, a T violating process is CP violating at the same time and vice versa.

2.2.4 CP Violation

As previously shown, the pion decay violates both P and C symmetries. Applying a combined CP transformation the pion decay process in Equation 2.4 transforms to Equation 2.5 and at the same time also converts the particles from a left-handed to a right-handed state. As a consequence, the pion decay processes conserve CP symmetry.

Instead, violation of CP symmetry was first observed in the neutral kaon sector. As pointed out by Gell-Mann and Pais, the neutral kaon can transform into its antiparticle (kaon-mixing) [27]. This process performs by interchange of two virtual W-bosons. The two kaon states can be expressed in the two mass eigenstates K_S and K_L, which have different lifetimes. In the Fitch-Cronin experiment in 1964 [28], CP violation was detected by measuring the decay rates of K_L into two- and three pions. If K_L had been a pure CP eigenstate, the decay into two pions would not have been possible, but instead a few decays into two pions have been measured. The observed CP violation could be incorporated into the Standard Model via the CKM-Matrix (Cabibbo-Kobayashi-Maskawa) [29, 30], but this required the proposal of three generations of quarks, even before the charm quark was detected. Nevertheless, this extension turned out to be successful. In more recent experiments, the CP violation was also observed in the B meson sector [31, 32]. The CP violation generated by the CKM mechanisms seems to be not sufficient to explain the matter-antimatter-asymmetry [33, 34]. Therefore, also permanent EDMs are proper candidates to search for additional CP violating sources as discussed in the next section.

2.3 Electric Dipole Moments

2.3.1 Definition

In electrodynamics, the EDM is defined as a separation of the "centers of gravity" of positive and negative charges in a system. In case of a continuous charge density $\rho(\vec{x})$ the EDM $\vec{d}^{ED}$ can be calculated as follows:

$$\vec{d}^{ED} = \int_V d\vec{x}\ \vec{x} \cdot \rho(\vec{x}) \ . \tag{2.7}$$

Analog the magnetic dipole moment (MDM) $\vec{\mu}^{ED}$ is defined as

$$\vec{\mu}^{ED} = \frac{1}{2} \int_V d\vec{x} \left(\vec{x} \times \vec{j}(\vec{x}) \right) \ . \tag{2.8}$$

Here, $j(\vec{x})$ denotes the current density. In particle physics, EDMs and MDMs are fundamental properties of particles. Since the spin quantization axis is the only marked direction, the dipole moments are defined either parallel or anti-parallel with respect to the spin direction [35]:

$$\vec{d} = \eta_{\mathrm{EDM}} \cdot \frac{q}{2mc} \vec{S} \ , \tag{2.9}$$

$$\vec{\mu} = g \cdot \frac{q}{2m} \vec{S} \ . \tag{2.10}$$

Here, q is the charge and m the mass of the particle. The speed of light is denoted as c and $\vec{S}$ is the spin. The dimensionless quantity g is called the g-factor, while in case of an EDM the parameter η_{EDM} is used as dimensionless scaling parameter. Since the neutron has no charge, the quantities for charge and mass of the proton are used in this case.

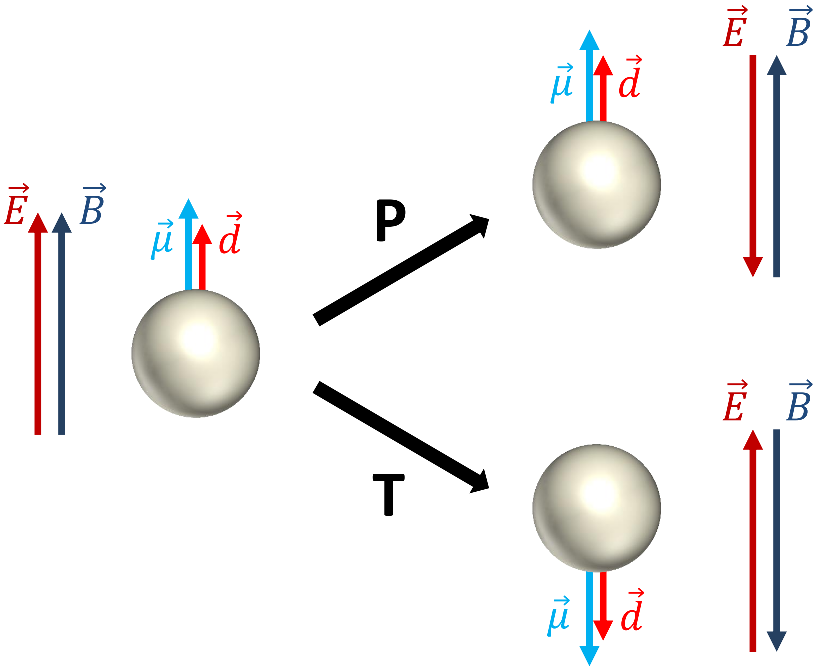

Figure 2.1: Schematic drawing of a particle with electric and magnetic dipole moment in electromagnetic fields. Applying a parity transformation flips only the sign of the electric field. A time reversal transformation flips the two dipole moments, provided that they are associated to the spin vector and η and g are scalars. In addition, the magnetic field changes its direction. Thus, both symmetries are violated in case of a nonzero EDM.

For a (neutral) particle with EDM and MDM in electromagnetic fields the non-relativistic Hamiltonian reads [1]:

$$H = -\vec{\mu}\vec{B} - \vec{d}\vec{E} \; . \tag{2.11}$$

In case of a P transformation, only the electric field E flips its sign, while for a T transformation the dipole moments and the magnetic field B are inverted. Thus, both parity transformation and time reversal transformation symmetry are violated, if $d \neq 0$. This is illustrated in Figure 2.1. Assuming the CPT theorem to be valid, this directly implies CP violation as well.

2.3.2 CP Violating Sources

The weak and strong sectors of the SM contain CP violating sources. Considering also various extensions of the Standard Model, the contributing CP violating processes to EDMs of different particles are manifold.

2.3.2.1 Weak Sector of the Standard Model

The only established sources of CP violation in the SM are contained in the already mentioned CKM-Matrix in the quark sector and, in case of massive neutrinos, its counterpart, the PMNS-Matrix (Pontecorvo-Maki-Nakagawa-Sakata) [36, 37] in the lepton sector. The CKM-Matrix V can be parametrized as [38]:

$$\begin{pmatrix} d' \\ s' \\ b' \end{pmatrix} = V \cdot \begin{pmatrix} d \\ s \\ b \end{pmatrix}, \quad V = \begin{pmatrix} c_{12}c_{13} & s_{12}c_{13} & s_{13}e^{-i\delta} \\ -s_{12}c_{23} - c_{12}s_{23}s_{13}e^{i\delta} & c_{12}c_{23} - s_{12}s_{23}s_{13}e^{i\delta} & s_{23}c_{13} \\ s_{12}s_{23} - c_{12}c_{23}s_{13}e^{i\delta} & -c_{12}s_{23} - s_{12}c_{23}s_{13}e^{i\delta} & c_{23}c_{13} \end{pmatrix}. \tag{2.12}$$

Here, d, s, b characterize the flavor eigenstates of the d-type quarks, while d', s', b' denote the basis of eigenstates, which couple to the u-type quarks via exchange of a W-boson. Explicit values for the entries of the matrix have been constrained in measurements and are given in [39]. The phase δ accounts for the imaginary content of this matrix. The position of the phase factors in this matrix can vary in different parameterizations, but the so called Jarlskog invariant [40]

$$J_{CP} = |\mathrm{Im}(V_{ij}V_{kl}V_{il}^*V_{kj}^*)| \tag{2.13}$$

is fixed in any parametrization and directly connected to CP violation. CP symmetry is conserved, if

$$2i(m_t^2 - m_c^2)(m_t^2 - m_u^2)(m_c^2 - m_u^2)(m_b^2 - m_s^2)(m_b^2 - m_d^2)(m_s^2 - m_d^2)J_{CP} \tag{2.14}$$

vanishes [13]. The current measured result for the Jarlskog invariant is [39]

$$J_{CP} = 3.06^{+0.21}_{-0.20} \cdot 10^{-5}. \tag{2.15}$$

It has been shown, that the one-loop level and two-loop level Feynman diagrams using only the CKM mechanism do not contribute to a non-vanishing quark EDM. At least three-loop level diagrams are required, which directly reveals the EDM suppression [19, 41]. This leads to estimates for the u-quark and d-quark in the order of [19]:

$$d_q^{\mathrm{CKM}} \simeq 10^{-34}\, e\,\mathrm{cm} - 10^{-35}\, e\,\mathrm{cm}\ . \tag{2.16}$$

For leptons the suppression is even stronger and the first non-vanishing contribution arises, when four-loop level diagrams are taken into account. This results in a significantly smaller EDM estimate for the electron [19, 42]:

$$d_e^{\mathrm{CKM}} \leq 10^{-38}\, e\,\mathrm{cm}\ . \tag{2.17}$$

In case of nucleon EDMs, the impact of the quark EDMs plays only a minor role. Considering effective field theory, the effects of CP-odd pion-nucleon couplings at one-loop level are dominating. For the neutron EDM, this leads to an estimate of [19, 43]:

$$d_n^{\mathrm{CKM}} \simeq 10^{-32}\, e\,\mathrm{cm}\ . \tag{2.18}$$

This estimate is many orders of magnitude smaller than the sensitivity of current experimental investigations. For that reason, further sources need to be scrutinized. They could lead to substantially larger EDMs required for an explanation of the matter-antimatter asymmetry in the Universe.

2.3.2.2 Strong Sector of the Standard Model

A further suitable source in the SM is known as the $\bar{\theta}$-term. The Lagrangian of the quantum chromodynamics (QCD) can be supplemented by an additional term [2]:

$$\mathcal{L}_{\bar{\theta}} = -\bar{\theta}\frac{g_s^2}{64\pi^2}\epsilon^{\mu\nu\alpha\beta}G^a_{\mu\nu}G^a_{\alpha\beta} \ , \tag{2.19}$$

where $G^a_{\mu\nu}$ denotes the gluon field strength tensor, $\epsilon^{\mu\nu\alpha\beta}$ is the total-asymmetric four-tensor, g_s denotes the strong coupling constant and $\bar{\theta}$ is a dimensionless parameter. The parameter $\bar{\theta}$ cannot be directly computed, but the EDMs of proton and neutron created by this contribution have been parametrized with respect to $\bar{\theta}$ in theoretical calculations, for instance in [44]:

$$d_n^{\bar{\theta}} = \bar{\theta}\cdot(-2.9\pm 0.9)\cdot 10^{-16}\,e\,\mathrm{cm} \ , \tag{2.20}$$

$$d_p^{\bar{\theta}} = \bar{\theta}\cdot(1.1\pm 1.1)\cdot 10^{-16}\,e\,\mathrm{cm} \ . \tag{2.21}$$

Naturally, $\bar{\theta}$ is expected to be $\mathcal{O}(1)$, but the present neutron EDM limit constrains [2]

$$\bar{\theta} < 10^{-10} \ . \tag{2.22}$$

The smallness of this parameter is a totally different situation with respect to the weak sector and therefore known as the strong CP problem. If one of the quark masses would be zero, the problem could be resolved and $\bar{\theta}$ could be set to zero. But experimental results suggest, that this solution is unlikely [13]. Another attempt to solve the problem required the postulation of a new particle, the axion, which has not been experimentally observed yet [45, 46, 47].

2.3.2.3 Sources Beyond the Standard Model

Various models beyond the Standard Model also include CP-odd contributions. Since these contributions can be substantially larger than in the weak sector, EDMs bear the potential to detect these sources. In Figure 2.2, a schematic overview including some of the BSM models and their possible contributions to various EDM observables is shown. For example, the left-right symmetric model primarily creates CP-odd four quark couplings, which could add to observable EDMs differently. Hence, EDM measurements for different particles could disentangle the sources beyond the Standard Model from the $\bar{\theta}$-term. In context of the proposed measurements for protons and light nuclei, this has been shown in [2]. For instance, the relation of the deuteron EDM d_d to the EDM of its constituents

$$d_d - d_p - d_n \tag{2.23}$$

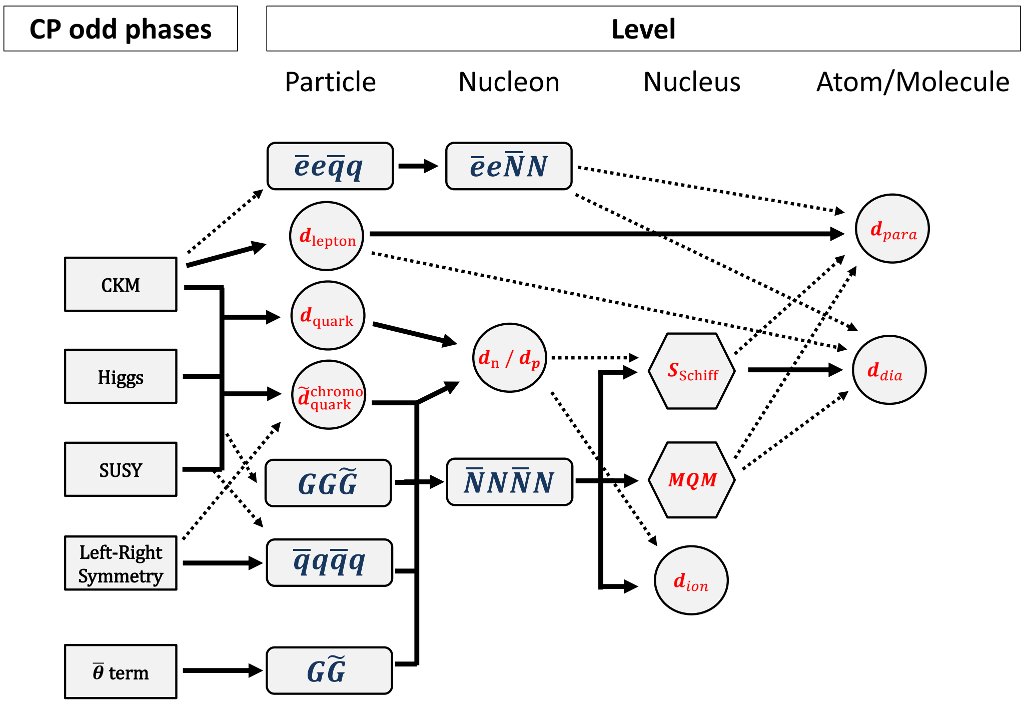

Figure 2.2: The connection of CP violating sources and the EDMs of various particles. The different momenta (EDM, magnetic quadrupole moment and Schiff moment) are shown in red, the effective couplings are shown in blue. Solid arrows represent a stronger contribution than dashed arrows (adapted from [19, 48, 49]).

indicates a suitable discrimination of the $\bar{\theta}$-term and BSM sources. In case of the $\bar{\theta}$-term, the deuteron EDM is mainly determined by the EDM of its constituents:

$$d_d^{\bar{\theta}} - d_p^{\bar{\theta}} - d_n^{\bar{\theta}} = \bar{\theta} \cdot (5.0 \pm 3.7) \cdot 10^{-17}\, e\,\mathrm{cm} \ , \tag{2.24}$$

while in other scenarios the contribution of the nucleon-nucleon interaction is estimated to be dominant:

$$\left| \frac{d_D - d_p - d_n}{d_p + d_n} \right| > 1 \ . \tag{2.25}$$

2.4 Experimental Searches in Neutral Systems

After pointing out the scientific prospects of EDM measurements for different particles, the experimental searches in neutral systems will be discussed in this section.

2.4.1 Neutron

Historically, the neutron was the first particle for which EDM measurements were proposed and conducted [1, 50]. The first neutron EDM experiment was performed in

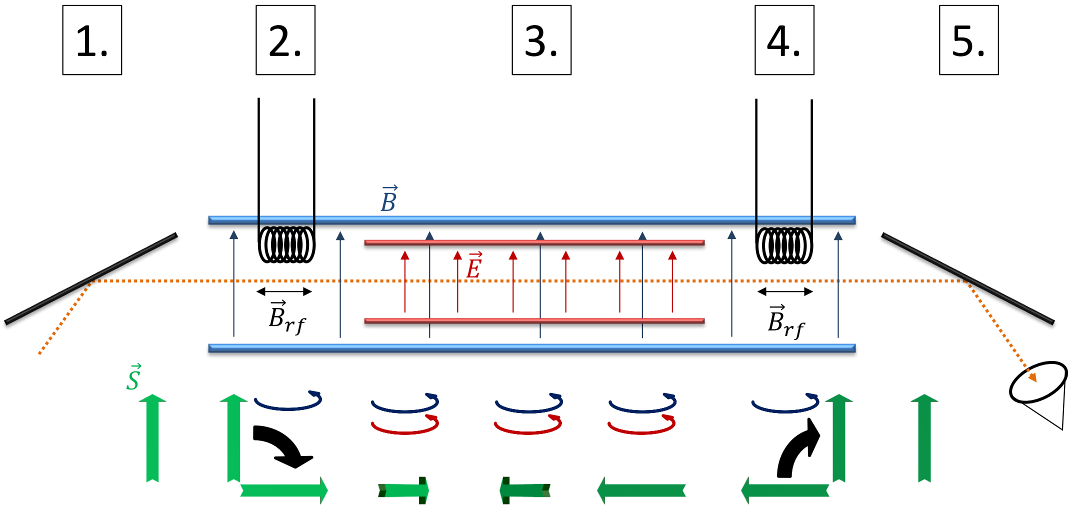

Figure 2.3: Ramsey's method of separated oscillatory fields consisting of five steps: (1.) Generating a spin-polarized ensemble. (2.) Inducing a $\pi/2$-pulse to flip the spin perpendicular to fields. (3.) Free precession in parallel magnetic and electric fields. (4.) Inducing a second $\pi/2$-pulse to flip the spin. (5.) Analyzing polarization of the ensemble (adapted from [1, 51]).

1949 at the Oak Ridge reactor [51]. Ramsey's method of separated oscillatory fields was applied to create an observable signal related to the EDM. This method will be subsequently outlined on basis of Figure 2.3 [1]. It consists of five steps:

1. A method to provide a neutron sample polarized parallel to the main magnetic field in the measurement apparatus is necessary. In the experiment discussed, the neutrons were created in the reactor and due to spin-dependent reverse scattering on a magnetic mirror, the neutron sample was spin-polarized and guided through the main apparatus.

2. While passing through the apparatus, an RF magnetic field is created by a coil. The frequency of the field is adjusted to the Larmor frequency of the neutrons in the main magnetic field. The superposition of the static field and the oscillatory field slowly moves the polarization into the plane perpendicular to the main magnetic field. This is called a $\pi/2$-pulse.

3. In the third step, the neutron sample enters a region of superimposed static magnetic and electric fields. Both fields are either aligned to anti-aligned to each other. They introduce a precession of the perpendicular polarization. The precession frequency is given by

$$\omega = \frac{2|\mu B \pm dE|}{\hbar} \ . \tag{2.26}$$

The sign between the two contributions refers to aligned or anti-aligned fields, respectively.

4. Behind the the electric field region, a second RF magnetic field induces another $\pi/2$-pulse to the spins of the neutrons. The frequencies of the RF fields in step 2 and 4 are equal. The phases are adjusted with respect to each other. Only the perpendicular polarization component, which is in phase with the RF field, flips slowly to the vertical direction, while the other component is essentially unchanged. Therefore the vertical polarization serves as a measure for the EDM and allows one to determine the frequency difference for aligned and anti-aligned fields:
$$\Delta\omega = \omega(E^{\uparrow\uparrow}) - \omega(E^{\uparrow\downarrow}) = \frac{4|d|E}{\hbar} \ . \tag{2.27}$$
The frequency slip transfers to a phase slip between the oscillatory field and the in-plane spin vector. Thus, the vertical polarization after the $\pi/2$-pulse can change.

5. The vertical polarization is measured, for instance by using the spin-dependent scattering on a magnetic mirror and counting the reflected neutrons.

The result of this first experiment could be converted to an upper neutron EDM limit of [51]
$$|d_n| < 5 \cdot 10^{-20}\, e\,\mathrm{cm} \ . \tag{2.28}$$
This method has established as the general method for neutron beam experiments.

A similar method is applied in more recent ultracold neutron (UCN) EDM experiments. In these experiments, very low energetic neutrons are contained in a storage cell. Static parallel magnetic and electric fields inside the cell are used to induce a spin precession. The small kinetic energy prevents them to overcome the effective potential barriers of the surrounding materials of below µeV. This neutron configuration allows to suppress systematic contributions arising from motional magnetic fields $\vec{v} \times \vec{E}$ [1]. The current upper limit was measured at the ILL experiment in Grenoble [52]. Two $\pi/2$-pulses with a duration of two seconds (now separated in time rather than location) have been used to flip the spin in the storage cell. The free precession lasts around 130 seconds. For further suppression of systematics mercury (^{199}Hg) was used as a magnetometer. Since the EDM limit of mercury is below the expected sensitivity of the neutron experiment, the introduced mimic EDM signal is minor. Overall the current most stringent neutron EDM limit amounts to [52]:

$$|d_n| < 2.9 \cdot 10^{-26}\, e\,\mathrm{cm} \ . \tag{2.29}$$

2.4.2 Diamagnetic and Paramagnetic Atoms and Molecules

Neutrons were the natural choice for the first EDM measurements, because they are not accelerated in external electric fields, like protons or electrons. Thinking of larger neutral systems like atoms and molecules introduces an additional challenge: The shielding effect. It states, that the the energy of a neutral system consisting of electrostatically interacting non-relativistic charged point-like particles with EDMs is unchanged by an external electric field, because the particles of the system rearrange themselves until the external field at each location is compensated and a new equilibrium is reached. Thus, there is no net acceleration of the system either [1]. This statement is called Schiff's theorem and has been quantum mechanically proven in [53]. The exact screening is violated, if one of the requirements (non-relativistic motion, point-like particles and only electrostatic interactions) is not fulfilled. Additionally, also CP-odd interactions of the constituents can contribute to atomic and molecule EDMs [54].

In diamagnetic atoms the finite size of the nucleus and magnetic plus higher-order interactions between nucleons and electrons give rise to an atomic EDM [55]. The so called Schiff moment is created by CP-odd nuclear forces. It can arise from the nucleon EDMs and CP-odd nucleon nucleon interactions and contributes to the electrostatic potential. Its interaction with the atomic electrons is the major contribution to the atomic EDM. This allows to deduce limits to the proton EDM using measurement in diamagnetic systems. Currently, the best limit was obtained in a measurement using mercury ^{199}Hg [4]. The atoms were polarized by a 254 nm laser system. The precession of the polarization was measured in two separated cells simultaneously. In one cell the static magnetic and electric field were aligned, in the other anti-aligned. The precession frequency was extracted continuously using polarized laser light. The EDM limit could be determined to [4]:

$$|d\left({}^{199}\mathrm{Hg}\right)| < 3.1 \cdot 10^{-29}\, e\,\mathrm{cm}\ . \tag{2.30}$$

Using the calculated contributions to the Schiff's moment [56], the proton EDM could be extracted indirectly from these results [4]:

$$|d_p| < 7.9 \cdot 10^{-25}\, e\,\mathrm{cm}\ . \tag{2.31}$$

Another class are the paramagnetic atoms and molecules, especially those with one unpaired electron. In this case, Schiff's theorem is evaded by relativistic effects [57] and the resulting atomic/molecular EDM can be interpreted in terms of the electron EDM [58]. The violation is stronger in heavy atoms, which leads to a substantially larger atomic EDM than the electron EDM. For thallium, the enhancement factor of the atomic EDM amounts to 585 [59]. In case of polar molecules, which are polarizable by a small external electric field, the violation due to relativistic effects is even stronger. Thus, the electron EDM interacts with a strong effective electric field, which drastically increases the frequency shift in any precession experiment. The current upper limit for the electron EDM was measured recently using the polar molecule thorium monoxide (ThO) [60]. In this experiment, the initial spin states of the ThO pulse were prepared and selected using laser pumping. As in all previously described methods, the spin precession was induced by parallel magnetic and electric fields. Afterwards a state readout laser was used to excite the ThO molecules and produce fluorescence light, which was measured in photomultipliers. The final result for the electron EDM was stated to [60]:

$$|d_e| < 8.7 \cdot 10^{-29}\, e\,\mathrm{cm}\ . \tag{2.32}$$

2.4.3 Summary

Up to now all EDM measurements result in upper limits. An overview of the current upper limits of the EDMs for a selection of particles is listed in Table 2.1. These measurements set stringent limits to extensions to the SM. For proton and electron the illustrated limits are deduced from indirect measurements in atoms and molecules. Therefore, the extraction requires a precise knowledge of the theory describing these

Table 2.1: Current upper limits of EDM searches in neutral systems.

System	Current EDM Limit
Neutron	$2.9 \cdot 10^{-26}\, e\,\mathrm{cm}$ (90 % C. L.) [52]
^{199}Hg	$3.1 \cdot 10^{-29}\, e\,\mathrm{cm}$ (95 % C. L.) [4]
Proton	$7.9 \cdot 10^{-25}\, e\,\mathrm{cm}$ (95 % C. L.) [4]
Electron	$8.7 \cdot 10^{-29}\, e\,\mathrm{cm}$ (90 % C. L.) [60]
Muon	$1.8 \cdot 10^{-19}\, e\,\mathrm{cm}$ (90 % C. L.) [3]

systems. Direct measurements of these EDMs could exclude uncertainties and verify the theoretical calculations. For charged particles, direct measurements in storage rings are an excellent opportunity. In the g−2 experiment, which was conducted to determine the anomalous magnetic moment a of the muon, a first direct measurement of the muon EDM was already performed [61, 3]. A new version of this experiment is currently setup [62, 63] and further measurements for protons and deuterons [5, 6] as well as light nuclei are proposed. As previously illustrated, the simultaneous measurement of EDMs in different systems allows for distinction of different CP violating sources, once non-vanishing EDMs will be found. In the next section, an introduction into beam and spin dynamics in accelerators and storage rings will be given. In this context, the muon measurement method is highlighted and the prospects for direct EDM measurements in storage rings will be discussed.

Chapter 3

Beam and Spin Dynamics in Storage Rings

The knowledge of beam and spin dynamics is essential for the investigation of EDM measurements in storage rings. In this chapter, an introduction into beam and spin dynamics is given and methods for EDM measurements in storage rings are presented. The description of the beam dynamics fundamentals are mainly taken from [64] and have been supplemented by information from [65, 66, 67, 68].

3.1 Beam Dynamics

A beam is defined as an ensemble of particles. The motion of each particle can be parametrized by its spatial coordinates and momentum. These coordinates form the six dimensional phase space in beam dynamics. The evolution of the particle coordinates in phase space is given by the equations of motion of the system.

3.1.1 Coordinate System

Naturally, the time t is often chosen as independent variable to express the evolution of a system in physics. In beam dynamics this choice is rather inconvenient. A particle accelerator usually consists of a set of deflectors or magnets with time-independent, static fields to guide and focus the beam. In the following, the description will focus on planar storage rings build-up by pure magnetic elements. Usually, these storage rings are made up of straight and arc sections. The electromagnetic fields of the storage ring elements define the reference orbit $\vec{r}_{\mathrm{ref}}(s)$, which is curved in case of a non-vanishing field. Here, the arc length s is chosen as independent variable, since the electromagnetic fields are usually known with respect to their location.

A beam usually consists of a set of particles following phase space trajectories close to the reference orbit. Therefore, a more convenient coordinate system is chosen to describe the motion. A reference particle is defined, which moves exactly on the reference orbit $\vec{r}_{\mathrm{ref}}$ and has the reference momentum $\vec{p}_{\mathrm{ref}}$ of the beam. A new Cartesian coordinate system is specified, whose origin moves and coincides with the position of this reference particle. In Figure 3.1, this is illustrated for the movement from an initial position s_i to a final position s_f on the reference orbit. The first basis vector $\vec{e}_s$ always points parallel to $\vec{p}_{\mathrm{ref}}$. The second basis vector $\vec{e}_x$, perpendicular to $\vec{e}_s$, lies in the plane of the storage ring (planar ring). The third vector completes the basis and is

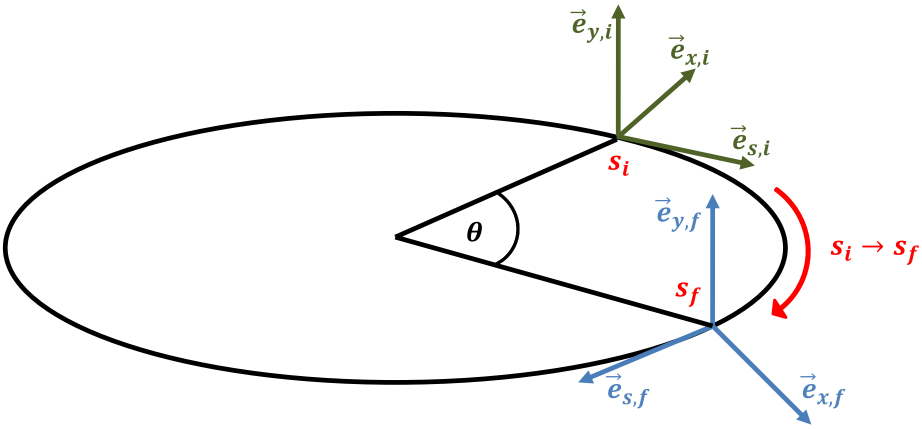

Figure 3.1: Illustration of the common co-moved Cartesian coordinate system used for the description of beam dynamics in accelerator physics. The corresponding coordinates (x, y, s) are called curvilinear coordinates.

given by $\vec{e}_y = \vec{e}_s \times \vec{e}_x$. The transformation of the basis vectors from s_i to s_f is defined by a simple rotation [66]:

$$\vec{e}_{x,f} = \cos(\theta)\vec{e}_{x,i} + \sin(\theta)\vec{e}_{s,i} \ , \tag{3.1}$$

$$\vec{e}_{y,f} = \vec{e}_{y,i} \ , \tag{3.2}$$

$$\vec{e}_{s,f} = -\sin(\theta)\vec{e}_{x,i} + \cos(\theta)\vec{e}_{s,i} \ . \tag{3.3}$$

with

$$\theta = \int_{s_i}^{s_f} \frac{\mathrm{d}s}{\rho(s)} = \int_{s_i}^{s_f} h(s)\mathrm{d}s \ . \tag{3.4}$$

Here, $\rho(s)$ denotes the bending radius of the reference orbit and $h(s)$ is its inverse, the curvature. The evolution of the basis vectors is characterized by:

$$\frac{\mathrm{d}}{\mathrm{d}s}\vec{e}_x = h(s)\vec{e}_s \ , \quad \frac{\mathrm{d}}{\mathrm{d}s}\vec{e}_s = -h(s)\vec{e}_x \ . \tag{3.5}$$

Now, the particle coordinates are given with respect to the origin of the new coordinate system. Since these relative deviations can be considered as small, perturbative techniques can be used to describe the motion and analyze the system [64]. Given the position (momentum) of the particle in the lab frame $\vec{r}$ ($\vec{p}$), the projections of $\vec{r} - \vec{r}_{\mathrm{ref}}$ ($\vec{p} - \vec{p}_{\mathrm{ref}}$) on $\vec{e}_x$ and $\vec{e}_y$ are denoted as the radial and vertical coordinates x and y (p_x and p_y), respectively. Furthermore, the momenta are normalized by the reference momentum $p_0 = |\vec{p}_{\mathrm{ref}}|$ resulting in $a = p_x/p_0$ and $b = p_y/p_0$. The subscript “0” denotes the reference particle in the initial state (not taking possible acceleration and deceleration in electric fields into account). Finally, the four coordinates x, a, y, b can be used to fully describe the transverse motion of each particle.

The longitudinal phase-space can be characterized by the deviation of the initial kinetic energy K of a single particle with respect to the reference particle K_0:

$$\delta_K = \frac{K - K_0}{K_0} \ . \tag{3.6}$$

Together with the space-like variable

$$l_K = -v_0 \frac{\gamma_0}{1+\gamma_0}(t - t_0) = -\kappa \Delta t \ , \tag{3.7}$$

it forms a canonical conjugate pair. Here, v_0 denotes the velocity and γ_0 denotes the Lorentz factor of the reference particle. In magnetic rings, the curvature in a magnetic field is proportional to the momentum rather than the kinetic energy. For that reason often the momentum difference is used:

$$\delta = \frac{p - p_0}{p_0} \ . \tag{3.8}$$

There are also different conventions used for the second longitudinal coordinate:

$$\Delta t = t - t_0 \ , \tag{3.9}$$

$$l = -v_0 \Delta t \ , \tag{3.10}$$

$$\phi = \omega \Delta t \ . \tag{3.11}$$

Using these six variables one can define a phase space vector containing the coordinates of one particle [64]:

$$\vec{z} = (x, a, y, b, l_K, \delta_K)^T \ . \tag{3.12}$$

The coordinate evolution from the location s_i to s_f can be obtained from the transfer map of the system:

$$\vec{z}(s_f) = \mathcal{M}(s_f, s_i)\,(\vec{z}(s_i)) \ . \tag{3.13}$$

The transfer map can be expanded in a Taylor series of the phase space coordinates. A constant part does not exist, since the reference particle coincides with the origin of the coordinate system by definition[2]. The first order expansion forms a so called transfer matrix $\hat{M}$. Assuming that all non-linear terms vanish, the motion of the system can be fully described by matrix multiplications:

$$\vec{z}(s_f) = \hat{M}(s_f, s_i) \cdot \vec{z}(s_i) \ . \tag{3.14}$$

Unfortunately, the study of the non-linear terms is often crucial, for example, to determine the long-term stability of a system. Therefore, more complex forms of $\mathcal{M}$ are mandatory.

[2]In context of this thesis, the term reference particle is used for a particle traveling on the design orbit. As soon as perturbing fields from imperfections or RF fields are introduced, this particle might be deflected and leaves the design orbit of the accelerator, while the origin of the reference coordinate system remains on the design orbit

3.1.2 Equations of Motion

The equations of motion for a relativistic particle in electromagnetic fields in a Cartesian coordinate can be expressed as:

$$\frac{\mathrm{d}\vec{r}}{\mathrm{d}t} = \vec{v} \ , \tag{3.15}$$

$$\frac{\mathrm{d}\vec{p}}{\mathrm{d}t} = \vec{F} = q\left(\vec{E} + \vec{v} \times \vec{B}\right) \ . \tag{3.16}$$

Equation 3.15 is the definition of the velocity v, while Equation 3.16 is the Lorentz force law. In the following, the contributions from gradients and higher moments have been neglected The position vector is given by $\vec{r}$ and the momentum vector is denoted by $\vec{p}$. Here, $\vec{E}$ and $\vec{B}$ are the magnetic and electric fields, respectively. These equations need to be transformed into curvilinear coordinates with s as independent variable. This is described in [64]. In a first step, the equations for the space-like variables are derived. In the following, the derivative with respect to s is denoted with the superscript "$'$". In case of a curved trajectory, the derivative of the path-length L of a particle depends on the horizontal position x in phase space:

$$L' = 1 + hx \ . \tag{3.17}$$

This reflects, that the circumference of a circle is proportional to its radius. Consequently, the first two equations for transverse motion are given by [64]:

$$x' = L'\frac{\mathrm{d}x}{\mathrm{d}L} = (1+hx)\frac{p_x}{p_s} = (1+hx)\frac{p_0}{p_s} \cdot a \ , \tag{3.18}$$

$$y' = L'\frac{\mathrm{d}y}{\mathrm{d}L} = (1+hx)\frac{p_y}{p_s} = (1+hx)\frac{p_0}{p_s} \cdot b \ . \tag{3.19}$$

These relations can be used to express the evolution of time along s:

$$t' = \frac{1}{v}\sqrt{x'^2 + y'^2 + L'^2} = \frac{1}{v}(1+hx)\frac{p}{p_s} \tag{3.20}$$

with $p = |\vec{p}|$.

For the longitudinal space-like coordinate, the energy change due to electric fields has to be taken into account. Therefore, a new quantity η is defined, which expresses the ratio of kinetic energy to the energy equivalent of the rest mass:

$$\eta = \gamma - 1 = \frac{K_0(1+\delta_K) - qV}{mc^2} = \eta_0(1+\delta_K) - \frac{qV}{mc^2} \ , \tag{3.21}$$

$$V = -\int \vec{E}(x,y,s,t) \cdot \vec{v}\,\mathrm{d}t \ . \tag{3.22}$$

The energy changes collected along s, which in general are position and time dependent, are contained in η. Finally, the derivative of l_K with respect to s can be expressed as:

$$l_K' = -v_0\frac{\gamma_0}{1+\gamma_0}(t' - t_0') = -\frac{1+\eta_0}{2+\eta_0}\left[(1+hx)\frac{1+\eta}{1+\eta_0}\frac{p_0}{p_s} - 1\right] \ , \tag{3.23}$$

yielding the third equation of motion.

To derive the equations of motion of the momentum-like variables, Equation 3.16 has to be transformed into the curvilinear coordinate system. Taking Equation 3.5 into account, it follows:

$$\begin{aligned}
\frac{\mathrm{d}}{\mathrm{d}s}\vec{p}(s) &= \frac{\mathrm{d}}{\mathrm{d}s}(p_x\vec{e}_x + p_y\vec{e}_y + p_s\vec{e}_s) \\
&= (p'_x\vec{e}_x + p'_y\vec{e}_y + p'_s\vec{e}_s) + (p_x\vec{e}\,'_x + p_y\vec{e}\,'_y + p_s\vec{e}\,'_s) \\
&= (p'_x\vec{e}_x + p'_y\vec{e}_y + p'_s\vec{e}_s) - h(s)\vec{e}_y \times \vec{p}(s) \qquad (3.24) \\
&= \vec{F}(s)t' \\
\Rightarrow \quad \frac{\mathrm{d}}{\mathrm{d}s}(p_x, p_y, p_s) &= \vec{F}(s)t' + h(s)\cdot(p_s, 0, -p_x) \ .
\end{aligned}$$

Using Equations 3.20 and 3.21, the first term can be expressed as:

$$\vec{F}(s)t' = q(\vec{E} + \vec{v}\times\vec{B})t' = (1+hx)\left[\frac{1+\eta}{1+\eta_0}\frac{\vec{E}}{\chi_{\mathrm{e}0}}\frac{p_0^2}{p_s} + \vec{p}\times\frac{\vec{B}}{\chi_{\mathrm{m}0}}\frac{p_0}{p_s}\right] \ . \qquad (3.25)$$

Here, the quantities magnetic rigidity and electric rigidity

$$\chi_{\mathrm{m}} = \frac{p}{q} \quad \text{and} \quad \chi_{\mathrm{e}} = \frac{pv}{q} \qquad (3.26)$$

have been introduced. Dividing Equation 3.24 by p_0 results in the equations of motion for the transverse momentum-like variables:

$$a' = (1+hx)\left[\frac{1+\eta}{1+\eta_0}\frac{E_x}{\chi_{e0}}\frac{p_0}{p_s} + \frac{B_s}{\chi_{m0}}\frac{p_0}{p_s}b - \frac{B_y}{\chi_{m0}}\right] + h\frac{p_s}{p_0} \ , \qquad (3.27)$$

$$b' = (1+hx)\left[\frac{1+\eta}{1+\eta_0}\frac{E_y}{\chi_{e0}}\frac{p_0}{p_s} - \frac{B_s}{\chi_{m0}}\frac{p_0}{p_s}a + \frac{B_x}{\chi_{m0}}\right] \ . \qquad (3.28)$$

The derivative of the sixth variable vanishes by definition:

$$\delta'_K = 0 \ , \qquad (3.29)$$

since all energy changes are treated in η. In many applications, δ_K is used to investigate the evolution of energy deviations along s. In this case, the magnitude of V needs to be regularly absorbed into δ_K.

Note, that the same set of linear equations of motion can be derived using Lagrangian and Hamiltonian methods in curvilinear coordinates. The Lagrangian for a charged particle in an electromagnetic field is given as follows [69]:

$$L(s,x,y,\dot{s},\dot{x},\dot{y};t) = -mc^2\sqrt{1-\frac{\vec{v}^2}{c^2}} - e\Phi + e\vec{v}\cdot\vec{A} \ , \qquad (3.30)$$

$$\vec{v}^2 = v_s^2 + v_x^2 + v_y^2 \ , \qquad (3.31)$$

$$\vec{v}\cdot\vec{A} = v_sA_s + v_xA_x + v_yA_y \ . \qquad (3.32)$$

Here, m and e denote the mass and the charge of the particle, Φ is the electrostatic potential and $\vec{A}$ is the magnetic vector potential. The speed of light is given as c. To derive the equations of motion in curvilinear coordinates, the common Hamiltonian is computed and a Legendre transformation is used to change the independent variable to s. A detailed description of this method is given in [69].

In summary, the equations of motion of the system in curvilinear coordinates are given by [64]:

$$x' = (1+hx)\frac{p_0}{p_s} \cdot a \ , \tag{3.33}$$

$$a' = (1+hx)\left[\frac{1+\eta}{1+\eta_0}\frac{E_x}{\chi_{e0}}\frac{p_0}{p_s} + \frac{B_s}{\chi_{m0}}\frac{p_0}{p_s}b - \frac{B_y}{\chi_{m0}}\right] + h\frac{p_s}{p_0} \ , \tag{3.34}$$

$$y' = (1+hx)\frac{p_0}{p_s} \cdot b \ , \tag{3.35}$$

$$b' = (1+hx)\left[\frac{1+\eta}{1+\eta_0}\frac{E_y}{\chi_{e0}}\frac{p_0}{p_s} - \frac{B_s}{\chi_{m0}}\frac{p_0}{p_s}a + \frac{B_x}{\chi_{m0}}\right] \ , \tag{3.36}$$

$$l'_K = -\frac{1+\eta_0}{2+\eta_0}\left[(1+hx)\frac{1+\eta}{1+\eta_0}\frac{p_0}{p_s} - 1\right] \ , \tag{3.37}$$

$$\delta'_K = 0 \ , \tag{3.38}$$

with

$$\frac{p_0}{p_s} = \sqrt{\frac{\eta(2+\eta)}{\eta_0(2+\eta_0)} - a^2 - b^2} \ . \tag{3.39}$$

3.1.3 Field Expansion

In this section, the field expansions of electric and magnetic fields in curvilinear coordinates are discussed. Assuming time-independent fields in a planar ring, both fields can be expressed by scalar potentials V, which satisfy Laplace's equation [64]:

$$\Delta V = \frac{1}{1+hx}\frac{\partial}{\partial x}\left((1+hx)\frac{\partial V}{\partial x}\right) + \frac{1}{1+hx}\frac{\partial}{\partial s}\left((1+hx)\frac{\partial V}{\partial s}\right) + \frac{\partial^2 V}{\partial y^2} = 0 \ . \tag{3.40}$$

Using an ansatz

$$V(x,y,s) = \sum_{k=0}^{\infty}\sum_{l=0}^{\infty} a_{k,l}(s) \cdot \frac{x^k y^k}{k!l!} \tag{3.41}$$

and inserting it into Equation 3.40 leads to an recursion relation for the coefficients $a_{k,l}(s)$. All coefficients $a_{k,l}(s)$ can be calculated from given values of $a_{k,0}(s)$ and $a_{k,1}(s)$.

In accelerator physics, the fields are usually characterized in terms of multipole components. For simplification the following discussion focuses on s-independent magnetic potentials, which excludes longitudinal fields. Furthermore,it is assumed, that each multipole order is spatially separated from each other. Thus, the curvature vanishes ($h = 0$) except for dipole fields. The dipole field terms in V are defined by $k + l = 1$. For an ideal planar ring the radial magnetic fields B_x vanish. This requires $a_{1,0} = 0$ for the magnetic case. The second parameter $a_{0,1}$ defines the vertical dipole field strengths. The next higher order is given by the quadrupole terms, characterized by $k+l = 2$. Here, the parameter $a_{1,1}(s)$ defines the gradient of a normal quadrupole field, which is mainly used for beam focusing. Rotating a normal quadrupole by 45° around the s-axis results in a skew quadrupole, which is commonly used for correction of the coupling between the horizontal and vertical phase spaces. The parameter $a_{2,0}(s)$ equals to half of its gradient. Each quadrupole field can be represented by a superposition of normal and skew part. The highest order considered are the sextupole fields, which are described by the coefficients with $k+l=3$. They can also be characterized by their normal ($a_{2,1}(s)$) and skew terms ($a_{3,0}(s)$, rotation by 30°). Since the resulting fields are non-linear, they contribute to non-linear transverse motion. Taking only normal components into account, the normalized fields can be expanded to [67]:

$$\frac{B_x(x,y)}{\chi_{m0}} = 0 - k \cdot y + k_2 \cdot xy + \dots \ , \tag{3.42}$$

$$\frac{B_y(x,y)}{\chi_{m0}} = h - k \cdot x + \frac{1}{2} k_2 \cdot (x^2 - y^2) + \dots \ . \tag{3.43}$$

Here, k and k_2 denote the quadrupole and sextupole strengths, respectively.

3.1.4 Transverse Motion

In this section, the linear motion in the transverse phase space in case of a storage ring built up only by transversal magnetic fields will be discussed. Allowing only components to linear order, the horizontal and vertical motion decouples and is similar. In this case, the Equations 3.33 and 3.34 can be simplified to:

$$x' = a \ , \tag{3.44}$$

$$\begin{aligned} a' &= (1+hx)\left(-\frac{B_y}{\chi_{m0}}\right) + h\left(1 + \frac{1+\eta_0}{2+\eta_0}\delta_K\right) \\ &= (1+hx)(-(h-k\cdot x)) + h + h\delta \\ &= -(h^2-k)x + h\delta \ . \end{aligned} \tag{3.45}$$

In the last step, the variable δ_K has been transformed to the relative momentum difference δ, since it is more suitable in case of only magnetic fields. Equations 3.44 and 3.45 can be combined to an inhomogeneous differential equation of second order [66]:

$$x'' + (h^2 - k)x = h\delta \tag{3.46}$$

and similar for the vertical case:

$$y'' + ky = 0 \ . \tag{3.47}$$

Thus, a positive k refers to horizontal defocusing and vertical focusing simultaneously. Assuming no momentum deviation ($\delta = 0$), Equation 3.46 transforms into an equation of Hill's type [70]. It is similar to an harmonic oscillator except the s-dependent frequency, which is not necessarily constant, but periodic. In a storage ring of length C_0, the following relation holds:

$$K(s + C_0) = K(s) \quad \text{with} \quad K(s) \equiv h^2(s) - k(s) \ . \tag{3.48}$$

The solution of the homogeneous part of Equation 3.46 can be written as:

$$x(s) = \sqrt{\varepsilon \cdot \beta(s)} \cos\left(\Psi(s) + \Psi_{s_0}\right) \ . \tag{3.49}$$

Insertion leads to the relations:

$$\frac{1}{2}\beta\beta'' - \frac{1}{4}\beta'^2 + K(s)\beta = 1 \ , \tag{3.50}$$

$$\Psi(s) = \int_{s_0}^{s} \frac{1}{\beta(\tilde{s})} \mathrm{d}\tilde{s} \ . \tag{3.51}$$

The constant parameter ε will be discussed in the subsequent section. The parameters $\beta(s)$ and $\Psi(s)$ are called the betatron function and betatron phase, respectively. The betatron function can be obtained by numerical integration or from the linear part of the transfer map.

3.1.4.1 Phase Space Ellipse and Beam Emittance

Equation 3.49 and its first derivative can be combined by eliminating the betatron phase $\Psi(s) + \Psi_{s_0}$. This results in an ellipse equation given by:

$$\gamma(s)x^2(s) + 2\alpha(s)x(s)x'(s) + \beta(s)x'(s) = \varepsilon \ . \tag{3.52}$$

Here, the two further optical functions

$$\alpha(s) = -\frac{\beta'(s)}{2} \ , \tag{3.53}$$

$$\gamma(s) = \frac{1 + \alpha^2(s)}{\beta(s)} \tag{3.54}$$

have been introduced. The area of the ellipse is given by $F = \pi\varepsilon$. According to Liouville's theorem the phase space volume in the six dimensional phase space is conserved, if the particle dynamics can be explained by canonical equations of motion and only conservative forces are present. Considering both transverse and the longitudinal phase space as uncoupled, this holds also true for them. This is reflected by the s-independent parameter $\varepsilon \equiv \varepsilon_{\mathrm{CS}}$, which is called the Courant-Snyder-Invariant [71]. The particle motion at a particular location $s = s_0$ is illustrated in Figure 3.2. The extreme values and the values at the zero crossings of x and x' can be also described by the optical functions.

A beam consists of particles with different Courant-Snyder-Invariants and thus different phase space amplitudes. Often the particle coordinate distribution in the two dimensional phase space can also be characterized by an ellipse. The equation of the phase space ellipse can be written as [65]:

$$\begin{pmatrix} x & x' \end{pmatrix} \hat{\sigma}_x^{-1} \begin{pmatrix} x \\ x' \end{pmatrix} = 1 \ . \tag{3.55}$$

The beam matrix is denoted by $\hat{\sigma}_x$ and can be expressed as [65]:

$$\hat{\sigma}_x = \begin{pmatrix} \sigma_{11} & \sigma_{12} \\ \sigma_{12} & \sigma_{22} \end{pmatrix} = \begin{pmatrix} \mathrm{Var}(x) & \mathrm{Cov}(x, x') \\ \mathrm{Cov}(x, x') & \mathrm{Var}(x') \end{pmatrix} \ . \tag{3.56}$$

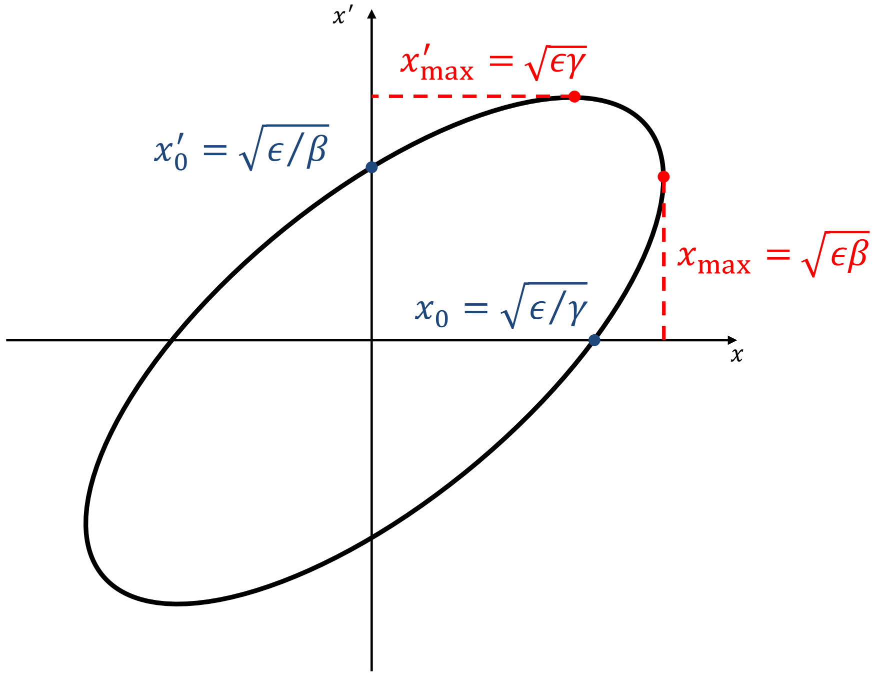

Figure 3.2: Linear transverse particle motion described by a phase space ellipse in (x, x'). The extreme values and zero crossings can be expressed by the optical functions (adapted from [64]).

In many cases, a Gaussian function is suitable to describe the particle distribution:

$$\rho(x, x') = N \exp\left(-\frac{\sigma_{22}x^2 - 2\sigma_{12}xx' + \sigma_{11}x'^2}{2\varepsilon_x^{1\sigma}}\right) . \tag{3.57}$$

The parameter $\varepsilon_x^{1\sigma}$ is connected to the determinant and is called the r.m.s. beam emittance:

$$\varepsilon_x^{1\sigma} = \det(\sigma_x) = \sqrt{\sigma_{11}\sigma_{22} - \sigma_{12}^2} . \tag{3.58}$$

39.3% of all particles are contained in the phase space ellipse characterized by $\varepsilon_x^{1\sigma}$. This definition of beam emittance is not unique [72, 73, 74, 75]

$$\varepsilon_x^{2\sigma} = 4 \cdot \varepsilon_x^{1\sigma} , \tag{3.59}$$

$$\varepsilon_x^{95\%} = 6 \cdot \varepsilon_x^{1\sigma} , \tag{3.60}$$

$$\varepsilon_x^{3\sigma} = 9 \cdot \varepsilon_x^{1\sigma} , \tag{3.61}$$

and required to know for comparison purposes. Usually, the beam is produced in a particle source and injected into the storage ring. At the injection point, it is of particular interest to match the phase space ellipse of the beam and the shape of the ellipse defined by the optical functions in Equation 3.52. In the perfectly matched case, the beam matrix can be also expressed by the optical functions of the storage ring at injection:

$$\hat{\sigma}_x = \varepsilon_x^{1\sigma} \begin{pmatrix} \beta & -\alpha \\ -\alpha & \gamma \end{pmatrix} . \tag{3.62}$$

During acceleration or deceleration the emittance shrinks or grows. This process is called adiabatic damping. For that reason, a normalized emittance ε_N can be introduced as follows:

$$\varepsilon_N = \beta\gamma\varepsilon \ . \tag{3.63}$$

Here, β and γ denote the relativistic Lorentz parameters and scale the emittance according to the momentum change.

3.1.4.2 Betatron Tune and Stability Criterion

Once the beam is injected, it is desirable to track the evolution of the particle trajectory along the storage ring. The solution of the homogeneous part, given in Equation 3.49, can be used to derive the transfer matrix of the coordinates in terms of the optical functions. Setting the initial conditions at $s = s_0$ to

$$\begin{aligned} x_0 &= x(s_0) \ , & x_0' &= x'(s_0) \ , & \Psi_{s_0} &= 0 \ , \\ \alpha_0 &= \alpha(s_0) \ , & \beta_0 &= \beta(s_0) \ , & \gamma_0 &= \gamma(s_0) \ , \end{aligned} \tag{3.64}$$

the transformation matrix is fully defined by [65]

$$\begin{pmatrix} x(s) \\ x'(s) \end{pmatrix} = \begin{pmatrix} \sqrt{\frac{\beta}{\beta_0}}(\cos\Psi + \alpha_0 \sin\Psi) & \sqrt{\beta\beta_0}\sin\Psi \\ \frac{\alpha_0-\alpha}{\sqrt{\beta\beta_0}}\cos\Psi - \frac{1+\alpha\alpha_0}{\sqrt{\beta\beta_0}}\sin\Psi & \sqrt{\frac{\beta_0}{\beta}}(\cos\Psi - \alpha_0\sin\Psi) \end{pmatrix} \begin{pmatrix} x_0 \\ x_0' \end{pmatrix} \ . \tag{3.65}$$

Thus, the transfer matrix for a full turn can be expressed as:

$$\hat{M} = \begin{pmatrix} \cos\mu + \alpha\sin\mu & \beta\sin\mu \\ -\gamma\sin\mu & \cos\mu - \alpha\sin\mu \end{pmatrix} \ . \tag{3.66}$$

Here, μ denotes the betatron phase advance in a full turn:

$$\mu = \int_s^{s+C_0} \Psi(\tilde{s})\mathrm{d}\tilde{s} \ . \tag{3.67}$$

According the Liouville's theorem the two-dimensional phase space volume is conserved (in case there is no coupling). For that reason, all eigenvalues must have unit magnitude:

$$\begin{aligned} |\lambda_{1,2}| &= \left|\cos\mu \pm \sqrt{(\cos\mu)^2 - 1}\right| \stackrel{!}{=} 1 \\ &\Rightarrow |\cos\mu| \leq 1 \\ &\Rightarrow \mu \text{ must be real} \ . \end{aligned} \tag{3.68}$$

The edge cases $\lambda_{1,2} = \pm 1$ can be excluded due to practical purposes: A slightest imperfection would lead to a non-stable solution. Thus, in a stable, periodic system all eigenvalues needs to be complex. They can be expressed as $\lambda_{1,2} = e^{\pm i\mu} = e^{\pm i2\pi Q}$. The phase advance per turn divided by 2π is defined as the betatron tune:

$$Q = \frac{\mu}{2\pi} \ . \tag{3.69}$$

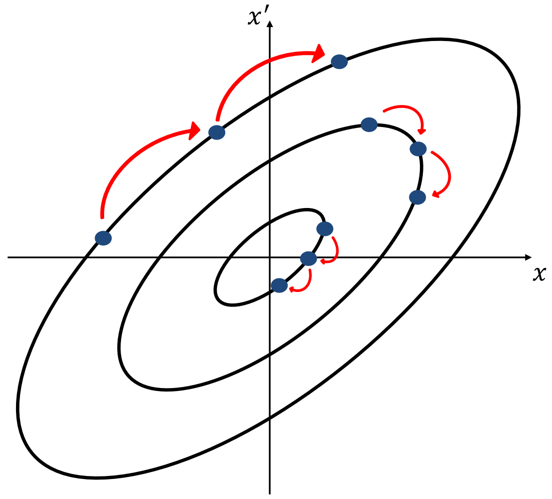

Figure 3.3: Different particles travel on different phase space ellipses. The phase advance per turn is illustrated by the red arrows and is denoted as the tune. The tune is the same for each particle considering only linear motion (adapted from [64]).

It characterizes the advance that each particle performs on the phase ellipse in each turn as illustrated in Figure 3.3. Constraining the solution for β to positive values only, it is possible to extract a unique solution of the optical functions at position s from the transfer matrix according to [64]:

$$\alpha = \frac{M_{11} - M_{22}}{2\sin\mu} \ , \tag{3.70}$$

$$\beta = \frac{M_{12}}{\sin\mu} \ , \tag{3.71}$$

$$\gamma = -\frac{M_{21}}{2\sin\mu} \ . \tag{3.72}$$

3.1.4.3 Dispersion

The complete solution $x_g(s)$ of Equation 3.46 consists of a full set of homogeneous solutions, discussed in the previous sections, and a particular solution of the inhomogeneous equation:

$$x_g(s) = x(s) + x_D(s) \ . \tag{3.73}$$

In connection to optics $x_D(s)$ is called the dispersive part. In case of a magnetic storage ring, it is usually associated with the momentum deviation of a particle according to:

$$x_D(s) = D(s) \cdot \delta \ . \tag{3.74}$$

The function $D(s)$ is called the periodic dispersion function. Inserting Equation 3.73 into Equation 3.46 leads to the following differential equation:

$$D''(s) + K(s)D(s) = h(s) \ . \tag{3.75}$$

Its solution is given by

$$D(s) = \frac{\sqrt{\beta(s)}}{2\sin\mu/2} \int_s^{s+c} h(\tilde{s})\sqrt{\beta(\tilde{s})} \cos\left[\Psi(\tilde{s}) - \Psi(s) - \mu/2\right] \mathrm{d}\tilde{s} \; . \tag{3.76}$$

Similar to the β-function, the dispersion can also be extracted from the transfer map. Given the linear transfer matrix $\hat{M}$, the dispersion function and its derivative satisfy the following equation [64]:

$$\begin{pmatrix} D \\ D' \\ 1 \end{pmatrix} = \hat{M} \begin{pmatrix} D \\ D' \\ 1 \end{pmatrix} = \begin{pmatrix} M_{11} & M_{12} & M_{16} \\ M_{21} & M_{22} & M_{26} \\ 0 & 0 & 1 \end{pmatrix} \begin{pmatrix} D \\ D' \\ 1 \end{pmatrix} \; . \tag{3.77}$$

The dispersion and its derivative can be extracted according to:

$$D = \frac{(1 - M_{22})M_{16} + M_{12}M_{26}}{2 - M_{11} - M_{22}} \; , \tag{3.78}$$

$$D' = \frac{(1 - M_{11})M_{26} + M_{21}M_{26}}{2 - M_{11} - M_{22}} \; . \tag{3.79}$$

The momentum deviation of a particle is also associated with a path-length change with respect to the reference particle. This is described by the momentum compaction formalism. To first order, it is given by:

$$\frac{\Delta C}{C_0} = \alpha_p \frac{\Delta p}{p} \; . \tag{3.80}$$

The parameter α_p denotes the momentum compaction factor. It can be directly connected to the dispersion function and the curvature of the storage ring:

$$\alpha_p = \frac{1}{C_0} \int_s^{s+C_0} D(\tilde{s})h(\tilde{s})\mathrm{d}\tilde{s} \; . \tag{3.81}$$

It is important for the stability of the longitudinal motion of the beam, as will be discussed in a subsequent section.

3.1.4.4 Chromaticity

The dispersion is connected to the curvature $h(s)$ and occurs due to a mismatch of bending power of the main dipoles in presence of a momentum deviation. A similar effect can be observed for the focusing strengths. Effectively, all quadrupole strengths k are reduced for particles with larger momenta [66]:

$$k(p) = -\frac{q}{p}\frac{\partial B_y}{\partial x} = -\frac{q}{p_0}\frac{\partial B_y}{\partial x}\frac{1}{1+\delta} \approx k_0(1-\delta) \; . \tag{3.82}$$

This effect is schematically illustrated in Figure 3.4. The tune change associated with a momentum deviation is given by:

$$(\Delta Q)_{\mathrm{quad}} = Q'^{,\mathrm{n}} \cdot \delta = \pm\frac{1}{4\pi} \oint \beta(\tilde{s})k(\tilde{s})\mathrm{d}\tilde{s} \cdot \delta \; . \tag{3.83}$$

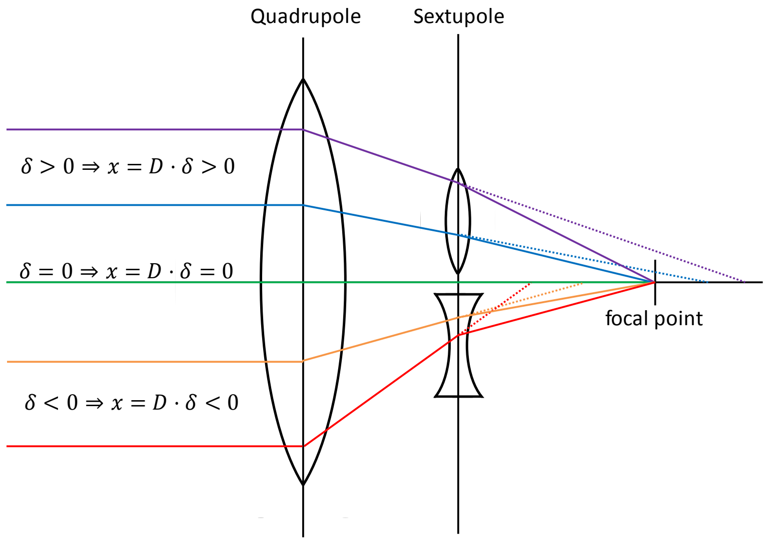

Figure 3.4: The focusing strengths of a magnetic quadrupole depends on the particle momentum. This effect is called chromaticity. Sextupoles generate a local quadrupole component depending on the radial position of the particle. In dispersive regions, they can correct for chromatic effects (adapted from [66]).

Here, the negative sign corresponds to the radial, the positive sign to the vertical motion. The quantity $Q'^{,\mathrm{n}}$ is called the natural chromaticity. It can be compensated by sextupole fields in dispersive regions, where a local gradient can be defined as follows:

$$\frac{q}{p}\frac{\partial B_y}{\partial x} = k_2 \cdot x = k_2 \cdot D\delta \; . \tag{3.84}$$

The total chromaticity is the sum of the induced tune changes:

$$\Delta Q = (\Delta Q)_{\mathrm{quad}} + (\Delta Q)_{\mathrm{sext}} = Q' \cdot \delta = \pm\frac{1}{4\pi}\oint \beta(\tilde{s})\left[k(\tilde{s}) - k_2(\tilde{s})D(\tilde{s})\right]\mathrm{d}\tilde{s} \cdot \delta \; . \tag{3.85}$$

In general, at least two sextupole families are required to correct the chromaticities in both planes. Often the chromaticity is expressed relative to the corresponding betatron tune:

$$\xi = \frac{Q'}{Q} \; . \tag{3.86}$$

Note that the quantities α, β, γ, Ψ, μ, D, Q and Q' defined in the previous sections exist for the radial and the vertical phase space, respectively. But in a perfect planar ring the dispersion in the vertical direction vanishes, since a curvature does not exist.

3.1.4.5 Field Errors

Up to now, the motion in an ideal storage ring was considered. In this section, distributed perturbations, i. e. dipole or quadrupole field errors, in the storage ring and their influence on the beam motion are investigated. First, a localized dipole field error ΔB_y at the location s_i is introduced, which induces an angular kick:

$$\Delta x'(s_i) = \frac{q}{p} \Delta B_y(s_i) \ . \tag{3.87}$$

A set of N dipole field errors distributed in the entire storage ring can be parametrized by a function F(s):

$$F(s) = \sum_{i=1}^{N} \Delta x'(s_i)\delta(s_i - s) \ . \tag{3.88}$$

These kicks lead to a disturbed closed orbit $x_c(s)$, which in general does not agree with the reference orbit. Neglecting momentum deviations it is defined by the differential equation:

$$x_c'' + K(s)x_c = F(s) \ . \tag{3.89}$$

It can be shown, that the disturbed closed orbit along the ring is given by [68]:

$$\begin{aligned} x_c(s) &= \frac{\sqrt{\beta(s)}}{2 \sin Q\pi} \int_s^{s+C_0} F(\tilde{s})\sqrt{\beta(\tilde{s})} \cos\left[\Psi(\tilde{s}) - \Psi(s) + Q\pi\right] \mathrm{d}\tilde{s} \\ &= \frac{Q \cdot \sqrt{\beta(s)}}{2 \sin Q\pi} \int_\phi^{\phi+2\pi} \left[\beta^{3/2}(\tilde{\phi})F(\tilde{\phi})\right] \cos(Q(\phi - \tilde{\phi} + \pi))\mathrm{d}\tilde{\phi} \ , \end{aligned} \tag{3.90}$$

where the transformation $\phi(s) = \frac{\Psi(s)}{Q}$ was applied in the last step. Furthermore, the closed orbit solution can be expressed by using a Fourier series, which yields:

$$f(\phi) = \beta^{3/2}(\phi)F(\phi) = \sum_{k=-\infty}^{\infty} f_k \cdot e^{ik\phi} \ , \tag{3.91}$$

$$f_k = \frac{1}{2\pi} \oint \beta^{3/2}(\phi)F(\phi)e^{-ik\phi}\mathrm{d}\phi \ , \tag{3.92}$$

$$x_c(s) = \sqrt{\beta(s)} \sum_{k=-\infty}^{\infty} \frac{Q^2 f_k}{Q^2 - k^2} e^{ik\phi} \ . \tag{3.93}$$

This relation directly shows, that betatron tunes close to an integer values lead to huge amplitudes. This condition, which is called an integer resonance, has to be avoided for stable operation. The Fourier amplitude is called the integer stopband integral.

In general, orbit distortions of any kind are undesirable and in practice a distributed set of radial and vertical corrector magnets is used to correct these orbit deviations. From Equation 3.90 a direct relation between angular kicks and the resulting orbit change can be obtained. This allows one to calculate the orbit change Δx_i at position s_i with respect to an angular kick $\Delta x_j'$ at position x_j, which can be expressed by a simple relation [76]:

$$\Delta x_i = O_{ij} \cdot \Delta x_j' \ . \tag{3.94}$$

Usually, the positions s_i are the locations of the beam position monitors (BPMs) in the storage ring, which are used to determine the orbit at several positions in the ring. In this case, the matrix $\hat{O}$ is called the Orbit Response Matrix (ORM). Besides calculation of the ORM, which requires a precise model of the storage ring, the entries O_{ij} can be measured by variation of the angular kicks induced by the corrector magnets.

Consequently, the ORM entries are determined by the resulting orbit shifts at each BPM. Solving the equation system

$$x_c(s_i) = -\sum_j O_{ij}\Delta x_j \tag{3.95}$$

for each BPM i simultaneously yields the needed angular kicks to correct the disturbed orbit $x_c(s)$. But, since either the number of BPMs and correctors might be unequal, or the ORM is necessarily well-conditioned, the orbit correction often results in a minimization problem. Various algorithms can be applied to find the optimum solution for this minimization problem.

Besides dipole field errors, also distributed quadrupole errors can disturb the beam motion. They are strongly associated with the betatron motion and lead to a change of the β-functions and tunes. Small tune changes can be approximated by [65]:

$$\Delta Q = \frac{1}{4\pi}\oint \beta(\tilde{s})\Delta K(\tilde{s})\mathrm{d}\tilde{s} \ . \tag{3.96}$$

Here, the quadrupole errors are considered by a variation of the quadrupole strengths given as $K(s) = -k(s)$ in the radial and $K(s) = k(s)$ in the vertical case. The change of the betatron function is given by:

$$\Delta\beta(s) = \frac{\beta(s)}{2\sin(Q2\pi)}\int_s^{s+C_0} \Delta K(\tilde{s})\beta(\tilde{s})\cos\left(2\left[\Psi(\tilde{s}) - \Psi(s) + Q\pi\right]\right)\mathrm{d}\tilde{s} \ . \tag{3.97}$$

For betatron tunes close to a half integer the induced changes become large. This can be explained by reconsidering Equation 3.68. Half integer tunes correspond to the edge cases $\lambda_{1,2} = \pm 1$. These eigenvalues define the transition from bound elliptical solutions with two complex eigenvalues to unbound hyperbolic solutions with two real eigenvalues, of which one is larger than unity. Thus, the motion in the second case becomes unstable, which is called a half integer resonance.

In general, the beam resonance conditions are given by the following equation:

$$m \cdot Q_x + n \cdot Q_y = k \ , \qquad k, m, n \in \mathbb{N} \ . \tag{3.98}$$

The sum $|m| + |n|$ characterizes the order of the resonance. The resonance strength strongly depends on the multipole content of the storage ring.

3.1.5 Longitudinal Motion

In the preceding sections, the transverse motion has been discussed, which is similar in both transverse planes. For the longitudinal motion, Equations 3.37 and 3.38 are reconsidered. This discussion is restricted to pure magnetic fields and small values of the two longitudinal coordinates, for which the linearized equations are valid:

$$l'_K = -h\frac{1+\eta_0}{2+\eta_0}x + \frac{1}{(2+\eta_0)^2}\delta_K \ , \tag{3.99}$$

$$\delta'_K = 0 \ . \tag{3.100}$$

3.1.5.1 Phase Slip Factor

Equation 3.99 describes a potential time-of-flight change in case of radial offsets and energy deviations. The contribution from betatron oscillations tends to average out to first order [64], but there is a contribution arising from momentum deviations at locations of non-zero dispersion: $x = D \cdot \delta$. In connection with the substitution of δ_K by δ, this yields:

$$l'_K = \left[-h\frac{1+\eta_0}{2+\eta_0}D + \frac{1}{(2+\eta_0)^2} \cdot \frac{2+\eta_0}{1+\eta_0}\right] \cdot \delta \; . \tag{3.101}$$

$$\tag{3.102}$$

The phase slip factor η_{ph} is used to describe the revolution time change in case of momentum deviations:

$$\frac{\Delta T}{T_0} = -\eta_{\text{ph}}\frac{\Delta p}{p_0} = -\eta_{\text{ph}}\delta \; . \tag{3.103}$$

Making use of Equation 3.101 it can be expressed as:

$$\begin{aligned}
\eta_{\text{ph}} &= -\frac{v_0 \Delta T}{C_0 \delta} \\
&= \frac{1}{C_0\delta}\frac{1+\gamma_0}{\gamma_0}\int_0^{C_0} l'_K(\tilde{s})\mathrm{d}\tilde{s} \\
&= -\frac{1}{C_0}\frac{1+\gamma_0}{\gamma_0}\int_0^{C_0}\left[h\frac{1+\eta_0}{2+\eta_0}D - \frac{1}{(2+\eta_0)^2}\cdot\frac{2+\eta_0}{1+\eta_0}\right]\mathrm{d}\tilde{s} \\
&= \frac{1}{\gamma_0^2} - \alpha_p \; .
\end{aligned} \tag{3.104}$$

Here, the definition of the momentum compaction factor α_p given in Equation 3.80 was used. The first term in the second last line describes the contribution from path-lengthening in case of a non zero curvature as shown in Equation 3.17. The second term is the revolution time change induced by a velocity variation. The phase slip factor has a strong impact on longitudinal beam focusing, as will be discussed in the next section.

3.1.5.2 Synchrotron Oscillations

The different revolution times for different momenta can be used to focus the beam in the longitudinal direction by a time-varying electric field. In this section, the influence of a homogeneous RF electric field of a cavity is investigated:

$$E(t) = E_0 \cdot \cos(\omega t) \; . \tag{3.105}$$

Assuming a thin cavity of length L, its effect can be approximated as a kinetic energy kick:

$$\Delta K(l) = qV_0 \cos(\phi(t)) = qV_0 \cos\left(\phi_0 - \frac{\omega}{\kappa}\cdot l_K\right) \; . \tag{3.106}$$

The effective voltage difference per pass is denoted as V_0. The kinetic energy kick also depends on the phase: $\phi = \omega t$. Thus, it is connected to the time of arrival of an individual particle at the cavity. The spatial transverse coordinates, as well as the time of arrival, are not affected by this particular cavity representation, but the transfer functions for the momentum-like variables can be represented as follows [64]:

$$a_f = \frac{p_{0,i}}{p_{0,f}} a_i, \qquad b_f = \frac{p_{0,i}}{p_{0,f}} b_i \ , \tag{3.107}$$

$$\delta_{K,f} = \frac{K_0}{K_0 + qV_0\cos(\phi_0)}\delta_{K,i} + \frac{qV_0}{K_0 + qV_0\cos(\phi_0)} \cdot \left[\cos\left(\phi_0 - \frac{\omega}{\kappa}\cdot l_K\right) - \cos(\phi_0)\right] \ . \tag{3.108}$$

This is a typical example, where the collected energy changes (see Equation 3.21) are absorbed to the optical coordinates. In case the reference particle is accelerated, $\frac{p_{0,i}}{p_{0,f}} < 1$ and $K_0 + qV_0\cos(\phi_0) > 0$. This leads to a shrinking of the phase space volumes in all three dimensions, which was previously described as adiabatic damping.

The repetitive interaction of such a cavity in a storage ring can be represented by the combination of the transfer maps of the static storage ring and the RF cavity. A different definition for the momentum-like variable is used, such that the phase space is conserved, although the kinetic energy might change:

$$\tilde{\delta}_K = \frac{\Delta K}{K_0} \ . \tag{3.109}$$

The nominator still describes the absolute energy difference between an individual particle and the reference particle, but the denominator is kept constant in contrast to Equation 3.108. In the following, the phase slip factor is also defined with respect to the momentum deviation with a constant denominator. For the static storage ring, the linear transfer map can be written as:

$$l_{K,f} = l_{K,i} + \eta_{\mathrm{ph}}\left(\frac{\gamma_0}{1+\gamma_0}\right)^2 C_0 \cdot \tilde{\delta}_{K,i} \ , \tag{3.110}$$

$$\tilde{\delta}_{K,f} = \tilde{\delta}_{K,i} \ . \tag{3.111}$$

Applying the transformation due to a subsequent thin cavity only changes the second coordinate. The linearization of the cosine functions yields:

$$\left[\cos\left(\phi_0 - \frac{\omega}{\kappa}\cdot l_K\right) - \cos(\phi_0)\right] = -\frac{\omega}{\kappa}\cdot\sin(\phi_0)\cdot l_K \ . \tag{3.112}$$

Thus, the second coordinate after one turn can be expressed by:

$$\tilde{\delta}_{K,f} = -\frac{qV_0}{K_0}\frac{\omega}{\kappa}\sin(\phi_0)\cdot l_{K,i} + \left[1 - \frac{qV_0}{K_0}\frac{\omega}{\kappa}\eta_{\mathrm{ph}} \ , \left(\frac{\gamma_0}{1+\gamma_0}\right)^2 C_0\sin(\phi_0)\right]\tilde{\delta}_{K,i} \ . \tag{3.113}$$

The trace of the new transfer map $\hat{M}$ can be used to determine the regions for stable bound solutions. The phase advance per turn for the synchrotron motion μ_{sync} is given by [64]:

$$\cos(\mu_{\mathrm{sync}}) = \frac{\mathrm{Tr}\ \hat{M}}{2} = 1 - \frac{qV_0}{2K_0}\frac{\omega}{\kappa}\eta_{\mathrm{ph}}\left(\frac{\gamma_0}{1+\gamma_0}\right)^2 C_0\sin(\phi_0) \ . \tag{3.114}$$

Analog to the transverse motion $|\cos(\mu_{\mathrm{sync}})| \leq 1$ is required for a stable solution. Hence, the relation between phase slip factor η_{ph} and reference phase ϕ_0 needs to be maintained. Assuming a beam of positively charged particles stable motion can only be achieved for:

$$\eta_{\mathrm{ph}} > 0 \rightarrow \phi_0 \in [0, \pi] \ , \tag{3.115}$$

$$\eta_{\mathrm{ph}} < 0 \rightarrow \phi_0 \in [\pi, 2\pi] \ . \tag{3.116}$$

The parameter η_{ph} is energy-dependent and may flip its sign during acceleration. Thus, a cavity phase-jump may be required to preserve stable motion. The corresponding energy is denoted as transition energy:

$$\gamma_{\mathrm{tr}} = \frac{1}{\sqrt{\alpha_0}} \ . \tag{3.117}$$

The second term in Equation 3.114 is usually significantly smaller than unity and can be treated perturbatively. This approximately yields:

$$\begin{aligned} \mu_{\mathrm{sync}} &= \sqrt{\frac{qV_0}{K_0}\frac{\omega}{\kappa}\eta_{\mathrm{ph}}\left(\frac{\gamma_0}{1+\gamma_0}\right)^2 C_0 \sin(\phi_0)} \\ &= \sqrt{\frac{2\pi h \cdot qV_0\eta_{\mathrm{ph}}\sin(\phi_0)}{\beta_0 p_0}} \ . \end{aligned} \tag{3.118}$$

Here, the cavity frequency was substituted by $\omega = 2\pi h/T_0$ with the harmonic number h, which defines the ratio of cavity frequency and revolution frequency. The synchrotron tune is defined analog to the transverse betatron tunes:

$$Q_{\mathrm{sync}} = \frac{\mu_{\mathrm{sync}}}{2\pi} \ . \tag{3.119}$$

It is usually in the order of 10^{-3} and hence much smaller than the betatron tunes, which often exceed one. This difference limits the coupling of the transverse and the longitudinal phase spaces.

3.2 Spin Dynamics

The layout of a storage ring based EDM experiment requires a detailed investigation of the spin dynamics in storage rings The spin motion is strongly coupled to the beam motion, which is denoted as spin-orbit-coupling. In the scope of this thesis, the spin motion in a magnetic storage ring for protons and deuterons was explored. Hence, in this section a general description of the spin equations of motion is given, but the subsequent discussion focuses mainly on pure magnetic storage rings. The information on spin dynamics is mainly taken from [77].

3.2.1 Polarization Formalism

First, the formalism for the description of the polarization for an ensemble of spin-$\frac{1}{2}$- and spin-1-particles is given. The following description is based on the information in [78, 79, 80].

3.2.1.1 Spin-$\frac{1}{2}$-particles

The state of a single spin-$\frac{1}{2}$-particle can be expressed as a two component Pauli spinor [81]:

$$\psi = \begin{pmatrix} u \\ d \end{pmatrix} \ . \tag{3.120}$$

The two complex amplitudes u and d satisfy the normalization condition: $|u|^2 + |d|^2 = 1$ In the following discussion, the Cartesian coordinate system $(\vec{e}_1, \vec{e}_2, \vec{e}_3)$ is used. Here, $\vec{e}_3$ is chosen as spin quantization axis. The two spinor components correspond to the two different spin states $m = \pm\frac{1}{2}$ along the spin quantization axis. Each spin observable is connected to an hermitian operator. In case of spin-$\frac{1}{2}$-particles, these operators can be defined using the Pauli spin operators:

$$\hat{\vec{S}} = \frac{\hbar}{2}\vec{\sigma} \tag{3.121}$$

with

$$\sigma_1 = \begin{pmatrix} 0 & 1 \\ 1 & 0 \end{pmatrix}, \qquad \sigma_2 = \begin{pmatrix} 0 & -i \\ i & 0 \end{pmatrix}, \qquad \sigma_3 = \begin{pmatrix} 1 & 0 \\ 0 & -1 \end{pmatrix}. \tag{3.122}$$

The three Pauli matrices can be extended by the identity matrix:

$$\sigma_0 = \begin{pmatrix} 1 & 0 \\ 0 & 1 \end{pmatrix}. \tag{3.123}$$

Together the four matrices are a complete basis of the hermitian 2×2-matrices. An observable is defined as the expectation value of the associated operator $\hat{A}$. It is given by:

$$\langle A \rangle = \langle \psi | \hat{A} | \psi \rangle = \psi^\dagger \hat{A} \psi \ . \tag{3.124}$$

In this context, it is convenient to define the density matrix:

$$\rho = |\psi\rangle\langle\psi| = \begin{pmatrix} |u|^2 & ud^* \\ u^*d & |d|^2 \end{pmatrix} . \tag{3.125}$$

The expectation value can also be expressed by the trace of the product of the density matrix and the operator:

$$\langle \hat{A} \rangle = \mathrm{Tr}\, \rho \hat{A} \; . \tag{3.126}$$

In case of a single particle, this yields:

$$\vec{S} = \langle \hat{\vec{S}} \rangle = \frac{\hbar}{2}\, \mathrm{Tr}\, \rho\vec{\sigma} = \frac{\hbar}{2} \begin{pmatrix} 2\ \mathrm{Re}(ud^*) \\ 2\ \mathrm{Im}(ud^*) \\ |u|^2 - |d|^2 \end{pmatrix} . \tag{3.127}$$

Often, in simulation codes, which can be used to track the spin motion in accelerators, $\vec{S}$ is treated as a classical vector, which can be used to describe the spin precession in electromagnetic fields. Usually, each spin is represented by such a vector, which is normalized to unity.

In general, billions of particle are injected and stored in a particle storage ring and one is rather interested in the expectation value of the spin observables for the whole ensemble. Given an ensemble of N particles, the density matrix can be extended to:

$$\rho = \frac{1}{N} \begin{pmatrix} \sum\limits_{i=1}^{N} |u^{(i)}|^2 & \sum\limits_{i=1}^{N} u^{(i)} d^{(i)*} \\ \sum\limits_{i=1}^{N} u^{(i)*} d^{(i)} & \sum\limits_{i=1}^{N} |d^{(i)}|^2 \end{pmatrix} . \tag{3.128}$$

Expanded in terms of Pauli spin operators, it reads:

$$\rho = \frac{1}{2} \left(\sigma_0 + \vec{P}\vec{\sigma} \right) . \tag{3.129}$$

The vector $\vec{P}$ is the polarization vector of the ensemble, which contains the expectation values of the spin operators:

$$\vec{P} = \frac{1}{N} \sum_{i=1}^{N} \vec{S}_i \; . \tag{3.130}$$

Assuming a beam composed of $N^{m=\frac{1}{2}}$ and $N^{m=-\frac{1}{2}}$ particles in the particular quantization state, the vector polarization P_V along the quantization axis is defined as [77]:

$$P_V = \frac{N^{m=\frac{1}{2}} - N^{m=-\frac{1}{2}}}{N^{m=\frac{1}{2}} + N^{m=-\frac{1}{2}}} \; . \tag{3.131}$$

3.2.1.2 Spin-1-particles

In case of spin-1-particles, a three component spinor is needed to fully describe the state of an individual particle [78]:

$$\psi = \begin{pmatrix} a_1 \\ a_2 \\ a_3 \end{pmatrix} . \tag{3.132}$$

The three components belong to the three quantization states $m = 1$, $m = 0$ and $m = -1$ along the quantization axis. The basic spin operators can be expressed as:

$$\hat{S}_1 = \frac{\hbar}{\sqrt{2}} \begin{pmatrix} 0 & 1 & 0 \\ 1 & 0 & 1 \\ 0 & 1 & 0 \end{pmatrix} , \quad \hat{S}_2 = \frac{\hbar}{\sqrt{2}} \begin{pmatrix} 0 & -i & 0 \\ i & 0 & -i \\ 0 & i & 0 \end{pmatrix} , \quad \hat{S}_3 = \hbar \begin{pmatrix} 1 & 0 & 0 \\ 0 & 0 & 0 \\ 0 & 0 & -1 \end{pmatrix} . \tag{3.133}$$

To characterize a spin-1-system a set of nine independent hermitian matrices is required. Taking the 3×3 identity matrix into account, at least five further matrices are required. A second-rank tensor can be constructed by the outer product:

$$\begin{pmatrix} \hat{S}_1 \\ \hat{S}_2 \\ \hat{S}_3 \end{pmatrix} \begin{pmatrix} \hat{S}_1 & \hat{S}_2 & \hat{S}_3 \end{pmatrix} = \begin{pmatrix} \hat{S}_1\hat{S}_1 & \hat{S}_1\hat{S}_2 & \hat{S}_1\hat{S}_3 \\ \hat{S}_2\hat{S}_1 & \hat{S}_2\hat{S}_2 & \hat{S}_2\hat{S}_3 \\ \hat{S}_3\hat{S}_1 & \hat{S}_3\hat{S}_2 & \hat{S}_3\hat{S}_3 \end{pmatrix} . \tag{3.134}$$

Basically, these nine operators could be used as a basis for the 3×3 hermitian operators, but for simplicity the commonly used operators $\hat{S}_1$, $\hat{S}_2$ and $\hat{S}_3$, as well as the identity matrix I should be retained. For this purpose, the tensor is split in the symmetric and antisymmetric contributions:

$$\begin{aligned} \hat{S}_i\hat{S}_j &= \frac{1}{2}\left(\hat{S}_i\hat{S}_j + \hat{S}_j\hat{S}_i\right) + \frac{1}{2}\left(\hat{S}_i\hat{S}_j - \hat{S}_j\hat{S}_i\right) \\ &= \frac{1}{2}\left(\hat{S}_i\hat{S}_j + \hat{S}_j\hat{S}_i\right) + \frac{i\hbar}{2}\varepsilon_{ijk}\hat{S}_k \ . \end{aligned} \tag{3.135}$$

In the last step, the commutation relation for angular momenta has been used, which reveals the connection between the commonly used spin operators and the asymmetric part. Therefore, only the symmetric part is relevant to complete the set of basis operators. In the standard Cartesian notation, the following operators are used as a basis:

$$\begin{aligned} & I, \hat{S}_1, \hat{S}_2, \hat{S}_3, \\ & \hat{S}_{ij} = \frac{3}{2}\left(\hat{S}_i\hat{S}_j + \hat{S}_j\hat{S}_i\right) - 2I\delta_{ij} \ , \quad i,j \in \{1,2,3\} \end{aligned} \tag{3.136}$$

This is a set of ten operators, where only nine are independent. The dependency relation is given by:

$$\hat{S}_{11} + \hat{S}_{22} + \hat{S}_{33} = 0 \ . \tag{3.137}$$

Conventionally the following normalization is applied to the basis operators $\hat{A}_i$:

$$\mathrm{Tr}\, \hat{A}_i\hat{A}_j = 3\delta_{ij} \ . \tag{3.138}$$

Thus, the density matrix for an ensemble of spin-1-particles can be expanded in terms of these operators:

$$\rho = \frac{1}{3}\left[I + \frac{3}{2}\sum_{i=1}^{3} P_i S_i + \frac{1}{3}\sum_{i=1}^{3}\sum_{j=1}^{3} P_{ij} S_{ij}\right], \text{ with } P_{ij} = P_{ji} . \tag{3.139}$$

In case of an ensemble of spin-1-particles, the parameters P_i and P_{ij} characterize its polarization state. The injected particles are usually produced in a polarized ion source. Using external magnetic fields a set of sub-states is selected along a defined quantization axis. Often it exists an axial symmetry about the quantization axis. In this case, only two parameters P_i and P_{ij} are required to characterize the system, once the quantization axis is defined. If the 3-axis is chosen as quantization axis, the density matrix can be simplified to:

$$\rho = \frac{1}{3}\left[I + \frac{3}{2} P_3 \hat{S}_3 + \frac{1}{2} P_{33} \hat{S}_{33}\right] . \tag{3.140}$$

Considering $N^{m=1}$, $N^{m=0}$ and $N^{m=-1}$ particles of the beam in the particular quantization state, the vector polarization P_V and tensor polarization P_T along the quantization axis are defined by [77]:

$$P_V = \frac{N^{m=1} - N^{m=-1}}{N^{m=1} + N^{m=0} + N^{m=-1}} , \tag{3.141}$$

$$P_T = \frac{N^{m=1} + N^{m=-1} - 2N^{m=0}}{N^{m=1} + N^{m=0} + N^{m=-1}} . \tag{3.142}$$

Besides the Cartesian notation presented here, the spin-1 system can also be characterized by spherical tensor operators [77].

3.2.2 Connection of Beam and Spin Coordinate Systems

The preceding illustration of the polarization formalism was performed in the Cartesian coordinate system $(\vec{e}_1, \vec{e}_2, \vec{e}_3)$. In this coordinate system,the $\vec{e}_3$-direction is used as quantization axis. The coordinate system defined for description of beam dynamics in a planar storage ring (see Section 3.1.1) possesses two basis vectors $\vec{e}_x$ and $\vec{e}_s$ in the ring plane. The $\vec{e}_y$-direction is perpendicular to the plane and points along the vertical guiding fields. The natural choice is to select the $\vec{e}_y$-axis as quantization axis:

$$(\vec{e}_1, \vec{e}_2, \vec{e}_3) \equiv (\vec{e}_x, \vec{e}_s, -\vec{e}_y) . \tag{3.143}$$

Assuming a positive magnetic guiding field along the vertical direction, a positive ion beam circulates clock-wise in the storage ring. For this particular choice the co-moved coordinate system of spin dynamics rotates counter-clockwise due to the opposite directions of $\vec{e}_3$ and $\vec{e}_y$. Thus, the rotation is performed in positive mathematical sense, which is advantageous for practical purposes.

Table 3.1: Magnetic properties for proton, deuteron, electron and muon [82].

Particle	S in $\hbar$	mc^2 in MeV	$\lvert\vec{\mu}\rvert$ in (μ_B, μ_N)	g	G or a
proton	$\frac{1}{2}$	938.272 081 3(58)	2.792 847 350 8(85)	5.585 695	1.792 847
deuteron	1	1875.612 928(12)	0.857 438 231 1(48)	1.714 025	−0.142 987
electron	$\frac{1}{2}$	0.510 998 946 1(31)	1.001 159 652 180 91(36)	2.002 319	$1.159652 \cdot 10^{-3}$
muon	$\frac{1}{2}$	105.658 374 5(24)	$4.84197048(11) \cdot 10^{-3}$	2.002 332	$1.165920 \cdot 10^{-3}$

3.2.3 Equations of Motion in Rest Frame

The Hamiltonian, which describes the spin interaction in electromagnetic fields in the particle rest frame, was given in Equation 2.11. The associated non-relativistic spin equation of motion for the spin vector $\vec{S}$ in electric and magnetic fields can be expressed as:

$$\frac{\mathrm{d}\vec{S}}{\mathrm{d}t} = \vec{\Omega} \times \vec{S} = \vec{\mu} \times \vec{B} + \vec{d} \times \vec{E} \; . \tag{3.144}$$

It reflects a spin precession in the plane perpendicular to $\vec{\Omega}$ with an angular frequency of $|\vec{\Omega}|$. The definitions for the magnetic dipole moment $\vec{\mu}$ and electric dipole moment $\vec{d}$ have been presented in Equations 2.9 and 2.10, respectively. The MDMs for several particles are determined from experimental measurements. Commonly, the MDM magnitudes are expressed in terms of the Bohr magneton for leptons or in terms of the nuclear magneton for hadronic systems [82]:

$$\mu_B = 5.788\,381\,801\,2(26) \cdot 10^{-5}\,\mathrm{eV/T} \; , \tag{3.145}$$

$$\mu_N = 3.152\,451\,255\,0(15) \cdot 10^{-8}\,\mathrm{eV/T} \; . \tag{3.146}$$

The magnetic properties for proton, deuteron, electron and muon are summarized in Table 3.1. The anomalous gyromagnetic g-factor G or a is defined as

$$G = a = \frac{g-2}{2} \; . \tag{3.147}$$

Here, G is usually used in the hadronic sector, while a is more common in the leptonic sector. Historically, anomalous gyromagnetic g-factor is related to the Dirac equation [83] for leptons. In the non-relativistic case, it yields $g = 2$ and $a = 0$. Corrections to the electromagnetic coupling introduce a small contribution to the anomalous g-factor. The values of g and G given in Table 3.1 correspond to the definition in Equation 2.10. Here, the charge and mass of the individual particle are taken into account.

3.2.4 Generalized Thomas-BMT Equation

In Equation 3.144, the spin vector and the electric and magnetic fields are defined in the rest frame of the particle, but in accelerator physics the fields are usually known in the curvilinear laboratory reference frame. Thus, the equation has to be transformed into the laboratory reference frame. This results in the Thomas-BMT equation [84, 85]. It describes the spin motion of relativistic particles in homogeneous electromagnetic fields. Usually, the Thomas-BMT equation refers only to the interaction of the magnetic dipole moment with the fields. Here, a generalized form is presented, which also includes the contribution of the electric dipole moment [35]:

$$\frac{\mathrm{d}\vec{S}}{\mathrm{d}t} = \vec{\Omega}_{\mathrm{MDM}} \times \vec{S} + \vec{\Omega}_{\mathrm{EDM}} \times \vec{S}\ , \tag{3.148}$$

$$\vec{\Omega}_{\mathrm{MDM}} = -\frac{q}{m}\left[\left(G + \frac{1}{\gamma}\right)\vec{B} - \frac{G\gamma}{\gamma+1}\left(\vec{\beta}\cdot\vec{B}\right)\vec{\beta} - \left(G + \frac{1}{\gamma+1}\right)\vec{\beta}\times\frac{\vec{E}}{c}\right], \tag{3.149}$$

$$\vec{\Omega}_{\mathrm{EDM}} = -\frac{q}{mc}\frac{\eta_{\mathrm{EDM}}}{2}\left[\vec{E} - \frac{\gamma}{\gamma+1}\left(\vec{\beta}\cdot\vec{E}\right)\vec{\beta} + c\vec{\beta}\times\vec{B}\right]. \tag{3.150}$$

The spin vector $\vec{S}$ is defined in the rest frame of the particle, whereas the electric field $\vec{E}$ and magnetic field $\vec{B}$ are evaluated in the curvilinear laboratory reference frame. Recent efforts aim to also include additional terms arising from higher moments, i.e. field gradients, in simulation codes [86]. Since the additional contributions are expected to be small in comparison to the experimental sensitivity limits, predicted for the direct measurements at the Cooler Synchrotron, they have not been included in the applied simulation software used within this thesis, yet. Instead this work focuses on the benchmarking and investigation of systematic limitations for EDM measurements arising from the dominating MDM part contained in Equation 3.148, neglecting also non-linear contributions with respect to the spin.

In the following, the implications on spin motion for protons and deuterons in presence of explicit transverse or longitudinal magnetic and electric fields assuming a vanishing EDM are illustrated. Two different scenarios are considered: In the first scenario, the influence of a vertical magnetic field of 1 T along the negative vertical axis in a pure magnetic storage ring is evaluated. Analog a radial electric field, which produces an equivalent Lorentz force ($|\vec{E}| = |c\vec{\beta}\times\vec{B}|$), in a pure electric ring is considered. In the second scenario, a storage ring bending radius of $\rho = 10\,\mathrm{m}$ is assumed and the required pure magnetic or electric fields are scaled according to the beam momentum. The electromagnetic field strengths are shown in Figure 3.5 for a momentum range of 0.1 to 10 GeV/c. The magnetic field strengths of the first scenario is constant by definition, while it scales linearly in the second scenario. Since the magnetic bending radius is inverse proportional to the momentum, the required magnetic field strengths for protons and deuterons is equal in both scenarios. In case of pure electric guiding fields, the particle mass is relevant. The required electric field strengths exceeds the currently technically achievable field strengths at higher momenta. That is one of the major reasons, why conventional storage rings usually employ magnetic guiding fields.

The total $\vec{\Omega}_{\mathrm{MDM}}$-vector can be divided into contributions from parallel and perpendicular field components[3]:

$$\begin{aligned}\vec{\Omega}_{\mathrm{MDM}} &= \vec{\Omega}_{B_\perp} + \vec{\Omega}_{B_\parallel} + \vec{\Omega}_{E_\perp}\\ &= -\frac{q}{\gamma m}\left[(1+G\gamma)\,\vec{B}_\perp + (1+G)\,\vec{B}_\parallel - \left(G\gamma + \frac{\gamma}{\gamma+1}\right)\vec{\beta}\times\frac{\vec{E}}{c}\right].\end{aligned} \tag{3.151}$$

[3] with respect to the particle motion

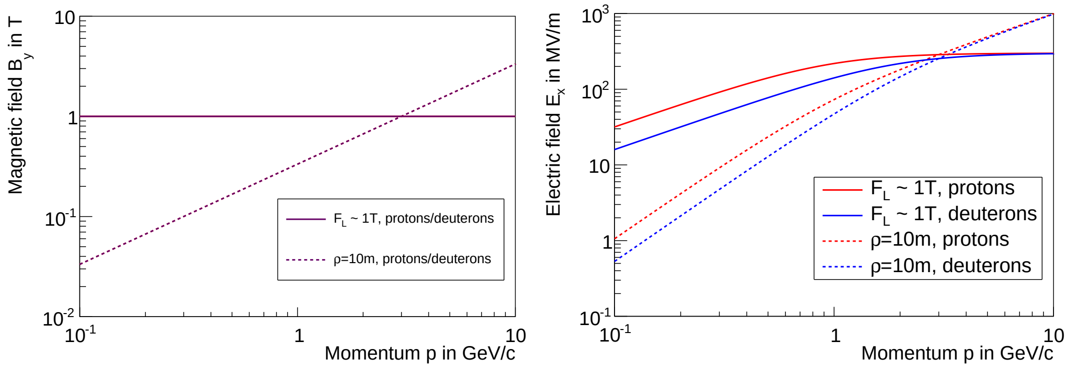

(a) (b)

Figure 3.5: Magnetic (a) and electric field strengths (b) required for two different storage ring scenarios and various momenta of protons and deuterons. The first scenario demands a Lorentz force F_{L}, which is equivalent to the Lorentz force produced by a pure transverse magnetic field of 1 T. In the second scenario, either a pure magnetic or pure electric storage ring with a constant bending radius of 10 m is considered. The shown field strengths scale linearly with the variation of the Lorentz force amplitude and reciprocally with the bending radius, respectively.

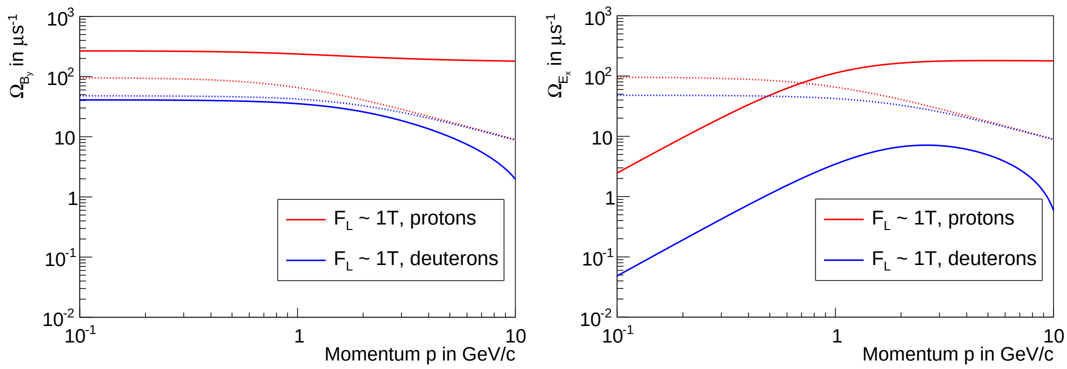

(a) (b)

Figure 3.6: Induced spin rotation frequency in case of a pure vertical magnetic (a) or pure radial electric field (b) according to Equation 3.151. Various momenta for protons and deuterons are chosen. For comparison purposes, the electric field strength is scaled in order to produce a Lorentz force, which is equivalent to a Lorentz force produced by a transverse magnetic field of 1 T. For comparison, the cyclotron frequencies are shown as dotted lines.

Figure 3.6 shows the absolute value of $\vec{\Omega}_{\text{MDM}}$ in case of pure magnetic or electric transverse fields. Here, the first scenario of a Lorentz force corresponding to a magnetic field strength of 1 T is presented. The cyclotron frequency, given as

$$\vec{\Omega}_{\text{cyc}} = -\frac{q}{\gamma m}\left(\vec{B}_{\perp} - \frac{\vec{\beta}\times\vec{E}}{\beta^2 c}\right), \tag{3.152}$$

expresses the rotation of the momentum induced by the electromagnetic fields according to:

$$\frac{\mathrm{d}\vec{p}}{\mathrm{d}t} = \vec{\Omega}_{\text{cyc}} \times \vec{p}\,. \tag{3.153}$$

Its value is shown as dotted lines for the different scenarios. Due to relativistic effects, the cyclotron frequency decreases for increasing momenta. In the non-relativistic limit, the spin precession frequency $\vec{\Omega}_{\text{MDM}}$ agrees with Equation 3.144. Thus, the interaction of the magnetic dipole moment with electric fields vanishes, while it takes the value $\Omega_{\text{MDM}} = |\frac{\vec{\mu}}{s\cdot\hbar}\cdot\vec{B}|$ for magnetic fields. Here, $s = \frac{1}{2}$ for protons and $s = 1$ for deuterons. For increasing momenta the impact of electric fields increases rapidly. In the ultra-relativistic limit, a constant Lorentz force requires also constant magnetic and electric fields. Hence, for magnetic and for electric fields the term proportional to $G\gamma$ in equation 3.151 becomes dominant. Due to the negative G in the deuteron case, this leads to a decrease of the spin precession frequency in the momentum regime up to 10 GeV/c.

The comparison of the cyclotron and spin precession frequencies reveals a single crossing point of the frequencies in case of protons in the pure electric case. This can be obtained mathematically by comparing Equations 3.151 and 3.152:

$$\tilde{\vec{\Omega}}_{\text{MDM}} = \vec{\Omega}_{\text{MDM}} - \vec{\Omega}_{\text{cyc}} = -\frac{q}{\gamma m}\left[G\gamma\vec{B}_{\perp} + (1+G)\,\vec{B}_{\parallel} - \left(G\gamma - \frac{\gamma}{\gamma^2-1}\right)\vec{\beta}\times\frac{\vec{E}}{c}\right]. \tag{3.154}$$

At the crossing point the precession speeds of the momentum vector and spin vector are equal. Thus, a spin vector, which is initially aligned to the momentum direction, stays aligned to the momentum direction. Hence, this is called the "frozen spin" effect. For protons, the corresponding "magic" momentum amounts to:

$$\left(G\gamma - \frac{\gamma}{\gamma^2-1}\right) = 0 \quad \Rightarrow \quad p = \frac{mc}{\sqrt{G}} \approx 0.7\,\text{GeV/c}\,. \tag{3.155}$$

This configuration is relevant for the EDM measurement methods discussed in Section 3.3.

In order to predict the influence on spin arising from imperfection fields in the accelerator or from the introduction of a new element for spin manipulation, the ratios of the spin precession frequencies for different momenta are examined. The results are illustrated in Figure 3.7. On the one hand, the frequency ratio of transverse electric to magnetic fields is shown. On the other hand, the ratio induced by a longitudinal compared to a transverse magnetic field of same strength is presented. In case of protons, the electric to magnetic spin frequency ratio continuously grows and finally reaches unity in the ultra-relativistic limit. Due to the negative G of deuterons the ratio decreases at the end of the illustrated interval. Considering momenta up to 10 GeV/c the longitudinal

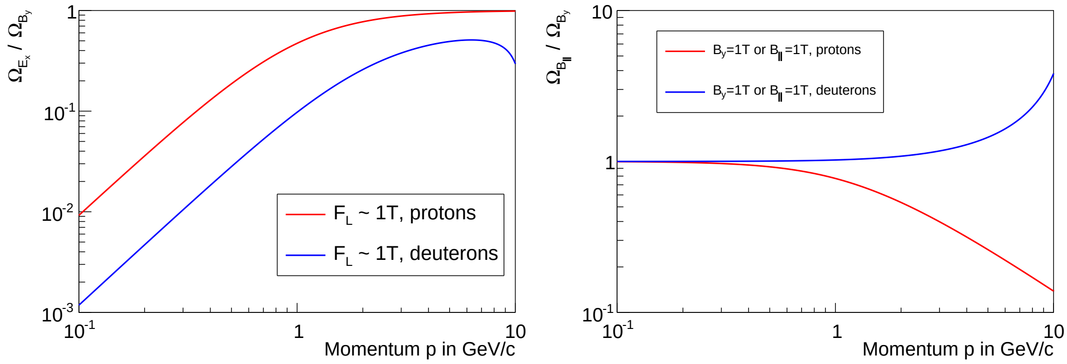

(a) (b)

Figure 3.7: Figure (a) shows the ratio of spin precession frequencies induced by a radial electric field and a vertical magnetic field according to Equation 3.151. Each field strength is scaled to act with an equal Lorentz force on a proton or deuteron moving along the longitudinal direction. Figure (b) pictures the ratio of spin precession frequencies for vertical and longitudinal magnetic fields in the same momentum range.

to transverse magnetic field spin frequency ratio increases only for deuterons, but decreases for protons. In the ultra-relativistic limit, longitudinal fields become inefficient for protons and deuterons.

3.2.5 Spin Motion in Terms of Particle Coordinates

The phase space coordinates of the stored particles are usually expressed in the co-moved curvilinear coordinate system defined in Section 3.1.1. The spin equation of motion can also be formulated in terms of these particle phase space coordinates as pointed out by Courant and Ruth [87]. For this purpose, the derivative of the spin vector with respect to the ring angle θ is obtained. Reformulating Equation 3.148 yields:

$$\frac{\mathrm{d}\vec{S}}{\mathrm{d}\theta} = \rho\frac{\mathrm{d}\vec{S}}{\mathrm{d}s} = \rho t'\frac{\mathrm{d}\vec{S}}{\mathrm{d}t} = \rho t'\left[\vec{\Omega}_{\mathrm{MDM}} + \vec{\Omega}_{\mathrm{EDM}}\right] \times \vec{S}\ . \tag{3.156}$$

In the following, only the magnetic dipole moment in a pure magnetic ring is considered. To first order, the transverse and longitudinal magnetic field can be written as:

$$\begin{aligned}\vec{B}_\perp &= \frac{1}{v^2}\left(\vec{v}\times\vec{B}\right)\times\vec{v} = \frac{p}{q}\left(1-\frac{x}{\rho}\right)\left(\vec{v}'\times\vec{v}\right)\\ &= \frac{p}{q}\left(1-\frac{x}{\rho}\right)\left[y''\vec{e}_x + \left(\frac{1}{\rho}-x''\right)\vec{e}_y - \frac{1}{\rho}y'\vec{e}_s\right]\ ,\end{aligned} \tag{3.157}$$

$$\vec{B}_\parallel = \frac{p}{q}\left(\frac{y}{\rho}\right)'\vec{e}_s\ . \tag{3.158}$$

Here, the longitudinal field was obtained using Maxwell equations and assuming a vanishing B_s component on the reference orbit. Instead of the $(\vec{e}_x, \vec{e}_y, \vec{e}_s)$ coordinate system, the $(\vec{e}_1, \vec{e}_2, \vec{e}_3)$ defined in Section 3.2.1 is utilized. Neglecting the EDM contribution Equation 3.156 can be expressed as

$$\frac{\mathrm{d}\vec{S}}{\mathrm{d}\theta} = \rho t' \vec{\Omega}_{\mathrm{MDM}} \times \vec{S} = \vec{S} \times \vec{F} \ . \tag{3.159}$$

For small transverse and longitudinal perturbation fields, it follows:

$$F_1 = \rho(1+G\gamma)\frac{B_1}{\chi_{\mathrm{m}}} = \rho y''(1+G\gamma) \ , \tag{3.160}$$

$$F_2 = \rho(1+G)\frac{B_\parallel}{\chi_{\mathrm{m}}} = \rho(1+G)\frac{B_2 - y'B_3}{\chi_{\mathrm{m}}} = -(1+G\gamma)y' + \rho(1+G)\left(\frac{y}{\rho}\right)' \ , \tag{3.161}$$

$$F_3 = \rho(1+G\gamma)\frac{B_3}{\chi_{\mathrm{m}}} = -(1+G\gamma) + (1+G\gamma)\rho x'' \ . \tag{3.162}$$

Analog to Equation 3.24, the equations for the spin vector components in the rotating frame can be obtained:

$$\frac{\mathrm{d}}{\mathrm{d}\theta}(S_1, S_2, S_3) = \vec{S} \times \vec{F} + (S_2, -S_1, 0) \ . \tag{3.163}$$

Considering only the reference orbit of a perfect magnetic accelerator, the vector $\vec{F}$ can be simplified to:

$$\vec{F} = -(1+G\gamma)\vec{e}_3 \ . \tag{3.164}$$

In this case, the solution of the linear equation system presented in Equation 3.163 is trivially solved:

$$\begin{pmatrix} S_1 \\ S_2 \\ S_3 \end{pmatrix} = \begin{pmatrix} \cos(G\gamma\theta) & -\sin(G\gamma\theta) & 0 \\ \sin(G\gamma\theta) & \cos(G\gamma\theta) & 0 \\ 0 & 0 & 1 \end{pmatrix} \begin{pmatrix} S_{1,i} \\ S_{2,i} \\ S_{3,i} \end{pmatrix} \ , \tag{3.165}$$

where i denotes the initial conditions. Similar to Equation 3.68 the eigenvalues of the spin transfer matrix for the ideal ring are given by

$$\lambda_{1,2} = e^{\pm iG\gamma\theta}, \lambda_3 = 1 \ . \tag{3.166}$$

This illustrates that in an ideal ring, the spin component along the $\vec{e}_3$-axis is preserved, while the perpendicular components precess in the $\vec{e}_1$-$\vec{e}_2$-plane. In this case, the vertical axis is called the spin closed orbit or invariant spin axis $\vec{n}_{\mathrm{c}}$. Analog to the betatron tune, one also can define a spin tune, which represents the number of spin rotations per revolution. According to the eigenvalues in Equation 3.166 it amounts to

$$\nu_s = G\gamma \tag{3.167}$$

for the ideal ring. To avoid confusion, for the spin motion the American notation for tunes ν is chosen, while the tunes of the particle motion are denoted in the European Notation by Q.

3.2.6 Spinor Equation and Spin Transfer Matrix

Equation 3.159 can be rewritten as [77]:

$$\frac{\mathrm{d}\vec{S}}{\mathrm{d}\theta} = \vec{n} \times \vec{S}, \quad \vec{n} = G\gamma\vec{e}_3 - F_1\vec{e}_1 - F_2\vec{e}_2 \; . \tag{3.168}$$

Here, additional vertical fields along the $\vec{e}_3$ axis have been neglected and the F_3 component has been exchanged by the average value $G\gamma$. This equation can be transformed into the two-component spinor formalism introduced in Section 3.2.1. This yields:

$$\frac{\mathrm{d}\psi}{\mathrm{d}\theta} = -\frac{i}{2}H\psi = -\frac{i}{2}(\vec{\sigma}\vec{n})\psi = -\frac{i}{2}\begin{pmatrix} G\gamma & -\xi \\ -\xi^* & -G\gamma \end{pmatrix}\psi \; . \tag{3.169}$$

Here, H denotes the spin precessing kernel and the $\vec{F}$-components, representing the perturbing fields, have been expressed in a complex notation:

$$\xi(\theta) \equiv F_1 - iF_2 \; . \tag{3.170}$$

The spinor equation directly illustrates, that the spinor components are conserved only, if the perturbing fields vanish. In general case, the spinor equation can be solved by the "time" evolution operator. Considering a spinor given at an initial angle θ_i, the state at a final angle θ_f is obtained by:

$$\psi(\theta_f) = \mathcal{T}\exp\left(\int_{\theta_i}^{\theta_f} -\frac{i}{2}H(\theta)d\theta\right) \cdot \psi(\theta_i) = t(\theta_f, \theta_i) \cdot \psi(\theta_i) \; . \tag{3.171}$$

Here, the operator $\mathcal{T}$ is the "time" ordering operator. The spin transfer matrix is defined for the general case and is denoted by t. Assuming, that the magnetic fields in an accelerator element are piecewise constant along θ, the spin transfer matrix for each element can be easily calculated using the T-BMT equation. Consequently, the spinor wave function at the final location f is given by the product of the spin transfer matrices of each element, which is finally multiplied by the initial spinor state. The spin transfer matrix for a full turn, also called the one turn map, can be represented as:

$$t(\theta_i + 2\pi, \theta_i) = e^{-\frac{i}{2}\nu_s\vec{n}_{\mathrm{co}}\vec{\sigma}\cdot 2\pi} \; . \tag{3.172}$$

Here, the spin tune ν_s and the spin closed orbit $\vec{n}_{\mathrm{c}}$ are defined for the general case including perturbation fields. Since the Pauli Matrices supplemented by the identity matrix form a complete basis of the hermitian 2×2-matrices, the spin transfer matrix can be parametrized as follows:

$$t = t_0\sigma_0 - it_1\sigma_1 - it_2\sigma_2 - it_3\sigma_3 \; . \tag{3.173}$$

Using this expansion, the spin transfer matrix T for the classical spin vector $\vec{S}$ can be written as ($\vec{S} = T \cdot \vec{S}_i$):

$$T = \begin{pmatrix} t_0^2 + t_1^2 - t_2^2 - t_3^2 & 2(t_1t_2 - t_0t_3) & 2(t_1t_3 + t_0t_2) \\ 2(t_1t_2 + t_0t_3) & t_0^2 - t_1^2 + t_2^2 - t_3^2 & 2(t_2t_3 - t_0t_1) \\ 2(t_1t_3 - t_0t_2) & 2(t_2t_3 + t_0t_1) & t_0^2 - t_1^2 - t_2^2 + t_3^2 \end{pmatrix} . \tag{3.174}$$

On the reference orbit of an ideal magnetic ring:

$$t_0 = \cos\left(\frac{G\gamma}{2}\theta\right), \quad t_3 = \sin\left(\frac{G\gamma}{2}\theta\right), \quad t_1 = t_2 = 0 \ , \tag{3.175}$$

and the one turn map T equals to the solution given in the previous section. For particles performing betatron and synchrotron oscillation, the phase space coordinates vary in each revolution. Hence, the spin precession axis and the spin phase advance about this axis are different each turn. The definition of the spin closed orbit can be extended to the invariant spin field [88] or equilibrium spin field $\vec{n}(\vec{z})$ taking the phase space motion $\vec{z}$ into account. It satisfies the following condition:

$$\vec{n}(\vec{z}_f) = A(\vec{z}_i)\vec{n}(\vec{z}_i) \ . \tag{3.176}$$

Here, A is the phase space dependent spin transfer matrix ($A(\vec{0}) = T$). The initial and final phase space coordinates are denoted by i and f, respectively. It is important to note, that, in general, $\vec{n}(\vec{z})$ is not an eigenvector of $A(\vec{z})$. Taking the quasiperiodicity into account, a phase space dependent spin tune can be defined as the average number of spin precessions per turn. For this purpose, the phase space coordinates are usually transformed to the action-angle-variables J, ϕ, where J denotes the invariant amplitudes of the phase space motion. In many cases, the extended definition of the spin tune only depends on the the amplitudes J and is therefore called the amplitude-dependent spin tune. More details on this formalism are given in [89].

3.2.7 Depolarizing Resonances

The spin motion is affected by the perturbing fields represented by ξ defined in Equation 3.170. Due to the repetitive motion in a circular accelerator and storage ring, ξ can be expanded into a Fourier series [77]:

$$\xi(\theta) = F_1 - iF_2 = \sum_K \epsilon_K e^{-iK\theta} \ . \tag{3.177}$$

The Fourier amplitude ϵ_K is called the resonance strength corresponding to a resonance tune specified by K. The resonance strength can be expressed in terms of the perturbing fields B_1 and $B_\parallel$, as well as in terms of the phase space coordinates:

$$\begin{aligned} \epsilon_K &= \frac{1}{2\pi}\oint \left[(1+G\gamma)\frac{B_1}{\chi_\mathrm{m}} + (1+G)\frac{B_\parallel}{\chi_\mathrm{m}}\right] e^{iK\theta}\mathrm{d}s \\ &= \frac{1}{2\pi}\oint \left[(1+G\gamma)(\rho y'' + iy') - i\rho(1+G)\left(\frac{y}{\rho}\right)'\right] e^{iK\theta}\mathrm{d}\theta \ . \end{aligned} \tag{3.178}$$

3.2.7.1 Classification

The spin resonance type can be classified by the value of K as presented in Table 3.2. Assuming that vertical misalignments of the focusing quadrupoles are the main

Table 3.2: Classification of depolarizing spin resonances. K is the resonance tune and P the super periodicity of the accelerator/storage ring. The variables j, k, m_s, m_x, m_y are integer values (adapted from [77]).

K	resonance type
j	imperfection resonance
$kP \pm Q_y$	intrinsic resonance
$j + kP \pm m_s Q_{\text{sync}} \pm m_x Q_x \pm m_y Q_y$	higher-order resonance

contribution, the resonance strengths simplifies to:

$$\begin{aligned} \epsilon_K &= \frac{1}{2\pi}(1+G\gamma) \oint y'' e^{iK\theta} \mathrm{d}s \\ &= \frac{1}{2\pi}(1+G\gamma) \oint \frac{1}{\chi_{\mathrm{m}}} \frac{\partial B_x}{\partial y} y e^{iK\theta} \mathrm{d}s \\ &= \frac{1}{2\pi}(1+G\gamma) \oint \frac{B_x}{\chi_{\mathrm{m}}} e^{iK\theta} \mathrm{d}s \;, \end{aligned} \tag{3.179}$$

by taking Equations 3.42 and 3.47 into account. Two main contributions lead to a vertical offset of the particle trajectory with respect to the field free quadrupole centers:

$$y = (y_{\mathrm{c}} - y_{\mathrm{offset}}) + y_\beta \;. \tag{3.180}$$

The first term refers to the closed orbit offset with respect to the quadrupole centers. Here, y_{c} is the closed solution in the reference coordinate system given in Equation 3.93 and y_{offset} refers to the random offsets of the quadrupole centers in this system. The second term is the betatron motion of the particle defined in Equation 3.49, here denoted by y_β. These two terms contribute to different classifications of spin resonances listed in Table 3.2.

The closed orbit y_{c} (as well as y_{offset}) correspond to the periodic fixed point solution of the orbital transfer map. Hence, it only contributes to to the imperfection resonances, which are associated to the integer resonance tunes. Assuming that the misalignments of the quadrupoles and the corresponding radial perturbing fields are known, they could be substituted into Equation 3.179 to calculate the resonance strength. Due to the periodicity it is sufficient to evaluate the loop integral for only one turn to determine the resonance strength. In case there are no misalignments, the resonance strength is zero. That is the reason, why this type of resonance is called imperfection resonance.

In case of pure quadrupole fields, the betatron motion y_β is independent of the closed orbit solution. Instead, the resulting resonance strength is strongly connected to the vertical betatron tune. The betatron motion is only quasi-periodic, because integer betatron tunes have to be avoided for stability reasons. Thus, the betatron phase is different after each turn and a calculation of the loop integral for only one turn in order to evaluate the resonance strength is not sufficient. Instead the integral has to be averaged over a certain number of turns to obtain the resonance strength. The spin resonances associated to the betatron motion are classified as intrinsic spin resonances of the accelerator, since they occur in absence of any imperfection. The resonance strength usually depends on the phase space amplitude of the individual particle, i.e. the Courant-Snyder invariants $\varepsilon_{\mathrm{CS}}$.

Further important spin resonances occur in case of phase space coupling (coupling resonances) and synchrotron motion, i.e. the momentum oscillations (synchrotron sideband resonances). In the first case, the resonance strength can be minimized by coupling correction routines, which are applied during the setup of the accelerator configuration [90]. In the latter case, the momentum oscillations induce a oscillation of the spin phase advance per turn, which has an impact on the resonance strength. The derivation of the resonance strength modification is illustrated in the next section.

3.2.7.2 Synchrotron Sideband Resonances

Up to linear order, the synchrotron motion of a off-momentum particle can be parametrized to first order as:

$$\delta = \hat{\delta}\cos(Q_{\mathrm{sync}}\theta + \phi) \ . \tag{3.181}$$

Here, a smooth oscillation along the ring angle θ is assumed. The momentum deviation δ has been introduced in Section 3.1 and ϕ is an arbitrary phase. The spin precession rate in each turn oscillates in case of momentum deviations:

$$G\gamma = G\gamma_0\left(1 + \frac{\Delta\gamma}{\gamma_0}\right) = G\gamma_0\left(1 + \beta_0^2\hat{\delta}\cos(Q_{\mathrm{sync}}\theta + \phi)\right) \ . \tag{3.182}$$

The integrated spin phase advance yields:

$$\int_0^\theta G\gamma \mathrm{d}\theta = G\gamma_0\theta + \frac{G\gamma_0\beta_0^2}{Q_{\mathrm{sync}}}\hat{\delta}\sin(Q_{\mathrm{sync}}\theta + \phi) \ . \tag{3.183}$$

In the following, the illustrative analytical solvable model of an isolated spin resonance with the resonance tune K is considered. Only the dominating summand of Equation 3.177 is taken into account. As long as the strengths of nearby resonances are small compared to their distance in spin tune space $\delta_\nu = G\gamma - K$, this model can be used to investigate the effect of spin resonances. Consequently, the perturbing term of the spinor equation simplifies to:

$$\xi = \epsilon_K e^{-iK\theta} \ , \tag{3.184}$$

and hence the spinor equation for this particular case reads [77]:

$$\frac{\mathrm{d}\psi}{\mathrm{d}\theta} = -\frac{i}{2}\begin{pmatrix} G\gamma & -\epsilon_K e^{-iK\theta} \\ -\epsilon_K^* e^{iK\theta} & -G\gamma \end{pmatrix}\psi \ . \tag{3.185}$$

To study the pure impact of the disturbing fields the equation is transformed into the interaction picture. Therefore a new spinor is defined according to [77]:

$$\psi = e^{-\frac{i}{2}\int_0^\theta G\gamma \mathrm{d}\theta \sigma_3}\psi_I \ . \tag{3.186}$$

The new spinor equation in this frame is given by:

$$\frac{\mathrm{d}\psi_I}{\mathrm{d}\theta} = -\frac{i}{2}\begin{pmatrix} 0 & -\epsilon_K e^{-i(K\theta-\int_0^\theta G\gamma \mathrm{d}\theta)} \\ -\epsilon_K^* e^{i(K\theta-\int_0^\theta G\gamma \mathrm{d}\theta)} & 0 \end{pmatrix}\psi_I \ . \tag{3.187}$$

It can be easily observed, that in case the resonance strength vanishes the spinor in this frame is constant, since the coordinate system and the spinor have the same precession speed and direction around the vertical axis. The driving term in the spinor equation can be expanded into a Fourier series:

$$\begin{aligned} \epsilon_K e^{-iK\theta-\int_0^\theta G\gamma \mathrm{d}\theta} &= \sum_{m=-\infty}^{\infty} \epsilon_K J_m(g) e^{-i(K-G\gamma_0-mQ_{\mathrm{sync}})\theta} \\ \text{with} \qquad g &= \frac{\beta_0^2 G\gamma_0}{Q_{\mathrm{sync}}}\hat{\delta} \ . \end{aligned} \tag{3.188}$$

The terms for $m \neq 0$ are called the synchrotron sideband resonances. In case the condition $|\epsilon_K J_m(g)| < Q_{\mathrm{sync}}$ holds, the contribution of each sideband resonance is separated from the others. This allows one to treat them as isolated resonances. The effective resonance strengths of each sideband resonance is modified by a Bessel function:

$$\tilde{\epsilon}_K = \epsilon_K J_m(g) \ . \tag{3.189}$$

Finally, two numerical examples are considered. Subsequent chapters deal with the examination of protons and deuterons at an energy around 1 GeV/c. In an ion synchrotron, the synchrotron tunes are typically around $Q_{\mathrm{sync}} \approx 10^{-3}$. Thus, two subsequent synchrotron sidebands are separated by the same amount. The maximum momentum deviation is considered to be also in the order of $\hat{\delta} = 10^{-3}$. The ratio of the effective resonance strengths of the first sideband resonances $m = \pm 1$ and of the the main resonance $m = 0$ for the given numerical estimates can be obtained:

$$\text{protons:} \left|\frac{\tilde{\epsilon}_K(m=\pm 1)}{\tilde{\epsilon}_K(m=0)}\right| \approx 0.9 \ , \qquad \text{deuterons:} \left|\frac{\tilde{\epsilon}_K(m=\pm 1)}{\tilde{\epsilon}_K(m=0)}\right| \approx 0.02 \ . \tag{3.190}$$

Considering a main resonance strength $\tilde{\epsilon}_K(m=0) \ll Q_{\mathrm{sync}}$ the synchrotron sidebands are well separated in these scenarios.

3.2.7.3 Induced Spin Resonances by a Radiofrequency Device

A further class of spin resonances are artificially introduced spin resonances. They can be provided by RF electromagnetic fields. In general case, these fields can introduce additional spin rotations as well as beam excitations. In this section, RF elements that produce a negligible beam excitation are considered. Such situation can be realized by an RF solenoid with a longitudinal magnetic field. Alternatively, also an RF device providing a superposition of transverse electric and magnetic fields in a Wien filter [91] configuration can be used. For this device, the strengths of superimposed transverse electric and magnetic fields are adjusted to cancel the net Lorentz force. This allows one to construct spin rotators with minimized beam excitation about the transverse and longitudinal axes. A field strength variation implies a change of the resonance strength, while the frequency of the RF device controls the resonance tune. The frequency can also be expressed in terms of the resonance tune of the RF device:

$$\nu_{\mathrm{rf}} = 2\pi \frac{f_{\mathrm{rf}}}{f_{\mathrm{rev}}} \ , \tag{3.191}$$

where f_{rev} denotes the revolution frequency. Since the RF device is located at a particular position in the ring with a small length compared to the ring circumference, it can be approximated by a point-like device. The spin resonance condition is fulfilled in case [92]:

$$\nu_{\mathrm{rf}} = \nu_s + k, \quad k \in \mathbb{Z} \ . \tag{3.192}$$

The strength of the RF device can be parametrized in terms of its rotation vector $\vec{\Omega}$ and maximum rotation angle α_0. Considering an oscillating longitudinal magnetic field of an RF solenoid $B_{\mathrm{sol}} = \hat{B}_{\mathrm{sol}} \cos(\nu_{\mathrm{sol}}\theta + \phi)$, the rotation vector is given by:

$$\vec{\Omega} = -\frac{q}{\gamma m}(1+G)\vec{B}_{\mathrm{sol}} \ . \tag{3.193}$$

The maximum rotation angle α_0 per pass depends on the maximum field strength and can be obtained by integration:

$$\alpha_0 = \int\limits_0^{t_{\mathrm{pass}}} \Omega \, \mathrm{d}t \ . \tag{3.194}$$

Using $t_{\mathrm{pass}} = L_{\mathrm{sol}}/v$, this yields:

$$\alpha_{\mathrm{sol}} = (1+G) \int\limits_0^{L_{\mathrm{sol}}} \frac{\hat{B}_{\mathrm{sol}}}{\chi_{\mathrm{m}}} \, \mathrm{d}s \ . \tag{3.195}$$

In the previous step, the field variation during one particle passage has been neglected. In case of an RF Wien filter, a similar derivation can be pursued. Assuming perfectly adjusted field strengths ($\hat{\vec{E}}_{\mathrm{wf}} = -\vec{v} \times \hat{\vec{B}}_{\mathrm{wf}}$) oscillating with same frequency and phase, this leads to the a maximum rotation angle of:

$$\alpha_{\mathrm{wf}} = \frac{(1+G)}{\gamma} \int\limits_0^{L_{\mathrm{wf}}} \frac{\hat{B}_{\mathrm{wf}}}{\chi_{\mathrm{m}}} \, \mathrm{d}s \ . \tag{3.196}$$

The additional γ in the denominator reflects the same amount of spin rotation for transverse electric and magnetic fields in the ultra-relativistic limit, if they produce an equal Lorentz force contribution. Further note, that an explicitly vanishing EDM was not required for these derivations, since the EDM induced spin rotation is connected to a non-vanishing Lorentz force. Thus, an RF Wien filter does not interact with any particle EDM.

In the following, an RF device with an arbitrary spin rotation axis $\vec{\Omega}$ characterized by its orientation $\vec{m}$ in a storage ring is considered. At the particular location of the RF device the spin precession per turn in the static storage ring can be characterized by the spin tune ν_s and the spin closed orbit, here denoted as $\vec{n}$. The subsequent illustration of the formalism strongly benefited from internal discussions [93, 94]. The spinor equation of this configuration reads:

$$\frac{\mathrm{d}\psi}{\mathrm{d}\theta} = -\frac{i}{2}\left[\nu_s(\vec{n}\vec{\sigma}) + \nu_o(\theta)(\vec{m}\vec{\sigma})\right]\psi \ . \tag{3.197}$$

The first term in the square brackets characterizes the rotation induced by the static ring, and the second term takes the contribution of the RF device into account. The parameter $\nu_o(\theta)$ reflects the spin rotations induced by the RF device and can be parametrized as:

$$\nu_o(\theta) = \frac{\alpha_0}{2\pi}\cos(\nu_{\mathrm{rf}}\theta + \phi)\sum_{k=-\infty}^{\infty} 2\pi\delta(\theta - 2\pi k) \ . \tag{3.198}$$

In this section, the effects of betatron and synchrotron oscillation are neglected and only the reference particle is considered. The equation is transformed into the resonance precessing frame (here: $K = \nu_{\mathrm{rf}}$)

$$\psi = e^{-\frac{i}{2}\nu_{\mathrm{rf}}\theta(\vec{n}\vec{\sigma})}\psi_K \ , \tag{3.199}$$

which changes the spinor equation according to:

$$\begin{aligned}\frac{\mathrm{d}\psi_K}{\mathrm{d}\theta} &= -\frac{i}{2}e^{\frac{i}{2}\nu_{\mathrm{rf}}\theta(\vec{n}\vec{\sigma})}\left[\delta_\nu(\vec{n}\vec{\sigma}) + \nu_o(\theta)(\vec{m}\vec{\sigma})\right]e^{-\frac{i}{2}K\theta(\vec{n}\vec{\sigma})}\psi_K \\ &= -\frac{i}{2}T(\theta)\psi_K \ .\end{aligned} \tag{3.200}$$

The first term accounts for the difference between spin tune and resonance tune $\delta_\nu = \nu_s - \nu_{\mathrm{rf}}$. The second term can be treated as a small perturbation as long as the spin rotation induced by the RF device is small compared to the spin precession frequency in the storage ring. Using the following relation for Pauli matrices:

$$(\vec{a}\vec{\sigma})(\vec{b}\vec{\sigma}) = (\vec{a}\cdot\vec{b})\sigma_0 + i(\vec{a}\times\vec{b})\vec{\sigma} \ , \tag{3.201}$$

the operator $T(\theta)$ can be simplified to:

$$\begin{aligned}T(\theta) = \delta_\nu\vec{n}\vec{\sigma}& \\ &+ \nu_o(\theta)\cos(\nu_{\mathrm{rf}}\cdot\theta)\left[\vec{n}\times(\vec{m}\times\vec{n})\right]\vec{\sigma} \\ &+ \nu_o(\theta)\sin(\nu_{\mathrm{rf}}\cdot\theta)\left[\vec{m}\times\vec{n}\right]\vec{\sigma} \\ &+ \nu_o(\theta)\left(\vec{m}\cdot\vec{n}\right)\vec{n}\vec{\sigma} \ .\end{aligned} \tag{3.202}$$

It is important to note, that the first and the last term act in the same plane as the spin precession induced by the static ring. Hence, they shift or modulate the spin tune of the static ring within the resonance precessing frame. However, the second and third term act perpendicular to that plane and induce a spinor oscillation in the precessing frame. In the next step, the θ-dependent perturbations are averaged, since they are considered to be small $\nu(\theta) \ll 1$. The summation of the discrete spin rotations induced by the RF device is defined by $\nu_o(\theta)$. It is replaced by a continuously acting perturbation with averaged strength, assuming that ν_{rf} is not a ratio of two rational numbers with a small denominator. In this case, the following relations can be applied:

$$\frac{1}{2\pi}\int_0^{2\pi}\sin(\nu_{\mathrm{rf}}\theta)\mathrm{d}\theta = \frac{1}{2\pi}\int_0^{2\pi}\cos(\nu_{\mathrm{rf}}\theta)\mathrm{d}\theta = \frac{1}{2\pi}\int_0^{2\pi}\sin(\nu_{\mathrm{rf}}\theta)\cos(\nu_{\mathrm{rf}}\theta)\mathrm{d}\theta = 0\ , \tag{3.203}$$

$$\frac{1}{2\pi}\int_0^{2\pi}\sin(\nu_{\mathrm{rf}}\theta)\sin(\nu_{\mathrm{rf}}\theta)\mathrm{d}\theta = \frac{1}{2\pi}\int_0^{2\pi}\cos(\nu_{\mathrm{rf}}\theta)\cos(\nu_{\mathrm{rf}}\theta)\mathrm{d}\theta = \frac{1}{2}\ . \tag{3.204}$$

Applying these relations leads to an effective θ-independent operator $\tilde{T}$:

$$\begin{aligned} T(\theta) \quad \rightarrow \quad \tilde{T} = {} & \delta_\nu \vec{n}\vec{\sigma} \\ & + \frac{\alpha_0}{4\pi}\cos(\phi)\left[\vec{n}\times(\vec{m}\times\vec{n})\right]\vec{\sigma} \\ & + \frac{\alpha_0}{4\pi}\sin(\phi)\left[\vec{m}\times\vec{n}\right]\vec{\sigma}\ . \end{aligned} \tag{3.205}$$

The spin rotation axes of the first ($\vec{n}$), the second ($\vec{n}\times(\vec{m}\times\vec{n})$) and the third term ($\vec{m}\times\vec{n}$) are perpendicular to each other. Together they build a basis, in which the initial spinor can be expanded. Assuming only one term of $\tilde{T}$ is non-zero, the spinor component along this direction would be preserved, while the perpendicular contributions precess in this frame. In case of $\delta_\nu = 0$, only the spin interaction induced by the RF device remains. In the following discussion, the spin motion in absence of the RF device is denoted as unperturbed, although the spin closed orbit might be tilted. The perturbation induced by the RF device, which leads to a variation of the spin component parallel to the spin closed orbit, can be characterized by a specific resonance strength. In the new frame, the resonance strength is given by:

$$\begin{aligned} |\epsilon_K| &= \sqrt{\left(\frac{\alpha_0}{4\pi}\cos(\phi)\left[\vec{n}\times(\vec{m}\times\vec{n})\right]\right)^2 + \left(\frac{\alpha_0}{4\pi}\sin(\phi)\left[\vec{m}\times\vec{n}\right]\right)^2} \\ &= \frac{\alpha_0}{4\pi}\left|\vec{m}\times\vec{n}\right|\ . \end{aligned} \tag{3.206}$$

Only if the spin closed orbit of the static ring in absence of an RF device $\vec{n}$ and the spin rotation axis in the RF device $\vec{m}$ are not parallel, an oscillation of the spin component parallel to the spin closed orbit of the static ring is induced. The formal solution to Equation 3.200 can be represented as

$$\psi_K(\theta) = e^{-\frac{i}{2}\tilde{T}\theta}\psi_K(0)\ . \tag{3.207}$$

Using the Equations 3.127, 3.199 and 3.207, the components of the classical spin vector can be calculated according to

$$S_i = \psi^\dagger(0) e^{\frac{i}{2}\tilde{T}\theta} e^{\frac{i}{2}\nu_{\mathrm{rf}}\theta}\sigma_i e^{-\frac{i}{2}\nu_{\mathrm{rf}}\theta} e^{-\frac{i}{2}\tilde{T}\theta}\psi(0)\ . \tag{3.208}$$

Here, the spin vector has been normalized to unity and the relation:

$$\psi_K(0) = \psi(0) \tag{3.209}$$

has been used. The evolution of the spin components S_i given in Equation 3.208 will be explored in Section 3.2.8.2.

3.2.8 Perturbation of Spin Motion due to Depolarizing Resonances

After classifying the different types of spin depolarizing resonances in particle storage rings, their impact on spin motion is studied in more detail. For this purpose different scenarios are examined. The first scenario deals with the influence of a spin resonance in case of a constant particle momentum. In the second scenario, the crossing of spin resonances utilizing a constant acceleration is explored. The last scenario covers the spin motion expressed in Equation 3.208 and illustrates the connection of the spin closed orbit and the spin rotation axis of an RF device.

3.2.8.1 Spin Motion at Constant Momentum or Constant Acceleration

In this scenario, the unperturbed spin closed orbit is oriented in the vertical direction and the unperturbed spin tune is given by $\nu_s = G\gamma$. Introducing an isolated spin resonance $\xi = \epsilon_K e^{-iK\theta}$ with the strength ϵ_K, the spinor equation given in Equation 3.169 and transformed into the resonance precessing frame can be expressed as [77]:

$$\frac{\mathrm{d}\psi_K}{\mathrm{d}\theta} = -\frac{i}{2}\left(\delta_\nu\sigma_3 - \epsilon_R\sigma_1 + \epsilon_I\sigma_2\right)\psi_K \tag{3.210}$$

with

$$\psi_K(\theta) = e^{-\frac{i}{2}K\theta\sigma_3}\psi(\theta)\ , \tag{3.211}$$

$$\epsilon_K = \epsilon_R - i\epsilon_I\ , \tag{3.212}$$

$$\delta_\nu = G\gamma - K\ . \tag{3.213}$$

The spin tune and the spin closed orbit in the precessing frame are given by:

$$\lambda = \sqrt{\delta_\nu^2 + |\epsilon_K|^2}\ , \tag{3.214}$$

$$\vec{n}_c = \frac{\epsilon_R}{\lambda}\vec{e}_1 - \frac{\epsilon_I}{\lambda}\vec{e}_2 - \frac{\delta_\nu}{\lambda}\vec{e}_3\ . \tag{3.215}$$

The spin vector precesses around the spin closed orbit vector as illustrated in Figure 3.8. The orientation of the spin closed orbit as well as the magnitude of the spin tune depend $|\epsilon_K|$ on the resonance strength and the difference between resonance and unperturbed spin tune δ_ν. In case δ_ν vanishes, the spin closed orbit lies in the horizontal plane and the spin tune amounts to the resonance strength. If the ratio $\delta_\nu/|\epsilon_K|$ approaches $\pm\infty$ the magnitude of the vertical spin closed orbit grows steadily. If the spin is injected parallel to the spin closed orbit in the resonance precessing frame, it does not precess in this frame. The average projection of the spin vector onto the vertical axis amounts to δ/λ. If the unperturbed spin tune $G\gamma$ is slowly changed, such that the spin vector can follow the spin closed orbit adiabatically, the average spin component is still remains at this ratio. The situation is different, if a vertically oriented spin vector is injected into the perturbed system. In this case, the spin precesses around the spin closed orbit and the average projection onto the vertical axis amounts to the ratio δ^2/λ^2. This illustrates, that for values δ/λ close to unity the impact of a resonance is negligible in many situations, while the average projection onto the vertical axis vanishes, when the unperturbed spin tune $G\gamma$ matches the resonance tune.

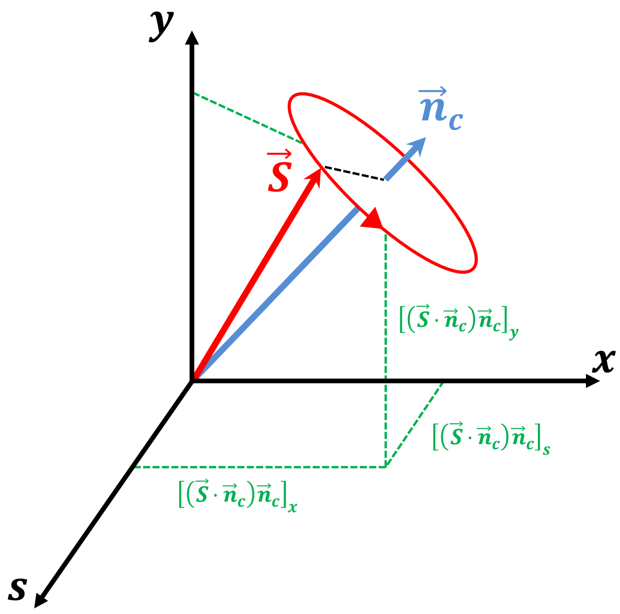

(a)

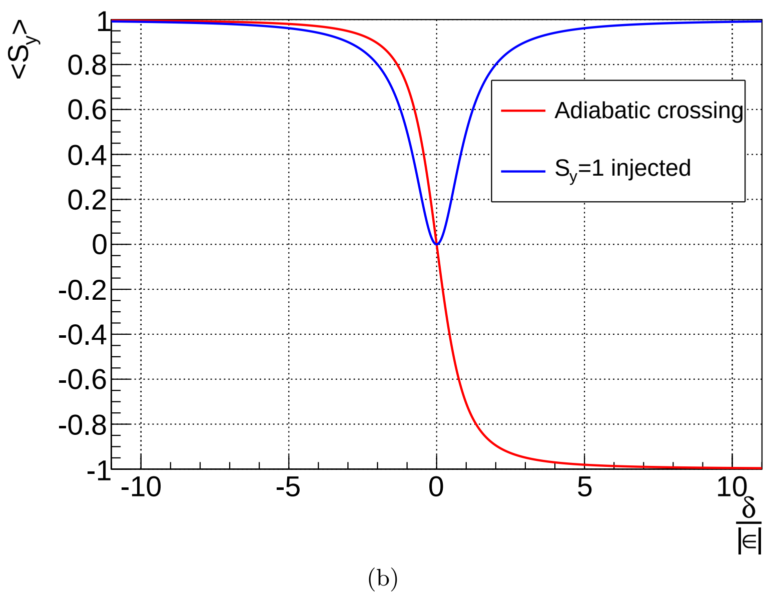

(b)

Figure 3.8: Figure (a) illustrates the precessing spin vector with respect to an arbitrary orientation of the spin closed orbit $\vec{n}_c$. In Figure (b), the averaged vertical spin component with respect to the ratio of deviation from resonance $\delta \equiv \delta_\nu$ to resonance strength $\epsilon \equiv |\epsilon_K|$ is shown. In the "adiabatic crossing" case, a spin vector stays aligned to the spin closed orbit, while the resonance is crossed. The "$S_y = 1$ injected" case deals with an initially vertical spin injected at a certain δ/ϵ value. The spin precession reduces the averaged vertical spin component $\langle S_y \rangle$.

In the following, the resonance crossing process is studied in more detail. A linear change of the difference between the unperturbed spin tune and the resonance tune can be parametrized as:

$$\alpha = \frac{\mathrm{d}\delta_\nu}{\mathrm{d}\theta} = \frac{\mathrm{d}G\gamma}{\mathrm{d}\theta} - \frac{\mathrm{d}K}{\mathrm{d}\theta} \ . \tag{3.216}$$

The first term characterizes the acceleration process, where the magnitude of γ is changed, while a change of the resonance tune in the second term can be introduced by betatron tune variations in case of intrinsic resonances or by changing the frequency of the RF device in case of artificially introduced resonances. The ratio between the final vertical polarization P_f and the initial vertical polarization P_i of a beam after crossing an isolated resonance can be calculated by the Froissart-Stora-formula [95]:

$$\frac{P_f}{P_i} = 2 \cdot \exp\left(-\frac{\pi|\epsilon_K|^2}{2\alpha}\right) - 1 \ . \tag{3.217}$$

Here, a complete resonance crossing from $\delta_\nu \to -\infty$ to $\delta_\nu \to \infty$ is assumed. Three different scenarios can be identified:

- $\alpha \ll |\epsilon_K|^2$: In this case, the crossing speed α is much smaller than the resonance strength. Thus, the spin/polarization vector can follow the spin closed orbit adiabatically and the complete polarization is flipped ($P_f = -P_i$). In this case, the vertical polarization during the crossing process is described by the red curve in Figure 3.8.

- $\alpha \gg |\epsilon_K|^2$: The crossing of the resonance occurs quickly and the the spin depolarizing resonance is barely noticed. Consequently, the polarization along the spin closed orbit is preserved in this case as well ($P_f = P_i$).

- $\alpha \approx |\epsilon_K|^2$: The crossing speed and the squared resonance strength are approximately of the same order of magnitude. In terms of polarization preservation, this is the most critical case. The polarization is partially lost after crossing the resonance ($|P_f| < |P_i|$).

The initial polarization of an ion beam is completely determined by the setup of the polarized ion source. For ions no effective mechanism to increase the polarization of the particle ensemble after injection into an accelerator or storage ring is available. Thus, during the acceleration process it is absolutely mandatory to maintain the polarization, while crossing spin depolarizing resonances. If the relation of the spin resonance crossing speed and the resonance strength matches the third criterion in the previous list, the polarization will be partially lost after crossing. Different methods are commonly used in accelerators to avoid such a polarization loss. They rely on transforming the condition of item three into the conditions of either item one or two. Hence, either the crossing speed needs to be increased or decreased or the resonance strength needs to be varied. Different routines are applicable for imperfection and intrinsic resonances. In case of imperfection resonances a harmonic correction of the closed orbit [96] can be performed requiring a particular variation of the corrector magnet strengths to increase or decrease the imperfection resonance strength. In many cases this is not sufficient, such that so called (partial) snakes are introduced [97]. They generate a strong spin rotation around a defined axis and can enhance the resonance strength, such that a full spin flip is induced.

Intrinsic resonances can be crossed by adjusting the resonance crossing speed. The variation of the energy gain per turn induced by the RF cavity is often not sufficient. Instead, a quick variation of the betatron tune can be induced by tune jump quadrupoles [98] to introduce a fast change of the resonance tune. In other scenarios the resonance strength is enhanced by the usage of an RF dipole with a radial magnetic field [99]. The frequency of the RF dipole is adjusted close to a vertical betatron sideband frequency. Near intrinsic spin resonances connected to the vertical betatron tune, this enhances the resonance strength in two different ways [100, 101]. First, the radial RF field introduces additional resonant spin rotations. Second, vertical betatron oscillations are excited, which enhance the resonance strength of the intrinsic resonance.

3.2.8.2 Spin Motion in Presence of an Arbitrarily Oriented Radiofrequency Device

RF devices are planned to generate an EDM related spin resonance, which introduces a corresponding measurable polarization signal. Simulation routines for such devices have been implemented and benchmarked within this thesis. In this section, the spin motion described by Equation 3.208, which has been used for the benchmarking process, is illustrated in detail. As already pointed out in Section 3.2.7.3, the effective operator $\tilde{T}$ characterizing the spin motion can be divided into contributions parallel and perpendicular to the spin closed orbit $\vec{n}_c$. For that reason, it is convenient to introduce a new coordinate system $(\vec{e}_{\perp_1}, \vec{e}_{\perp_2}, \vec{e}_{\|})$. The basis vectors are defined with respect to the original coordinate system as follows:

$$\vec{e}_{\|} = \vec{n}_c \ , \tag{3.218}$$

$$\vec{e}_{\perp_1} = \vec{e}_{\perp_2} \times \vec{e}_{\|} \ , \tag{3.219}$$

$$\vec{e}_{\perp_2} = \vec{n}_c \times \vec{e}_1 / |\vec{n}_c \times \vec{e}_1| \ . \tag{3.220}$$

In this particular choice, the third basis vector $\vec{e}_{\perp_2}$ is constructed such that the $\vec{e}_1$-component vanishes for any orientation of $\vec{n}_c$. In case of an unperturbed static ring, the new coordinate system coincides with the original one $((\vec{e}_{\perp_1}, \vec{e}_{\perp_2}, \vec{e}_{\|}) = (\vec{e}_1, \vec{e}_2, \vec{e}_3))$.

The vector components of the spin closed orbit $\vec{n}_c$ and the spin rotation axis of the RF device in the new coordinate system are denoted as $\tilde{n}_1, \tilde{n}_2, \tilde{n}_3$ and $\tilde{m}_1, \tilde{m}_2, \tilde{m}_3$, respectively. They are related to their components in the original $(\vec{e}_1, \vec{e}_2, \vec{e}_3)$-system in the following way:

$$\begin{pmatrix} \tilde{n}_1 \\ \tilde{n}_2 \\ \tilde{n}_3 \end{pmatrix} = \begin{pmatrix} 0 \\ 0 \\ 1 \end{pmatrix} , \begin{pmatrix} \tilde{m}_1 \\ \tilde{m}_2 \\ \tilde{m}_3 \end{pmatrix} = \begin{pmatrix} \frac{1}{\sqrt{n_2^2+n_3^2}} \left[m_1(n_2^2+n_3^2) - m_2 n_1 n_2 - m_3 n_1 n_3 \right] \\ \frac{1}{\sqrt{n_2^2+n_3^2}} (m_2 n_3 - m_3 n_2) \\ m_1 n_1 + m_2 n_2 + m_3 n_3 \end{pmatrix} . \tag{3.221}$$

In the following, the three Pauli matrices are reassigned to the three basis vectors of the new coordinate system. Here, the basis vector $\vec{e}_{\|}$ is used as new quantization axis. Hence, the effective operator $\tilde{T}$ defined in Equation 3.205 can be rewritten to:

$$\begin{aligned}\tilde{T} &= \delta_\nu \sigma_3 \\ &+ \frac{\alpha_0}{4\pi}\cos(\phi)\left[\tilde{m}_1\sigma_1 + \tilde{m}_2\sigma_2\right] \\ &+ \frac{\alpha_0}{4\pi}\sin(\phi)\left[\tilde{m}_2\sigma_1 - \tilde{m}_1\sigma_2\right]\ .\end{aligned} \tag{3.222}$$

In this particular representation, the static ring is assumed to be the unperturbed system, although the spin closed orbit might be tilted. The perturbing terms introduced by the RF device are connected to the Pauli matrices σ_1 and σ_2 via the components of the spin rotation axis in the RF device given in the new coordinate system: $\tilde{m}_1$ and $\tilde{m}_2$. The representation in the new coordinate system depicts, that the resonance strength is given by:

$$|\epsilon_K| = \frac{\alpha_0}{4\pi}\sqrt{\tilde{m}_1^2 + \tilde{m}_2^2}\ . \tag{3.223}$$

The evolution of the spin components can be calculated using Equation 3.208. In the following the on-resonance case $\delta_\nu = 0$ is studied. The component $\tilde{S}_3$ characterizes the projection of the spin vector onto $\vec{e}_{\|}$. It is preserved, if the RF device is turned off. The evolution of $\tilde{S}_3$ in presence of a running RF device is illustrated here. It depends on the initial orientation of the spin vector at $\theta = 0$. The evaluation of Equation 3.208 yields:

$$\tilde{S}_1(0) = 1: \quad \tilde{S}_3(\theta) = \frac{\tilde{m}_1\sin(\phi) - \tilde{m}_2\cos(\phi)}{\sqrt{\tilde{m}_1^2 + \tilde{m}_2^2}}\sin\left(\frac{\alpha_0}{4\pi}\sqrt{\tilde{m}_1^2 + \tilde{m}_2^2}\cdot\theta\right)\ , \tag{3.224}$$

$$\tilde{S}_2(0) = 1: \quad \tilde{S}_3(\theta) = \frac{\tilde{m}_1\cos(\phi) + \tilde{m}_2\sin(\phi)}{\sqrt{\tilde{m}_1^2 + \tilde{m}_2^2}}\sin\left(\frac{\alpha_0}{4\pi}\sqrt{\tilde{m}_1^2 + \tilde{m}_2^2}\cdot\theta\right)\ , \tag{3.225}$$

$$\tilde{S}_3(0) = 1: \quad \tilde{S}_3(\theta) = \cos\left(\frac{\alpha_0}{4\pi}\sqrt{\tilde{m}_1^2 + \tilde{m}_2^2}\cdot\theta\right)\ . \tag{3.226}$$

In case the spin vector initially points along one of the perpendicular basis vectors, the interaction with the RF device generates an oscillating spin vector projection onto the spin closed orbit. The oscillation frequency is determined by the resonance strength, while the oscillation amplitude depends on the relation of the components $\tilde{m}_1$ and $\tilde{m}_2$ with respect to the initial phase ϕ of the field of the RF device For a spin vector initially parallel to the spin closed orbit, the amplitude amounts to unity. These equations illustrate, that the spin perturbation introduced by an RF device can be used to probe for the magnitude of the components $\tilde{m}_1$ and $\tilde{m}_2$. As discussed below, the EDM is proportional to $\tilde{m}_1$ in certain configurations of the RF device. This idea is considered as a possible method for measuring EDMs in magnetic storage rings as discussed in the subsequent section.

3.3 EDM Searches in Storage Rings

In Section 2.4, methods for measuring the EDMs of neutral particles have been elaborated. This section focuses on the EDM search for charged particles in storage rings and some of the proposed methods are described. Until now, the muon is the only particle, whose current EDM limit was determined by a storage ring experiment [3].

3.3.1 Parasitic Method

The current EDM limit of the muon was determined parasitically during the $g-2$ experiment in Brookhaven [61]. Primarily, this experiment was designed to measure the anomalous magnetic moment a of the muon. For this purpose, a storage ring consisting of a magnetic guiding field and electric focusing elements was employed. The experiment was performed utilizing muons with "magic" momentum to minimize the interaction between electric fields and the magnetic dipole moment (see also Equation 3.155). The muon spins were initially placed in the horizontal plane, where they precesses around the vertical guiding field. The precession frequency is connected to the anomalous magnetic moment ($\nu_s = G\gamma$) as shown in Equation 3.148. The limited muon lifetime leads to continuous decays of the muons during the store. Due to maximum parity violation in the muon (anti-muon) decay, the preferred direction of the emitted electron (positron) is connected to the spin direction of the muon (anti-muon). This enabled the measurement of the spin precession frequency by determining the counting rates of emitted electrons (positrons). For a vanishing EDM ($\vec{\Omega}_{\text{EDM}}$=0), the spin precession in such a ring takes place exactly in the horizontal plane. Consequently, the spin closed orbit is aligned to the vertical direction. A non-vanishing EDM introduces a tilt of this precession plane [3] as shown in Figure 3.9, because $\vec{\Omega}_{\text{EDM}} \perp \vec{\Omega}_{\text{MDM}}$. Hence, the tilt angle ξ can be characterized by the ratio of EDM and MDM contribution (Equations 3.148 and 3.154):

$$\tan\xi = \frac{\eta_{\text{EDM}}\beta}{2a} \, . \tag{3.227}$$

This tilt corresponds to a radial contribution to the spin closed orbit and as long the EDM compared to the MDM is small: $n_x \approx \xi$ holds. Therefore, an oscillation of a vertical polarization is induced, which in fact was used for the muon EDM measurement. The most stringent upper limit obtained is [3]:

$$|d_\mu| < 1.8 \cdot 10^{-19}\, e\,\text{cm} \, . \tag{3.228}$$

Future experiments measuring the muon g-2 precession also aim to improve the current upper bound on the muon EDM.

The sensitivity of this measurement method strongly depends on the amplitude of the induced vertical polarization oscillation. The maximum oscillation amplitude is given by $A = \sin\xi$. Assuming ultra-relativistic muons and a muon EDM of $1 \cdot 10^{-19}\, e\,\text{cm}$ the tilt amounts to $\xi \approx 9 \cdot 10^{-4}$. This can be compared to a potential proton or deuteron EDM measurement based on this method. Protons and deuterons possess a two to three orders of magnitude larger anomalous magnetic moment than muons. Hence, an EDM measurement at a beam momentum of $1\,\text{GeV/c}$ and an EDM of $1 \cdot 10^{-19}\, e\,\text{cm}$ would induce a significantly smaller tilt angle ξ. The values are $\xi \approx 4 \cdot 10^{-6}$ for the

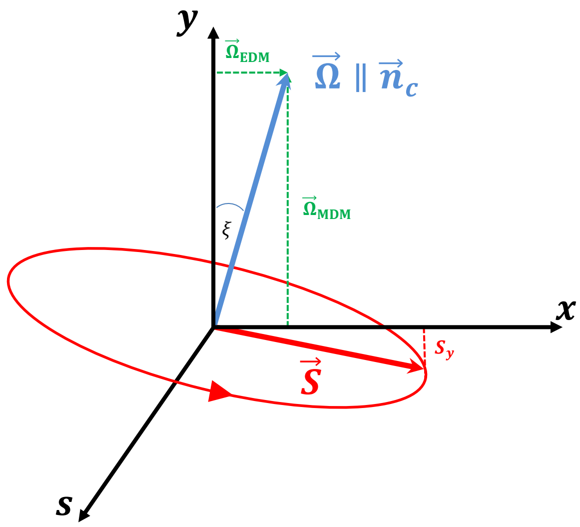

Figure 3.9: Tilt ξ of the spin closed orbit $\vec{n}_c$ due to spin interaction in the guiding fields of a magnetic storage ring. The contributions of MDM and EDM to the spin precession frequency vector $\vec{\Omega}$ are perpendicular to each other. The tilt induces an oscillation of a vertical spin component.

proton and $\xi \approx -3 \cdot 10^{-5}$ for the deuteron case, respectively. EDM magnitudes of $|d_p| \approx 2 \cdot 10^{-17}\, e\,\text{cm}$ and $|d_d| \approx 3 \cdot 10^{-18}\, e\,\text{cm}$ would be required to produce the same tilt angle as in the muon scenario described. In terms of polarimetry small tilt angles are very challenging. For that reason, further measurement methods have been proposed [5, 6].

3.3.2 Frozen Spin Method

The Frozen Spin method is based on the idea to increase the sensitivity of the measured signal by increasing the tilt angle ξ. As indicated in Figure 3.9, the tilt angle is defined by the ratio of $\vec{\Omega}_{\text{EDM}}$ and $\vec{\Omega}_{\text{MDM}}$. Thus, an enhancement of the tilt angle can be achieved by minimizing the MDM induced precession with respect to the momentum vector, as defined in Equation 3.154. In a pure electric storage ring, this is possible for protons at the "magic" momentum (see Equation 3.155). For deuterons, this method is only available when using a superposition of magnetic and electric bending fields, as proposed in [6]. In case of a non-zero EDM the tilt angle within this method is maximized to $\xi = \frac{\pi}{2}$. At the same time the precession frequency is significantly reduced, because the MDM contribution is completely canceled. For particle spins initially aligned to the momentum direction, the interaction of the EDM with the guiding fields of the storage ring will cause a slow buildup of a vertical polarization, which serves an an indication of a non-zero EDM.

The statistical sensitivity for the proton case in a pure electric ring has been investigated in [5]. In this reference it is given by:

$$\sigma_{d(p)} = \frac{2\hbar}{PAE\sqrt{N_{\mathrm{cycle}} f T_{\mathrm{tot}} \tau_{\mathrm{p}}}} \ . \tag{3.229}$$

Here, P denotes the beam polarization, A is the analyzing power of the polarimeter and E is the electric field strength of the guiding fields. The effective detection efficiency is f. The number of stored particles per measurement cycle is given by N_{cycle}. Besides this parameters, also the total measurement time T_{tot} and the spin coherence time for protons τ_{p} are important. Latter characterizes, for which amount of time the particle spins stay aligned to each other and participate at the vertical polarization buildup. A numerical example using $P = 0.8, A = 0.6, E = 10.5\,\mathrm{MV/m}, f = 0.011/2, N_{\mathrm{cycle}} = 4 \cdot 10^{10}, T_{\mathrm{tot}} = 10^7\,\mathrm{s},$ and $\tau_p = 10^3\,\mathrm{s}$ yields a statistical sensitivity of

$$\sigma_{d(p)} = 1.8 \cdot 10^{-29}\,\mathrm{e\ cm} \ . \tag{3.230}$$

In summary, EDM experiments using the frozen spin method would be conducted on an imperfection spin resonance tune. Systematic contributions arising from field imperfections and device misalignments might also lead to a tilt of the invariant spin axis. Hence, they can introduce a not EDM related vertical polarization buildup. For instance, spurious radial magnetic fields, which couple to the magnetic dipole moment, give rise to a growing vertical polarization component. Measurements using clockwise and counter-clockwise beams within the same storage ring are considered to identify these contributions. In pure electric fields both beams would share the same closed orbit, but radial magnetic fields would act differently on the clockwise and counter-clockwise beams. Thus, they introduce a splitting of the vertical orbit of both beams, which is detectable by beam position monitors. A more complete list of systematic error contributions is also discussed in [5].

Dedicated pure electric or combined magnetic/electric storage rings for EDM searches are not yet available. Unfortunately, the frozen spin method is not applicable in a pure magnetic ring. Therefore, a different method using an RF Wien filter is proposed to enhance the sensitivity compared to the parasitic method in a pure magnetic ring like the Cooler Synchrotron COSY.

3.3.3 RF Wien Filter Method

This method is based on the insertion of an RF Wien filter to introduce an EDM related polarization signal [102, 103]. The spin tune of an ideal pure magnetic ring without EDM is given by $\nu_s = G\gamma$, which directly reveals that a "magic" momentum does not exist. In case of a non-vanishing EDM, it couples to the motional electric field $\vec{\Omega}_{\mathrm{EDM}} \propto \vec{\beta} \times \vec{B}$. As discussed in section 3.3.1, this leads to a tilt of the spin closed orbit: $n_x = n_1 \approx \xi$. But as pointed out, the resulting oscillation signal of the vertical polarization is significantly smaller compared to the muon measurement. An enhancement of this signal can be achieved by introducing an induced spin resonance of an RF Wien filter. The two relevant parameters $\tilde{m}_1$ and $\tilde{m}_2$ given in Equation 3.221 and evaluated for $n_1 \ll 1, n_2 \ll 1, n_3 \approx 1$ can be expressed as:

$$\tilde{m}_1 = m_1 - m_3 n_1 \ , \tag{3.231}$$

$$\tilde{m}_2 = m_2 - m_3 n_2 \ . \tag{3.232}$$

These parameters determine the amplitude of the induced polarization oscillation in case the spins are initially perpendicular to the spin closed orbit of the static storage ring, as discussed previously. The coefficients m_i define to the spin rotation axis in the RF device given in the $(\vec{e}_1, \vec{e}_2, \vec{e}_3)$-coordinate system. Reconsidering the RF Wien filter concept discussed in the previous sections, the RF Wien filter is designed for a minimized beam excitation, while a spin rotation axis is induced about the the $\vec{e}_3$-direction. Consequently, the coefficient $\tilde{m}_1$ is proportional to n_1, which contains the EDM related tilt due to the motional electric fields in the storage ring. Assuming the EDM contribution is the sole contribution to a non vertical spin closed orbit, the induced resonance strength as defined in Equation 3.223 is proportional to the EDM magnitude. Thus, in the ideal setup, this method can be applied for a EDM measurement. But also in this method systematic contributions due to field imperfections and misalignments can introduce a tilt of the spin closed orbit in the static storage ring, which is not related to the EDM. These effects will be discussed in Chapter 8. A different approach to illustrate the RF Wien filter method is illustrated in [102]. In this reference, the authors explain the measurement method by a modulation of the spin tune induced by the RF Wien filter in a unperturbed machine and show, that the Fourier series expansion of this modulation possesses a 0-mode contribution, which leads to a vertical polarization buildup related to the EDM. Since the 0-mode contribution is the essential contribution in the frozen spin method, the RF Wien filter method has been denoted as a method based on the "partially frozen spin“ effect.

Studies towards a final conception for a dedicated ring are supported by measurements in pure magnetic rings, e.g. the Cooler Synchrotron COSY in Jülich. Along with these studies, first EDM measurements at COSY at a lower sensitivity level are planned using the RF Wien filter method [7, 104]. Within this thesis, different aspects for the use of this method at COSY are explored:

- Similar to the frozen spin method the spin coherence time limits the measurement period in a single particle store. A study of relevant beam optics parameters to achieve a long spin coherence time as an requirement for the RF Wien filter method has been conducted in Chapter 6.
- Further the study of EDM measurement method requires the development and benchmarking of simulation procedures for RF fields in transfer map based tracking codes (Chapter 5). Their implementation has been verified in Chapter 7 during the investigation of artificial spin resonances induced by an RF solenoid.
- Finally, the new algorithms for RF fields have been applied for a systematic investigation of field imperfections and misalignments faking an EDM signal in the RF Wien filter method. Details are presented in Chapter 8.

In the next chapter an overview of the accelerator complex and the experimental environment for these studies is given.

Chapter 4

Experimental Setup at COSY

In this chapter, the accelerator complex around the Cooler Synchrotron COSY [8, 9] of the Forschungszentrum Jülich and the utilized experimental setup for the polarization measurements are described.

4.1 The Accelerator Facility COSY

The accelerator facility at the Forschungszentrum Jülich consists of (polarized) ion sources, the cyclotron JULIC and the synchrotron and storage ring COSY. They are interconnected by injection and transfer beam lines. The individual areas are illustrated in the following.

4.1.1 Polarized Ion Source

Similar to Ramsey's method of oscillatory fields described in Section 2.4.1, the first requirement for a polarization experiment is a source of polarized particles. In Jülich, a polarized source for negatively charged hydrogen and deuterium ions is in operation. the following information are mainly taken from [105]. The ions are produced by direct charge exchange of colliding hydrogen/deuterium and cesium beams:

$$\mathrm{H}^0 + \mathrm{Cs}^0 \rightarrow \mathrm{H}^- + \mathrm{Cs}^+ \ . \tag{4.1}$$

The neutral hydrogen/deuterium beam is produced in an atomic beam source. An RF dissociator is used to provide the atom beam, which afterwards passes two sextupole magnets. The first magnet is utilized to select a certain spin state defined by the electron spin orientation in the atoms. The second magnet acts as a achromatic lens to focus the beam towards the collision and ionization region. Before reaching the ionization region, the electron polarization is transformed to a nuclear polarization using RF transition units. Two RF transition units are available to select the desired spin states. The cesium beam is produced in the opposite part of the source. It is required for the production of the negatively charged hydrogen/deuterium ions in the ionization region. The afterwards negatively charged ions are deflected by 90 degree into the injection beam line. A static Wien filter is used to separate the ions from electrons and to align the beam polarization with respect to the cyclotron main magnetic field. This way, the polarization is preserved during the subsequent pre-acceleration process in the cyclotron.

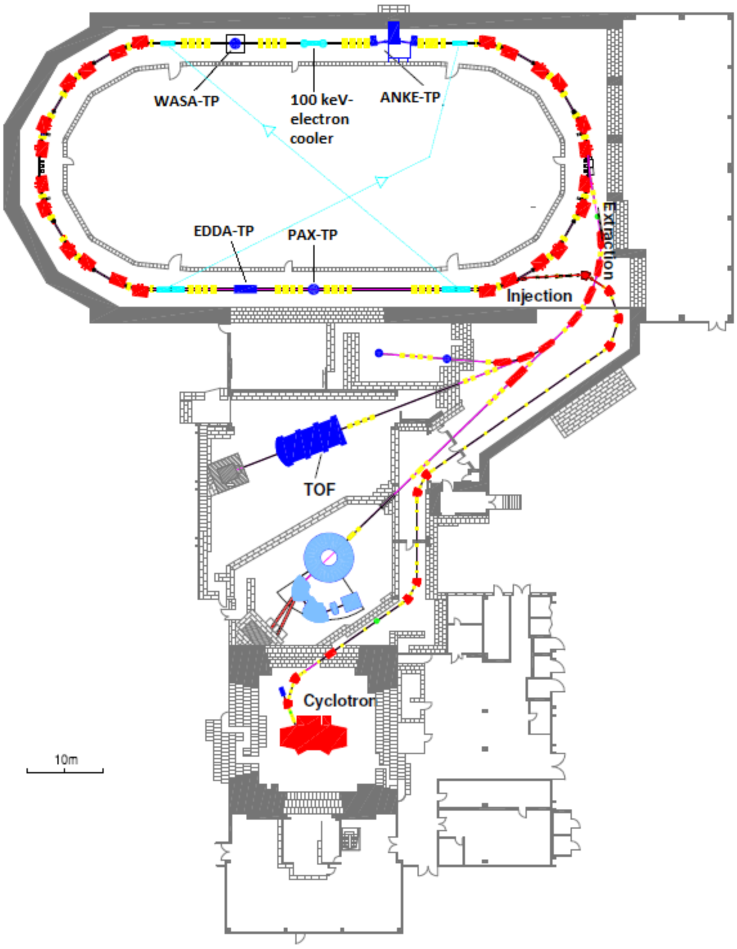

Figure 4.1: Overview of the accelerator complex around COSY in Jülich

During the past years, many test experiments towards EDM measurements have been performed utilizing polarized deuteron beams. Commonly, three different deuteron polarization states are provided for these experiments. The first two states are optimized for a maximized positive or negative vertical vector polarization together with a vanishing tensor polarization. The setup of the third state was chosen to provide vanishing vector and tensor polarizations.

4.1.2 The Cooler Synchrotron COSY

The H^- (D^-) ions are accelerated up to momenta of 300 MeV/c (600 MeV/c) in the cyclotron JULIC. A 100 m beam line is employed to further guide them towards the main synchrotron and storage ring COSY [8, 9]. This is depicted schematically in Figure 4.1. A stripping injection is used to inject the particles into the COSY storage ring. In this process, the negatively charged ions pass a thin foil and the two electrons are stripped off. The resulting polarized protons or deuterons are stored in COSY. This stripping mechanism is one order of magnitude more efficient than directly injecting H^+ or D^+ ions [105] and also allows one to stack new injections on top of already stored particles.

COSY is based on a racetrack design with a circumference of about 183.4 m [8, 9]. The synchrotron principle enables a further acceleration of the stored particles up to momenta of 3.8 GeV/c. This requires a continuous ramping of the magnetic fields according to the beam momentum. The RF acceleration cavity is located in one of the straight sections. Once the desired energy is reached, the stored particle beams can be used at internal experiments at several target locations in the straight sections. In the past, several experiments like the ANKE [106], the WASA [107] and the PAX [108] experiment have been conducted at the internal target locations. Additionally, the beam can also be extracted to external target stations.

The acronym COSY results from the utilization of cooling systems based on two different principles [109]. The following illustration is mainly based on this reference. Since 1993, an 100 keV electron cooler has been used to shrink the phase space volume after injection. In the electron cooler region, an electron beam is injected and placed coaxial to the stored proton or deuteron beam [110]. This electron beam possesses a smaller velocity spread in transverse and longitudinal direction than the ion beam. Due to Coulomb interactions between the ions and the electrons, energy is transferred between the two systems. This energy transfer reduces the velocity spread of the ion beam. Effective cooling requires the same mean velocity of the ion and the electron beam. The maximum electron energy of 100 keV limits the cooling range to roughly 600 MeV/c for protons and 1200 MeV/c for deuterons. A more detailed description of the 100 keV electron cooler is given in section 4.1.2.3. Additionally, a 2 MeV electron cooler has been recently installed to enable electron cooling in the full momentum range of COSY [111]. Besides electron cooling, stochastic cooling is available for protons and deuterons. The corresponding range depends on the ion velocity. For protons it is given by 1500 MeV/c to 3300 MeV/c [109]. It is utilized to limit beam heating due to interactions in the internal experiments and maintain an equilibrium between heating and cooling [109].

4.1.2.1 Ion Optics

The 183.4 m long racetrack design of COSY consists of two 180° arcs, each 52 m long, which are separated by two straight sections with a length of 39.7 m, respectively. An overview of the magnetic structure is depicted in Figure A.1 in the Appendix.

Eight quadrupole families[4] (MQT1-MQT8), each consisting of four quadrupoles, are located in the straight sections [98]. They are arranged in four quadrupole triplets (either FDDF or DFFD[5]) per straight section. The adjustment of the quadrupole strengths enables a telescope configuration with a 1:1-imaging and a betatron phase advance of either π or 2π per straight section. For that reason, the straight sections are denoted as the “Target Telescope” and the “Cooler Telescope”, respectively. In case of a phase advance of 2π the linear transfer matrix of the horizontal and vertical coordinates becomes a unity matrix for each straight section. Thus, in linear order the straight sections are ion optically transparent and do not affect the optical functions in the arc sections. This is the intended configuration for the currently conducted EDM test experiments.

[4] A quadrupole family is a set of identical quadrupoles connected to the same power supply
[5] F = horizontally focusing quadrupole, D = horizontally defocusing quadrupole

In the arc sections, 24 dipoles and 24 quadrupoles guide and focus the beam. They are grouped into six identical mirror symmetrical unit cells with a FODO-OFOD structure[6]. The arc quadrupoles are combined into six families of four quadrupoles (MQU1-MQU6), which enables the tuning of the ion optics in different configurations. The two focusing (defocusing) magnets of the two cells opposite to each other belong to the same family. Hence, both arcs are also mirror symmetric with respect to the center of the straight sections. A sixfold symmetry ($P = 6$) is created by equally powering each cell. The betatron functions and the horizontal dispersion function for a particular choice of this configuration ($Q_x = 3.62$ and $Q_y = 3.59$) are shown in Figure 4.2. The acceleration of polarized protons requires the crossing of intrinsic spin resonances [112], but as discussed in the previous chapter, a higher super periodicity P suppresses certain intrinsic spin resonances. Unfortunately, the proton acceleration to the maximum momentum also requires the crossing of the transition energy of the lattice. Usually, this is achieved by shifting the transition energy due to a strengths variation of the quadrupole families MQU3 or MQU4. This reduces the lattice to a twofold symmetry ($P = 2$). The additionally introduced intrinsic resonances can be suppressed by adjusting the quadrupole strengths [113]. The variation of MQU4 further allows one to minimize the dispersion in the straight sections. This is used to optimize the conditions for the internal experiments. An example for the optical functions in this configuration is also shown in Figure 4.2.

The sextupole magnets are the highest multipole order mounted at COSY. Initially, eight sextupole magnets were placed in the straight sections (MX1-MX8), but one of them, MX1, was removed during the installation of the 2 MeV electron cooler. The ten sextupole magnets in the arcs are grouped into three families (MXS, MXL, MXG). In case of a minimized dispersion in the straights, these families can be used to correct the horizontal and vertical chromaticities. The chromaticity change induced by each family varies due to a significant difference of the optical functions at the sextupole locations.

During the test experiments described within this thesis, a minimized dispersion configuration has been used. The MQU4 family has been employed to minimize the dispersion, while the MQU1/MQU5 and MQU2/MQU6 families have been used to adjust both betatron tunes, preserving the twofold symmetry. In routine operation the horizontal and vertical betatron tunes are usually located between 3.55 and 3.7. The sextupole magnets in the arcs have been used to vary the chromaticities and study their impact on spin motion, especially on the spin coherence time.

4.1.2.2 Spin Manipulators

The polarization of the injected ion beam is initially oriented parallel to the spin closed orbit of COSY. In context of the EDM experiments, spin manipulators are required to rotate the spin into the plane perpendicular to the spin closed orbit. This enables studies of the spin tune and the lifetime of the precessing polarization denoted as spin coherence time. The corresponding spin resonance strengths introduced by these devices have been already discussed in Section 3.2.7.3.

[6]the “O” denotes the space between focusing and defocusing quadrupoles. At COSY a guiding dipole is located there.

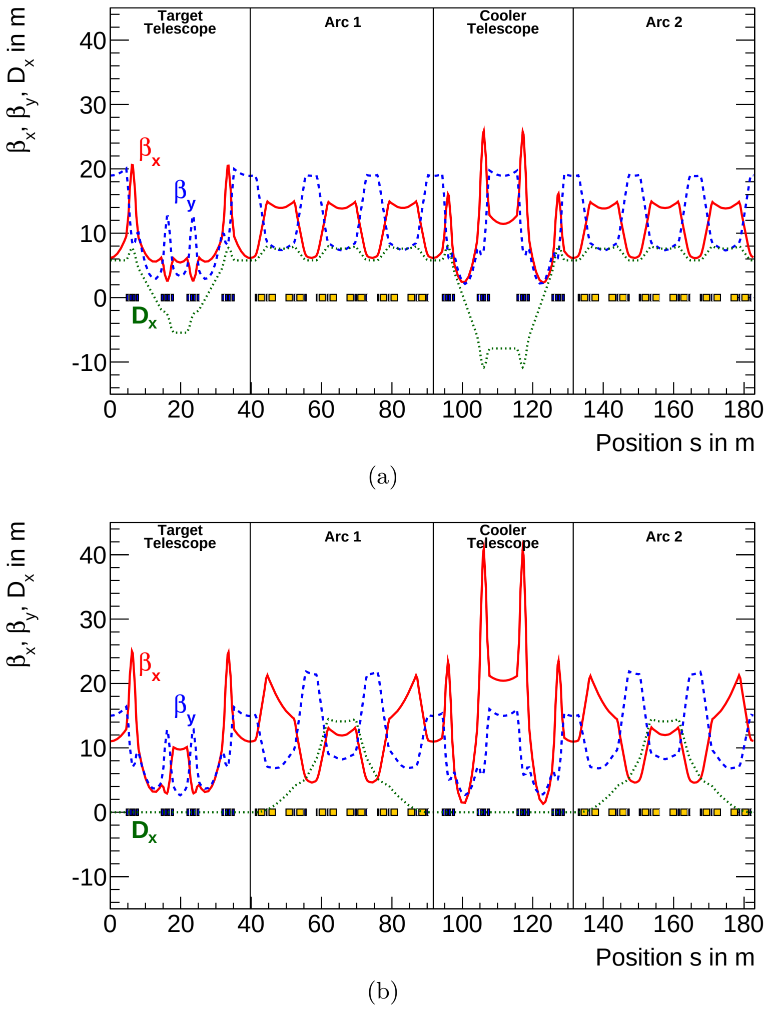

Figure 4.2: The optical functions of the COSY lattice in two configurations. A telescope configuration with betatron phase advances of 2π is used in the straights. (a): The quadrupole strengths of the focusing and the defocusing quadrupoles are equal, respectively. This leads to a sixfold symmetry of the lattice. (b): The quadrupole of the family MQU4 is adjusted to minimize the dispersion in the straights. This reduces the optics to a twofold symmetry (layout adapted from [114]).

At present, different RF spin manipulators are installed. Figure 4.3 depicts the RF solenoid located in the first arc of COSY. It has a length of 57.5 cm and an average diameter of 21 cm [115]. A nominal current of 10 A produces an integrated longitudinal field $\int \hat{B}_{\text{sol}} dl = 0.67\,\text{T mm}$. The RF solenoid is routinely used for flipping the vector polarization of the beam. Recently, also a RF Wien filter has been commissioned [104]. An explosion drawing is shown in Figure 4.4. It produces superimposed radial magnetic and vertical electric fields, whose strengths can be adjusted independently from each other. Thus, it can be operated as a pure magnetic or electric dipole, but also in an RF Wien filter configuration. Its length is about 0.6 m. A nominal current in the coil of 5 A produces a magnetic field of $\int \hat{B}_{\text{wf}} dl = 0.175\,\text{T mm}$. In this case, the required electric field amounts to $\int \hat{E}_{\text{wf}} dl = 24.1\,\text{kV}$ for a Lorentz force compensation in Wien filter configuration. Due to a different shape of the magnetic and electric fringe fields a local

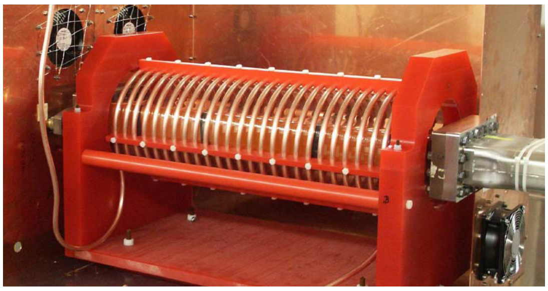

Figure 4.3: Image of the RF solenoid located in the first arc of COSY (taken from [115]).

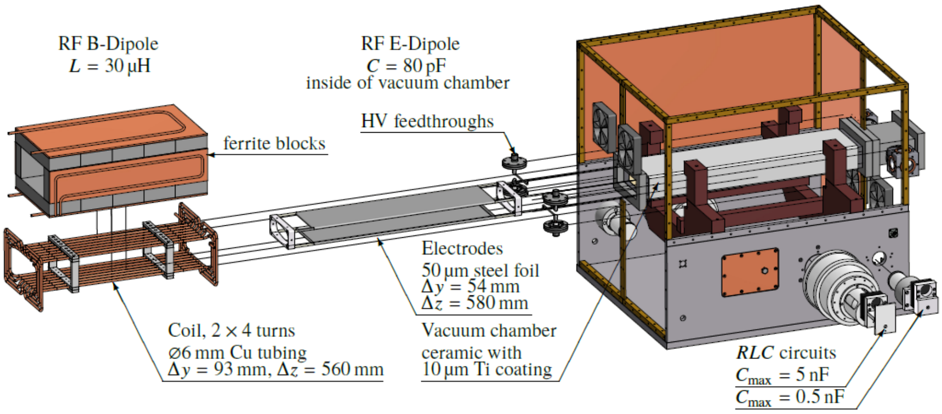

Figure 4.4: Explosion drawing of the RF Wien filter located in the first arc of COSY (taken from [104]).

Lorentz force compensation is not achievable. Here, the aim is a global minimization to reduce the resonance strength contribution arising from the excitation of betatron oscillations [100].

4.1.2.3 100 keV Electron Cooler

The 100 keV electron cooler is located in the center of the Cooler Telescope. A schematic drawing is depicted in Figure 4.5. The electron beam is produced in a flat thermionic cathode in the electron gun [117]. The electrons, electrostatically accelerated to the velocity of the stored ion beam in COSY, are guided and focused by a longitudinal magnetic field, which is generated by the gun solenoid. A subsequent toroid is used to deflect the electrons by 90° into the drift solenoid region with a length of 2 m. In this region the paths of the approximately 2.5 cm wide electron and the ion beam overlap. The effective cooling length is roughly 1.5 m long [118]. At the end of the cooling region, the electron beam is separated from the ion beam in a second toroid towards the collector solenoid. Before dumping, it is electrostatically decelerated to the gun potential. The main purpose of the electron cooler is the reduction of the beam emittances and the momentum spread of the ion beam in the low momentum region of COSY. Cooling at injection energy also allows one to apply a cooling-stacking-injection technique [109]. Here, the ions are cooled between subsequent injections to increase

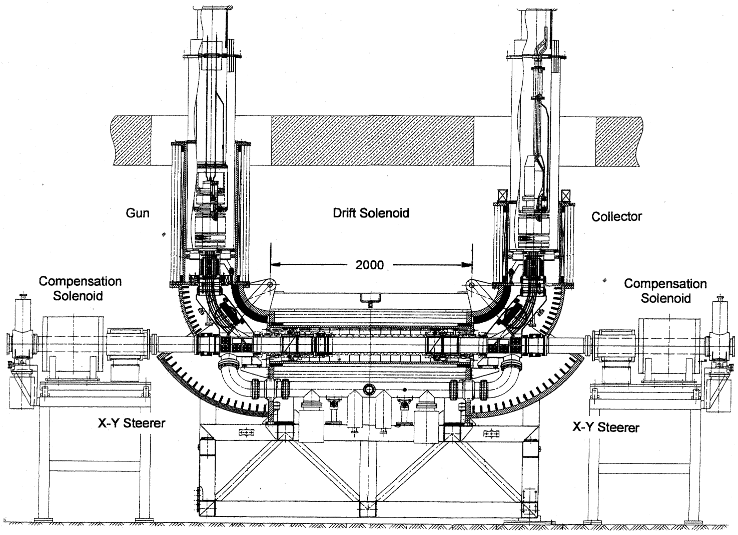

Figure 4.5: Layout of the 100 keV electron cooler located in the center of the Cooler Telescope (taken from [116]).

the total number of stored particles. Furthermore, the electron cooling at injection energy optimizes the conditions for beam diagnostics conducted at higher energies [109], where the beam emittances are additionally reduced by adiabatic damping.

In the current experiments, polarized deuteron beams with a momentum of 970 MeV/c are used. Electron cooling is applied to minimize the beam widths and improve the conditions for polarization experiments. This is an important requirement for spin coherence times (see Chapter 6). Further, the control of the beam chromaticities is mandatory. A variation of the electron velocity can be used to slightly decelerate or accelerate the ion beam. At the same time, the COSY lattice remains unchanged. The beam chromaticities can be obtained from tune measurements at the different beam velocities. Afterwards, they can be corrected by an appropriate selection of sextupole families.

4.1.2.4 Diagnostics

The control of the particle beam requires a precise knowledge of accelerator and beam parameters. The following list summarizes a selection of important parameters and measurement methods required during the setup of the EDM test experiments:

Beam Position The horizontal and vertical beam position is measured by a set of about 30 beam position monitors (BPMs) in the horizontal and vertical plane, respectively. Due to different shapes of the beam pipe a rectangular tube design has been chosen for the arcs, while cylindrical tubes are used in the straight sections [119]. A typical BPM consist of 130 mm long electrode pairs [120]. Each turn, the bunched ion beam generates signals on the electrodes. The signals of the two opposite electrodes are combined to a difference and a sum signal. The latter is proportional to the intensity of the beam, while the ratio of difference and sum signal allows one to determine the beam position with respect to the center of the BPM. A linear dependence between this ratio and the beam position is achieved by the diagonally cut structure of the rectangular or cylindrical tubes. The beam position can be controlled by a about 20 corrector magnets distributed in the ring. An overview is given in Figure A.2 in the Appendix.

Beam Intensity Beam intensity monitoring is required to estimate the amount of particles in the ring. On one hand, it provides information about the beam lifetime, required for the optimization of the accelerator setup. On the other hand, it permits conclusions about the beam interaction rate with the internal target. A beam current transformer (BCT) is used to measure the current I of the stored ion beam. Knowing the revolution frequency f_{rev} of the circulating beam, the number of stored ions N is given by:

$$N = \frac{I}{e \cdot f_{\mathrm{rev}}} \ . \tag{4.2}$$

Beam Profiles Profile measurements are used to determine the transverse ion beam widths. Taking the values of the optical functions at the measurement location into account, enables the calculation of the beam emittances. In synchrotrons, non-destructive methods for beam profile monitoring are preferred [121]. For this purpose, ionization profile monitors (IPM) are a suitable choice. An IPM is located in the first half of the second arc of COSY. Ions and electrons are produced in collisions of the circulating ion beam with residual gas atoms. Biased electrodes of the IPM produce an electric field to accelerate the ions / electrons towards a micro-channel plate (MCP) [122]. A high field homogeneity is required to achieve straight trajectories, needed to reconstruct the beam profiles. The accelerated electrons hit a phosphor screen mounted behind the MCPs. The created light spots are recorded by CCD cameras. A spatial resolution of about 100 µm is achievable.

Betatron Tunes and Chromaticities The knowledge of the betatron tunes is required to avoid betatron resonances as well as intrinsic spin resonances during the accelerator setup. At COSY, tune measurements are performed by the excitation of coherent betatron oscillations [123]. These excitations are achieved by a stripline unit. Commonly, a network analyzer is used to sweep the excitation frequency of the stripline unit in a predefined range. At the same time, it evaluates the induced signal on a single BPM electrode, either in the horizontal or in the vertical direction. Resonant oscillations occur, if the excitation frequency matches a betatron sideband frequency. From these measurements the fractional part of the betatron tunes can be determined. As previously noted, the beam chromaticities can be obtained by repetitive tune measurements for different ion beam velocities, which are induced by a variation of the electron acceleration voltage of the electron cooler.

A selection of recorded diagnosis measurements for a typical experimental setting is presented in the last section of this chapter.

4.2 EDDA Polarimeter

The goal of a storage based EDM experiment is the detection of an EDM related polarization signal. This requires precise polarimetry of the proton and deuteron polarization. In the EDM test experiments the existing EDDA[7] detector [124] is used as a polarimeter. In this section, the detector principle, layout and data acquisition is presented. A more detailed description is given in [125].

4.2.1 Detector Principle and Layout

The principle of the detector is the observation of elastically scattered protons or deuterons emerging in interactions of the circulating beam with an internal target. A carbon block target mounted above the stored beam has been selected during the experiments described within this thesis. Once the stored beam has reached its final conditions required for the experiment, the beam is moved closer to the target and the measurement period is initiated. Different methods have been considered to achieve a continuous rate of elastic scatterings during measurement periods of hundreds of seconds. A set of corrector magnets could be combined to create an orbit bump, which slowly moves the ion beam towards the carbon target. Here, the target interaction rate of the outermost beam particles is adjustable by the magnitude variation of the orbit bump. This method has been replaced recently, due to an observed effect on spin motion induced by the variation of the additional magnetic fields of the corrector magnets. The alternative method utilizes an RF electric field produced by the stripline unit. A white noise signal in a frequency interval around a sideband of the betatron oscillation frequency is used to heat the beam in vertical direction. Since the target is mounted above the beam, the outermost ions elastically scatter on the carbon block.

For spin-1/2-particles the polarization-dependent elastic scattering cross section σ is given by [78]:

$$\sigma = \sigma_0 \left[1 + A_y P_y \cos\phi - A_y P_x \sin\phi\right] \ . \tag{4.3}$$

Here, σ_0 is the cross section for an unpolarized beam and P_x and P_y denote the vector polarizations in the transverse directions. The analyzing power A_y characterizes the spin dependent part of the cross section. It depends on the momentum of the incident particle and the polar scattering angle ϑ. The angle ϕ is the azimuthal angle in the x-y-plane. In case of spin-1-particles the polarization-dependent elastic scattering cross section σ can be written as [78]:

$$\begin{aligned} \sigma = \sigma_0 \Bigg[& 1 + \frac{1}{2} A_{zz} P_{zz} + \left(\frac{3}{2} A_y P_y + \frac{2}{3} A_{xz} P_{xz}\right) \cos\phi \\ & + \frac{1}{6} \left(A_{xx} - A_{yy}\right) \left(P_{xx} - P_{yy}\right) \cos(2\phi) \\ & + \left(-\frac{3}{2} A_y P_x + \frac{2}{3} A_{xz} P_{yz}\right) \sin(\phi) \\ & + \frac{1}{3} \left(A_{xx} - A_{yy}\right) P_{xy} \sin(\phi) \Bigg] \ . \end{aligned} \tag{4.4}$$

[7] Excitation function Data acquisition Designed for Analysis of phase shifts

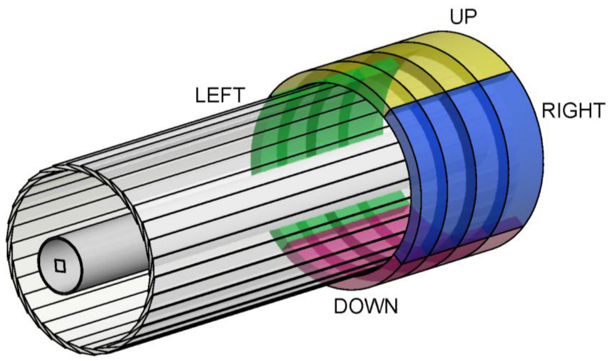

Figure 4.6: Sketch of the EDDA detector (taken from [125]).

The tensor polarization terms are denoted by $P_{ij}, (i, j \in x, y, z)$ and the different analyzing powers are defined by A_i and A_{ij}. Assuming an initial beam polarization setup providing a negligible tensor polarization, Equation 4.4 transforms to Equation 4.3 plus additional factors $\frac{3}{2}$:

$$\sigma = \sigma_0 \left[1 + \frac{3}{2} A_y P_y \cos\phi - \frac{3}{2} A_y P_x \sin\phi \right] . \tag{4.5}$$

These factors are based on the particular definition described in Section 3.2.1. They reflect the fact, that for a vanishing tensor polarization, the maximum achievable vector polarization is $\frac{2}{3}$.

The polarization measurement is performed by measuring the angular dependency of the events detected in the EDDA detector. The layout of the EDDA detector enables the observation of the angular dependency of the scattered particles. A setup of two scintillator layers is used. The inner layer consists of 32 bars mounted cylindrically around the beam pipe oriented parallel to the beam direction. These bars separate the azimuthal angle in equally sized segments. They are combined into four groups each containing eight bars and covering an azimuthal angle of 90°. The center of each group is located directly above, beside or below the center of the beam pipe. Hence, the groups are denoted as up, down, left or right depending on their geometrical arrangement as shown in Figure 4.6. The outer layer consists of cylindrical scintillator half rings mounted perpendicular to the bars. Two facing half rings cover a certain polar scattering angle range. Thus, the choice of a subset of rings allows to restrict the recorded events to a defined range of polar scattering angles. For the particular setup, the four downstream rings providing an angular range from 9° to 14.4° have been selected [125]. Each detector quadrant covers a certain solid angle Ω. This allows one to define average analyzing powers according to:

$$\overline{A}_y^{\mathrm{c}} = \frac{\int A_y \cos\phi \; \mathrm{d}\Omega}{\int \mathrm{d}\Omega} , \tag{4.6}$$

$$\overline{A}_y^{\mathrm{s}} = \frac{\int A_y \sin\phi \; \mathrm{d}\Omega}{\int \mathrm{d}\Omega} . \tag{4.7}$$

Assuming a perfect alignment of the four detector quadrants, $\overline{A}_y^{\mathrm{s}} = 0$ for the left and right quadrants, while $\overline{A}_y^{\mathrm{c}} = 0$ for the up and down quadrants. Thus, using Equation

4.5 and assuming equal detection efficiencies and acceptances of the four quadrants, the average cross section can be written as:

$$\overline{\sigma} = \overline{\sigma}_0 \left(1 + \frac{3}{2}\overline{A}_y^{\mathrm{c}} P_y\right) \qquad \text{for left and right ,} \tag{4.8}$$

$$\overline{\sigma} = \overline{\sigma}_0 \left(1 + \frac{3}{2}\overline{A}_y^{\mathrm{s}} P_x\right) \qquad \text{for up and down .} \tag{4.9}$$

Consequently, the scattering event rates towards the left and right quadrants are sensitive to the vertical beam polarization P_y. Similarly, the scattering towards the up and down quadrant is affected by the radial beam polarization P_x. The asymmetries of the scattering event rates L, R, U, D in two facing regions are proportional to vertical or radial beam polarization, respectively:

$$\varepsilon_{\mathrm{LR}} = \frac{L-R}{L+R} = \frac{3}{2}\overline{A}_y^{\mathrm{c,L}} P_y \ , \qquad \varepsilon_{\mathrm{UD}} = \frac{U-D}{U+D} = \frac{3}{2}\overline{A}_y^{\mathrm{s,U}} P_x \ . \tag{4.10}$$

Here, the following relations hold for the analyzing powers for the left, right, up and down quadrant: $\overline{A}_y^{\mathrm{c,L}} = -\overline{A}_y^{\mathrm{c,R}}, \overline{A}_y^{\mathrm{s,U}} = -\overline{A}_y^{\mathrm{s,D}}$. Furthermore, the magnitudes of the two averaged analyzing powers are equal ($|\overline{A}_y^{\mathrm{c,L}}| = |\overline{A}_y^{\mathrm{s,U}}|$) in the particular arrangement. In case of a temporally constant discrepancy between acceptances or efficiencies of facing quadrants, the corresponding asymmetry is shifted by a constant offset.

4.2.2 Data Acquisition

The following description of the data acquisition has been taken from [125]. The light yield produced by a scattered particle passing the scintillator material is detected by photomultiplier tubes (PMTs). The sum of the PMT signals from the group of four scintillator rings are generated. Similarly, also the sums of the PMT signals of the eight scintillator bars corresponding to one detector quadrant are produced. Thresholds and coincidences are setup to select deuteron-carbon elastic scattering events. If the required conditions are met, a trigger signal associated to a certain detector quadrant is released. In recent beam times average analyzing powers of $\hat{A}_y = 0.37 \pm 0.02$ could be obtained by optimizing the thresholds [125]. The four trigger channels (one for each quadrant) are connected to a time-to-digital converter (TDC). Each trigger signal of the four quadrants leads to a recorded scattering event with an associated timestamp. Besides these four signals, a logical signal corresponding to the COSY RF cavity frequency, prescaled by a factor 100, is used as a TDC input. Since the revolution frequency for a deuteron beam at $p = 970\,\mathrm{MeV/c}$ amounts to $750\,602.5\,\mathrm{Hz}$, the prescaled signal produces an event each $0.13\,\mathrm{ms}$. This guarantees, that the full operational range of the TDC will not be exceeded and each event time can be precisely recorded. In addition, the frequency information of the cavity allows one to assign a revolution number (turn) to each recorded scattering event. Depending on the experimental setup, also the RF signals of the spin manipulators are used as further TDC inputs. They provide information about the state of the particular spin manipulator during the cycle. In summary, an event file containing the timestamps of the scattering events and the prescaled RF signals is produced in each measurement. Further details are given in [125].

4.3 Typical Measurement Setup

Various beam conditions are required depending on the different purposes of the experiments. In this section, a typical setup is presented. The time period starting from the initial particle injection procedure until the end of the measurement period and ramp down of the COSY magnets is called a cycle. At the end of each cycle, the magnets are ramped down to allow for the next injection. Subsequent cycles sharing the same accelerator and beam conditions define a run. One exception is the choice of different initial polarization states in various cycles of the same run. Most of the experiments are performed with vector polarized deuteron beams. A typical cycle consists of the following steps:

1. A vector polarized ion beam is injected into COSY. The initial beam polarization is parallel to the spin closed orbit of COSY, i.e. almost vertical and parallel to the dipole guiding fields. Commonly three different polarization states are used.

2. Acceleration of the deuteron beam to the final momentum of 970 MeV/c is performed

3. Beam preparation phase before the measurement period: Electron cooling of bunched or coasting beam is applied to reduce the beam emittances and momentum spread. If necessary, also machine parameters like betatron tunes and chromaticities are adjusted to study their influence on spin motion and polarization. Furthermore, a correction of the horizontal and vertical orbit is conducted during this period.

4. After cooling, a vertical orbit bump is applied to move the beam to a position directly below the carbon target of the EDDA detector

5. White noise is fed to the stripline unit to heat the beam in vertical direction and initiate scattering processes of the outermost deuterons onto the internal carbon target.

6. The initial beam polarization is manipulated by using the RF solenoid or the RF Wien filter. This step depends on the purpose of the current experimental run.

7. The following step is the measurement period. Scattering events are recorded continuously for a subsequent analysis of the polarization behavior. Typically this period lasts hundred seconds and more until most deuterons have been removed from the beam.

8. Finally, in some experimental runs a horizontal and vertical betatron tune measurement is conducted, before the COSY magnets ramp down at the end of each cycle. This way a continuous monitoring of the tunes over several runs is achieved.

Figure 4.7 depicts a selection of recorded diagnostic and detector signals for a typical cycle with a length of about 210 s. After acceleration to the final momentum, electron cooling is applied for about 75 s. The measured profiles illustrate the significant reduction of the beam emittances. At 80 s a global orbit correction is performed and the beam is moved closer to the the carbon target. This results in a slightly increased detector rate and a radial and vertical shift of the measured profiles. A continuous

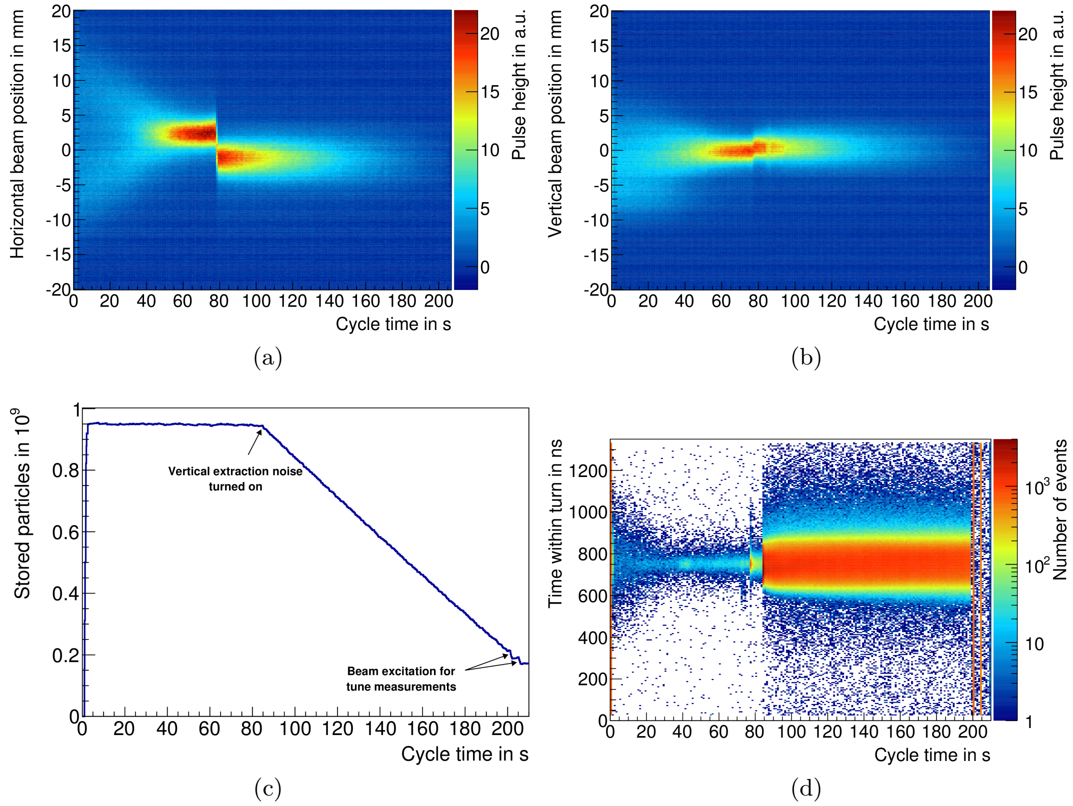

Figure 4.7: Summary of plots for diagnosis of a typical measurement cycle. Figures (a) and (b) illustrate the measured horizontal and vertical profiles in a cycle. The electron cooling period, orbit correction and measurement period are clearly visible. Figure (c) illustrates the BCT signal, where vertical noise was fed to the stripline starting at about 90 s. Figure (d) depicts the recorded detector events summed over all detector quadrants.

detector rate is achieved by the vertical extraction noise turned on at about 85 s. The measurement periods last until 195 s in the cycle. Finally, the beam is debunched and excited two times for a horizontal and vertical betatron tune measurements. Since the beam is close to the edge of the target, this leads to small beam losses and enhanced detector rates.

Chapter 5

Development and Setup of the Simulation Framework

The preparation and evaluation of the experiments require a fast and powerful simulation framework. In the scope of this thesis a new framework written in the programming language C++ has been developed. It interfaces with existing software tools to model the beam and spin dynamics of the particles in an accelerator and storage ring like the Cooler Synchrotron COSY. An overview of this framework has been already presented in [126]. In the first section of this chapter, the layout of this framework is discussed. Afterwards, the available and developed algorithms for the study of beam and spin motion within this framework are presented. Finally, benchmarking results of the implemented COSY model with experimental results are covered in the last section.

5.1 Layout of the Simulation Framework

The description of the simulation framework layout can be divided into two main aspects. The first aspect is the illustration of external programs and embedded libraries of the new framework, for which the codename COSY Toolbox has been established. The second aspect is the internal class hierarchy to model the accelerator and evaluate the results.

5.1.1 Interfaced Software Tools

Figure 5.1 gives an overview of the used software tools. The configuration of the ion beam setup, i.e. initial emittances and momentum spread as well as the lattice configuration is defined in the framework COSY Toolbox. The framework gains its main functionality from the arbitrary order beam and spin dynamics simulation and analysis code COSY INFINITY [10], the ROOT framework [127, 128] and the open-source library Armadillo [129]. These software tools are described in the following:

COSY INFINITY The code COSY INFINITY developed at the Michigan State University allows the quantitative study of the beam and spin dynamics for a defined accelerator lattice. Although the name may suggest otherwise, it is not directly related to the Cooler Synchrotron COSY. The code provides differential algebraic methods to efficiently calculate the transfer maps for orbital and spin coordinates. These maps express the final coordinates of a particle behind an accelerator element in terms of their initial coordinates in front of the element. The map

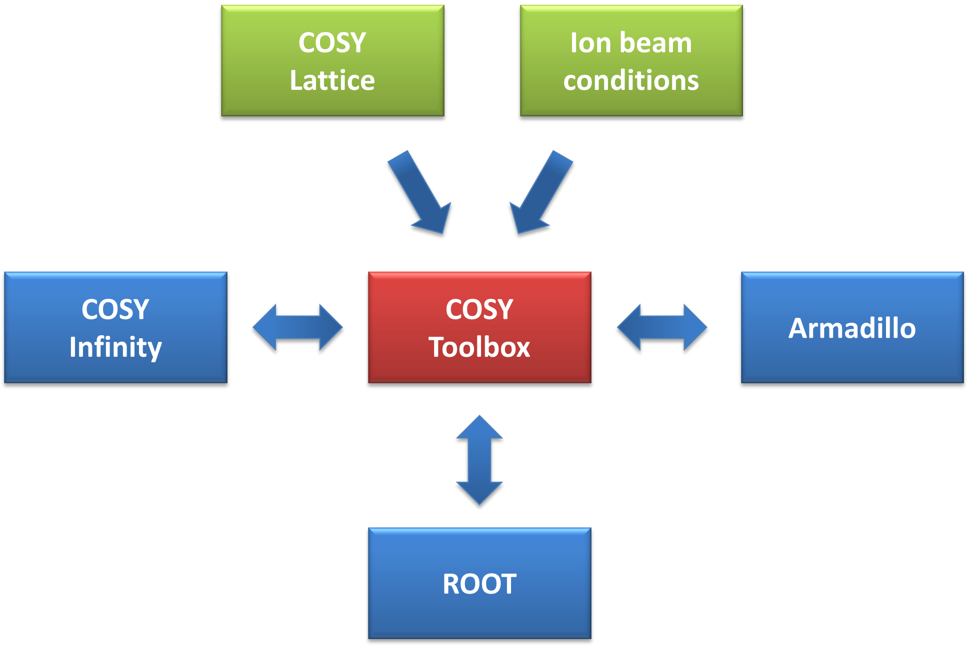

Figure 5.1: Layout of the simulation framework. The ion beam settings and accelerator lattice are implemented in a new framework COSY Toolbox, which interfaces existing simulation codes and libraries.

calculation is based on the solution of the equations of motion [130], presented in the Sections 3.1 and 3.2. Different algorithms are available to solve these equations to arbitrary order in terms of the initial coordinates. Several routines for electrostatic and magnetic elements, like dipoles and quadrupoles, are available to provide the required field information for the transfer map calculation [131]. The evaluation of the transfer maps enables the calculation of the optical functions, tunes, chromaticities, closed orbits and various other parameters of the lattice. Furthermore, parallelized multi-particle tracking over several millions of turns is available. Here, each particle is defined by its initial orbital and spin coordinates. The repetitive application of the transfer maps results in the final coordinates after each turn. The new framework COSY Toolbox takes care of the production of the input files for COSY INFINITY, triggers the execution and finally reads in the simulation results for further processing.

ROOT ROOT is a modular scientific software framework for data processing, whose development was started at CERN[8]. Huge amounts of data can be efficiently stored in binary ROOT files. The stored information can be accessed and fast evaluated in subsequent analysis routines. A large repository of C++ classes is available to finally visualize the results. In the COSY Toolbox framework this functionality is used to process the COSY INFINITY results. The huge amount of information about the particle coordinates of subsequent turns in tracking simulations are preprocessed and stored in the binary file format. This drastically reduces the required amount of disk space.

[8]Conseil Européen pour la Recherche Nucléaire (European Organization for Nuclear Research)

Armadillo Armadillo is a high quality C++ linear algebra library. It provides fast and easy access to operations like matrix inversion and solving of linear equation systems. In the COSY Toolbox framework it is mainly used for the closed orbit correction routines. Here, it calculates orbit response matrices based on COSY INFINITY results and allows for their (pseudo-)inversion using singular value decomposition.

5.1.2 Class Hierarchy

The class hierarchy of the COSY Toolbox framework is depicted in Figure 5.2. The classes are assigned to different categories. The simulation setup provides the basis of the beam and the accelerator lattice representation. It contains information about the particle type, the beam momentum and other beam details. In addition, also information about the computation order used in the differential algebraic algorithms and additional parameters required for the COSY INFINITY configuration are stored in this class. The particles of a beam are created by a ParticleGenerator class. It has direct access to the lattice information to retrieve information about the optical functions and machine parameters. This enables the random generation of the initial particle orbital coordinates according to predefined distributions, i.e. given by the beam emittances and momentum spread for normal distributed beam particles. The elements of the COSY accelerator are represented by individual classes in the framework. They are divided into static and RF elements. A set of elements is grouped into an ElementList, which can contain either static or RF elements. The entire accelerator or storage ring is finally represented by an object of the class Beamline consisting of several ElementLists. The beam and beamline objects contain all information, which are mandatory for the simulation tasks. Currently, a calculator and a tracker class are implemented. The former is used to calculate the transfer maps and retrieve the lattice

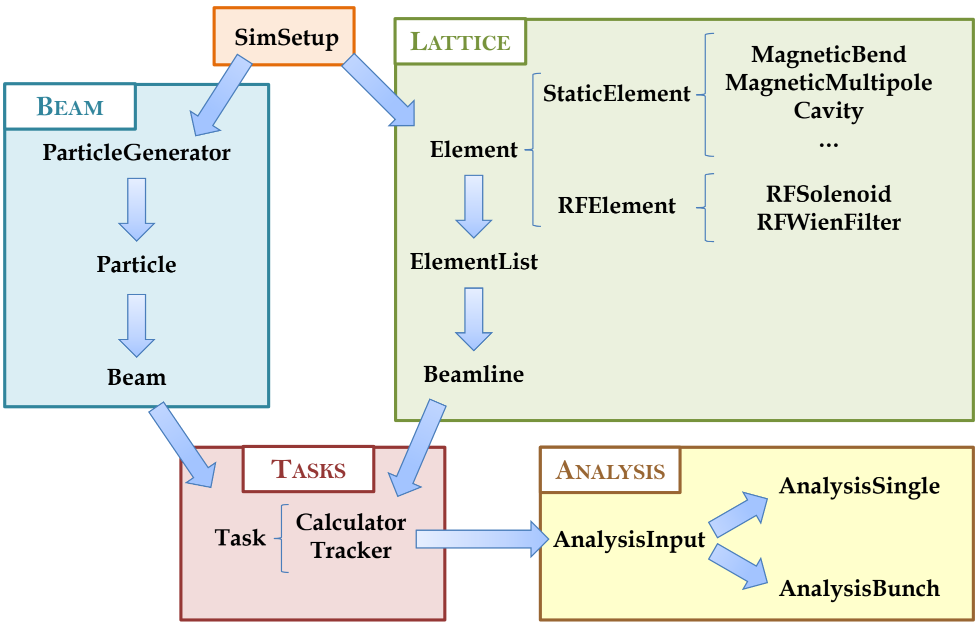

Figure 5.2: Class structure implemented in the COSY Toolbox framework.

parameters. The latter prepares and executes parallelized tracking simulations for the given beam information and a fixed number of turns. For this purpose, each element of the beam line adds its COSY INFINITY representation to an input file. Subsequently, this input file is extended by required commands for calculation or tracking provided in the internal language COSYScript of COSY INFINITY. The results are automatically stored to the ROOT binary file format. Analysis classes access these files, process the stored information and finally visualize results either for single particles or for the full bunch of particles.

5.2 Utilized and Developed Algorithms

In this section a collection of algorithms used within the framework is presented. These algorithms are either part of the COSY INFINITY framework or extensions to it, which combine existing and further developed methods into new routines. These routines can be easily accessed by the COSY Toolbox framework.

5.2.1 Calculation of Transfer Maps

The calculation of transfer maps to arbitrary order is an important feature of COSY INFINITY. These maps can be used to efficiently study the dynamics of an repetitive system like a storage ring [132]. They relate the final to the initial phase space coordinates based on the solution of the equations of motion of the system under consideration:

$$\vec{z}_f = \mathcal{M}\left(\vec{z}_i, \vec{d}\right) \ . \tag{5.1}$$

Here, the vector $\vec{d}$ contains additional parameters of the system, which can be defined to study their influence on the transfer map. A similar transfer map can be obtained for the spin:

$$\vec{S}_f = \mathcal{A}\left(\vec{z}_i, \vec{d}\right) \cdot \vec{S}_i \ . \tag{5.2}$$

The transfer map calculation requires an analytical description of the magnetic and electric fields, since they are part of the equations of motion. In COSY INFINITY, these descriptions are provided in various routines for individual elements as discussed before. The initial setup of COSY INFINITY allows one to use either hard edge representations or fringe field models to describe the particular field fall-off (see Section 5.2.3). These field descriptions are used during the evaluation of the equations of motion. Often, these equations can not be solved analytically. In this case, it is still possible to find a solution to arbitrary order using numerical integration methods [132, 133]. In COSY INFINITY different methods are available [130]. One of them is the implementation of an eighth-order Runge-Kutta integrator with automatic step-size control using a seventh-order algorithm. This integrator is used within this thesis, inter alia, to obtain the transfer maps of the rectangular guiding dipoles of the Cooler Synchrotron COSY including the default fringe field descriptions implemented in COSY INFINITY.

5.2.2 Transfer Maps for RF Fields

Commonly, a static arrangement of magnetic or electrostatic elements is considered for the study of beam dynamics in storage rings. Once the one turn map is calculated, it can be repetitively applied for all subsequent turns, since it contains the full information of the dynamics of the system. Because the fields of each element are static, the transfer map does not depend on the fifth phase space coordinate l_K. This coordinate is related to the time or more specifically to the time deviation with respect to the reference particle Δt. As soon as time-varying fields are taken into account, such a dependence is introduced. The most frequent elements with time-varying fields are RF cavities. The corresponding fields are often shaped sinusoidally and used to accelerate the particles to their final energy and to preserve the longitudinal bunch structure. During a store, the cavity frequency matches the beam revolution frequency (or a particular higher harmonic of it). Hence, the oscillation phase of the cavity fields with respect to the reference particle stays constant for each turn. A recalculation of the transfer map for subsequent turns is not required. Considering oscillating fields with a frequency, which is not a multiple of the revolution frequency, this condition is not fulfilled. In general, this is the case for RF spin manipulators, whose frequencies are often adjusted with respect to the spin precession frequency of the stored beam. Naively, a recalculation of the transfer map with respect to the time of arrival of the reference particle is required each turn. This would imply a huge computational effort in long-term tracking applications. For that reason, new algorithms have been developed and implemented to reduce the computational time. In the following, these algorithms are illustrated for the case of an oscillation longitudinal field of an RF solenoid.

A fast but less accurate approach is a representation of the oscillating field by a simple spin kick. In this approach the RF solenoid is treated as a point-like device. Since $\vec{\beta} \cdot \vec{B} = 0$, the RF solenoid does not influence the motion of the reference particle. Only the spin vector of the reference particle is rotated around the longitudinal axis by an angle ψ:

$$\psi = (1 + G) \cdot \frac{q}{p} \int_0^{l_{\text{sol}}} B_{\text{sol}}(t_{\text{arrival}}, s) ds \; . \tag{5.3}$$

Approximately, this spin rotation angle can be applied for every particle of the beam depending on its time of arrival at the solenoid location t_{arrival}. This quantity can be obtained from the turn number n, the revolution frequency f_{rev} and the time deviation Δt, which can be obtained from the fifth phase space coordinate of each individual particle:

$$t_{\text{arrival}} = \frac{n}{f_{\text{rev}}} + \Delta t \; . \tag{5.4}$$

The rest of the storage ring is expressed by a one turn map, starting and ending at the solenoid location, but excluding the point-like solenoid itself. This map transforms the orbital and spin coordinates between the subsequent interactions of the solenoid. In tracking simulations, the spin kick ψ has to be calculated and executed between each application of the transfer map of the static storage ring. This serves as an approximation of the beam and spin motion influenced by the oscillating field of an RF solenoid.

A second ansatz has been implemented to improve the accuracy by using a map representation of the RF device, but at the same time avoiding the computationally expensive recalculation for every revolution. In the following, a solenoid field given by

$$B_{\text{sol}} = \hat{B}_{\text{sol}}(x, y, s) \cdot \sin(2\pi f_{RF} t + \phi_0) = \hat{B}_{\text{sol}}(x, y, s) \cdot \sin(\phi + \phi_0) \tag{5.5}$$

is considered. In map form, the time dependence is expressed by a Taylor expansion of the sine wave in terms of the fifth phase space coordinate. This expansion has to cover at least a full period of the field oscillation. An individual particle arrives at the solenoid at

$$\phi_{\text{arrival}} + \phi_0 = 2\pi f_{RF} t_{\text{arrival}} + \phi_0 \ . \tag{5.6}$$

For an arbitrary oscillation frequency, this phase can take on any value. In terms of a Taylor expansion, deviations from $\phi + \phi_0 = 0$ can not be treated as small deviations. Hence, even for the reference particle a sufficiently large computation order is required. A reduction of the required computation order is achieved by the following approach chosen for implementation. The oscillating field is represented by 36 instead of one transfer map. Each map is an individual expansion at different values of ϕ_0 denoted as $\phi_{0,i}$:

$$\phi_{0,i} = \frac{2i+1}{2} \cdot \frac{1}{36} \cdot 2\pi, \quad i \in [0, 35] \ . \tag{5.7}$$

The tracking routine has been extended, such that RF devices of this type are available. The following steps are performed for a tracking simulation of a bunch of particles:

1. When the location of the RF device is reached along the reference trajectory, the phase ϕ_{arrival} is calculated for each individual particle.

2. Each particle is assigned to a particular map i depending on its phase ϕ_{arrival}. The map satisfying the condition $\phi_{\text{arrival}} \in \left[\phi_{0,i} - \frac{1}{2} \cdot \frac{1}{36} \cdot 2\pi, \phi_{0,i} + \frac{1}{2} \cdot \frac{1}{36} \cdot 2\pi\right]$ is selected.

3. Each map contains an expansion about the point $\phi_{0,i}$. This point does not agree with the phase ϕ_{arrival} of the reference particle. For that reason, the fifth phase space coordinate of each particle is shifted taking the distance $\phi_{\text{arrival}} - \phi_0$ into account. This corresponds to a transformation into a local coordinate system, required before applying the individual transfer map in tracking.

4. The particular transfer map is applied to the phase space coordinates of each particle.

5. The shifts of the fifth phase space coordinates performed in the third step are reversed. After this step all phase space coordinates are expressed in the global coordinate system again.

6. The particles are grouped back into one bunch and the subsequent transfer map can be applied.

Various implementations are available to express the spatial field dependence defined in Equation 5.5 [134]. The currently used implementation of the time-varying solenoid is based on a thin solenoid approximation with a hyperbolic tangent approximating the fringe fields of the longitudinal field:

$$\hat{B}_z, \text{sol}(s) = \frac{B_0}{2\tanh(l/2R)} \cdot [\tanh(s/R) - \tanh((s-l)/R)] \ . \tag{5.8}$$

Besides the solenoid, also an RF Wien filter has been integrated into the code. Its implementation is based on a superposition of the existing templates for electrostatic and magnetic bending dipole elements, which are rotated appropriately. In COSY INFINITY, the curvature of the reference trajectory is automatically calculated at each integration step according to the reference particle deflection due to vertical magnetic and radial electric fields, respectively. In general, this curvature is zero outside of the guiding dipoles. This assumes, that all field components on the reference trajectory belong to the accelerator design. Consequently, constant terms of the transfer maps vanish per definition. Introducing time-varying fields, which deflect the reference particle, this deflection may be different each turn. For this purpose, the reference trajectory is subsequently defined for the situation when the RF fields are off. In this scenario, the particular device can be replaced by a drift space. To preserve a valid calculation of the phase space motion, the automatic calculation of the curvature has to be taken into account. For the implementation of the RF Wien filter, it has been turned off. Consequently, constant terms are introduced to the transfer maps, if the reference particle is deflected by the time-varying fields. Hence, particles, which are initially traveling on the reference trajectory for a disabled Wien filter, are deflected and leave the design orbit, if the Wien filter is running.

The control of the two different RF devices, solenoid and Wien filter, is realized by two associated RFElement classes within the COSY Toolbox framework. ElementLists for either a set of static elements or an RF element are grouped together into a Beamline object. During execution, the transfer map of each element is calculated and stored to disk. For tracking applications all maps associated to the same ElementList are combined to a single transfer map. Then, these combined maps are applied to the orbital and spin coordinates in subsequent order until the desired number of revolutions is reached.

5.2.3 Fringe Fields and Misalignments

Often, a realistic field profile can be described by a rise of the field magnitude in the entrance fringe field region, a constant flat top value and a fall-off in the exit fringe field region. Sufficiently far away from the element the field vanishes. Usually, the fringe field regions of a magnetic element are small compared to its extent along the reference trajectory. For that reason, these magnetic field distributions are often approximated by a hard edge model in simulations. The real field distribution is replaced by a constant field present over a constant effective length l_{eff} along the reference trajectory. Assuming the flat-top value is reached at the center of the element at $s = 0$, the effective length is given by:

$$l_{\text{eff}} = \frac{\int_{-\infty}^{\infty} B(s)\, ds}{B(0)} \ , \quad \text{with } B(s) \to 0 \text{ for } s \to \pm\infty \ . \tag{5.9}$$

Consequently, the element is represented by a constant field region $B(0) \cdot l_{\text{eff}}$[9] connected to field free regions in front and behind the element. This simplification often leads to optimistic results of beam dynamics studies [135]. Instead of the hard edge model, COSY INFINITY provides the option to use fringe fields following Enge functions

[9] in case of multipoles, constant gradients are considered

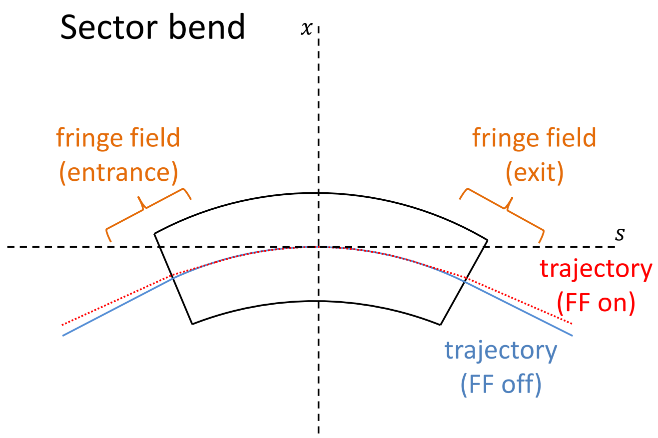

Figure 5.3: Influence of the fringe fields (FF) on the reference trajectory based on the example of a sector bend (not to scale). The comparison shows a hard edge model compared to modeled fringe fields using Enge functions.

[133, 136]. Considering a one-sided fringe field, the main field is modulated by the following function:

$$F(d) = \frac{1}{1 + \exp[a_1 + a_2 \cdot (d/D)^2 + \cdots + a_6 \cdot (d/D)^6]} \, . \tag{5.10}$$

In this representation, d is the distance to the effective field boundary in s-direction (at the entrance or exit respectively) and D is a scaling parameter. In COSY INFINITY the full aperture of the element is commonly used for D. Default values for the coefficients a_i are implemented for electric and magnetic fields and different multipole orders. The multiplication of two modulation functions is required to take entrance and exit fringe fields into account. In the simulations, this fringe field representation is chosen and the default a_i are used.

Fringe fields can significantly influence the quadrupole strengths in comparison to the strengths obtained by the hard edge model [135]. Also the deflection in guiding dipoles is affected. This is depicted in Figure 5.3. The algorithm implemented in COSY INFINITY forces a symmetric solution for the reference trajectory with respect to the center of the dipole. In the hard edge model, the reference trajectory outside a dipole is a straight line, while it describes a circle with constant radius inside the dipole. The length of the circular trajectory corresponds to the effective length. A fringe field representation based on Enge functions affects the particle trajectory in the fringe field regions due to a different arrangement of the field components. In general, this introduces changes of bending radius and angle. For many common applications, these variations of bending angle and radius are negligible. Nevertheless, the total sum of the deflections in all guiding dipoles per revolution slightly deviates from 2π in this scenario. This leads, for example, to a tiny change of the calculated spin tune compared to the nominal one (hard edge model). For the calculations within this thesis, the total bending angle has been restored to its design value by scaling the main field for each guiding dipole. This also corrects the spin tune to its nominal value. The remaining small offsets of the trajectory compared to the hard edge model are treated as part of the new reference trajectory. Thus, they do not lead to spatial offsets with respect to the magnetic centers of adjacent elements.

To take spatial shifts, tilts and rotations of the optical axis into account, various commands are implemented into COSY INFINITY. These commands do not directly affect the transfer map of the misaligned element, but perform a coordinate transformation of the phase space coordinates in front and behind of the element. A combination of these commands is required to model a certain misalignment of an element. These combinations have been realized in routines within the COSY Toolbox framework. These routines generate the particular part of the source code for the COSY INFINITY input file. All misalignments have been defined with respect to the center of the element. Thus, the transfer map of the misaligned element is generated in the following way:

1. A transfer map of a field-free drift is used to transfer the phase space coordinates to the center of the element. At this location, the optical axis is transformed by the necessary shifts, tilts and rotations. The transfer map of a field-free drift with equal length as the first one is applied in opposite direction to return to the new initial point of the reference trajectory.

2. The original transfer map of the non-misaligned element is applied, since the misalignments are governed by the transformations of the optical axis in the previous step.

3. The transformation applied in the first item is reversed to complete the transfer map calculation of the misaligned element.

In general, the application of misalignments also introduces constant terms into the transfer maps and induce a change of the closed orbit solution (see Section 3.1.4.5).

5.2.4 Orbit Diagnosis and Correction

The orbit diagnosis and control system of the Cooler Synchrotron COSY consists of several BPMs and corrector magnets as discussed in the previous chapter. Closed orbit studies require the integration of these elements into the simulation code. In ideal case without misalignments and field imperfections, all correctors are disabled. Hence, the design reference trajectory inside a corrector magnet usually describes a straight line. This is similar to the situation of time-varying fields as previously discussed. A new template for a corrector magnet based on the existing guiding dipole template has been implemented to COSY INFINITY. For the transfer map calculation the curvature has also been fixed to zero, independent from the applied corrector field. Some correctors within the storage ring COSY are realized as additional coils mounted on the quadrupole magnets. These have been represented by a corrector magnet object with additional quadrupole component. Thus, each corrector magnet is represented by an object with spatial extent, instead of a point-like kick used in various other simulation codes. These new templates are interfaced by a new class added to the COSY Toolbox framework. A BPM is represented as a specially flagged drift space to determine the closed orbit coordinates at certain positions in the storage ring. One application of these elements is the calculation of the orbit response matrix, as discussed in Section 3.1.4.5. Here, the corrector fields are varied and the induced closed orbit changes are evaluated. The orbit change at each BPM per angular kick induced by each corrector magnet is stored in the matrix class of the Armadillo library. Matrix inversion methods can be used to find the corrector strength required to correct a distorted closed orbit induced by simulated storage ring imperfections.

5.2.5 Repetitive Tracking

Considering a ring circumference of 183.4 m, a storage time of 1000 s and revolution frequencies in the order of 1 MHz, the length of a single particle trajectory in a complete store amounts to more than 10^{11} m. Efficient methods are needed to study the evolution of the phase space on this scale. The periodic structure of a storage ring allows the repetitive application of the same one turn map in subsequent turns. This drastically reduces the computational effort compared to a continuous numerical integration based on Runge-Kutta methods. Often, a storage ring can be considered as a Hamiltonian system. In this case, the transformation of the phase space coordinates satisfies the symplectic condition [137]. One implication of this condition is the phase space conservation according to Liouville's theorem. Thus, transfer map based codes often aim to maintain this condition in long-term tracking simulations. It is important to note, that this maintenance does not necessarily lead to more accurate results. In general, the transfer maps obtained by the numerical integration methods presented here, do not fulfill the symplectic condition. For this purpose, various algorithms are implemented into COSY INFINITY to restore the symplectic motion. One of these algorithms is applied in the tracking routines responsible for transfer maps representing only static elements. The new implementation for time-varying fields uses various transfer maps for different groups of particles. Here, the existing algorithms do not guarantee to restore the symplectic motion in the particular implementation [138]. For that reason, these algorithms are currently disabled in case of time-varying fields. New algorithms are subject of on-going studies.

5.3 Benchmarking of the Accelerator Model

The COSY lattice is one of the major ingredients for the beam and spin dynamics simulations. An online accelerator model containing the specific setups of the experimental runs is available in the control system software. It is based on the lattice design and simulation code Methodical Accelerator Design 8 (MAD-8) [139]. The locations, effective lengths and field strengths of the magnetic elements have been transferred to a new accelerator model used within the COSY Toolbox and COSY INFINITY. The descriptions of the elements and especially their fringe fields of different simulation codes vary in different codes. Thus, the validation of the model requires a proper benchmarking with experimental measurements. Recent experimental runs use a storage ring setup with a vanishing dispersion in the straights as discussed in Section 4.1.2.1. For the benchmarking process, the simulated dispersion in the straights is minimized by an additional variation of the strength of quadrupole family MQU4. Furthermore, the simulated nominal horizontal and vertical betatron tunes are adjusted to the measured quantities by scaling the quadrupole strengths of the MQU1/MQU5 and MQU2/MQU6 families in the model.

5.3.1 Betatron Tune Variations Induced by Quadrupoles

According to Equation 3.96, a measured tune change induced by a quadrupole strength variation can be used to obtain the value of the betatron functions at the quadrupole

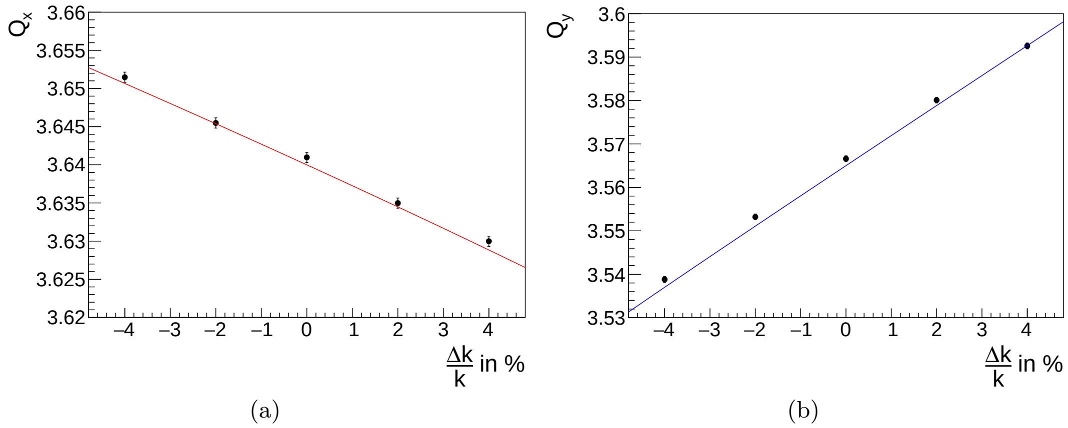

Figure 5.4: Changes of the horizontal (a) and vertical (b) betatron tunes induced by variations of the quadrupole strength of the MQU5 family. The points indicate the measurement, the solid lines represent the simulation. The offsets of this lines have been scaled artificially.

location. Unfortunately, all main quadrupoles at COSY are powered in families of four magnets. Thus, only an average betatron function at the four locations can be retrieved. Instead of a comparison of the betatron function, also the induced tune changes can be compared directly to validate the model. A series of tune measurements for the variation of each quadrupole family has been performed. The quadrupole strength of each family was varied in a certain range, according to the implemented calibration factors of the control system software. In the arcs the range was usually $\frac{\Delta k}{k} = \pm 4\,\%$, in the straights about a factor two smaller, because beam loss occurred for greater values. For each setting the tunes were measured. Similar changes were simulated using nominal tunes adjusted to $Q_x = 3.64$ and $Q_y = 3.565$ in the accelerator model. Exemplary, the comparison of a typical measurement with the simulation result is shown in Figure 5.4. The linear approximation is only valid for small changes of the quadrupole strengths. In most measurements this linear behavior is in fact observed over the full variation range. Only in a few measurements a quadratic coefficient appears. Linear fits are applied to extract the slopes of the measured tune changes. Figure 5.5 depicts the comparison between measurement and simulation for the 14 main quadrupole families. The error bars are approximated according to the estimated accuracy of the tune measurements. Some of the measurements, i.e. the horizontal measurement using MQT6 or the vertical measurement using MQT7, reveal larger discrepancies. In case the particular measurement suffers from an enhanced scattering of the measured tune values, the error bars are scaled accordingly to provide a χ^2/ndf[10] $= 1$. This is reflected in the larger error bar of the fitted slope. For these particular measurements a larger discrepancy between measurement and simulation is expectable. Overall, the comparison of measurements and model calculations reveals a good agreement for most quadrupole families. A direct comparison of the values obtained in measurements and simulations is given in Table B.1 and Table B.2. A further optimization of the model is the goal of present studies.

[10]number of degrees of freedom

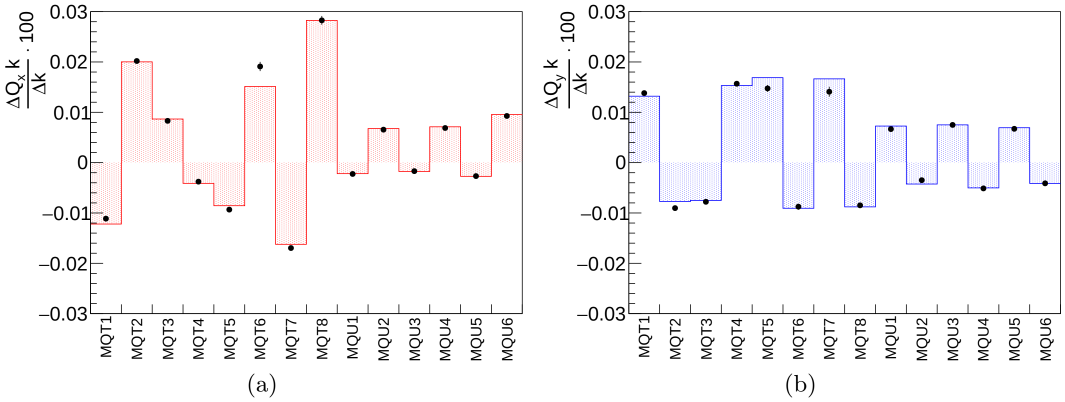

Figure 5.5: Fitted linear coefficients of horizontal (a) and vertical (b) tune changes in case of quadrupole strengths variations. The x-axes list all main quadrupole families in the straights and arcs of COSY. The points represent measured data, the colored bars correspond to the simulation.

5.3.2 Chromaticity Variations Induced by Sextupoles

In a further study, the chromaticity changes induced by the sextupole families located in the arcs was investigated. This is of particular interest for the spin coherence time studies. The three sextupole families MXS, MXL and MXG are available due to their non vanishing dispersion at their locations. The chromaticities were measured for different sextupole strength settings of these families. For these measurements a cycle of about 60 s was used. The deuteron beam was bunched and electron cooling was applied. A variation of the beam momentum was induced by a variation of the electron cooler's gun voltage as described in Section 4.1.2.3. For each sextupole strength and electron cooler voltage setting, the betatron tunes have been measured. The chromaticity at a particular sextupole setting can be obtained from the tune change in linear order with respect to a momentum variation. The measured chromaticity variation for different sextupole settings is illustrated in Figure 5.6. Here, two sextupole families have been kept at constant strengths, while the strength of the third family was varied.

In the following, the model was benchmarked against these chromaticity measurements. The measured chromaticities amount to $\xi_x = -4.68 \pm 0.05$ and $\xi_y = 2.60 \pm 0.05$, when all sextupole magnets were turned off. The calculation of the natural chromaticities of the bare model results in $\xi_x = -1.06$ and $\xi_y = -1.08$, which are both negative as expected. Additional sextupole components of the guiding dipoles are one candidate to explain these large discrepancies. Measurement results of these sextupole components are presented in [140]. The implementation of these components changes the horizontal chromaticity to $\xi_x = -1.41$ and increases the vertical chromaticity to $\xi_y = -0.63$. Thus, the change provides the correct tendency, but is about one order of magnitude too small. For further comparison of measurements and model calculations, the sextupole components of the dipoles are artificially scaled to reproduce the measured chromaticities in case all sextupoles are turned off. The influence of each sextupole component depends on the betatron and dispersion function at its location. In the underlying algorithm, the least needed changes are calculated by also taking the values of the betatron functions and the dispersion at the dipole locations into account.

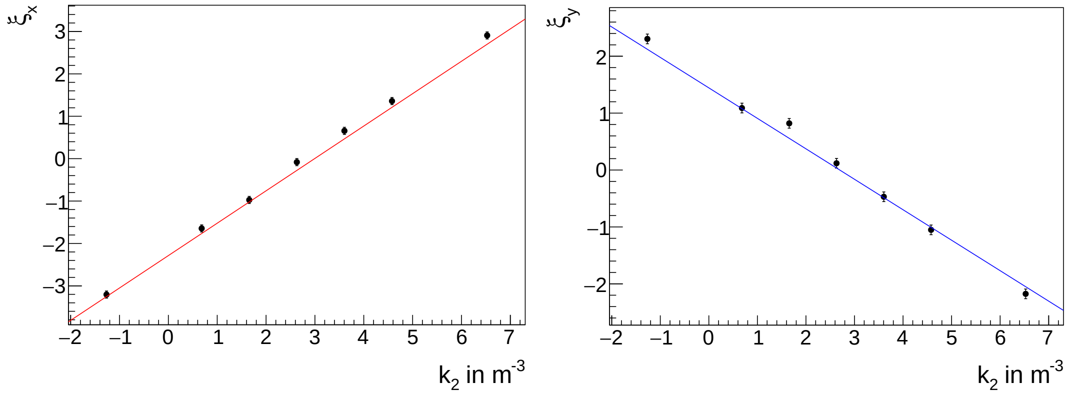

(a) (b)

Figure 5.6: Changes of the horizontal (a) and vertical (b) chromaticity induced by variations of the sextupole strength of the MXS family. The points indicate the measurement, the solid lines represent the simulation. The natural chromaticity of the model has been adjusted to the measured value.

This algorithm results in purely negative sextupole components of the dipoles up to strengths of $k_2 = -0.08\,\mathrm{m}^{-3}$. Using this setup as the nominal configuration, the chromaticity changes induced by sextupole variations are studied. The chromaticity change with respect to a sextupole strength variation is determined by a linear fit and compared to model calculations (see Figure 5.7). This linear relation is predicted in Equation 3.85. The measured and simulated values are summarized in Table B.3 and Table B.4. In some measurements, small discrepancies occur, which are larger than the statistical uncertainties of the measurements. Nevertheless, these deviations are in the order of only 2 % to 8 % of the corresponding chromaticity value. This reflects the good reproduction concerning relative lattice parameter changes.

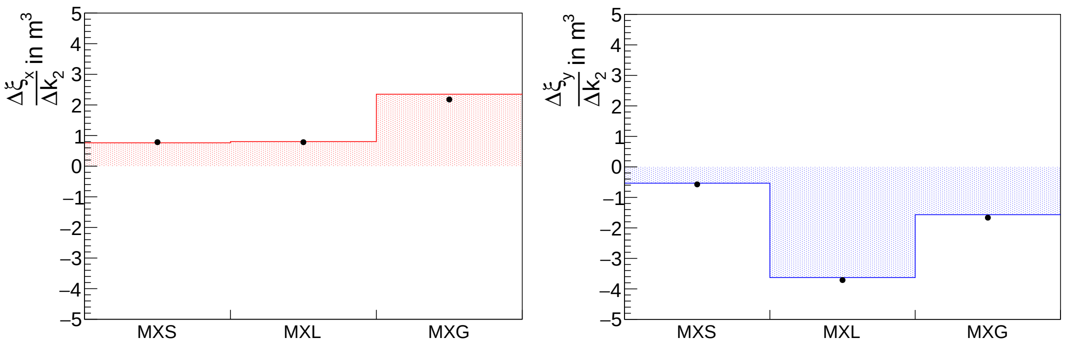

(a) (b)

Figure 5.7: Fitted linear coefficients of horizontal (a) and vertical (b) chromaticity changes in case of sextupole strengths variations. The x-axes lists all sextupole families in the arcs of COSY. The points represent measured data, the colored bars correspond to the simulation.

5.3.3 Measurements of the Dispersion Function and the Phase Slip Factor

A last benchmarking test is performed using a measurement of the dispersion function and the phase slip factor η_{ph}. First, the phase slip factor is determined. Similar as in the chromaticity measurement, the momentum of the unbunched ion beam was shifted. The induced change of the revolution frequency was measured. This is shown in Figure 5.8. Relative measurement uncertainties of 10^{-6} are assumed. A linear function is fitted to determine the phase slip factor $\eta_{\mathrm{ph}} = 0.5844 \pm 0.0001$ with a $\chi^2/\mathrm{ndf} = 7.5/5$. A model calculation yields: $\eta_{\mathrm{ph}}^{\mathrm{model}} = 0.6006$. In the various chromaticity measurements described in the previous section, the phase slip factor was measured parasitically. Here,

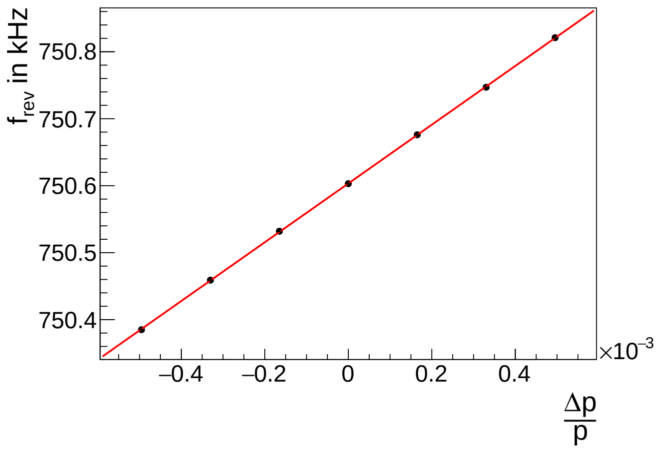

Figure 5.8: Measured shift of the revolution frequency induced by a momentum variation. The solid line shows a linear fit. The slope of the fit yields a phase slip factor of $\eta_{\mathrm{ph}} = 0.5844 \pm 0.0001$ with a $\chi^2/\mathrm{ndf} = 7.5/5$.

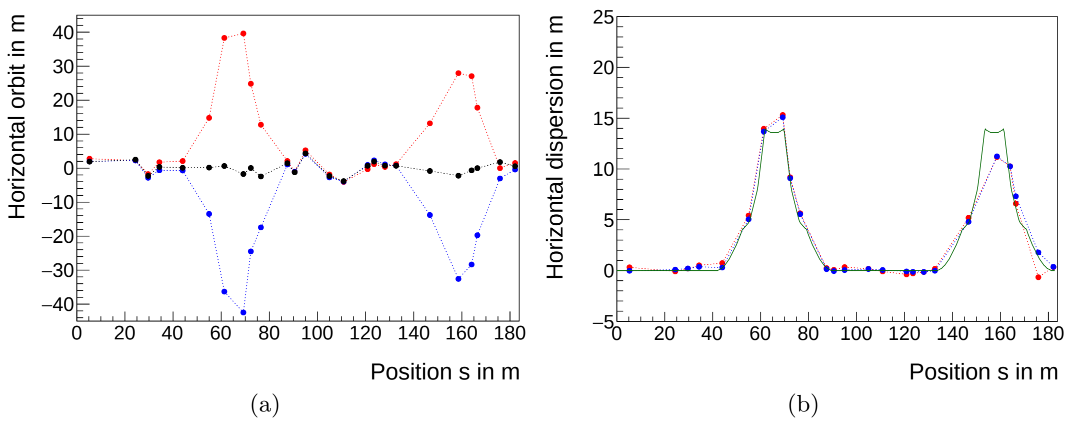

Figure 5.9: Measurement of the horizontal dispersion function. Figure (a) shows a measurement of the horizontal orbit for the nominal beam momentum (black) and induced momentum variations of about $\pm 2.7\,\%$ (red, blue). The dashed line is a linear interpolation of the measurement points. Figure (b) represents the difference orbit of the two measurements ("$+2.7\,\%$"–"$0\,\%$", "$0\,\%$"–"$-2.7\,\%$") normalized to the momentum variation yielding the dispersion function. This is compared to the model calculation shown by the green solid line.

the fluctuation of the phase slip factor is in the order of 0.02 for different sextupole settings. One source of this fluctuation are additional quadrupole components. They occur, if the beam is not centered in the sextupoles. In the model the beam is perfectly centered and these effects are not included. With regard to this fluctuations, a very good agreement is observed.

The dispersion function relates a momentum deviation to a horizontal orbit change. Thus, a measurement of the dispersion function can be accomplished by measuring the horizontal orbit for different beam momenta. The orbit measurement is performed using the BPMs of COSY, which requires a bunched beam. The momentum shift is commonly induced by a variation of the revolution frequency preset by the RF cavity. This frequency shift can be converted to a momentum shift using the measured phase slip factor. Figure 5.9 illustrates the orbit measurements without momentum change and with induced momentum variations of about $\pm 2.7\,\%$. The orbit deviations with respect to the nominal orbit are calculated and normalized to the momentum change to retrieve the dispersion function. The discrepancies between the two measurements with different momentum variations provide an estimate of the measurement uncertainty. The dispersion in the straight sections has been artificially adjusted to zero during the setup of the model. The simulated magnitude of the dispersion function in the arcs is equal, since the lattice setup in the model is fully symmetric. The almost vanishing dispersion in the straights is reproduced in the measurements. Also the majority of measurements in the arcs agrees well with the predicted magnitudes of the dispersion function. Here, the measurement at $s = 160\,\mathrm{m}$ sticks out, since it points either to an asymmetric dispersion function or a faulty BPM. Further measurements are required to revise this conspicuousness.

In summary, the benchmarking results reveal a promising agreement between measured and simulated quantities. In the following this model is used to prepare and to evaluate the polarization test experiments, which are described in the next chapters.

Chapter 6

Spin Coherence Time Studies

The methods proposed for EDM measurements require a long lifetime of the polarization precessing perpendicular to the spin closed orbit of the storage ring. Different precession speeds of the various particles stored in the ring lead to a spin decoherence and a vanishing polarization. The time until the initial polarization drops below a certain level is denoted as the spin coherence time (SCT). In this chapter, different contributions to the spin decoherence are illustrated and discussed. COSY INFINITY calculations based on the model described in the previous chapter are used to validate the theoretical considerations. Subsequently, conditions to maintain a long SCT in the COSY storage ring are obtained. Finally, they are verified by experimental results.

6.1 Motivation

In an ideal planar magnetic storage ring, the trajectory of the reference particle is fully defined by the deflection in the guiding dipoles. Due to a vertical spin closed orbit in absence of an EDM, the associated perpendicular plane is referred to as the horizontal plane in the following. As already discussed, the spin tune of the reference particle is energy dependent and given by:

$$\nu_s = G\gamma \; . \tag{6.1}$$

The momentum of the stored particles slightly varies, which introduces a spin tune change. In case the beam is unbunched, it amounts to the constant value:

$$\Delta\nu_s = G\Delta\gamma = G\gamma\beta^2 \frac{\Delta p}{p_0} \; . \tag{6.2}$$

The deviation of the spin phase advance in the horizontal plane can be defined as:

$$\Delta\phi = \Delta\nu_s \cdot \theta = \Delta\nu_s \cdot 2\pi \cdot n \; . \tag{6.3}$$

Here, n is the number of revolutions. This spin tune spread leads to a rapidly decreasing polarization component in the horizontal plane. Figure 6.1 illustrates the spin tune changes for typical momentum deviations for protons and deuterons at COSY. The results from COSY INFINITY calculations (markers) are in perfect agreement with Equation 6.2 (solid lines). The currently performed experiments use a deuteron beam with a momentum of 970 MeV/c and a revolution frequency of 750 kHz. Assuming a spin tune spread of about 10^{-5}, an additional full spin precession with respect to the reference particle is achieved in only 100 000 revolutions. This results in tiny SCTs in the order of several milliseconds, which are not sufficient for the planned EDM

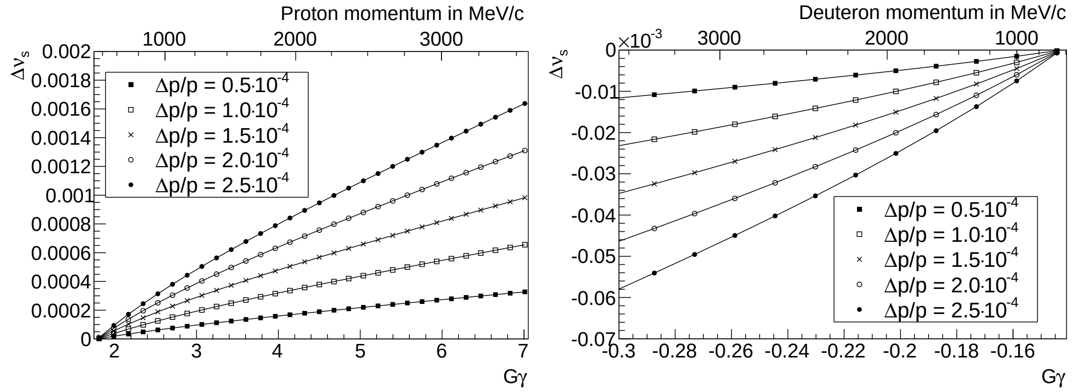

(a) (b)

Figure 6.1: Spin tune deviations $\Delta\nu_\mathrm{s}$ induced by momentum deviations of an individual particle. Unbunched proton (a) or deuteron (b) beams with different reference momenta are considered. Points illustrate tracking results, while the solid lines express theoretical calculations.

experiments. The first order effect given in Equation 6.2 can be canceled by bunching the beam. Similarly, focusing of the beam eliminates additional linear contributions to $\Delta\phi$ introduced by the the transverse phase space motion. Figure 6.2 depicts the momentum oscillation and the associated $\Delta\phi$ assuming an initial momentum deviation of 10^{-4} from the reference momentum of 970 MeV/c. The initial spin vectors have been aligned and placed in the horizontal plane, hence $\Delta\phi(n = 0) = 0$. In linear order $\Delta\phi$ oscillates, as shown in Equations 3.182 and 3.183. These oscillations lead to a spread

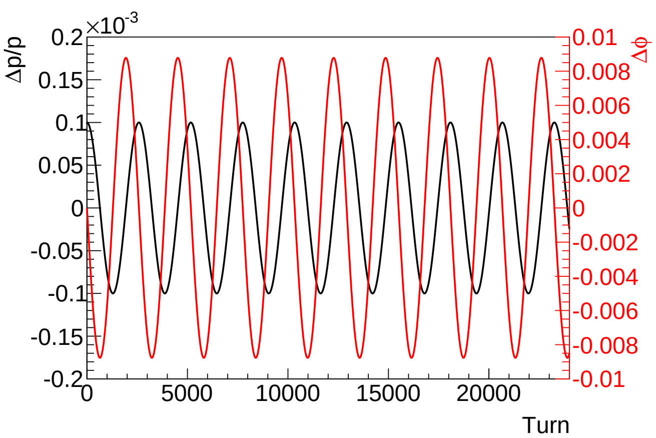

Figure 6.2: Synchrotron oscillations of the momentum deviation of an individual deuteron in a bunched beam (black). Due to the energy dependent spin tune, the momentum variation introduces a change of the spin phase advance each turn. The red line illustrates the angle between the spin vector of the individual particle with respect to a reference particle on the ideal closed orbit.

of the spin directions of different particles in the horizontal plane, decreasing the beam polarization. The amplitude of these oscillations is given by

$$\frac{G\gamma_0\beta_0^2}{Q_{\mathrm{sync}}}\hat{\delta}\ , \tag{6.4}$$

where $\hat{\delta}$ is the amplitude of the momentum deviation. In the present example, it is below 0.01 and the effective polarization decrease is marginal. But, considering larger momentum spreads and greater anomalous magnetic moments, it might be necessary to decrease the synchrotron tune to limit the magnitude of $\Delta\phi$. Two important contributions to the synchrotron tune are the RF cavity voltage and the phase slip factor η_{ph} (see Equations 3.118 and 3.119). The latter strongly depends on the lattice configuration and has to be taken into account during the layout of the experiment.

Besides the linear contributions discussed in this section, a proper treatment of non-linear effects are required to achieve long spin coherence times in COSY. The following discussion focuses on this contributions.

6.2 Theoretical Considerations on Spin Decoherence

In this section, the second order effects leading to a spin tune deviation with respect to the reference particle in a bunched beam are discussed. They contribute to a spin tune shift of individual particles and introduce a continuously growing $\Delta\phi$. Assuming an ideal storage ring the spin tune of the reference particle is defined by Equation 6.1. Since it travels on its reference trajectory, strength changes of quadrupoles or higher order multipole magnets do not influence on the spin tune. The spin tunes of all the other particles in the bunch are generally affected by those changes. Thus, the spin tune spread has to be controlled with respect to the reference particle. In the following, theoretical predictions are compared to COSY INFINITY spin tracking simulations. For the calculation of the spin tune deviation an efficient algorithm is required.

6.2.1 Algorithm for Spin Tune Spread Calculation

Considering only the reference particle, its spin component in the horizontal plane precesses by an amount of $\phi_0 = 2\pi G\gamma$ per revolution. For an individual particle, this precession rate varies as already observed in Figure 6.2. An equal precession rate of the horizontal spin component is a necessary condition to achieve a long spin coherence time. Additionally, an equal orientation of the spin precession axes of all particles in the bunch is favorable. A phase space dependent tilt of this axis is introduced by intrinsic spin resonances. This is taken into account by the extension of the spin closed orbit to the invariant spin field. Tilts of this axis tend to become small, if the distances between the nominal spin tune and the resonance tunes are large compared to the resonance strength as discussed in Section 3.2.8.1. Since the nominal spin tune is usually chosen at a sufficient distance to a spin resonance, the implemented algorithm focuses on the calculation of the average precession rate of each individual particle in the horizontal plane. For the calculation an individual particle with an initially longitudinal spin direction is launched in a tracking simulation and its motion is calculated for 200 000 turns. In the next step, the spin phase advance in the horizontal plane ϕ^i_{xz} between subsequent turns i and $i+1$ is determined. The deviation from the reference spin tune is calculated by averaging:

$$\Delta\nu_s = \frac{\sum_i(\phi^i_{xz} - \phi_0)}{\sum_i 2\pi} \ . \tag{6.5}$$

Since the deviations $(\phi^i_{xz} - \phi_0)$ are small compared to the fluctuations of ϕ^i_{xz} in individual turns, it is mandatory to take the quasiperiodicity of the phase space motion in the averaging process into account. The synchrotron oscillation frequency is small with respect to the revolution frequency, while the betatron oscillation frequencies exceed it by a factor of about 3.6 (Q_x, Q_y). In case of the common deuteron experimental setup the synchrotron oscillation frequency amounts to about 300 Hz compared to a revolution frequency of 750 kHz. Thus, the number of terms included in the summation in Equation 6.5 is constrained to cover an integer number of synchrotron oscillations within the amount of tracked revolutions. This way the bias introduced to $\Delta\nu_s$ is minimized. A similar method was also performed in [141]. Since the number of tracked turns is also about three orders of magnitude larger than the number of turns per synchrotron oscillation, the bias is further reduced.

6.2.2 Contributions to Spin Tune Spread

This section discusses the different contributions introducing a deviation of the spin precession rate for an individual particle. One source is an average path length change due to betatron and synchrotron oscillations [142]. This has been previously discussed in [143]. A second source is the presence of intrinsic resonances.

6.2.2.1 Path Lengthening

The following ansatz has been taken from [143] for reinvestigation and comparison to spin tracking simulations. Intermediate results have been published in [144, 145]. The revolution time of the reference particle is given by the ratio of ring circumference and reference velocity:

$$T_0 = \frac{C_0}{v_0} \ . \tag{6.6}$$

A deviation of the revolution time for an individual particle can be expressed by its path length change per turn ΔC and its velocity change Δv . A second order expansion yields:

$$\frac{\Delta T}{T_0} = \frac{\Delta C}{C_0} - \frac{\Delta v}{v_0} - \frac{\Delta C}{C_0}\frac{\Delta v}{v_0} + \left(\frac{\Delta v}{v_0}\right)^2 . \tag{6.7}$$

The path length changes due to betatron and synchrotron motion are considered to be uncoupled. They can be expressed as:

$$\begin{aligned}\frac{\Delta C}{C_0} &= \left(\frac{\Delta C}{C_0}\right)_\beta + \left(\frac{\Delta C}{C_0}\right)_{\Delta p} \\ &= \left(\frac{\Delta C}{C_0}\right)_\beta + \alpha_0\frac{\Delta p}{p_0} + \alpha_1\left(\frac{\Delta p}{p_0}\right)^2 .\end{aligned} \tag{6.8}$$

Here, α_0 and α_1 denote the momentum compaction factor of first and second order, respectively. The velocity deviation can also be expressed in terms of the momentum deviation:

$$\frac{\Delta v}{v_0} = \frac{1}{\gamma_0^2}\frac{\Delta p}{p_0} - \frac{3\beta_0^2}{2\gamma_0^2}\left(\frac{\Delta p}{p_0}\right)^2 . \tag{6.9}$$

The combination of the previous equations yields:

$$\begin{aligned}\frac{\Delta T}{T_0} &= \left(\frac{\Delta C}{C_0}\right)_\beta + (\alpha_0 - \frac{1}{\gamma^2})\frac{\Delta p}{p_0} + \left(\alpha_1 + \frac{3\beta_0^2}{2\gamma_0^2} - \frac{\alpha_0}{\gamma_0^2} + \frac{1}{\gamma_0^4}\right)\left(\frac{\Delta p}{p_0}\right)^2 \\ &= \left(\frac{\Delta C}{C_0}\right)_\beta - \eta_{\mathrm{ph}}\frac{\Delta p}{p_0} + \left(\alpha_1 + \frac{3\beta_0^2}{2\gamma_0^2} + \frac{\eta_{\mathrm{ph}}}{\gamma_0^2}\right)\left(\frac{\Delta p}{p_0}\right)^2 .\end{aligned} \tag{6.10}$$

The term $\left(\frac{\Delta C}{C_0}\right)_\beta \cdot \frac{\Delta p}{p_0}$ has been neglected, since terms like $x \cdot \frac{\Delta p}{p_0}$ tend to vanish, when averaged over a long time period, since the betatron and synchrotron tunes are substantially different. For a bunched beam the average revolution time for each particle is constant by definition. It follows:

$$\left\langle\frac{\Delta T}{T_0}\right\rangle = \left\langle\left(\frac{\Delta C}{C_0}\right)_\beta\right\rangle - \eta_{\mathrm{ph}}\left\langle\frac{\Delta p}{p_0}\right\rangle + \left(\alpha_1 + \frac{3\beta_0^2}{2\gamma_0^2} + \frac{\eta_{\mathrm{ph}}}{\gamma_0^2}\right)\left\langle\left(\frac{\Delta p}{p_0}\right)^2\right\rangle = 0 . \tag{6.11}$$

Here, the angle brackets denote an averaging over time. The averaged path length change due to betatron motion can be expressed in terms of the beam chromaticities Q'_x and Q'_y and the Courant-Snyder invariants ε_x and ε_y [146].

$$\left\langle\left(\frac{\Delta C}{C_0}\right)_\beta\right\rangle = -\frac{\pi}{C_0}\varepsilon_x Q'_x - \frac{\pi}{C_0}\varepsilon_y Q'_y . \tag{6.12}$$

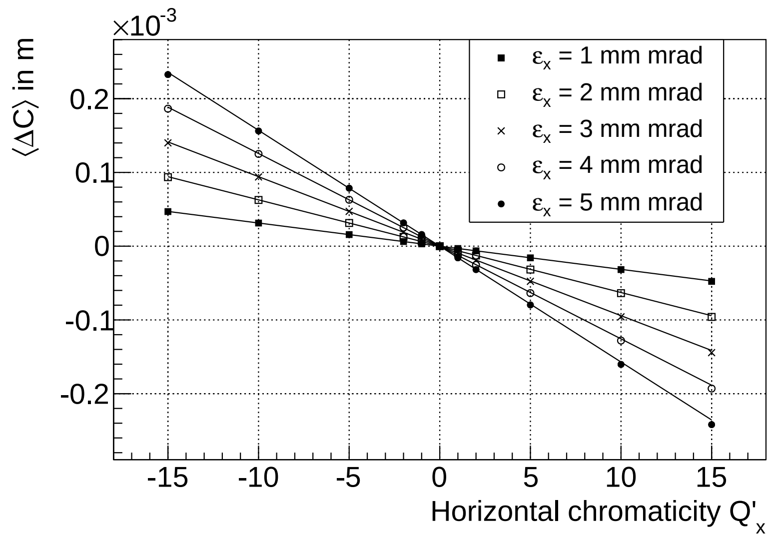

Figure 6.3: Average path length change due to horizontal betatron motion for different horizontal chromaticities and phase space amplitudes. The points correspond to tracking results, the solid lines depict theoretical calculations.

Figure 6.3 depicts simulation results compared to Equation 6.12 for the average path length change in case of different Courant-Snyder invariants ε_x in radial phase space. The initial ε_y and momentum deviation have been set to zero. The chromaticities were adjusted by variation of the strengths of the arc section sextupole families in the COSY ring. Using the second order relation

$$\frac{\Delta p}{p_0} = \frac{1}{\beta^2}\frac{\Delta\gamma}{\gamma_0} - \frac{1}{2\beta_0^4\gamma_0^2}\left(\frac{\Delta\gamma}{\gamma_0}\right)^2 , \tag{6.13}$$

Equation 6.11 can be transformed to:

$$\left\langle\frac{\Delta T}{T_0}\right\rangle = \left\langle\left(\frac{\Delta C}{C_0}\right)_\beta\right\rangle - \frac{\eta_{\mathrm{ph}}}{\beta_0^2}\left\langle\frac{\Delta\gamma}{\gamma_0}\right\rangle + \frac{1}{\beta_0^4}\left(\alpha_1 + \frac{3}{2\gamma_0^2}\left[\beta_0^2 + \eta_{\mathrm{ph}}\right]\right)\left\langle\left(\frac{\Delta\gamma}{\gamma_0}\right)^2\right\rangle = 0 \ . \tag{6.14}$$

The spin tune deviation given by $\Delta\nu_s = G\Delta\gamma$ can be minimized by canceling the energy change. Two conditions can be derived from Equation 6.14:

$$\left\langle\frac{\Delta\gamma}{\gamma_0}\right\rangle = \frac{\beta_0^2}{\eta_{\mathrm{ph}}}\left\langle\left(\frac{\Delta C}{C_0}\right)_\beta\right\rangle + \frac{1}{\eta_{\mathrm{ph}}\beta_0^2}\left(\alpha_1 + \frac{3}{2\gamma_0^2}\left[\beta_0^2 + \eta_{\mathrm{ph}}\right]\right)\left\langle\left(\frac{\Delta\gamma}{\gamma_0}\right)^2\right\rangle \tag{6.15}$$

$$\Rightarrow \quad \left\langle\left(\frac{\Delta C}{C_0}\right)_\beta\right\rangle = 0 \tag{6.16}$$

$$\wedge \quad \kappa \equiv \left(\alpha_1 + \frac{3}{2\gamma_0^2}\left[\beta_0^2 + \eta_{\mathrm{ph}}\right]\right) = 0 \ . \tag{6.17}$$

Figure 6.4 shows a comparison to simulation results, which are in very good agreement with the theoretical formulas. The connection between horizontal chromaticity/κ and the spin tune deviation is clearly reproduced. If the beam chromaticities and κ are minimized, the spin tune deviation introduced by path lengthening vanishes. A similar behavior is obtained for the vertical chromaticity.

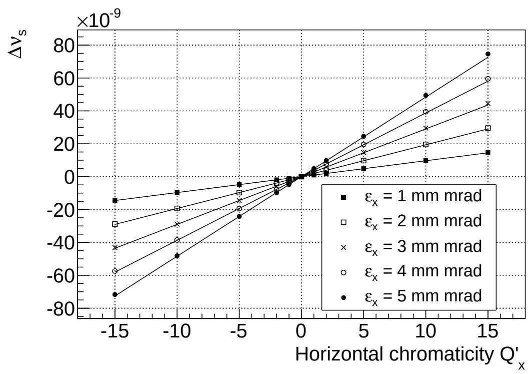

(a)

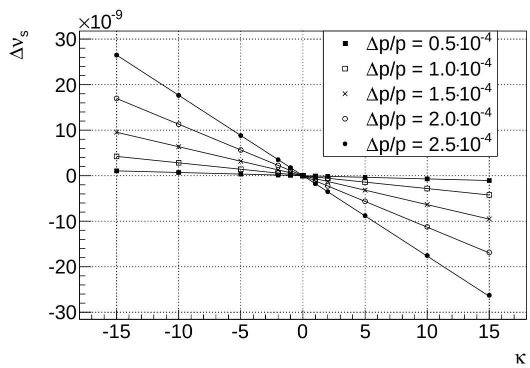

(b)

Figure 6.4: Spin tune deviations calculated for the horizontal (a) and longitudinal (b) phase spaces using different horizontal chromaticities/different values of κ and various phase space amplitudes. The points correspond to tracking results, the solid lines depict theoretical calculations.

6.2.2.2 Intrinsic Resonances

The strengths of intrinsic resonances strongly depend on the amplitudes of phase space motion, i.e. the Courant-Snyder invariants. Thus, the spin motion of different particles is affected incoherently, which could introduce spin tune deviations. In this section, the impact of a single isolated resonance with strength $\epsilon_K = \epsilon_R - i\epsilon_I$ and the resonance tune K is considered. Effects on spin motion in the resonance precessing frame have been discussed intensively in Section 3.2.8.1. Here, some of the results are summarized. The solution of the spinor equation of motion for a two component spinor is given by:

$$\psi(\theta) = e^{\frac{i}{2}K\theta\sigma_3} \exp\left[-\frac{i}{2}\left(\delta_\nu\sigma_3 - \epsilon_R\sigma_1 + \epsilon_I\sigma_2\right)\right]\psi(0) \ . \tag{6.18}$$

The values for the radial and longitudinal spin component can be computed via:

$$S_x(\theta) = \psi^\dagger(\theta)\sigma_1\psi(\theta) \ , \tag{6.19}$$
$$S_z(\theta) = \psi^\dagger(\theta)\sigma_2\psi(\theta) \ . \tag{6.20}$$

From these quantities the spin phase advance in the horizontal plane ϕ_{xz} with respect to θ can be calculated by

$$\frac{\mathrm{d}\phi_{xz}}{\mathrm{d}\theta} = \frac{\mathrm{d}}{\mathrm{d}\theta}\mathrm{atan2}(S_z(\theta), S_x(\theta)) \ . \tag{6.21}$$

To obtain the spin tune deviation $\Delta\nu_s$, the averaged spin phase advance has to be calculated. The spin tune in the resonance precessing frame is given by $\lambda = \sqrt{\delta_\nu^2 + |\epsilon_K|^2}$ (Equation 3.214) with $\delta_\nu = G\gamma - K$. Thus, the spin tune deviation yields:

$$\Delta\nu_s = \frac{\int_0^{2\pi/\lambda}\mathrm{d}\theta\frac{\mathrm{d}\phi_{xz}}{\mathrm{d}\theta}}{2\pi/\lambda} \ . \tag{6.22}$$

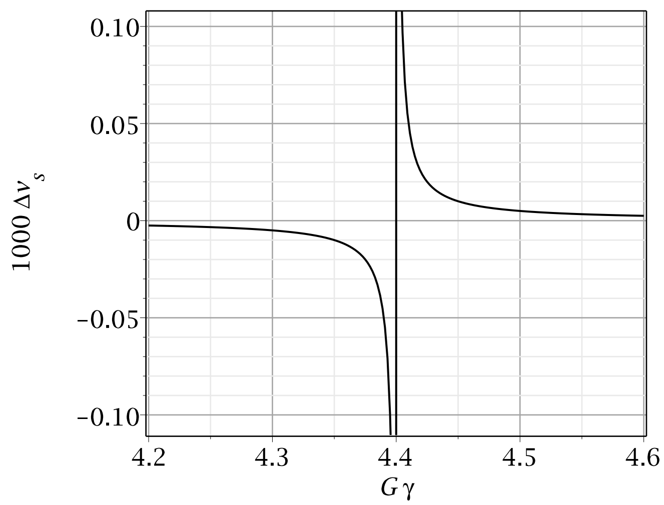

Figure 6.5: Calculated spin tune deviation for a particle with an initial longitudinal spin vector in presence of an isolated spin resonance at $K = 4.4$ with a strength of $\epsilon_R = 10^{-3}$ and $\epsilon_I = 0$.

In Figure 6.5, this is exemplarily shown for $K = 4.4$ and $|\epsilon_K| = 10^{-3}$. In case the distance to the resonance $\delta_\nu \gg |\epsilon_K|$, the spin tune deviation can be expressed as:

$$\Delta\nu_s = \mathrm{sign}(\delta_\nu)\lambda - \delta_\nu \approx \frac{|\epsilon_K|^2}{2\delta_\nu} \; . \tag{6.23}$$

The strong intrinsic resonances are related to vertical betatron motion. In general, the corresponding resonance strengths depend on the vertical betatron oscillation amplitudes. Thus, up to second order the spin tune deviation is proportional to the Courant-Snyder invariant:

$$\Delta\nu_s \propto \varepsilon_y \; . \tag{6.24}$$

This proportionality behavior is similar to the path lengthening introduced by vertical betatron motion. Consequently, the spin tune deviation from intrinsic resonances can be corrected by an opposite deviation due to path lengthening in presence of a non-vanishing vertical chromaticity. For the nominal betatron tunes of about 3.6, there is no strong intrinsic spin resonance for deuterons in the accessible momentum range of COSY. Thus, the effect of intrinsic resonances is subsequently demonstrated for the protons. The intrinsic resonance strengths of COSY have been already investigated in [112]. Within this thesis, COSY INFINITY simulations based on the present model configuration are used to determine the resonance strengths of the different intrinsic resonances in the operational range. A special adjustment of the COSY optics, i.e. required for the crossing of the transition energy, is not taken into account, since the aim of this study is the demonstration for different momenta, but fixed quadrupole strengths k_1. Figure 6.6 depicts the various resonance strengths. The intrinsic resonances appear at $K = n \cdot P \pm (Q_y - 2)$, where P is the super periodicity. The value 2 needs to be subtracted from the vertical betatron tune to consider the phase advance of 2π in

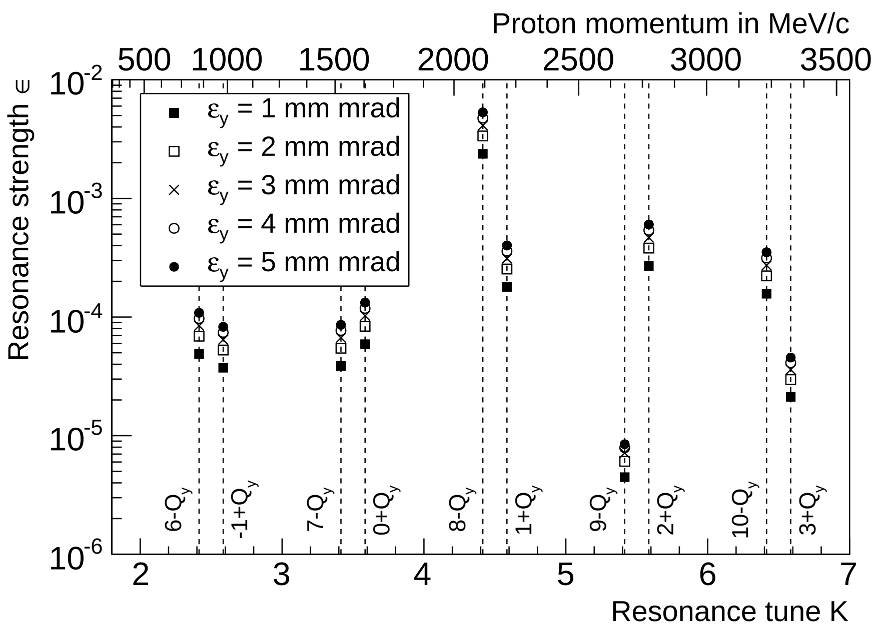

Figure 6.6: Calculated intrinsic resonance strengths for various vertical Courant-Snyder-invariants. The lattice configuration with zero dispersion in the straights benchmarked in the previous chapter has been used.

each telescopic straight section. Since COSY possesses six similar cells in the arcs, the strongest resonance appears at $K = 8 - Q_y$. The additional resonances do not vanish, since in the ideal case the lattice setup with dispersion free straights offers only a two-fold symmetry. Furthermore, the straights are not perfectly transparent, which is also included in the present model. Note that, for resonance crossing studies the resonance strengths with respect to normalized emittances are in general of more interest due to adiabatic damping. This normalization is not performed in the present study, since the impact and overlap of intrinsic resonances (Equation 6.23) should be explored for resonance strengths ϵ_K, which are constant for all beam momenta and δ_ν.

6.2.3 Spin Tune Spread of Protons and Deuterons at COSY

In this section, the spin tune deviations for protons and deuterons are investigated in the COSY momentum range. To illustrate the effect of intrinsic resonances, a more detailed description for protons is presented. Two different lattice configurations are utilized. In the first setup, the strengths of the sextupole families in the arc sections are adjusted to minimize the horizontal and vertical chromaticities, as well as the value of κ. In the second setup, the arc section sextupoles are turned off completely and the sextupole components of the guiding dipoles are tuned to match with the measured relative chromaticities of $\xi_x = -4.68$ and $\xi_y = 2.60$ in absence of active sextupole magnets. The κ factor defined in Equation 6.17 is currently not determinable in real experiments at COSY due to the unknown contribution depending on α_1. Hence, κ could not be tuned to a measured value, but varies due to its energy dependency. For the current investigation it takes on values between six and seven.

Figure 6.7 illustrates the spin tune deviations for five particles with different horizontal phase space amplitudes. The red curve depicts the variation of the phase slip factor η_{ph} for the different reference momenta. As already mentioned, the lattice configuration is not adjusted for different momenta intentionally. Thus, a vanishing phase slip factor required to maintain longitudinal phase focusing is not avoided and the associated crucial amplification of the spin tune deviations is outlined. In the first scenario, the horizontal chromaticity is minimized. Consequently, the betatron motion induces no energy change according to Equation 6.15 and the spin tune deviation vanishes for all particles. Note that, the oscillation of the spin phase deviation $\Delta\phi$ discussed in the first section of this chapter is not part of this study. In particular for a vanishing η_{ph} the impact of such an oscillation is expected to be large and might drastically reduce the precessing polarization component, although $\Delta\nu_s$ is minimized. In the second scenario the non-vanishing horizontal chromaticity leads to a spin tune deviation, which is clearly observed. This deviation diverges at $\eta_{\text{ph}} = 0$, which is located at $G\gamma \approx 4.1$. Considering, for example, $\varepsilon_x = 1\,\text{mm mrad}$ and a proton momentum of $1\,\text{GeV/c}$, the absolute chromaticity has to be reduced to about $|Q'_x| \approx 0.01$ to reach $|\Delta\nu_s| \leq 10^{-9}$ for this particular lattice setup. A similar behavior of the spin tune deviation is also observed for the longitudinal phase space. As expected, the deviation is minimized for $\kappa \approx 0$, if $\eta_{\text{ph}} \neq 0$ simultaneously. Otherwise, a diverging behavior occurs around $\eta_{\text{ph}} = 0$, too.

Up to now, only the effects of path lengthening have been illustrated. Considering the vertical phase space, a strong impact of intrinsic resonances is expected. Figure 6.8

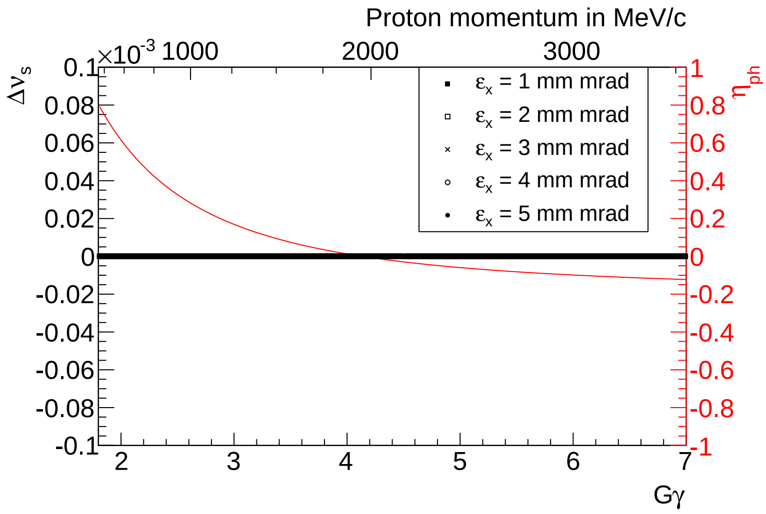

(a)

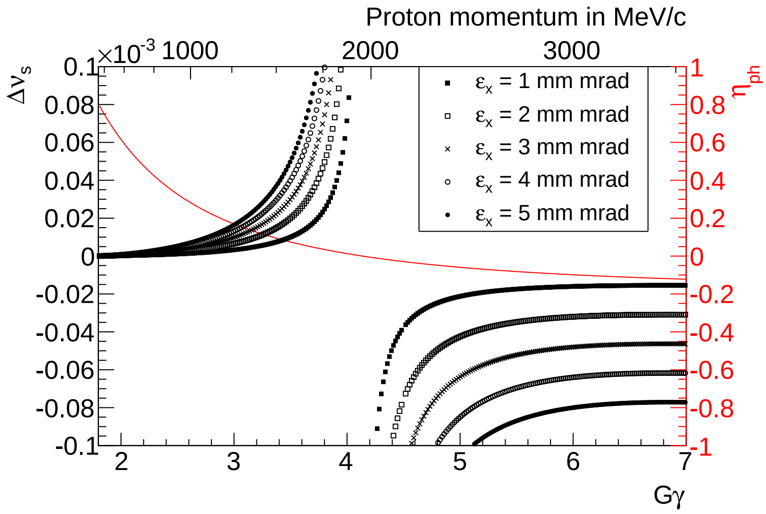

(b)

Figure 6.7: Spin tune deviations for individual protons with various horizontal betatron amplitudes in a bunched beam considering different reference momenta. Figure (a) shows the situation for minimized horizontal chromaticity, Figure (b) corresponds to $\xi_x = -4.68$.

shows the calculation results for the spin tune deviations in the entire reference momentum range for protons. Together with the intrinsic resonances the location of $\eta_{\text{ph}} = 0$ is indicated. Five different values for ε_y are investigated. The influence of path lengthening is suppressed in the first scenario with a vanishing vertical chromaticity. Thus, no divergence of $\Delta\nu_s$ is observed for a vanishing η_{ph}. However, a similar $\Delta\nu_s$-response as predicted in Figure 6.5 appears at the locations of the intrinsic resonances. The strongest resonances at $K = n \cdot 6 \pm (Q_y - 2)$ are responsible for the largest spin tune deviations. In the shown momentum interval, only one strong resonance at $K = 8 - Q_y$ exists, but the results at the edges of the momentum interval indicate the large contribution of resonances located at $K = -2 + Q_y$ and $4 + Q_y$. In between these strong resonances, the spin tune deviation for the different ε_y crosses zero at

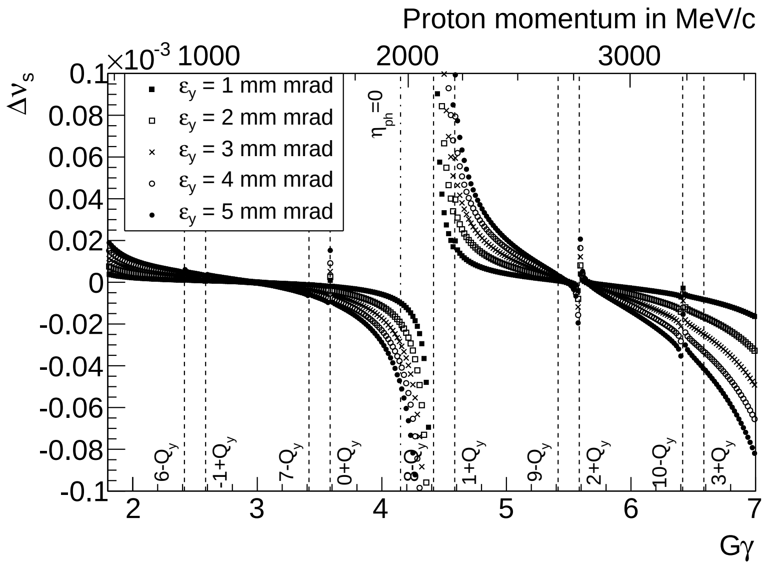

(a)

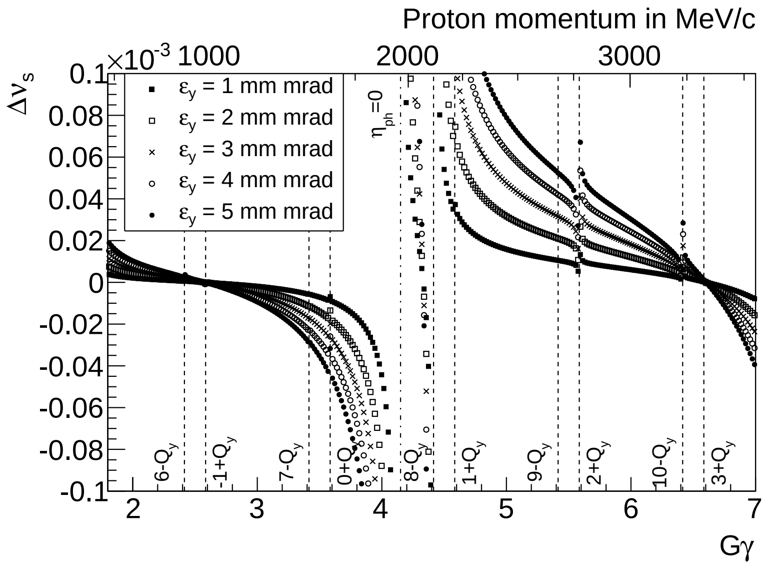

(b)

Figure 6.8: Spin tune deviations for individual protons with various vertical betatron amplitudes in a bunched beam with respect to different reference momenta. Figure (a) shows the situation for minimized vertical chromaticity, Figure (b) corresponds to $\xi_y = 2.60$.

nearly the same value of $G\gamma$. Two interesting effects appear when comparing the two scenarios. First, a strong spin tune deviation around $\eta_{\text{ph}} = 0$ occurs, which is similar to the observations for the horizontal and longitudinal phase spaces. Second, the locations of the zero crossings are shifted due to the overlapping contributions of intrinsic resonances and path lengthening. For an isolated intrinsic resonance a pure shift is expected, since the second order contributions (discussed in Section 6.2.2) are proportional to ε_y. But even for large δ_ν the spin tune deviation induced by a specific resonance remains at a certain non-vanishing magnitude. Thus, the contributions from

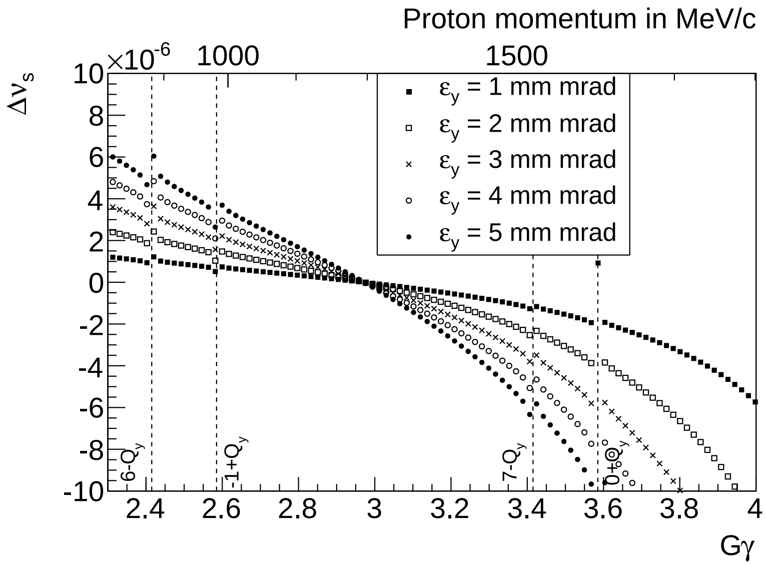

(a)

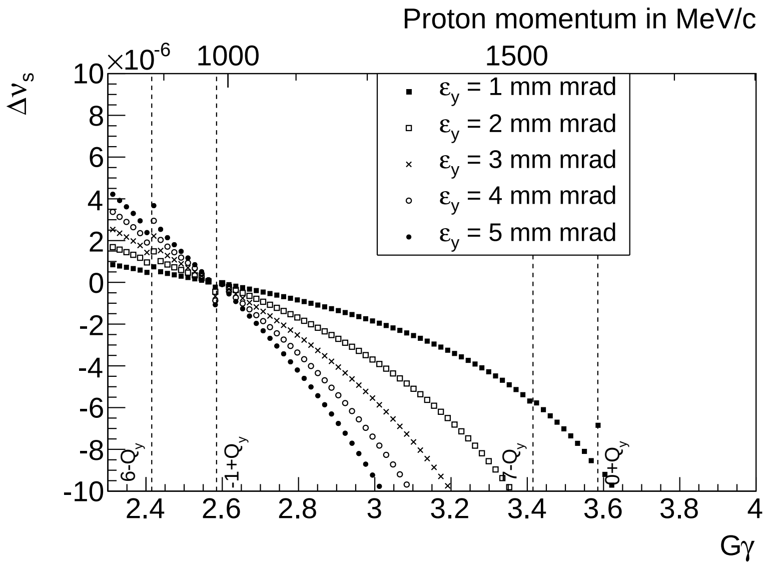

(b)

Figure 6.9: Spin tune deviations for individual protons with various vertical betatron amplitudes in a bunched beam with respect to different reference momenta. Figure (a) shows the situation for minimized vertical chromaticity, Figure (b) corresponds to $\xi_y = 2.60$. This figure depicts a detail of Figure 6.8.

different intrinsic resonances overlap and considering the required level of $\Delta\nu_s$ to achieve a long SCT, they can not be fully treated as isolated. Additionally, also higher than second order contributions enter at smaller scales. Thus, a perfect overlap of the zero crossings for different ε_y is not guaranteed.

For a more detailed investigation, Figure 6.9 depicts a detail of the momentum range around 1 GeV/c to 1.5 GeV/c for the two scenarios. On this scale, also the induced spin tune deviations from the small intrinsic resonances are observable, but the zero crossing locations for different values of ε_y are still not distinguishable. The locations of the zero crossings are expected to provide the longest spin coherence times. The induced shifts of these zero crossing locations are proportional to the vertical chromaticity, which controls the amount of path lengthening for individual particles. Thus, an adjustment of the vertical chromaticity by the sextupole magnets allows one to move the zero crossing location to a desired reference beam momentum. The actual value of the SCT finally depends on the beam emittances, the stability of the machine and the proximity to the zero crossing locations for different emittances. Hence, once the desired momentum is fixed, a detailed lattice layout study has to be performed to scrutinize the spin coherence time expectable in the final experiment. Here, also variations of the quadrupole strengths have to be considered, since they influence the resonance strengths and the betatron tunes, which define the locations of the intrinsic resonances.

In the scope of this thesis, deuterons at the currently used beam momentum of 970 MeV/c at COSY are investigated. For that purpose, the final discussion within this section deals with the spin tune deviations observed in case of deuterons. Figure 6.10 illustrates these deviations for the horizontal, vertical and longitudinal phase spaces

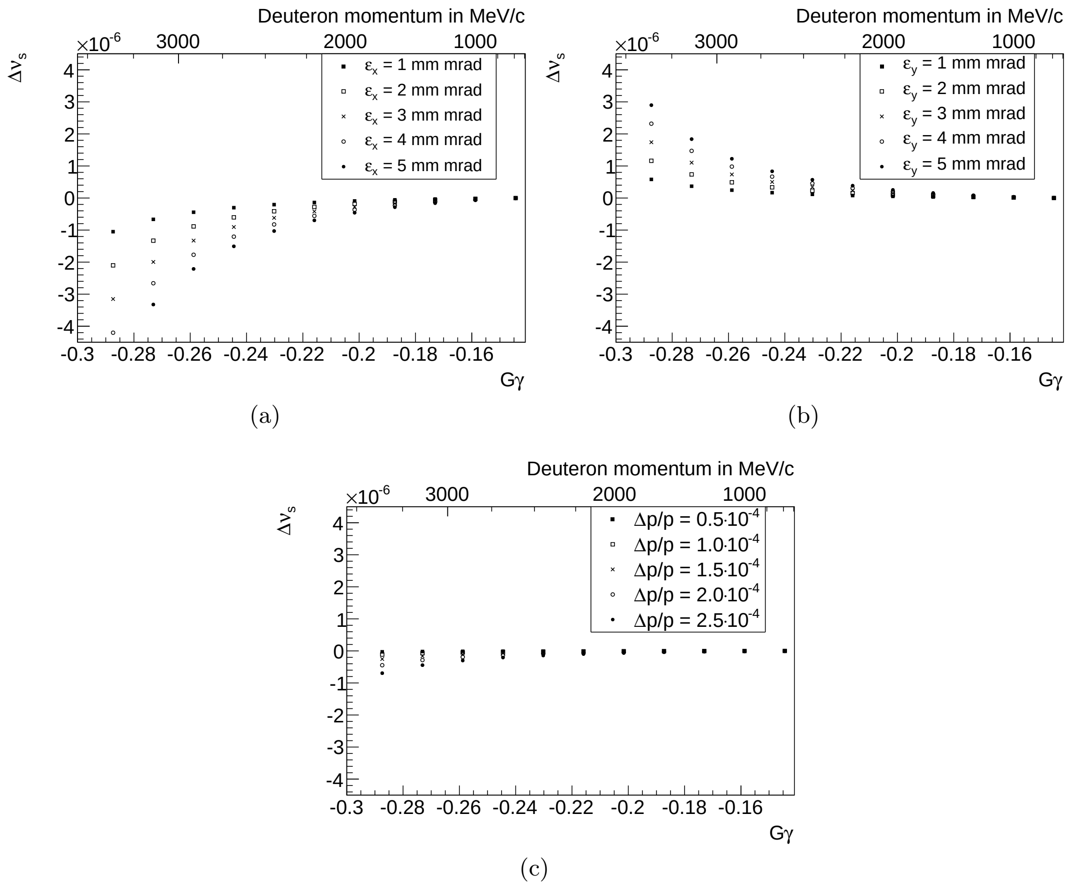

Figure 6.10: Spin tune deviation for individual deuterons with various betatron (a,b) and synchrotron (c) amplitudes in a bunched beam with respect to different reference momenta. The experimental measured conditions $\xi_x = -4.68$ and $\xi_y = 2.60$ have been kept constant.

using the lattice setup of the second scenario, which has been adjusted to the measured chromaticities. Compared to the proton case, these deviations are in general orders of magnitude smaller, since the anomalous magnetic moment is approximately a factor 13 smaller and there are no intrinsic resonances in the COSY momentum range for the nominal betatron tunes $Q_x = 3.62$ and $Q_y = 3.585$. The additional spread towards larger momenta mainly arises due to a smaller absolute value of η_{ph} and an increased nominal spin tune $G\gamma$. The deviations at a momentum of 970 MeV/c are in the order of $\Delta\nu_s \approx 10^{-7}$ or even less. To further reduce these remaining deviations, a study of the sextupole configurations is conducted.

6.2.4 Spin Tune Spread Minimization and Predictions for Measurements at COSY

In the previous section, the strong connection of the spin tune deviations with respect to the beam chromaticities and the parameter κ was shown. Therefore, it can be concluded, that the spin tune deviations can be strongly influenced by a variation of the sextupoles. At least three families are required to independently vary the two beam chromaticities and κ. Since the induced changes of these parameters hinges on the dispersion at the sextupole locations, the three available families MXS, MXL and MXG have been selected for this study. An algorithm for the minimization of the spin tune deviations has been developed and is subject of this section. These algorithm acts as follows: A set of 15 particles (five distributed in horizontal, vertical and longitudinal phase space, respectively) is tracked for several sextupole configurations. For each configuration, the spin tune deviation of each particle with respect to the reference particle is calculated. Figure 6.11 depicts the results retrieved for the variation of the sextupole family MXL in two iterations. As expected, the response is linear and at certain sextupole strengths a vanishing spin tune spread is observed. Together with the two other sextupole families, this forms a linear equation system allowing one to minimize the spin tune spread for all particles simultaneously. The solution determines the sextupole strengths of MXS, MXL and MXG for which the spin tune spread is minimized in all three sub-phase spaces. Two iterations are performed to locate this minimum. Initially, all sextupole families are turned off. The first iteration induces sextupole changes on a larger scale to locate roughly the best operational point. These sextupole values are used as starting point for the second iteration to further refine the optimum point. The resulting sextupole configuration is adopted in order to calculate the required chromaticities and κ for a minimized spin tune spread.

The results for different vertical betatron tunes are shown in Figure 6.12. As expected, the horizontal chromaticity and the parameter κ are supposed to vanish for a minimized spin tune spread. The optimum vertical chromaticity depends on the value of the vertical betatron tune. At $Q_y = 3.84$, the intrinsic resonance $K = -4 + Q_y$ appears, since the nominal spin tune about $G\gamma \approx -0.16$. The marker at 3.69 is missing, due to an unstable beam motion at the beam resonance $Q_x + 2Q_y = 11$ in the simulations. If the impact of intrinsic resonances is not taken into account, a long spin coherence time could be observed at vanishing vertical chromaticities. The theoretical results indicate, that also for the deuteron case, these resonances play an important role. Two vertical betatron tunes, $Q_y = 3.585$ and $Q_y = 3.86$ have been chosen for an experimental verification of the presented theoretical estimates. The former tune is

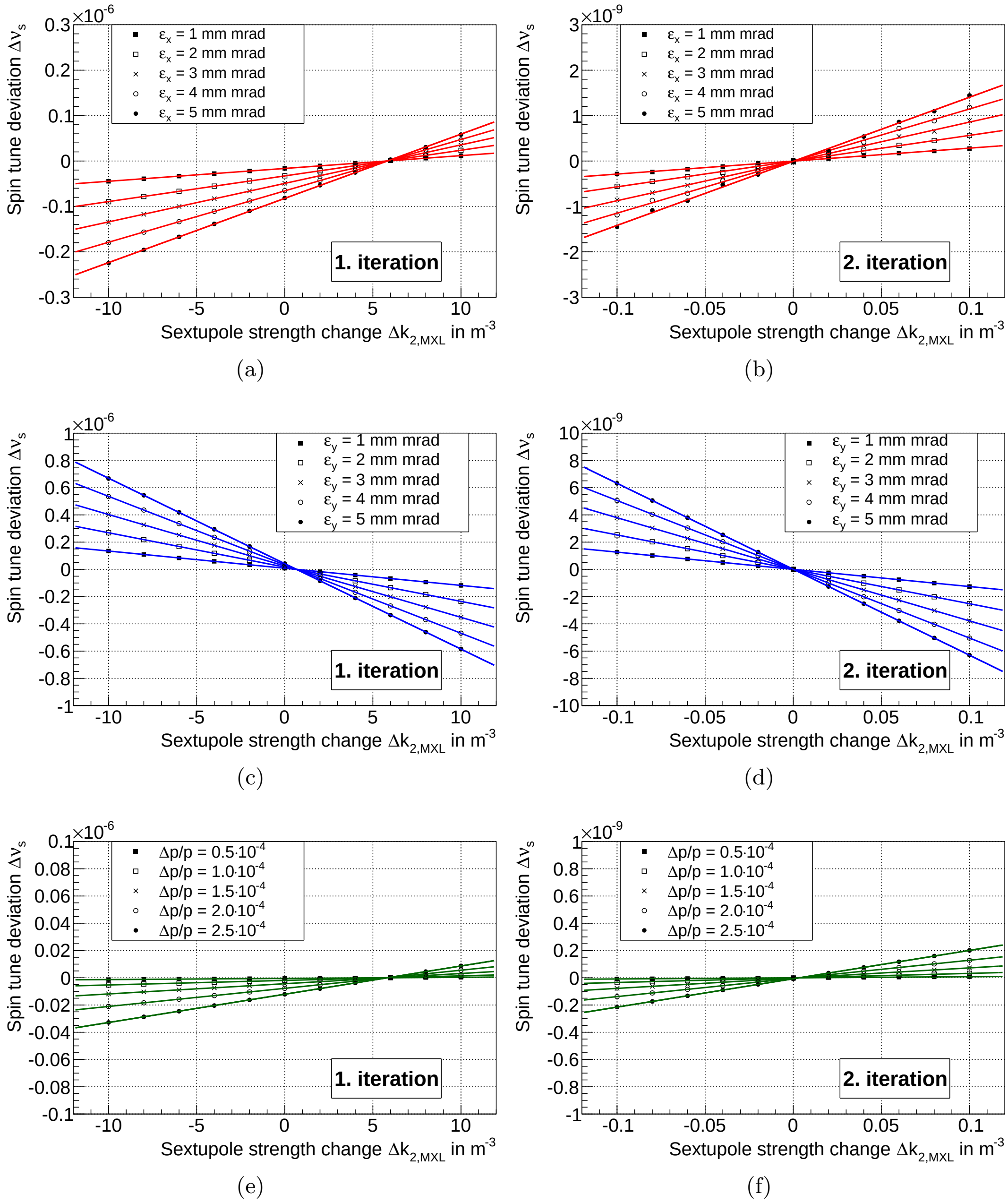

Figure 6.11: Algorithm to find the optimum sextupole configuration with minimized spin tune deviation. The spin tune deviation for individual particles from the horizontal [(a) and (b)], vertical [(c) and (d)] and longitudinal [(e) and (f)] phase space with respect to a change of the sextupole strengths $k_{2,\mathrm{MXL}}$ of the MXL family is illustrated. Together with the information of MXS and MXG, a linear equation system is constructed to obtain the optimum sextupole settings. In the first iteration [(a), (c) and (e)] a larger strength interval is selected, while the second iteration [(b), (d) and (f)] serves for a fine-tuning.

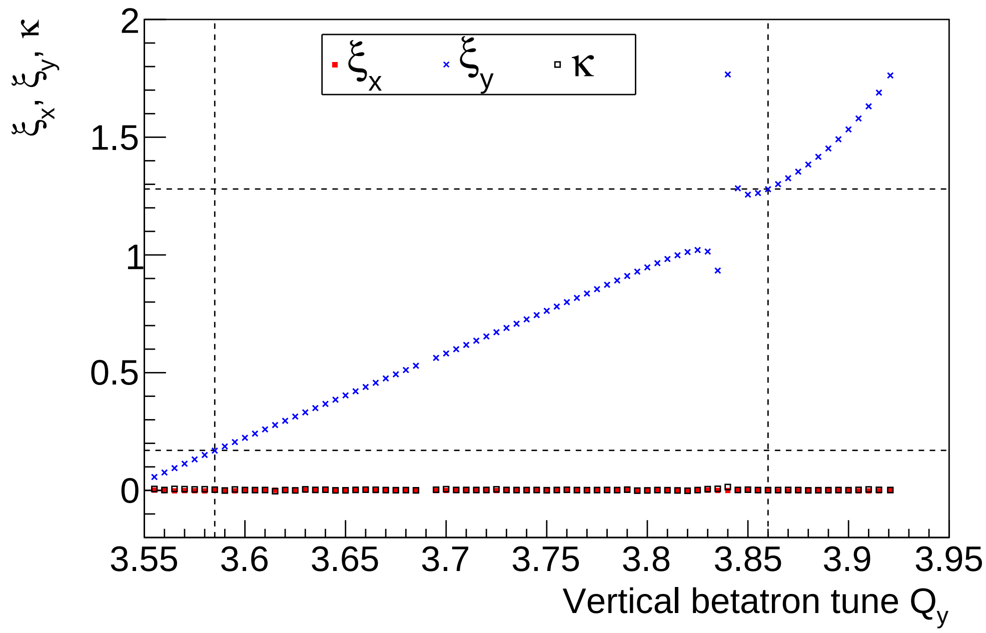

Figure 6.12: Simulated optimum settings of the chromaticities ξ_x and ξ_y and the parameter κ for minimized spin tune spread with respect to different vertical betatron tunes. A lattice setup with minimized dispersion in the straights and a deuteron reference momentum of $p = 970\,\mathrm{MeV/c}$ is selected.

the nominal operating tune, where a long SCT is required for the EDM studies at COSY. The calculations predict a small positive vertical chromaticity close to zero as best operational point. The latter tune aims for a measurement of a long SCT at a vertical chromaticity substantially different from zero to validate the simulated influence of intrinsic resonances. The corresponding experimental results are discussed in the subsequent section.

6.3 Spin Coherence Time Measurements

In this section, the experimental results for spin coherence time measurements for deuterons at 970 Mev/c at two different lattice configurations are presented. First, the measurement setup and the analysis method to obtain the SCT is illustrated.

6.3.1 Measurement Setup and Analysis Method

A measurement run consists of several cycles with same experimental setup except for a varying initial polarization state. During the beam time associated to these measurements, two polarization states were used for the SCT studies. Both states possessed a vertical vector polarization of slightly different amplitude and opposite sign and a negligible tensor polarization. A typical cycle setup has been presented in Section 4.3. The polarized beam with about 10^9 deuterons per injection was accelerated to its final momentum of $970\,\mathrm{MeV/c}$. In case of the nominal vertical betatron tune $Q_y = 3.585$, the beam was electron cooled for about 75 s. To achieve the higher betatron

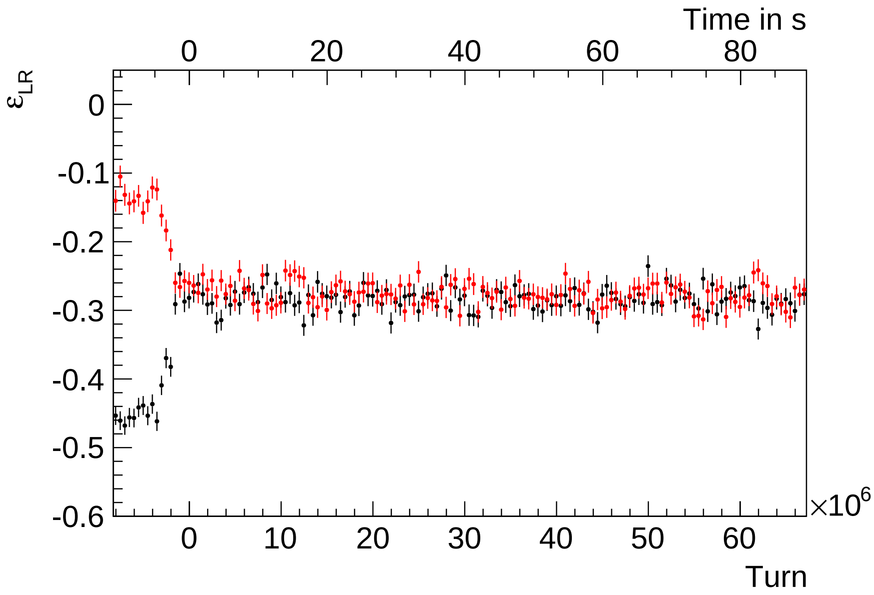

Figure 6.13: Measured left-right-asymmetry ε_{LR} with respect to turn/time in the cycle. The black points show the accumulated data for one run and polarization state 1, the red points correspond to polarization state 2. A polarization flip from the vertical direction into the horizontal plane was set up. A new zero-point of the horizontal axes has been selected as time shortly after the flip was completed.

tune $Q_y = 3.86$, a different setup was necessary, since several betatron resonances needed to be crossed between the nominal tunes at injection and the final tunes required for the experiment. For this purpose, the beam was electron cooled at the nominal betatron tunes. Afterwards, additional quadrupole ramps using the MQU1/2 and MQU5/6 families were applied to shift the vertical betatron tune up to $Q_y = 3.86$ keeping the already injected beam. Due to beam heating during the betatron resonance crossing, additional electron cooling time was reserved for emittance reduction after the final betatron tune was reached. Furthermore, a global orbit correction was applied in both scenarios, reducing the measured orbit Root Mean Square (RMS) to below 3 mm. After the cooling period, the beam was moved directly below the EDDA carbon target using a vertical orbit bump applied by variation of four vertical corrector magnets. A controlled vertical heating using white noise on the stripline unit was activated to obtain a constant detector count rate for the remaining cycle duration of about 100 s. About five to ten seconds later, the RF solenoid was turned on running at a frequency close to a spin resonance frequency. A slow ramp of the solenoid frequency lasting a few seconds was applied to move the beam polarization from the vertical direction into the horizontal plane according to the Froissart-Stora method. The solenoid was turned off exactly on the spin resonance frequency. Consequently, the beam polarization precessed in the horizontal plane and the spin coherence time could be measured. Figure 6.13 exemplarily shows the measured left-right-asymmetry ε_{LR} for all events of the two polarization states accumulated in one measurement run. For equal detector acceptances and efficiencies, this asymmetry is proportional to the vertical vector polarization (Equation 4.10). The polarization flip induced by the solenoid was adjusted such that the left-right-asymmetries of both polarization states agree after the frequency ramp, when the solenoid was turned off. In general, This setup produces the largest polarization amplitude in the horizontal plane. Its decay is studied to retrieve the spin coherence time. For that purpose, a new time scale with an origin shortly after the flip was defined. The left-right-asymmetries shown in Figure 6.13 reveal a large offset of about -0.28 for a vanishing vertical vector polarization, which hints towards different detector acceptances/efficiencies for the left and right quadrant. In the most recent beam time, a significant contribution to this offset could be traced back to a malfunction of one of the detector half rings, which has been fixed recently. Additionally, a strong impact on the offsets of the measured asymmetries connected to the adjustment of the trigger thresholds has been observed.

The fast precession of the polarization in the horizontal plane leads to a sinusoidal oscillation of the radial polarization component P_x at the location of the EDDA detector. This manifests in a measurable oscillation of an up-down-asymmetry, which is proportional to the P_x component. The amplitude decay of this oscillation relates to the SCT, while its frequency allows one to obtain the spin tune with a relative precision of 10^{-9} in a measurement period of about 100 s using a setup with sufficiently long SCT [147]. The corresponding analysis method, also illustrated in [147], provides amplitude and frequency information. It has been slightly adapted, which will be exemplarily discussed in the following. A detailed systematic study of the analysis method is scope of a different thesis [148]. The detector event rate in a typical cycle is about $5000\,\mathrm{s}^{-1}$. Given a spin tune of about -0.16 and a revolution frequency of 750 kHz, this results in about one event per 24 revolutions. Thus, a direct least squares fit of the P_x oscillation is not applicable. Rather, an algorithm is defined, which maps the recorded events of a certain interval into one oscillation period. The accumulation of events permits a least squares fit to extract the amplitude and phase of the oscillation. Each recorded event i contains information about the detector quadrant, in which it was generated, and a precise timestamp t_i. Furthermore, the associated turn number n_i, in which the event was recorded, can be obtained. A first guess of the spin oscillation frequency, i.e. the spin tune in a turn based analysis, is obtained from the calculation of the Fourier amplitudes A. For determination of the amplitude A, values of the spin tune ν_s in a certain interval in a certain interval are assumed. All recorded events in the up and down detector quadrants of one cycle in a run are processed as follows:

$$c_i = \pm 1 \quad (+\text{: up, -: down}) \ , \tag{6.25}$$

$$A_r = \frac{1}{N}\sum_{i=1}^{N} c_i \cos(2\pi\nu_s n_i) \ , \tag{6.26}$$

$$A_i = \frac{1}{N}\sum_{i=1}^{N} c_i \sin(2\pi\nu_s n_i) \ , \tag{6.27}$$

$$A = \sqrt{A_r^2 + A_i^2} \ . \tag{6.28}$$

Figure 6.14 shows the calculation for an assumed value $\nu_{s,\text{central}} = 0.1609711$ and three different interval widths. A positive fractional number is sufficient as central value, since the sign and the integer part of the spin tune could not be resolved with only one detector and only P_x measured. The first scan using an interval width of 10^{-7} is used to roughly locate the temporal average of the spin tune in each cycle. In the two subsequent scans the interval is centered at the location of the maximum of the previous scan and its width is reduced by one order of magnitude, respectively. The

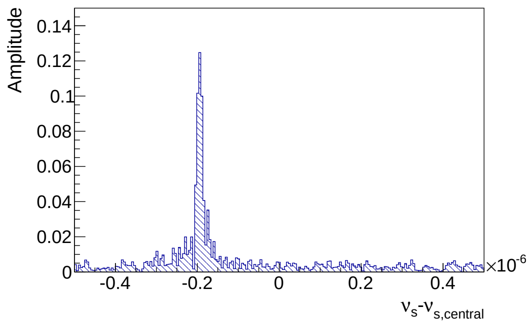

(a)

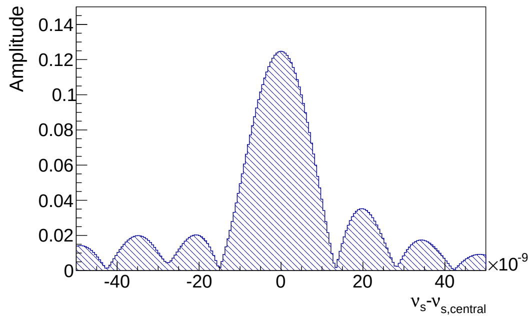

(b)

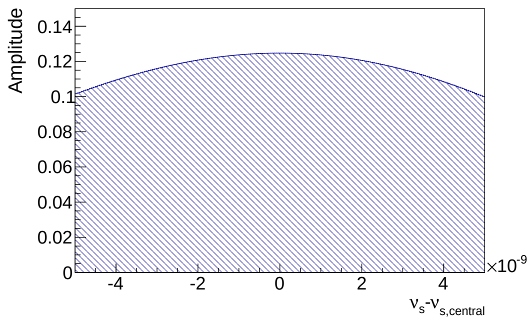

(c)

Figure 6.14: Fourier amplitudes calculated according to Equation 6.28 for different assumed spin tune values ν_s using all events detected in up and down detector quadrants in one cycle. The difference with respect to a central value $\nu_{s,\text{central}}$ was determined. In the first scan (a) with an interval of 10^{-7} a value $\nu_{s,\text{central}} = 0.1609711$ was selected. The second and third scan with intervals of 10^{-8} (b) and 10^{-9} (c) used the location of the maximum in the preceding scan as value for $\nu_{s,\text{central}}$.

slight asymmetry in the Fourier amplitude spectra, especially for the second scan, hints at a small drift of the spin tune during the cycle. The location of the maximum of the last scan provides the best guess ν_s^0 used for the event mapping into one oscillation period.

The applied mapping algorithm aims for the minimization of an offset due to different detector acceptances/efficiencies as follows: The full measurement period is split into turn bins with a width of 10^6 turns (1.33 µs), which are analyzed independently. The events of each turn bin recorded in the up and down detector quadrant are mapped into an individual spin phase interval of 4π. Therefore, the spin phase advance ϕ_s limited to a 4π-interval is calculated for each event according to

$$\phi_s = 2\pi\nu_s^0 n_i \bmod 4\pi \ . \tag{6.29}$$

Based on this quantity, the event counts in up and down detectors with respect to the spin phase $N_U(\phi_s)$ and $N_D(\phi_s)$ are determined.

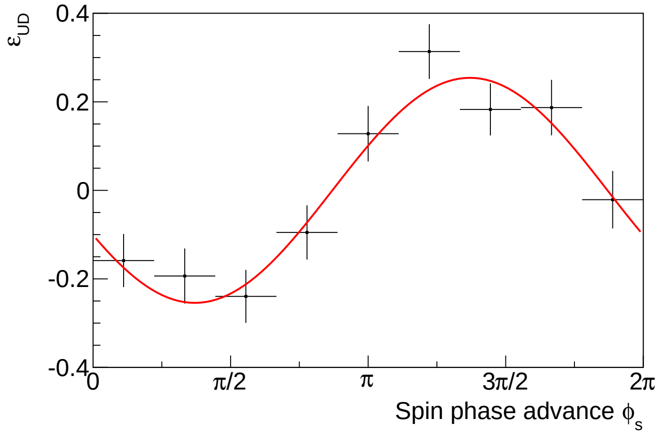

Figure 6.15: Up-down-asymmetry after sorting the events of up and down detector quadrant recorded according to their spin phase advance ϕ_s. Data recorded in a turn interval of 10^6 turns have been used. The solid line shows a sinusoidal fit to the data.

Subsequently, an asymmetry ε_{UD} defined in a 2π-interval is obtained as follows:

$$N_X^{\pm}(\phi_s) = \begin{cases} N_X(\phi_s) \pm N_X(\phi_s + 3\pi) & \text{for } 0 \leq \phi_s < \pi \\ N_X(\phi_s) \pm N_X(\phi_s + \pi) & \text{for } \pi \leq \phi_s < 2\pi \end{cases}, \tag{6.30}$$

$$\varepsilon_{UD}(\phi_s) = \frac{N_U^-(\phi_s) - N_D^-(\phi_s)}{N_U^+(\phi_s) + N_D^+(\phi_s)} = \frac{3}{2}\hat{P}_x \frac{\overline{\sigma}_{0,U}\overline{A}_y^{\text{s,U}} - \overline{\sigma}_{0,D}\overline{A}_y^{\text{s,D}}}{\overline{\sigma}_{0,U} + \sigma_{0,D}} \sin(\phi_s + \phi_0)\ . \tag{6.31}$$

This mapping algorithms tends to cancel a systematic offset of the calculated asymmetry. Thus, the asymmetry is directly proportional to the horizontal polarization.

Figure 6.15 exemplarily shows a measured asymmetry for a turn bin of 10^6 turns located directly after the flip of the polarization into the horizontal plane. Estimates for the amplitude $\tilde{\hat{\varepsilon}}_{UD}$ and phase $\tilde{\phi}_0$ are obtained by a sinusoidal fit using:

$$\begin{aligned} \varepsilon_{UD}(\phi_s) &= \tilde{A}\cos(\phi_s) + \tilde{B}\sin(\phi_s) \\ \Rightarrow \tilde{\hat{\varepsilon}}_{UD} &= \sqrt{\tilde{A}^2 + \tilde{B}^2}, \quad \tilde{\phi}_0 = \operatorname{atan2}(\tilde{A}, \tilde{B}). \end{aligned} \tag{6.32}$$

The amplitude estimate corresponds to the polarization component precessing in the horizontal plane averaged in the particular turn bin. From here, it is referred to as the envelope of the up-down-asymmetry. The same mapping and fitting procedure is applied for every turn bin. This allows one to measure the decay rate, i.e. the SCT, of the polarization in the horizontal plane, as well as the walk of the phase throughout subsequent turn bins.

In Figure 6.16, the fitted amplitude and phase estimates are depicted for two cycles of different runs with setups providable clearly distinguishable SCTs. A detailed study of the sextupole conditions applied in these runs is performed in the next section. The first cycle illustrates a vanishing envelope during the measurement period, while the magnitude of the envelope is preserved in the second cycle. Although the polarization is expected to be lost after 40 s in the first cycle, the extracted envelope takes on always positive values. Statistical fluctuations paired with a free phase in the fitting routine introduce this positive bias for the extracted envelopes [149, 150]. This bias becomes

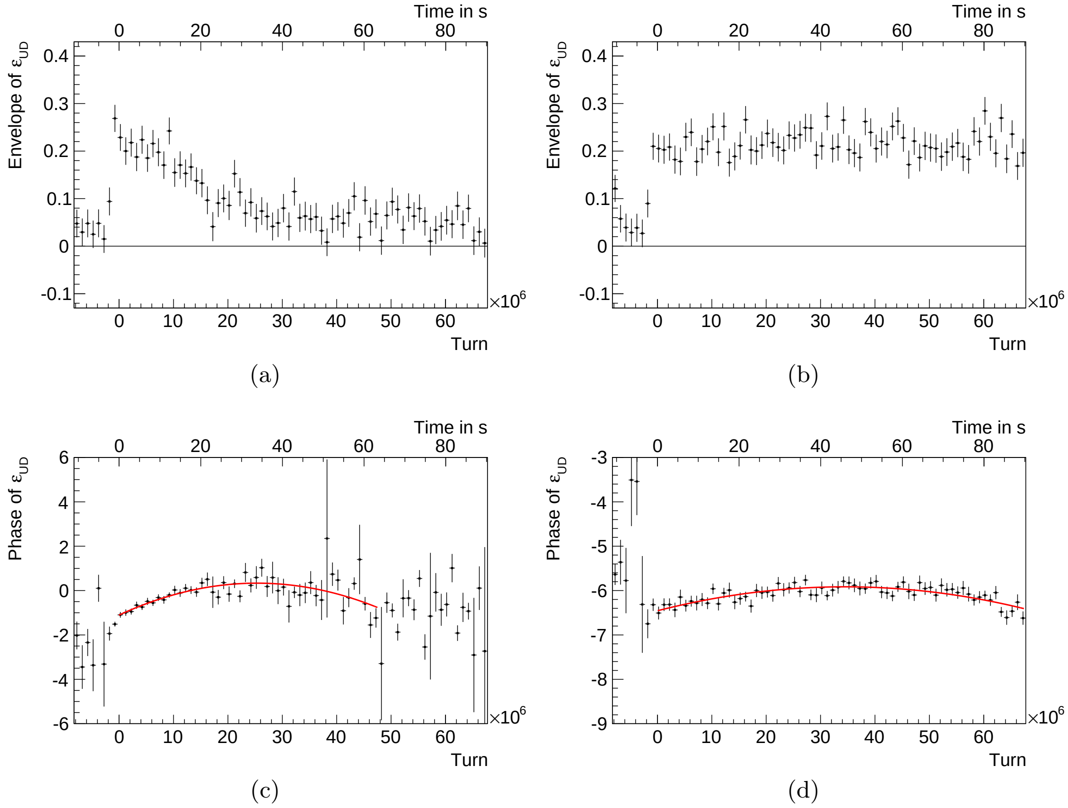

Figure 6.16: Fitted amplitude and phase estimates for various turn intervals of 10^6 turns throughout a cycle. Figure (a) and (c) depict a cycle with fast polarization decay, while figure (b) and (d) show a slow decay. The phase is fitted by a second order polynomial.

substantially larger, if the real horizontal polarization reaches values closer to zero. To reduce this bias, the analysis algorithm is extended for an smoothing procedure using the information of neighboring phase estimates. These phase estimates describe a parabolic curve in both cycles, as long as the horizontal polarization is reasonable large. From a second order polynomial fit the smooth turn-dependent phase $\phi_0(n)$ is obtained and extrapolated beyond regions with non-vanishing polarization. This turn-dependent phase $\phi_0(n)$ can be related to a linear change of the spin tune during the cycle:

$$\nu_s(n) = \nu_s^0 + \frac{1}{2\pi}\frac{\mathrm{d}\phi_0(n)}{\mathrm{d}n} \ . \tag{6.33}$$

Using this quantity, the same mapping procedure is repeated, replacing Equation 6.29 by

$$\phi_s = 2\pi\nu_s(n) \cdot n_i \ . \tag{6.34}$$

This enforces a phase offset $\phi_0 = 0$ in Equation 6.31 for regions with non-vanishing polarization. Hence, the estimate for the envelope of the horizontal polarization can be

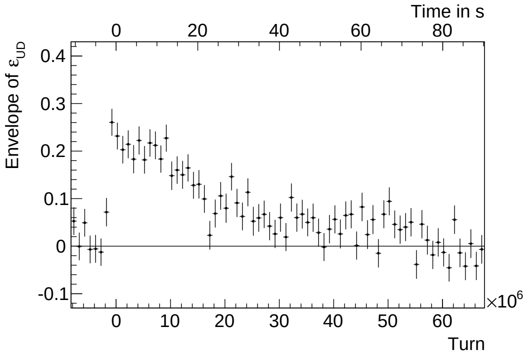

(a)

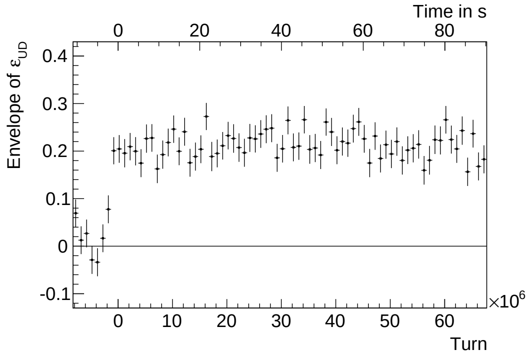

(b)

Figure 6.17: Fitted amplitude estimates for various turn intervals of 10^6 turns throughout a cycle. The sinusoidal fits (Figure 6.15) have been performed with a fixed phase based on the information obtained by the polynomial fit shown in Figure 6.16.

extracted by fitting the newly generated up-down-asymmetries, similar to Figure 6.15. For this purpose, a simplified functional form is used:

$$\varepsilon_{UD}(\phi_s) = \tilde{\hat{\varepsilon}}_{UD} \sin(\phi_s) \ . \tag{6.35}$$

Figure 6.17 shows the envelopes of the up-down-asymmetries obtained for the two cycles. For a vanishing polarization, the values are now oscillating around zero. Note that a trustworthy extrapolation of the phase is required to reduce the bias of the envelope in this analysis method. Since most cycles have a parabolic behavior of the phase on a 100 s time scale, the described scheme is applied to obtain graphs similar to Figure 6.17 for each run. The weighted averages over the horizontal polarization envelopes of different cycles with same polarization state are calculated for each run. They are used to obtain the SCT for different setups.

6.3.2 Experimental Results

The theoretical calculations and simulations predict a strong dependence of the SCT on the beam parameters like emittances and momentum spread paired with lattice parameters like the chromaticities and a parameter κ defined in the first section of this chapter. For a systematic exploration of the spin coherence time, chromaticity measurements have been performed to find ranges for a variation of the sextupole strengths. Additionally, the beam emittances have been measured using the beam profile monitor, while the momentum spread could be estimated from the time distribution of the recorded events (Figure 4.7).

6.3.2.1 Chromaticity Measurements

Chromaticity measurements have been performed for the two lattice configurations with different vertical betatron tunes: $Q_y = 3.585$ and $Q_y = 3.86$. A linear relation between the sextupole strength variations and the associated chromaticity changes has already been demonstrated in Section 5.3.2. Due to a variation of the quadrupole

Table 6.1: Results of the chromaticity measurements for two vertical betatron tunes: $Q_y = 3.585$ and $Q_y = 3.86$.

	$Q_y = 3.585$		$Q_y = 3.86$	
	ξ_x	ξ_y	ξ_x	ξ_y
ξ^n	-4.68 ± 0.05	2.60 ± 0.05	-5.83 ± 0.08	2.3 ± 0.1
$a_\mathrm{S} \cdot m^{-3}$	0.78 ± 0.01	-0.58 ± 0.01	0.91 ± 0.02	-0.38 ± 0.03
$a_\mathrm{L} \cdot m^{-3}$	0.78 ± 0.02	-3.71 ± 0.02	1.02 ± 0.03	-3.88 ± 0.04
$a_\mathrm{G} \cdot m^{-3}$	2.18 ± 0.03	-1.66 ± 0.03	2.56 ± 0.04	-1.89 ± 0.06
χ^2/ndf	14/18	19/18	9/14	12/14

strengths required for the adjustment of the vertical betatron tune, different proportionality factors between chromaticities and sextupole settings are expected. About 20 chromaticity measurements using different sextupole strengths have been performed. These sextupole strengths were defined by a grid. During these measurements, the strengths of the sextupole families MXS, MXL and MXG have been varied in ranges of $5\,\mathrm{m}^{-3}$ to $10\,\mathrm{m}^{-3}$, respectively. Finally, the measured chromaticities ξ_x and ξ_y were individually fitted according to:

$$\xi = \xi^n + a_\mathrm{S} \cdot k_{2,\mathrm{MXS}} + a_\mathrm{L} \cdot k_{2,\mathrm{MXL}} + a_\mathrm{G} \cdot k_{2,\mathrm{MXG}} \ . \tag{6.36}$$

The fit results are summarized in Table 6.1.

Based on the predictions obtained from Figure 6.12, a vanishing horizontal chromaticity and different values of the vertical chromaticity are desired to study the spin coherence time for different betatron tunes. A range of the vertical chromaticity that covers at least values from zero up to two was selected. Simultanously, the horizontal chromaticity was minimized. The required sextupole strengths for these conditions ranges are depicted in Figure 6.18. For both vertical betatron tunes examined, the families MXS and MXL are adjusted to provide a change of the vertical chromaticity preserving the horizontal chromaticity at the same time. Thus the sextupole strengths of MXS and MXL are proportional. The proportionality factor was obtained from the results given in Table 6.1. Based on results of preceding studies during this beam time the strength of MXG was adjusted to $k_{2,\mathrm{MXG}} = 1.41\,\mathrm{m}^{-3}$ and kept constant. Therefore, the sextupole configuration is fully characterized by the value of MXS. The black points correspond to the locations at which SCT measurements were performed during the beam time as shown later. The colored bands show the 1σ-confidence interval of the chromaticity measurements for the given sextupole values.

The parameter κ is proportional to the contribution from the longitudinal motion. Unfortunately, its magnitude is not accessible in measurements. A large momentum acceptance of the storage ring would be required to obtain the momentum compaction factor of second order α_1 from beam momentum variations. Similarly to the chromaticities, this parameter also depends on the sextupole strengths. Therefore, an order of magnitude estimate of the spin tune deviations due to path lengthening induced by synchrotron motion is performed. Subsequently, it is compared to the contribution from vertical betatron motion (Equation 6.15). For this purpose, the changes of Q'_y and κ in the selected sextupole range have been extracted from model calculations. In case of the nominal betatron tune $Q_y = 3.585$, the value of the absolute vertical chromaticity

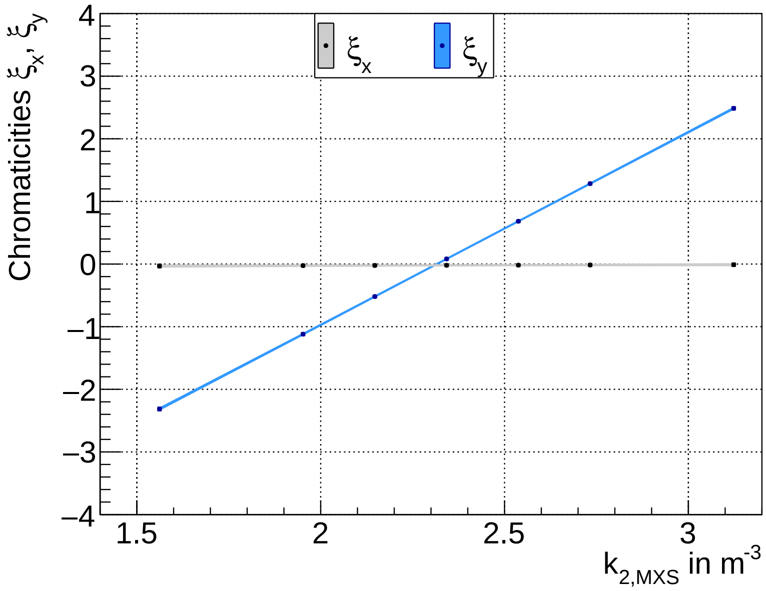

(a)

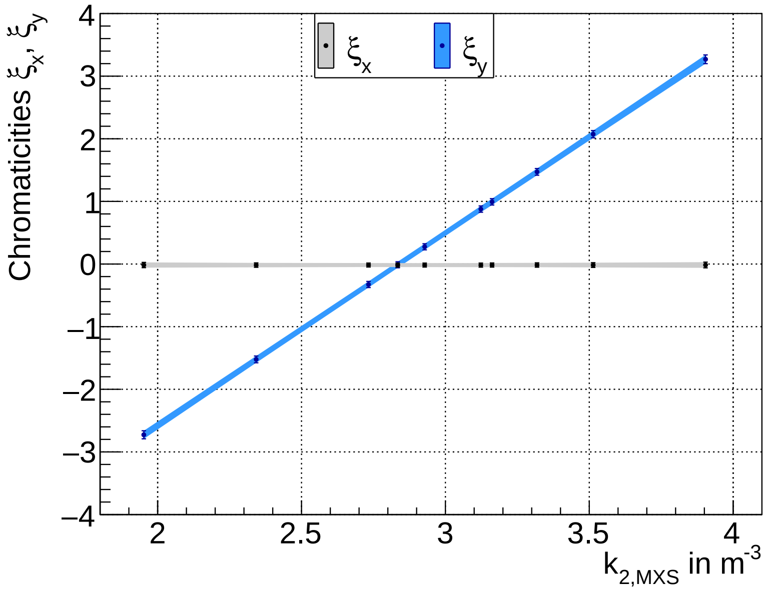

(b)

Figure 6.18: Measured chromaticities with respect to the different run setups chosen for the SCT studies at $Q_y = 3.585$ (a) and $Q_y = 3.86$ (b). Here the strength of the MXS family is selected as independent variable. The strength of the MXL family was changed to maintain a minimized horizontal chromaticity, while the strength of the MXG family was kept constant. The black points indicate the locations chosen for the SCT measurements and the colored bands illustrate the 1σ-confidence intervals.

Q'_y changes by about 17 between the smallest and largest strengths of MXS used. In the same sextupole range, model calculations predict a change of κ of about 1.7 only, which is one order of magnitude smaller. The induced spin tune changes depend on the product of chromaticities (κ) and the Courant-Snyder-Invariants (momentum spread). For the particular beam used during the experiments the emittances and the momentum spread are estimated in the subsequent section.

6.3.2.2 Beam Emittances and Momentum Spread

Figure 4.7 illustrates measurements of the beam profiles as well as the time resolved recorded events. These measurements correspond to a sextupole setting used at nominal tune in context of this SCT study. Due to an observed influence of the electric field of the profile monitor on spin tune and spin coherence time, the profile measurements are commonly performed in separate cycles with equal lattice setup as for the SCT studies. These measurements allow one to estimate the beam emittances. In the following the RMS emittances as defined in Section 3.1.4.1 are obtained from the widths of measured profiles. For that purpose, five profile measurements taken between 90 and 95 s seconds after injection are averaged. At this time, electron cooling and orbit correction were already completed. The accumulated signals are depicted in Figure 6.19. The dashed lines correspond to a fit of single Gaussian function, while the solid lines represent a superposition of two Gaussian functions. The latter case is used to take the cooled core and the uncooled tails of the beam into account. It shows an almost perfect agreement with the measured data. The fitted amplitudes A and widths σ are shown in Table 6.2.

The momentum spread of the beam can be estimated from the recorded detector events using a similar approach. For that purpose, the events recorded in the same time interval are accumulated. As seen in Figure 6.20, this clearly reveals the longitudinal bunch structure. Also here fits of single and double Gaussian functions are applied. The results are shown in Table 6.3. The goodness of fit is drastically improved by a

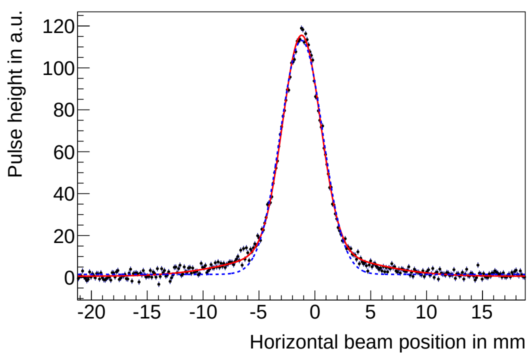

(a)

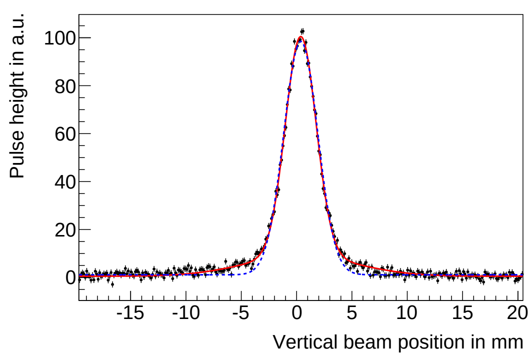

(b)

Figure 6.19: Accumulated data for five measurements of the horizontal (a) and vertical (b) beam profiles. The black points show the measurement, the blue dashed and the red solid line correspond to fits of a single Gaussian function and a superposition of two Gaussian functions, respectively.

Table 6.2: Fit results for amplitudes and widths of the profile measurements.

	Single Gaussian		Double Gaussian	
	horizontal	vertical	horizontal	vertical
A_1	111.6 ± 0.3	97.3 ± 0.4	103.6 ± 0.6	91.5 ± 0.7
σ_1/mm	1.893 ± 0.007	1.540 ± 0.007	1.69 ± 0.01	1.39 ± 0.01
A_2	-	-	11.3 ± 0.6	8.5 ± 0.7
σ_2/mm	-	-	5.6 ± 0.2	5.0 ± 0.3
χ^2/ndf	1997/635	1410/635	884/633	779/633

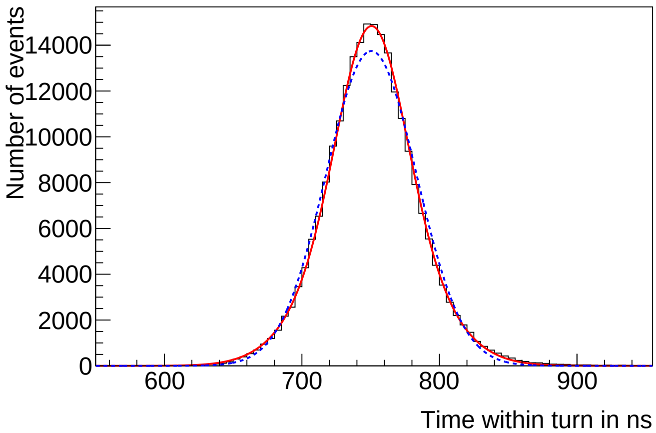

(a)

Figure 6.20: Accumulated detector events recorded in a five second measurement interval with respect to the time within a turn. Fits of a single Gaussian and a superposition of two Gaussian functions have been performed. This allows one to estimate the longitudinal bunch width.

Table 6.3: Fit results for amplitudes and widths of the accumulation of time resolved events.

	Single Gaussian	Double Gaussian
$A_1/10^3$	13.74 ± 0.04	8.4 ± 0.2
σ_1/ns	33.01 ± 0.06	23.9 ± 0.3
$A_2/10^3$	-	6.5 ± 0.2
σ_2/ns	-	39.9 ± 0.2
χ^2/ndf	3428/205	1206/203

double Gaussian function, but the large χ^2/ndf hints to additional systematic effects. The widths can be associated with a momentum spread assuming harmonic oscillations in the longitudinal phase space. The conversion from the time deviation with respect to the center of the bunch to the momentum deviation δ is given by:

$$c_{\Delta t \to \delta} = \frac{2\pi Q_{\mathrm{sync}} f_{\mathrm{rev}}}{\eta_{\mathrm{ph}}} \approx 0.033\,\mathrm{\mu s}^{-1}\ . \tag{6.37}$$

Using the single Gaussian approximation, this leads to an estimated momentum spread of

$$\delta^{1\sigma} = \sigma_\delta \approx 1 \cdot 10^{-4} \ . \tag{6.38}$$

Using this result, the beam emittances can be straightforwardly estimated from the single Gaussian fit of the measured beam profiles. For the radial direction it can be retrieved according to:

$$\varepsilon_x^{1\sigma} = \frac{\sigma_x^2 - D_x^2 \sigma_\delta^2}{\beta_x} \ . \tag{6.39}$$

The values of the betatron functions β_x and β_y and the dispersion function D_x at the location of the beam profile monitor are extracted from model calculations, yielding:

$$\beta_x \approx 21.2\,\mathrm{m} \ , \tag{6.40}$$

$$\beta_y \approx 7.1\,\mathrm{m} \ , \tag{6.41}$$

$$D_x \approx 2.0\,\mathrm{m} \ . \tag{6.42}$$

Taking the single Gaussian approximations, this leads to the following beam emittances:

$$\varepsilon_x^{1\sigma} \approx 0.2\,\mathrm{mm\,mrad} \ , \tag{6.43}$$

$$\varepsilon_y^{1\sigma} \approx 0.3\,\mathrm{mm\,mrad} \ . \tag{6.44}$$

Finally, the induced spin tune changes by path lengthening due to vertical and longitudinal phase space motion can be investigated, making use of Equation 6.15. For that purpose individual particles possessing Courant-Snyder-Invariants and momentum spreads similar to the corresponding RMS beam emittances and the beam momentum spread are compared to each other. In the selected sextupole variation range, the ratio of the spin tune changes induced by vertical and longitudinal phase space motion is given by the quotient of:

$$\Delta \left\langle \left(\frac{\Delta C}{C_0} \right)_\beta \right\rangle = -\frac{\pi}{C_0} \varepsilon_y^{1\sigma} \Delta Q_y' \approx -9 \cdot 10^{-8} \tag{6.45}$$

and

$$\Delta\kappa \cdot \left\langle \left(\frac{\Delta p}{p_0} \right)^2 \right\rangle \approx \Delta\kappa \cdot \frac{1}{2} \left(\delta^{1\sigma} \right)^2 \approx 8 \cdot 10^{-9} \ . \tag{6.46}$$

Here, $\Delta Q_y' \approx 17$ and $\Delta\kappa \approx 1.7$ obtained in the previous section have been used. Hence, the expected variation of the spin tune spread induced by the vertical phase motion is approximately one order of magnitude larger than induced by the longitudinal motion. The contribution from the horizontal phase space is minimized due to an almost vanishing horizontal chromaticity. This validates a direct investigation of the connection between the SCT and the vertical chromaticity, although the absolute contribution of the longitudinal phase space is not determinable, since the value of α_1 could not be obtained from measurements.

6.3.2.3 Spin Coherence Time Measurements at $\mathrm{Q_y} = 3.585$

The spin coherence time strongly depends on the beam emittances and chromaticities. In the following the SCT measurement results at the nominal vertical betatron tune are evaluated. For this purpose a fit function is defined, which is oriented towards the spin tune spread contributions characterized in Section 6.2.2. Since the influences of radial and longitudinal phase space motion are estimated to be substantially smaller than the influence of the vertical one, the fit function is simplified in order to take only the vertical emittance connected to a varying value of the vertical chromaticities into account. This fit function describes the evolution of the envelope of the up-down asymmetry $\hat{\varepsilon}_{\mathrm{UD},p}(n)$ with respect to the number of turns n in the following way:

$$\hat{\varepsilon}_{\mathrm{UD},p}(n) = A_p \cdot \sqrt{P_{\mathrm{r}}(n)^2 + P_{\mathrm{i}}(n)^2} \ , \tag{6.47}$$

$$P_{\mathrm{r}}(n) = \frac{1}{N} \cdot \sum_{j=1}^{N} \cos(\Delta\phi_s^j(n)) \ , \tag{6.48}$$

$$P_{\mathrm{i}}(n) = \frac{1}{N} \cdot \sum_{j=1}^{N} \sin(\Delta\phi_s^j(n)) \ , \tag{6.49}$$

$$\Delta\phi_s^j(n) = \frac{G\gamma_0\beta^2\pi}{\eta_{\mathrm{ph}}C_0} \cdot c_y \cdot \varepsilon_y^j \cdot \left(Q'_y - c_{\mathrm{ir}}\right) \cdot n \ . \tag{6.50}$$

The factor A_p denotes a scaling factor of the normalized initial polarization in the horizontal plane $\sqrt{P_{\mathrm{r}}(n)^2 + P_{\mathrm{i}}(n)^2}$. The value of A_p depends on the polarization state $p \in \{1, 2\}$. The polarization is calculated by averaging over N "particles" representing this beam. Each particle j possesses a characteristic spin-phase-advance deviation $\Delta\phi_s^j(n)$, which depends linearly on the turn number. Up to this point, this function is similar to the template function generation given in [125, 151]. The characteristic spin-phase-advance deviation $\Delta\phi_s^j(n)$ used in the analysis presented here, is directly related to the contributions illustrated in Section 6.2.2. The chromaticity measurement results a used to preset the value of Q'_y for each particular run fitted. In presence of intrinsic resonances, the minimum spin tune deviation does not necessarily coincide with zero chromaticity, as illustrated during the theoretical discussion. This is taken into account by introducing an additional parameter c_{ir}.

The Courant-Snyder-Invariant ε_y^j of an individual particle in vertical phase space varies. The corresponding distribution has been generated assuming a Gaussian distribution of the vertical amplitudes y of the beam particles. Further assuming uncoupled linear phase space motion, the corresponding maximum amplitude y_{max} follows a Maxwell-Boltzmann-distribution in two dimensions considering the two dimensional vertical phase space. This can be translated to $\varepsilon_y^j \propto y_{\mathrm{max},j}^2$. The probability density function (pdf) for a beam emittance of $\varepsilon_y^{1\sigma} = 1\,\mathrm{mm\,mrad}$ is shown in Figure 6.21. In the fitting process $N = 1000$ particles are used to represent the beam. Their values of ε_y^j are randomly generated according to the shown pdf. The factor c_y is used for a global scaling of the beam emittance. Thus, the functional form is determined by four free parameters $A_1, A_2, c_y, c_{\mathrm{ir}}$.

In the following analysis, the envelopes of the up-down-asymmetries measured in different runs are fitted independently. Consequently, c_y and c_{ir} can not be determined

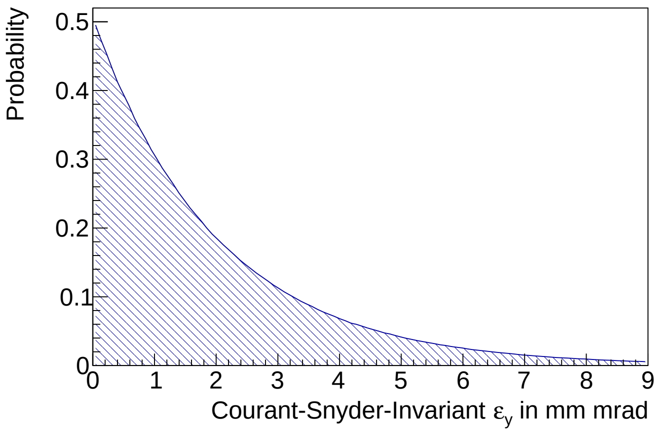

Figure 6.21: Probability density distribution for Courant-Snyder-Invariants of vertical phase space ε_y of individual particles for a beam with a vertical beam emittance $\varepsilon_y^{1\sigma} = 1\,\text{mm}\,\text{mrad}$. Only linear phase space motion and no coupling have been taken into account.

independently, since both lead to a similar scaling of $\Delta\phi_s^j(n)$. For that reason, c_y is used as fitting parameter, while c_{ir} is fixed according to the model estimate shown in Figure 6.12. An exemplary fit result is shown in Figure 6.22. It illustrates, that the defined function is able to describe the evolution of the horizontal polarization. Since, the fall-off is not describable by an exponential function, a threshold definition to estimate the SCT is not obvious. Within this thesis, the SCT is defined as the amount of time, until the normalized envelope drops below $\exp(-0.5) = 60.6\,\%$ of its initial value. Historically, this goes back to a definition according to a Gaussian width of 1σ [125], but it bears two advantages. First, this threshold is crossed in regions, where the phase of the precessing polarization is well known (see Figure 6.16). Second, shorter measurement intervals are sufficient to determine the SCT. The fitting routine to extract the SCT estimate consists of several steps. First, the best estimates of A_1, A_2 and c_y are determined by a simultaneous fit to the data of both polarization states. In the next step, the scaling parameters A_1 and A_2 are fixed at their best estimates

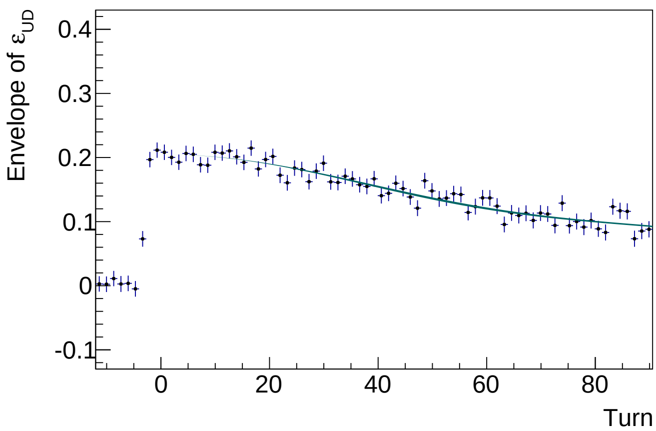

Figure 6.22: Exemplary fit result using the fit function defined in Equation 6.47. The small band shows an 1σ-confidence interval for fixed amplitude scaling factors.

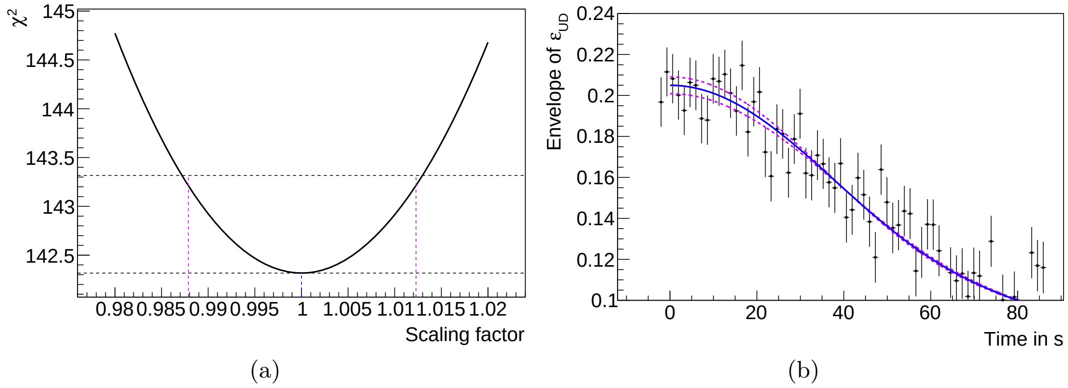

Figure 6.23: Variation of the amplitude scaling factors to obtain an estimate for the uncertainty of the extracted spin coherence time. Figure (a) shows the χ^2 for different values of the scaling factors. Figure (b) depicts the best fit (solid line) and the fit results obtained for an χ^2 increased by one (dashed lines).

to determine the confidence interval for the envelope fall-off depending on c_y. This constant level of the scaling parameters is required, since assuming a threshold of 100 % instead of 60.6 % would be used, the SCT is independent from the uncertainties of the fitted scalings. The resulting 1σ-confidence band is also shown in Figure 6.22. The intersection of the fitted function and the edges of its confidence band yield an estimate of the SCT and its corresponding uncertainty. The impact of the scaling parameter uncertainties on the SCT value is investigated by a different method. For that purpose, the fixed values of A_1 and A_2 are scaled until the resulting χ^2 of a new fit increases by one. This is exemplarily shown in Figure 6.23. The dashed curves in the right figure correspond to the best fits for a scaled amplitude. For each of them, the time until the envelope reaches 60.6 % of its new initial value is extracted and used as a second uncertainty estimate. In the following, the larger uncertainty of both contributions is used as estimate of the SCT uncertainty.

An overview of all fit results using the first polarization state of the run set taken at nominal tune of $Q_y = 3.585$ is shown in Figure 6.24. For illustration the initial horizontal polarization has been normalized using the best estimate of A_1 of each run. The fit results show a very good agreement for all different sextupole settings. A further improvement could not be achieved by replacing the probability distribution function of the emittances shown in Figure 6.21 by one taking the double Gaussian shape of the measured beam profiles into account (see Figure 6.19). With the modified emittance distribution a steep fall-off at early times is introduced, which is caused by the larger phase space amplitudes. Thus, this approach has not been further considered within this thesis.

Applying the described method to determine the SCT, the spin coherence time τ and its reciprocal is extracted for each sextupole configuration. The results are summarized in Figure 6.25. The maximum SCT is observed at $k_{2,\mathrm{MXS}} = 2.34\,\mathrm{m}^{-3}$. At this setting, no horizontal polarization loss occurred during the measurement interval. Consequently, the analysis algorithm suggests a nearly infinite SCT. A proper estimation of the uncertainty based on this algorithm fails at this location. Also, large uncertainties for SCTs of several hundred seconds based on a measurement interval of only 100 seconds

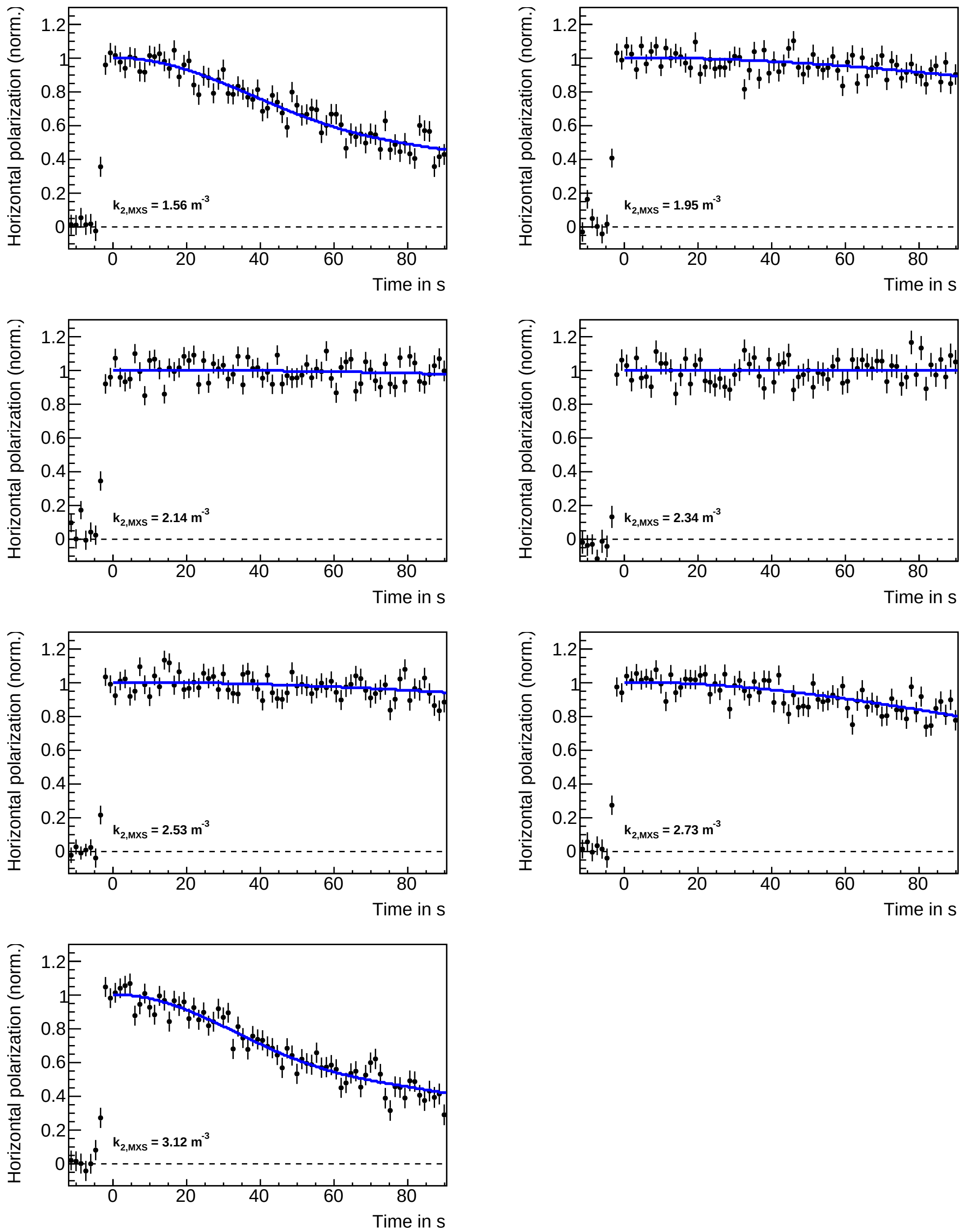

Figure 6.24: Overview of the horizontal polarization decay with respect to different sextupole settings measured at a nominal tune of $Q_y = 3.585$. The best fits are shown as solid curves. The initial horizontal polarization of each run was normalized to unity.

are expected due to the required extrapolation of the fit function. This is directly seen for the second largest SCT value in Figure 6.25. A longer measurement interval is required for a better estimation as discussed later. However, the measurement results can be used to verify the model calculations. The measured vertical chromaticity for the maximum SCT amounts to $\Delta Q'_{y,\text{meas}}(k_{2,\text{MXS}} = 2.34\,\text{m}^{-3}) = 0.29 \pm 0.07$. Considering the neighboring measurement results, the optimum $\Delta Q'_{y,\text{meas}}$ tends to be

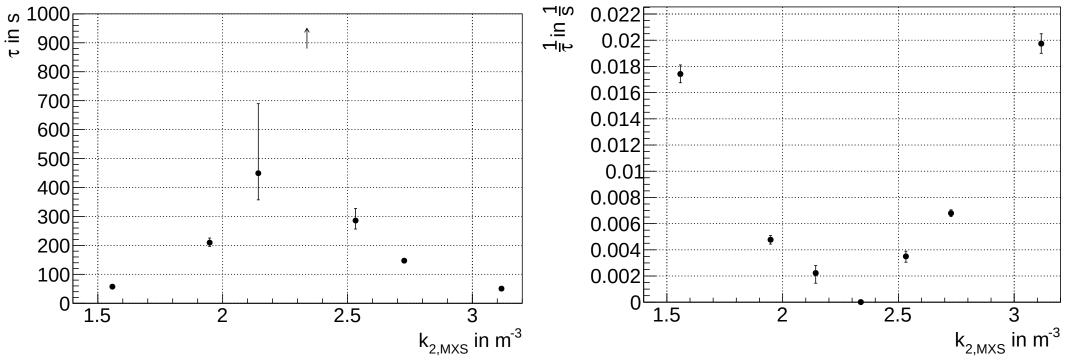

(a) (b)

Figure 6.25: Extracted spin coherence times τ, defined as time when the polarization has fallen below 60.6 % of its initial amplitude, for different sextupole settings. The right figure illustrates the reciprocal of the SCT. The algorithm applied for SCT extraction estimates an infinite SCT at $k_{2,\mathrm{MXS}} = 2.34\,\mathrm{m}^{-3}$ and also error intervals well above the axis range shown. This point is indicated by a small arrow.

at a slightly smaller sextupole strength. The model calculation predicts $\Delta Q'_{y,\mathrm{mod}} = \xi_y \cdot Q_y \approx 0.18 \cdot 3.585 = 0.65$ as the optimum value. Compared to the measured chromaticities at the neighboring points $\Delta Q'_{y,\mathrm{meas}}(k_{2,\mathrm{MXS}} = 2.14\,\mathrm{m}^{-3}) = -1.86 \pm 0.07$ and $\Delta Q'_{y,\mathrm{meas}}(k_{2,\mathrm{MXS}} = 2.53\,\mathrm{m}^{-3}) = 2.45 \pm 0.07$ the observed deviation between measurement and simulation is small. Different sources for the existing deviation can be noted: First, uncertainties present in the lattice model, which have been already observed during the benchmarking process, could introduce slightly different intrinsic resonance strengths. They would shift the optimum chromaticity value predicted by the model calculation. Second, an off-centered beam in sextupoles introduce betatron tune variations for different sextupole configurations. In the measurements, this changes were compensated by tiny adjustment of the quadrupole strengths. Third, a drift of the machine chromaticities during the SCT measurements, as well as a widening of the beam during the cycle has not been taken into account and could lead to further systematic shifts. However, the model fully satisfies the aim to find the required machine parameters for a long SCT. Furthermore, it validates the theoretically derived and simulated contributions to the spin tune spread.

The estimated vertical beam emittance amounts to $\varepsilon_y^{1\sigma} \approx 0.3\,\mathrm{mm\,mrad}$. This value can be compared to results of the fit parameter c_y, which has been determined from the measured polarization data. Figure 6.26 shows the values for the runs with different sextupole settings. The run with the longest SCT at $k_{2,\mathrm{MXS}} = 2.34\,\mathrm{m}^{-3}$ has been excluded due to the “infinite” SCT. The larger error bars for measurements close to this setting reflect the greater uncertainties at large SCTs. Four out of the six fits yield values $\varepsilon_y^{1\sigma} \approx 0.23$ to $0.33\,\mathrm{mm\,mrad}$. The two values near $k_{2,\mathrm{MXS}} = 2\,\mathrm{m}^{-3}$ amount to a factor of two smaller emittances. These two runs and the one with the longest SCT were taken at last in corresponding measurement series. Thus, a suitable drift of the machine could have introduced a bias to the SCT measurement and the extraction of the optimum point. A misconfigured parameter c_{ir} in the fitting function can introduce a bias to extracted vertical emittances. Tests reveal, that this bias is not sufficient to explain the deviation by a factor 2. Additional contributions not included in the

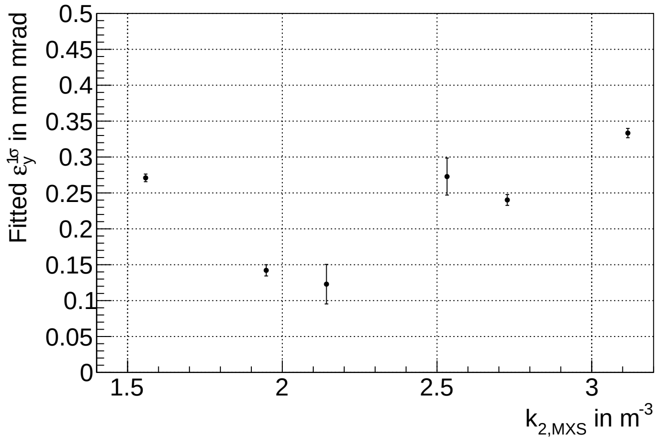

Figure 6.26: Results for the fit parameter c_y, which corresponds to the vertical RMS beam emittance.

simplified fit function might lead to a variation of the extracted vertical emittances. A similar parabolic behavior is also observed for other measurement series and requires a more detailed investigation.

An additional measurement using the sextupole settings that provide the longest SCT has been performed. For this purpose a longer measurement period of about 700 s was set up. The initial period of the cycle containing electron cooling, orbit correction and polarization flip to the horizontal plane were preserved. A continuous detector rate demanded the reduction of the vertical heating amplitude. Figure 6.27 shows the results obtained in this measurement. The right figure depicts the fitted phase of the up-down-asymmetry obtained for one cycle of this run. This reveals,

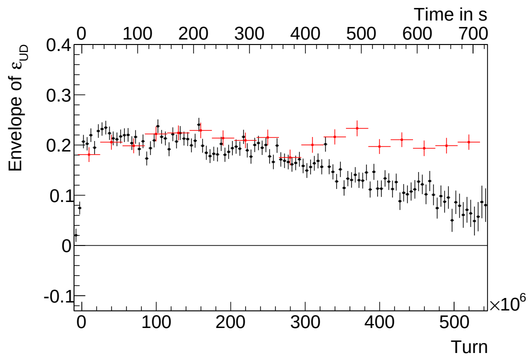

(a)

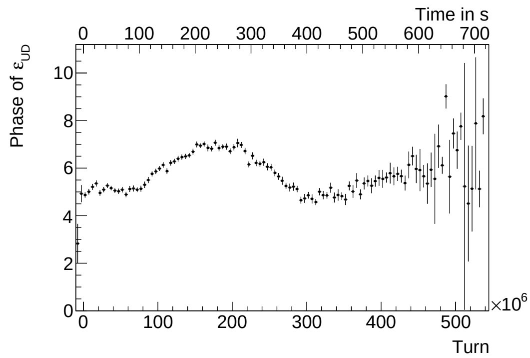

(b)

Figure 6.27: Figure (a) illustrates the envelope of the up-down-asymmetry for runs with extended measurement interval at the optimum sextupole setting $k_{2,\mathrm{MXS}} = 2.34\,\mathrm{m}^{-3}$ obtained from Figure 6.25. The black points correspond to an initial electron cooling time of 75 s, while for the red points cooling was turned on for the whole cycle. Due to limited measurement time, only one cycle was available for the particular run with continuous cooling. Figure (b) depicts the estimated phase of the up-down-asymmetry measured in one cycle of the run with initial cooling of 75 s. It is no longer describable by a second order polynomial.

that the phase no longer varies according to a second order polynomial on this time scale. Thus, a fixing of the phase has not been performed to extract the evolution of the envelope. Instead, the fitting results based on a variable phase are shown in the left figure. The black points correspond to an average over all cycles of this run at $k_{2,\mathrm{MXS}} = 2.34\,\mathrm{m}^{-3}$ with the initial electron cooling duration of 75 s. The horizontal polarization, preserved for about 150 s, starts to drop rapidly at later times. A spin coherence time of approximately 450 s is observed. This underlines the limited prediction power of measurement intervals of only 100 s for SCTs beyond several hundred seconds, as discussed earlier. Additional runs performed at the neighboring sextupole configurations $k_{2,\mathrm{MXS}} = 2.14\,\mathrm{m}^{-3}$ and $k_{2,\mathrm{MXS}} = 2.53\,\mathrm{m}^{-3}$ also provide smaller SCTs than estimated in the shorter measurement periods, but $k_{2,\mathrm{MXS}} = 2.34\,\mathrm{m}^{-3}$ is still close to the optimum sextupole setting providing the longest SCT. However, the beam widths and the momentum spread increase as soon as the electron cooling force is turned off. Since the spin decoherence strongly depends on these quantities, an increased decoherence is expected at later times. This statement is supported by an additional measurement with continuous electron cooling during the entire cycle as shown in red in Figure 6.27. This configuration provides a measured polarization, which is preserved significantly longer. Here, also an additional phase space mixing process introduced by electron cooling might increase the SCT, but the verification demands a more detailed simulation study. Unfortunately, only one cycle was recorded for the continuous electron cooling setup with this sextupole configuration, since this run was taken at the very end of the requested beam time.

6.3.2.4 Spin Coherence Time Measurements at $\mathbf{Q_y = 3.86}$

For verification of the model predictions presented in Figure 6.12, a second measurement series was conducted at a vertical betatron tune of $Q_y = 3.86$. The right graphs of Figure 6.18 illustrate the different sextupole values of the MXS family used for this measurement series. The envelopes of the up-down-asymmetries are fitted by the same functional form as described in the previous section. Figure 6.28 depicts the overview of the fit results for the first polarization state. In the runs with fastest decohering polarization, the shape of the fitted curve deviates from the data points, while at small decoherence, the evolution of the normalized distribution can be well explained by the selected function. Around $k_{2,\mathrm{MXS}} = 3.16\,\mathrm{m}^{-3}$ the largest SCT values are observed. For a closer investigation, three runs around this MXS sextupole strength have been taken with a tripled measurement period. Here, the modification of the cycle setup also requires a reduction of the heating noise used to establish a continuous detector rate. Figure 6.29 illustrates the evolution of the horizontal polarization for these runs. The fit function still provides a good description of the measured data for the increased range. The corresponding SCT values are obtained using the same algorithm as in the previous section. The resulting SCT values are shown in Figure 6.30. The black circles depict the SCT estimates obtained in the shorter measurement periods, while the red squares belong to the longer measurement periods. The points taken at longer periods reveal a significantly shorter spin coherence time in comparison with the measurements at shorter periods and with similar settings. Also in a direct comparison of the data points, the normalized polarization drops significantly faster in the first 80 s measurement time for the longer measurement periods. This could be caused due to the variation of the measurement configuration. The prolongation of the cycle leads

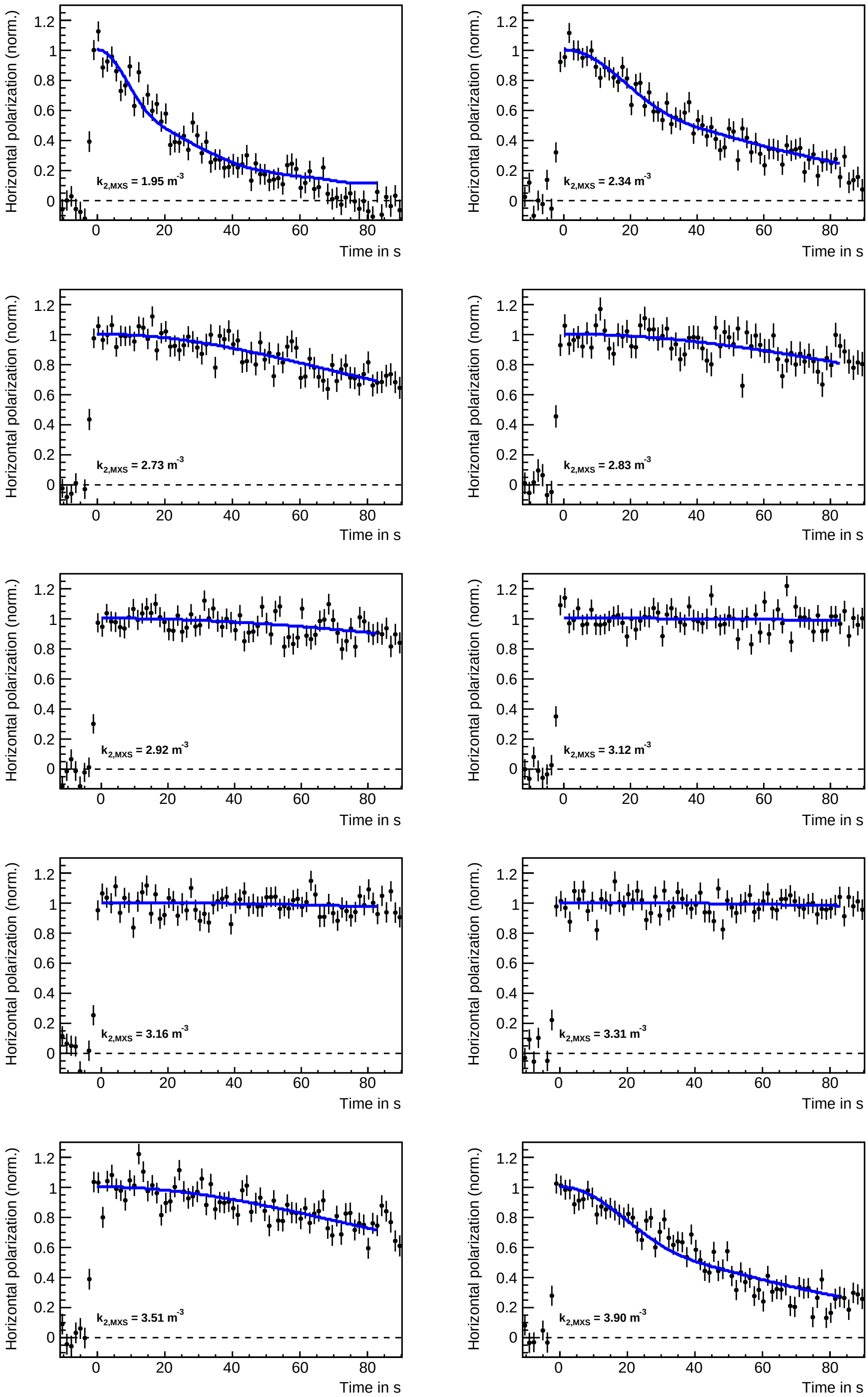

Figure 6.28: Overview of the horizontal polarization decay with respect to different sextupole settings measured at a vertical betatron tune of $Q_y = 3.86$ and a measurement interval of about 80 s. The best fits are shown as solid curves. The initial horizontal polarization of each run was normalized to unity.

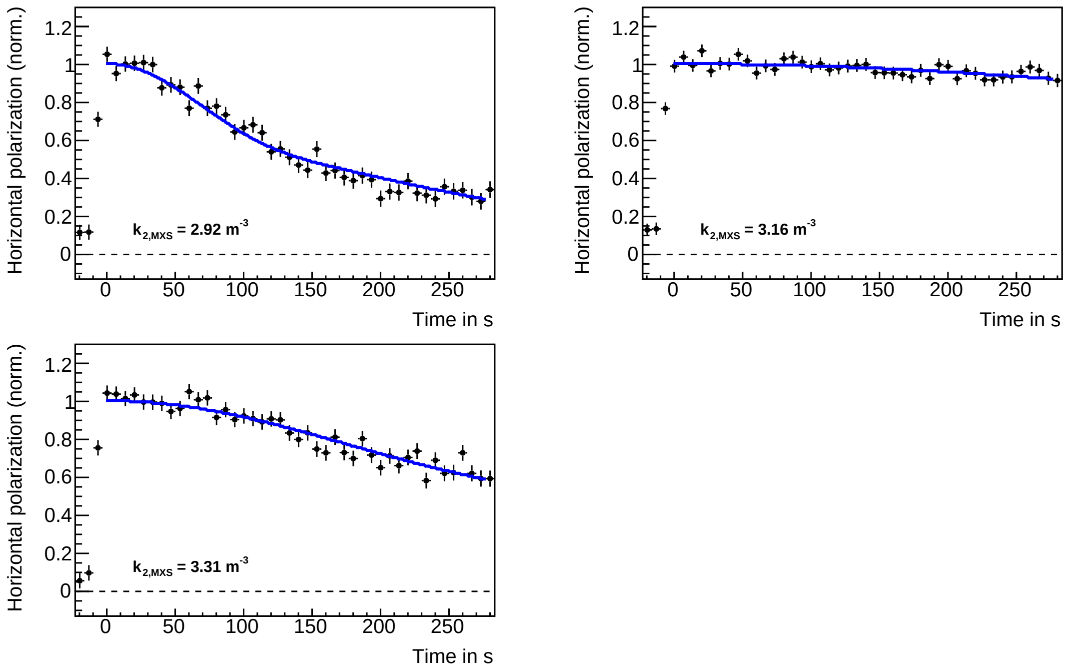

Figure 6.29: Overview of the horizontal polarization decay with respect to different sextupole settings measured at a vertical betatron tune of $Q_y = 3.86$ and a measurement interval of about 270 s. The best fits are shown as solid curves. The initial horizontal polarization of each run was normalized to unity.

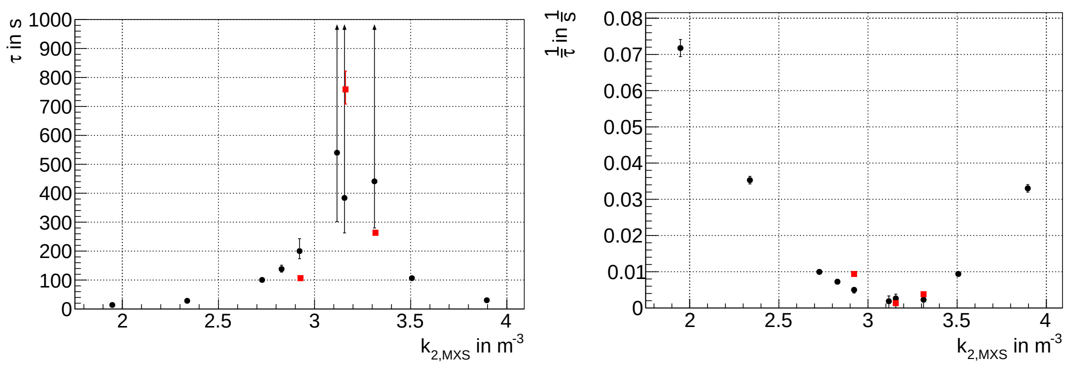

(a) (b)

Figure 6.30: Extracted spin coherence times τ measured for different sextupole settings at betatron tune $Q_y = 3.86$. The right figure illustrates the reciprocal of the SCT. The black circles correspond to runs with a shorter, the red squares belong to runs with a longer measurement intervals. The algorithm applied for SCT extraction estimates a maximum SCT at about $k_{2,\mathrm{MXS}} = 3.16\,\mathrm{m}^{-3}$.

to different timings for the magnet ramps. An impact on the chromaticities arising from the magnetic hysteresis of the dipole magnets has already been observed, but the order of magnitude of this effect still needs to be clarified in further investigations. Additionally a potential machine drift leaving the zero horizontal chromaticity setting could introduce a decrease of the spin coherence time. Also the impact of a strength variation of the vertical noise needs a detailed study to clarify the origin of the SCT decrease. Different vertical distances between the target location and the beam center, which influence on the required vertical heating power to establish the detector event rate, already showed a clear impact on the SCT. In these studies, a decreasing SCT was observed for larger target distances, if the contribution from vertical phase space motion is not perfectly compensated by the sextupole settings. After the discussion of potential systematic effects, the comparison of measurements and model calculations is examined. In the data set connected to the vertical betatron tune of $Q_y = 3.86$, the maximum SCT is observed at $k_{2,\mathrm{MXS}} = 3.16\,\mathrm{m}^{-3}$ and corresponds to

$$\tau = 759^{+63}_{-51}\,\mathrm{s}\ . \tag{6.51}$$

The same order of magnitude has been also observed during a 1500 s measurement period using a precooled beam [152]. Taking also the neighboring points into account, the optimum sextupole strength is approximately $k_{2,\mathrm{MXS}} = 3.2\,\mathrm{m}^{-3}$. This value corresponds to a vertical chromaticity of $\Delta Q'_{y,\mathrm{meas}} = 4.4 \pm 0.2$ in comparison to a model calculation of $\Delta Q'_{y,\mathrm{mod}} \approx 1.29 \cdot 3.86 = 4.98$. This confirms that a long spin coherence time can be obtained at a non vanishing vertical chromaticity as predicted by model calculations. These calculations slightly exceeds the approximated measurement value similar to the result obtained for the nominal tune $Q_y = 3.585$, but still provide a very good estimate of the required sextupole configuration.

6.4 Summary

In this chapter, two sources of spin decoherence, namely the impact of path lengthening and intrinsic resonances, have been discussed. The theoretical derivations were supported by numerical simulations based on the benchmarked COSY model. A strong connection between the spin coherence time and the beam chromaticities and second order momentum compaction factor has been pointed out. The values of these parameters required in order to achieve a long spin coherence time have been calculated for the experimental setup at COSY using a deuteron beam with a momentum of 970 MeV/c. Measurements were conducted to verify these predictions for different vertical betatron tunes. SCTs of of several hundred seconds were achieved at parameter values close to the predicted beam chromaticities. This achievement provides a mandatory requirement of the RF Wien filter method for EDM measurements in the COSY storage ring.

Chapter 7

Spin Resonances Induced by a Radiofrequency Solenoid

7.1 Motivation

EDM measurements based on the RF Wien filter method are planned to be performed at the COSY storage ring. In this method an artificial spin resonance is created, whose resonance strength is proportional to the magnitude of an EDM. This resonance induces a tiny buildup of the vertical polarization used as measurement signal. A long SCT is required to preserve the polarization, which initially precesses perpendicular to the spin closed orbit of the static ring. SCTs of several hundred seconds could be achieved for a pre-cooled beam in measurements presented in the previous chapter and provide the desired order of magnitude for the planned experiments. The study of systematic contributions of this method requires the simulation of RF fields. New algorithms to simulate RF fields have been recently implemented into COSY INFINITY as described in Chapter 5. To validate these algorithms, benchmarking with analytical predictions and measurement results needs to be performed, before an investigation of the the RF Wien filter method can be carried out. Artificial spin resonances induced by an RF solenoid introduce an oscillation of the vertical polarization and serve as a perfect test scenario for these algorithms, which could be examined in measurements at COSY. The behavior of the vertical polarization oscillation in presence of synchrotron oscillations has already been studied in [153, 154]. In these references, the oscillation of the momentum deviation has been taken into account, which leads to a variation of the spin phase advance per turn and reduces the resonance strength for the individual particle. This resonance strength is proportional to the oscillation frequency of the vertical polarization. Thus, the vertical spin component of individual particles oscillate with a different frequency, which leads to a reduction of the vertical polarization of the beam over time. In further calculations also the variation of the time of arrival of the individual particle at the location of the RF solenoid shows an important impact on the resonance strengths [155, 156, 93]. This includes a significant dependence of the oscillation frequency of the RF field on the polarization behavior . The underlying theory, which takes both effects into account, is presented in the next section. It adapts the results given in [155, 156] and strongly benefited from internal discussions [93, 94] Experimental studies at different solenoid spin resonance frequencies have been performed and are described afterwards. The benchmarking results of the algorithms implemented into the numerical tracking applications are illustrated at the end of this chapter.

7.2 Resonance Strength Variations due to Synchrotron Motion

This section illustrates the theoretical considerations for deuterons, which perform synchrotron oscillations in an ideal magnetic storage ring. The following derivation makes greater use of the formulas presented in the Sections 3.2.7.2, 3.2.7.3 and 3.2.8.2. In case an RF longitudinal field is turned on at a spin resonance frequency (Equation 3.192), an artificial spin resonance is created. The resonance strength of the reference particle is given by Equation 3.206:

$$|\epsilon_K| = \frac{\alpha_0}{4\pi} \ . \tag{7.1}$$

Here, the values for a vertical spin closed orbit of the static ring ($\vec{n} = \vec{e}_3$) and a longitudinal RF field ($\vec{m} = \vec{e}_2$) have been applied. The maximum spin rotation angle in the solenoid per pass $\alpha_0 = \alpha_{\text{sol}}$ has been defined in Equation 3.195. Note, that the derivation of Equation 7.1 is based on a set of preconditions. First, the resonance strengths is assumed to be significantly smaller than the spin precession frequency: $|\epsilon_K| \ll G\gamma_0$. Second, the resonance tune $K = \nu_{\text{sol}}$ is not a ratio of two rational numbers, with a small denominator. This allows one to approximate the RF solenoid spin perturbation by

$$\xi = |\epsilon_K| e^{-i\nu_{\text{sol}}\theta} \tag{7.2}$$

considering scales of several million turns.

In the next step, the derivation is extended for the study of synchrotron oscillations. The oscillations of the time deviation $\tau \equiv \Delta t$ and momentum deviation δ in the longitudinal phase space can be approximately expressed by:

$$\tau = \tau_{\text{max}} \sin(Q_{\text{sync}}\theta + \varphi) \ , \tag{7.3}$$

$$\delta = \hat{\delta} \cos(Q_{\text{sync}}\theta + \varphi) \ . \tag{7.4}$$

Here, a restoring force of the RF cavity linear in τ leads to phase space motion according to a harmonic oscillator. The amplitudes τ_{max} and $\hat{\delta}$ are connected by the relation (Equation 6.37):

$$\hat{\delta} = -\frac{2\pi Q_{\text{sync}} f_{\text{rev}}}{\eta_{\text{ph}}} \tau_{\text{max}} \ . \tag{7.5}$$

To calculate a variation of the resonance strength, the impact of synchrotron oscillations on spin motion is considered. As previously discussed the momentum oscillation introduces an oscillation of the spin precession rate (see Equations 3.182 and 3.183). The spin phase advance of the precession about the spin closed orbit in an unperturbed static ring can be expressed as:

$$\int_0^\theta G\gamma \mathrm{d}\theta = G\gamma_0\theta - \frac{2\pi G\gamma_0\beta_0^2 f_{\text{rev}}}{\eta_{\text{ph}}} \tau_{\text{max}} \left[\sin(Q_{\text{sync}}\theta + \varphi) - \sin(\varphi)\right] . \tag{7.6}$$

This changes the spin directions of various particles. A second effect arises from the variation of the time of arrival at the solenoid due to the oscillation of τ. Thus, the spins of the individual particles are affected by a different amount during the same turn due to the time-varying field. The time-dependent field strength of the solenoidal field is given by:

$$\begin{aligned} B_{\text{sol}} &= \hat{B}_{\text{sol}} \cos(\omega_{\text{sol}}(t+\tau)+\phi) \\ &= \hat{B}_{\text{sol}} \cos(\omega_{\text{sol}}(t+\tau_{\max}\sin(Q_{\text{sync}}\theta+\varphi))+\phi) \\ &= \hat{B}_{\text{sol}} \cos(\nu_{\text{sol}}\theta+2\pi\nu_{\text{sol}}f_{\text{rev}}\tau_{\max}\sin(Q_{\text{sync}}\theta+\varphi)+\phi)\ . \end{aligned} \tag{7.7}$$

Several ways are accessible to incorporate these two effects for the study of the spin perturbations. One opportunity is to include these effects into the spinor equation given in Equation 3.197. Here, the spin tune ν_s has to be replaced by $G\gamma$ taking the energy oscillation due to synchrotron motion into account. Furthermore, the definition of the parameter $\nu_o(\theta)$ (see Equation 3.198) needs to include the contribution of the oscillating field. This requires a modification of the term $\nu_{\text{rf}}\theta \equiv \nu_{\text{sol}}\theta$ taking the full argument of the cosine in Equation 7.7 into account. The solution of this equation includes the additional contribution induced by synchrotron motion. The same result can be obtained by using the formalism presented in Section 3.2.7.2, which discusses the synchrotron sideband resonances. This particular approach is discussed in the following. The perturbing term of the spinor equation is given by:

$$\xi = |\epsilon_K| \cdot \exp\left(-i\left[\nu_{\text{sol}}\theta+2\pi\nu_{\text{sol}}f_{\text{rev}}\tau_{\max}\sin(Q_{\text{sync}}\theta+\varphi)+\phi\right]\right)\ . \tag{7.8}$$

Here, the oscillating solenoidal field is represented by a variation of the phase defined in the complex exponential function. A further modification introduced by synchrotron oscillations is also incorporated. Applying the transformation into the interaction picture, the driving term of the spinor equation can be expanded into a Fourier series according to:

$$\begin{aligned} &|\epsilon_K| \cdot e^{-i(\nu_{\text{sol}}\theta+2\pi\nu_{\text{sol}}f_{\text{rev}}\tau_{\max}\sin(Q_{\text{sync}}\theta+\varphi)+\phi-\int_0^\theta G\gamma\mathrm{d}\theta)} \\ &\quad = \sum_{m=-\infty}^{\infty} e^{-i\tilde{\phi}}|\epsilon_K|J_m(g)e^{-i(\nu_{sol}-G\gamma_0-mQ_{\text{sync}})\theta} \\ \text{with}\qquad & \tilde{\phi} = \phi + \frac{2\pi G\gamma_0\beta_0^2 f_{\text{rev}}}{\eta_{\text{ph}}}\tau_{\max}\sin(\varphi) - m\varphi \\ \text{and}\qquad & g = \left(-\frac{G\gamma_0\beta_0^2}{\eta_{\text{ph}}} - \nu_{\text{sol}}\right)\cdot 2\pi f_{\text{rev}}\tau_{\max}\ . \end{aligned} \tag{7.9}$$

In the following, only resonance strengths $|\epsilon_K| \ll Q_{\text{sync}}$ are considered. Thus, only the mode $m = 0$ leads to a significant contribution to spin motion, if the resonance condition $\nu_{\text{sol}} = G\gamma_0 + k, k \in \mathbb{Z}$ is fulfilled. Similar to Section 3.2.7.2, the resonance strength is modified by a Bessel function:

$$\tilde{\epsilon}_K = \epsilon_K J_0(g)\ , \tag{7.10}$$

but this time it also depends on the resonance tune of the solenoid ν_{sol}. Inserting the spin resonance condition yields:

$$g = \left[G\gamma_0\left(-\frac{\beta_0^2}{\eta_{\text{ph}}} - 1\right) - k\right]\cdot 2\pi f_{\text{rev}}\tau_{\max}\ . \tag{7.11}$$

This reveals a strong connection between the resonance strength and the choice of k, which is defined by the relation between solenoid and spin precession frequencies. Note, that for $g = 0$ the resonance strength is independent of $\tau_{\max}$ and remains unchanged. To examine this effect in more detail, the variation of the vertical spin component is evaluated. Therefore, the results are transferred to Equations 3.224 - 3.226, resulting in:

$$\tilde{S}_1(0) = 1: \quad \tilde{S}_3(\theta) = \cos(\tilde{\phi}) \sin\left(\frac{\alpha_{\text{sol}}}{4\pi} J_0(g) \cdot \theta\right), \tag{7.12}$$

$$\tilde{S}_2(0) = 1: \quad \tilde{S}_3(\theta) = \sin(\tilde{\phi}) \sin\left(\frac{\alpha_{\text{sol}}}{4\pi} J_0(g) \cdot \theta\right), \tag{7.13}$$

$$\tilde{S}_3(0) = 1: \quad \tilde{S}_3(\theta) = \cos\left(\frac{\alpha_{\text{sol}}}{4\pi} J_0(g) \cdot \theta\right). \tag{7.14}$$

Consequently, the oscillation frequency of the vertical spin component ($S_y = -\tilde{S}_3$), which is given by the resonance strength, is modified by the Bessel function term. In case the initial spin vector is perpendicular to the vertical direction, also the phase $\tilde{\phi}$ has to be taken into account. It strongly depends on the phase relations between the spin phase in the horizontal plane, the phase of the solenoid field and the phase of the synchrotron motion of the individual particle, respectively. For an initially vertical spin direction, this phase dependence drops out.

In the experiments to investigate the artificial resonance of an RF solenoid, an initially vertically polarized beam is used. At a defined time in the cycle the solenoid is turned on to activate the resonance and act continuously on spin motion. This induces oscillations of the vertical spin component of the individual particles of the deuteron beam. To calculate the behavior of the vertical polarization, the distribution of the synchrotron amplitudes $\tau_{\max}$ of the particles in the bunch has to be considered. For this particular study, the width of the τ distribution is larger compared to the spin coherence time studies described earlier (see Section 6.3.2.2). The measured widths for different runs using single Gaussian fits vary and are in the order of 70 ns to 85 ns. For a width $\sigma = 75$ ns the calculated $\tau_{\max}$-distribution is shown in Figure 7.1. As mentioned in the

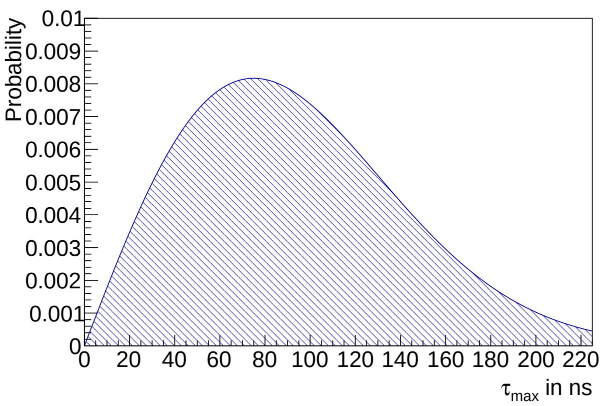

Figure 7.1: Distribution of the maximum amplitude of the time deviation $\tau_{\max}$ with respect to the reference particle. Here, a τ-distribution according to a Gaussian with a width $\sigma = 75$ ns has been assumed. This corresponds to the illustrated Maxwell-Boltzmann-distribution for $\tau_{\max}$ in two dimensions.

previous chapter, it follows a Maxwell-Boltzmann-distribution in a two-dimensional phase space.

The behavior of the vertical polarization is obtained using an ensemble of particles with a randomly distributed synchrotron amplitude τ_{max} according to this distribution. The results of analytical calculations are depicted in Figure 7.2. The upper figure shows the oscillation of the vertical spin component assuming a reference oscillation frequency $f_{\text{osc}} = \frac{\alpha_{\text{sol}}}{4\pi} f_{\text{rev}} = 1\,\text{Hz}$ and different values for τ_{max}. The value $k = -1$ corresponds to the resonance frequency of 871 kHz for a deuteron beam with $p = 970\,\text{MeV/c}$ at COSY, which is set as solenoid frequency. For larger values of τ_{max}, the resonance strength

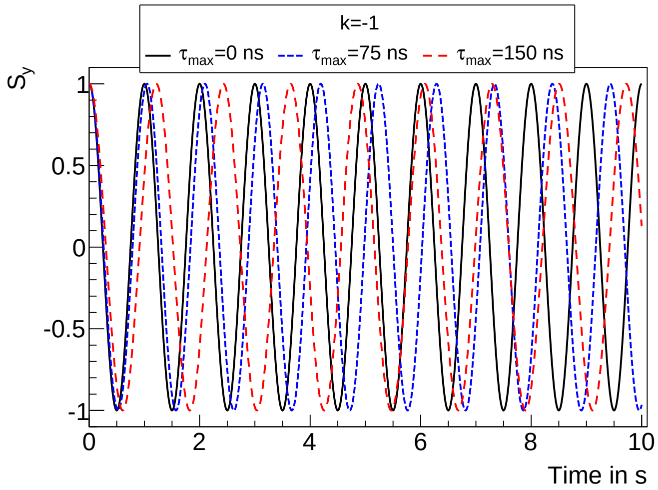

(a)

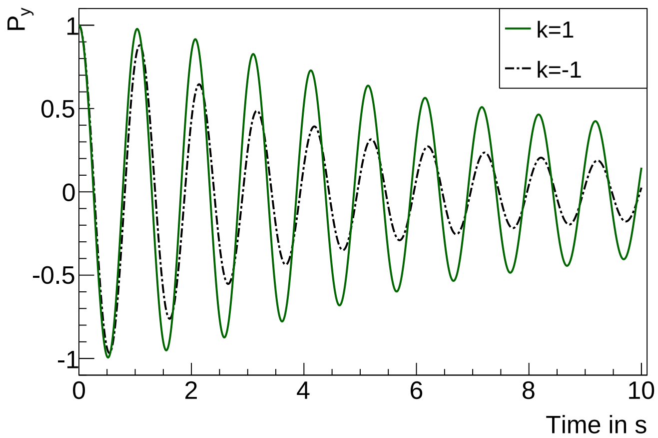

(b)

Figure 7.2: Figure (a) illustrates the calculated oscillation of the vertical spin component for deuterons with different time deviation amplitudes τ_{max} in presence of an RF solenoid. A reference momentum of 970 MeV/c is selected, which corresponds to a revolution frequency of approximately 750 kHz. The solenoidal field oscillates with a frequency of 871 kHz ($k = -1$). Figure (b) depicts the behavior of the vertical polarization in case the spins of a bunch of 1000 particles are considered. The τ_{max}-distribution was randomly selected following a distribution according to Figure 7.1. A second solenoid frequency of 630 kHz ($k = 1$) is shown for comparison.

decreases as expected, which leads to a smaller oscillation frequency with respect to the reference particle. The lower figure shows the calculated vertical polarization behavior for 630 kHz ($k = 1$) and 871 kHz ($k = -1$) using an ensemble of 1000 particles representing the beam. Due to the different oscillation frequencies of individual spins the vertical polarization amplitude decreases over time. Furthermore, the reduction depends on k as expected from Equation 7.11. Intermediate results of this phenomenon based on spin tracking simulations have been already presented in [144].

In the following, the damping time until the envelope of the vertical polarization undercuts a certain threshold is explored. Similar to the spin coherence time studies a threshold level of 60.6 % of the initial vertical polarization is selected. To determine the time period, until this threshold is reached, the envelope of the vertical polarization is examined. For this purpose, the absolute values at the extrema of the oscillating vertical polarization are interpolated. The crossing of the 60.6 % barrier defines the damping time. Since the damping time scales reciprocally with the reference oscillation frequency f_{osc}, the number of oscillations N_{osc}, until this threshold is reached, is characteristic for the combination of the beam reference momentum and the value of k. The obtained results are illustrated in Figure 7.3. For this study, the values of α_0 and Q_{sync} are kept constant over the full momentum range. Furthermore, the τ_{max}-distribution is scaled accordingly in order to take adiabatic damping into account. This reduces the momentum spread at larger reference momenta. This tends to increase the number of oscillations N_{osc} towards larger beam momenta for all values of k. For $k = 1$ and $k = 2$ values of the beam momentum exist, at which the envelope of the vertical polarization is entirely preserved. These momenta correspond to the condition [156]:

$$\left[G\gamma_0 \left(-\frac{\beta_0^2}{\eta_{\text{ph}}} - 1 \right) - k \right] = 0 \ , \tag{7.15}$$

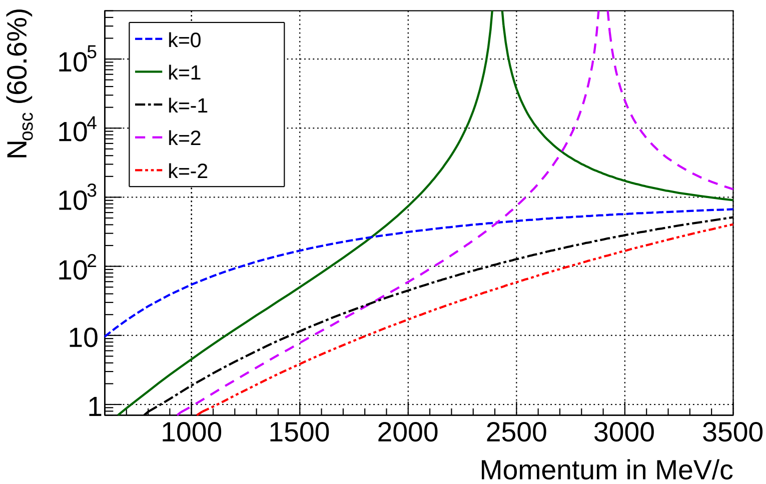

Figure 7.3: Calculated number of polarization oscillations until the vertical polarization envelope reaches a threshold of 60.6 % of its initial value. The figure depicts five different solenoid frequencies characterized by k for different deuteron momenta in the COSY range. A τ-distribution according to a Gaussian with a width $\sigma = 75$ ns has been assumed for the particle bunch at a momentum of 970 MeV/c. Adiabatic damping has been taken into account for the calculation at different momenta.

which is equivalent to $J_0(g) = 1$. Hence, the resonance strengths of all particles are equal and independent of τ_{max}.

7.3 Measurements of the Vertical Polarization Oscillation

In this section, the theoretical predictions are verified using experimental data at a momentum of 970 MeV/c. First, the chosen measurement setup and analysis method are presented.

7.3.1 Measurement Setup and Analysis Method

The deuteron beam setup was similar to the configuration chosen for the SCT studies. Two polarization states possessing opposite vertical vector polarizations and a negligible tensor polarization were used. Various cycles with the same machine configuration but alternating polarization state of the beam were combined to one run. The deuteron beam was injected, accelerated to 970 MeV/c and electron-cooled. A sextupole configuration with long SCT obtained in preceding measurements was selected to minimize the second order contributions described in the previous chapter. After switching off the electron-cooling, the voltage of the RF cavity was non-adiabatically raised to increase the momentum spread of the beam. This aimed for an increase of the vertical polarization damping, which was preferred for these studies. Vertical extraction noise was enabled to produce a continuous scattering event rate. About 10 s after turning on the noise the solenoid was switched on and kept running for a measurement period of about 80 s. Different magnetic field strengths and spin resonance frequencies have been investigated. In the following, the results for three different resonance frequencies 630 kHz ($k = 1$), 871 kHz ($k = -1$) and 1662 kHz ($k = -2$) are compared. Unfortunately, the smallest frequency of 120 kHz ($k = 0$), which promises the longest preservation of the vertical polarization envelope, was not accessible due to the limitations of the resonance circuit layout of the solenoid.

This measurement series was taken in the last week of the fall beam time of 2013. For the study of systematic contributions, two important notes have to be made. First, the vertical heating voltage was set to a fixed value, since the detector rate feedback was not yet available during these runs. Consequently, the event rate was larger at the beginning of each cycle and drops steadily towards the end similar to the beam current measured at the BCT. This rate change could have introduced systematic effects to the measured vertical polarization. Second, while the polarized ion source ran absolutely stable during the first half of the particular beam time, issues with the cesium part of the source lead to several interruptions during this measurement period. Thus, the number of recorded events for the runs at 871 kHz ($k = -1$) is significantly reduced due to a smaller beam current. Furthermore, the solenoid frequency had to be slightly adjusted multiple times during the measurement period to correct for small drifts of the spin tune in COSY and to maintain the spin resonance condition. For larger solenoid frequencies, this maintenance was hard to achieve, which can be observed by polarization oscillations not centered around zero. These runs are filtered and discarded during the data analysis as discussed below.

In each run, the events recorded in the left and right detector quadrants for all cycles running with the same polarization state are accumulated over time. This results in the four event rates $N_{L,1}(t), N_{R,1}(t), N_{L,2}(t)$ and $N_{R,2}(t)$. Here, the subscript letter denotes the detector quadrant, while the number reflects the polarization state. As previously discussed, the left-right-asymmetry of the event rates is proportional to the vertical polarization of the corresponding polarization state as long as the detector acceptances and efficiencies are equal for both quadrants. Otherwise a deviation between the polarization and the measured asymmetry is introduced. This deviation can be canceled at lowest order by calculating a cross-ratio using all four event rates according to [157]:

$$\varepsilon_{\mathrm{CR}} = \frac{\sqrt{N_{L,1} \cdot N_{R,2}} - \sqrt{N_{L,2} \cdot N_{R,1}}}{\sqrt{N_{L,1} \cdot N_{R,2}} + \sqrt{N_{L,2} \cdot N_{R,1}}} \propto \overline{A}_y^{\mathrm{c,L}} \overline{P}_y \ . \tag{7.16}$$

Here, $\overline{P}_y$ denotes the average vertical polarization of both polarization states. The time-dependent cross-ratios have been calculated for all runs of this measurement series. The binning of the event rates has been adjusted according to the expected polarization oscillation frequencies to ensure a reasonable number of bins per oscillation. To obtain the relevant parameters, i.e. oscillation frequency and damping time, the following fit function has been defined:

$$P_y(t) = \begin{cases} n_0 \cdot (1 + c_0) & \text{for } t \leq t_0 \\ n_0 \cdot \left(\frac{1}{N} \sum_{i=1}^{N} S_y^i(t - t_0) + c_0 \right) & \text{for } t > t_0 \end{cases} , \tag{7.17}$$

$$S_y^i(t) = \cos\left(J_0(g_i) \cdot 2\pi f_{\mathrm{osc}} t\right) \ , \tag{7.18}$$

$$g_i = \left[G\gamma_0 \left(-\frac{\beta_0^2}{\eta_{\mathrm{ph}}} - 1 \right) - k \right] \cdot 2\pi f_{\mathrm{rev}} c_\tau \tau_{\mathrm{max}}^i \ . \tag{7.19}$$

Here, n_0 is a normalization parameter and c_0 accounts for an off-resonance behavior, which introduces an offset of the oscillation. The activation time of the solenoid is defined by t_0. The vertical polarization is determined by the sum over the vertical spin components S_y^i. A value of $N = 1000$ particles is used in the fitting process. Each particle possesses an individual value τ_{max}^i, randomly set according to the distribution shown in Figure 7.1. The parameter c_τ allows for a global scaling of the distribution width. The parameter f_{osc} denotes the reference oscillation frequency of the vertical spin component of the reference particle. Overall five fit parameters $n_0, c_0, t_0, f_{\mathrm{osc}}$ and c_τ are obtained by the fitting routine for each run. The other parameters are determined either from theory, i.e. G, model calculations, i.e. η_{ph}, or measurement setup, i.e. $f_{\mathrm{rev}}, k, \gamma_0, \beta_0$. The results based on this analysis routine are discussed in the next section.

7.3.2 Experimental Results

For the analysis the measured cross-ratios are normalized to unity. Exemplary fit results are shown in Figure 7.4 for two different solenoid frequencies (630 kHz ($k = 1$) and 871 kHz ($k = -1$)). In both cases, the oscillation frequencies are comparable. Similar results have been also published in [158]. The decrease of the polarization oscillation amplitudes varies for the different solenoid frequencies as predicted by the theory. As expected, this also increases the number of oscillations in the same time range for $k = 1$ similar to Figure 7.2. The fitting range is limited to the first six oscillation periods. In

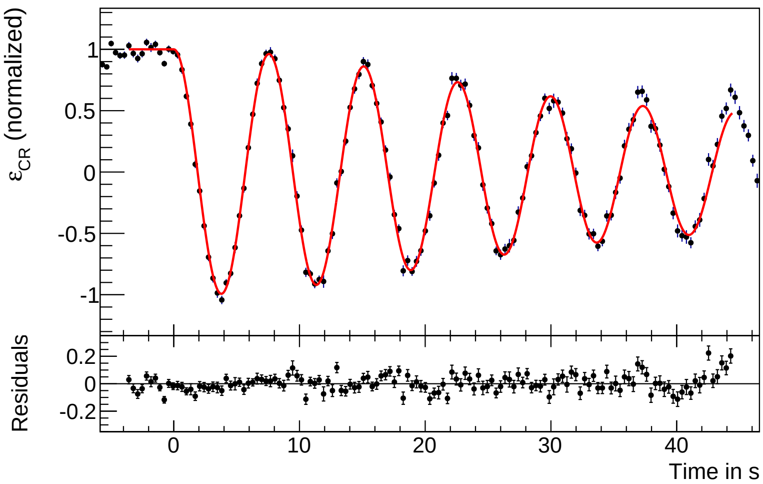

(a)

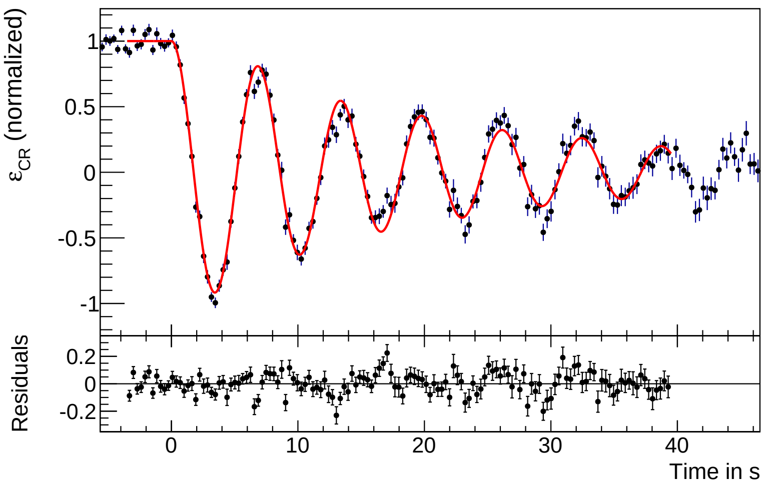

(b)

Figure 7.4: Measured cross-ratios (normalized) for two runs with different solenoid frequencies of 630 kHz ($k = 1$) (a) and 871 kHz ($k = -1$) (b), but approximately the same solenoid field strengths. The solenoid was turned on at 0 s, when the vertical polarization starts to oscillate. Fits according to Equation 7.17 have been performed (red line). The residuals of the fits are shown below the graphs, respectively.

this range the fit function describes the polarization behavior sufficiently well. The deviations between measurement and theoretic curve increase at later times. Here, the run at $k = -2$ illustrated in Figure 7.5 serves as a prominent example. At later times, the oscillation amplitude is significantly larger in comparison to the description of the fit function. This behavior could be caused by a real τ-distribution, which deviates from the description by a single Gaussian function. For example, tails with larger values of τ lead to a steeper polarization fall off at the beginning, while a smaller core preserves the polarization amplitude for a longer time. In order to still retrieve a proper estimate for the damping time the fitting range is reduced to approximately three oscillation periods for the solenoid frequency of 1662 kHz ($k = -2$).

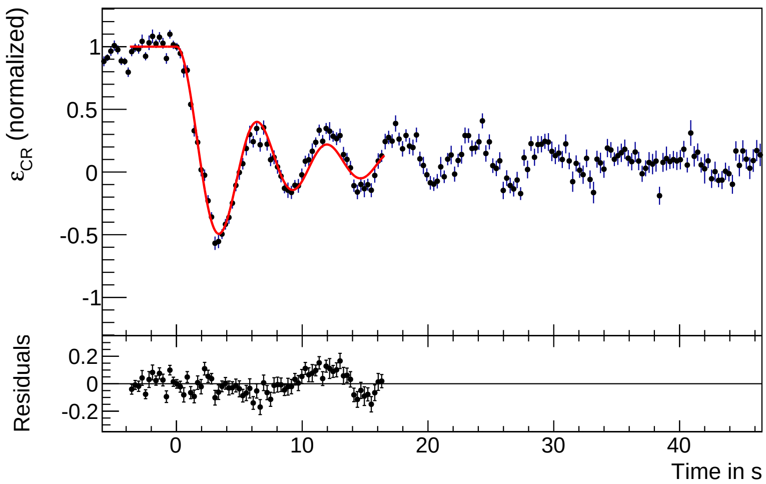

Figure 7.5: Example for a measured cross-ratio (normalized) for a runs with a solenoid frequency of 1662 kHz ($k = -2$). A fit according to Equation 7.17 has been performed and is illustrated as the red line. The fit interval is restricted to the first three oscillation periods.

To validate the fit results, the relation between the the estimated reference oscillation frequencies and the input values, which control the RF solenoid strength, is evaluated. In the used operational range, a linear relation between the input value and the resulting magnetic field strength was determined in preceding studies [159, 160]. This linear relation is also expected between the input value and the resulting reference oscillation frequency. Figure 7.6 depicts the reference oscillation frequency with respect to different input values and solenoid frequencies. The runs for which the fit returns an offset parameter $c_0 > 0.2$ are discarded, since they posses large off-resonance contributions,

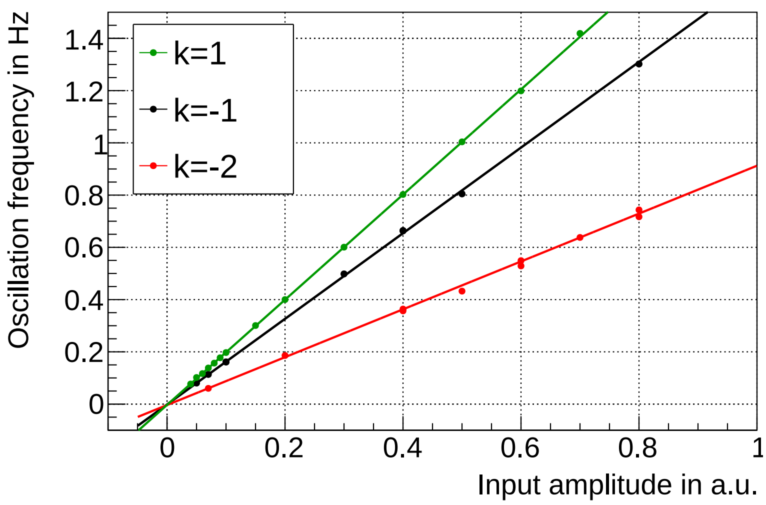

Figure 7.6: Fitting results of the oscillation frequency defined for the reference particle shown for different solenoid frequencies characterized by k and for different input values of the RF solenoid. The colored lines illustrate linear fits for the different frequencies, respectively. The runs, for which the fit hints towards an off-resonance setup of the solenoid, have been discarded.

which bias the results. For the remaining runs, the expected linear behavior is observed and is characterized by a linear fit. The different slopes reflect the variation of the field strengths for the same input value, but different resonance frequencies. Since the resonance circuit of the solenoid is primarily designed for frequencies below 1 Mhz, the resulting field amplitudes decrease at higher frequencies. The observed linear relations underline the quality of the fits.

Finally, the damping time is extracted from the fit function using the interpolation of the extrema, as described previously. In Figure 7.7 the obtained values of the damping time with respect to the different oscillation periods $1/f_{\mathrm{osc}}$ and the different solenoid frequencies are shown. The colored markers depict the data points, while the colored lines correspond to analytical calculations. For this comparison, the Gaussian width of τ assumed in the calculations is slightly increased to $\sigma = 90\,\mathrm{ns}$. For illustration, also impact of variations of the Gaussian width by $\pm 10\,\%$ is represented by the colored bands. Under these conditions, the theoretical predictions are in good agreement with the damping times for different solenoid frequencies. Thus, the predicted influence of the solenoid frequency on the damping time could be confirmed. The damping times obtained for $k = -2$ are smaller than one oscillation period. Most of the runs taken with larger oscillation periods at this solenoid frequency are plagued by off-resonance effects and are discarded in this analysis. The damping time of the runs with $k = 1$ and $k = -2$ show a slight increase with respect to the theoretical estimate for larger oscillation periods. Here, additional systematic effects arise from a variation of the τ distribution throughout the particle store and the different detector rates for early and late times in the cycle as discussed previously. Those contributions are not considered in the error bars presented in Figure 7.7. Further studies are required to estimate their impact.

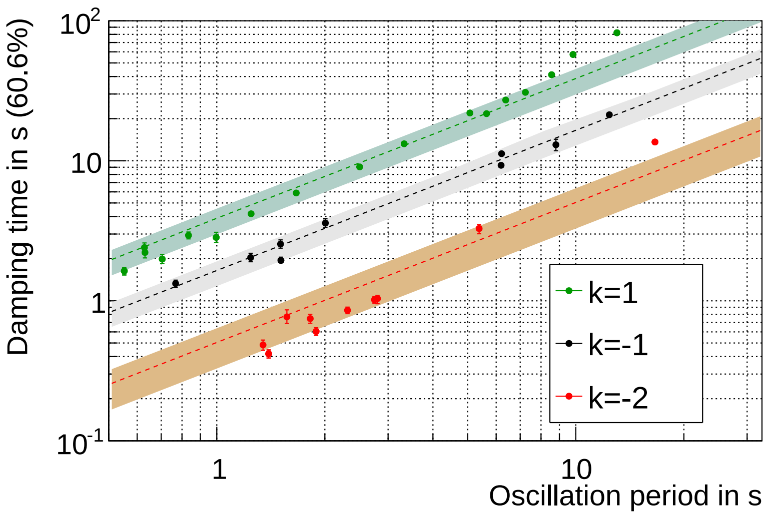

Figure 7.7: Damping time of the vertical polarization envelope with respect to the duration of the corresponding oscillation period. The measurements for various solenoid frequencies characterized by k reveal their different influence on the damping time. The colored lines illustrate an analytical calculation assuming a Gaussian width $\sigma = 90\,\mathrm{ns}$ for τ. The colored bands correspond to a change of the Gaussian width by $\pm 10\,\%$.

7.4 Bechmarking of the Algorithms for RF Fields

In the previous section, the theoretical expectation given in Equation 7.17 could be successfully confirmed with experimental data. The second purpose of this chapter is the validation of the newly implemented methods to simulate RF devices in COSY INFINITY. Two methods have been implemented. The first method considers a simple kick approach: the particles are tracked through the one-turn-map of the static ring and after each turn the spin is transformed by a rotation matrix taking into account the time-varying field strength of the RF device. In the second method, the RF device is implemented as a transfer map including the time dependence of the field. Thus, also the transverse phase space coordinates are taken into account during the calculation of their influence on spin motion. Furthermore, the impact of the RF device on beam motion can be studied in this approach. More details on these methods are given in Section 5.2.2. The correct reproduction of the variation of the resonance strength according to Equation 7.10 is an important test of these methods. In the following, both methods are applied for a solenoid frequency of 871 kHz ($k = -1$). The vertical spin component, which is initially set to unity, is tracked for 20 million turns for different particles. In Figure 7.8 the results for the reference particle and a particle with an initial amplitude $\tau_{\text{max}} \approx 172\,\text{ns}$ are depicted. The latter value corresponds to a 2σ-distance to the beam center assuming a Gaussian distributed τ and applying the fit results obtained for the run shown in Figure 7.4 (Gaussian distributed τ: $\sigma = 75\,\text{ns}$ and $c_\tau \approx 1.15$).

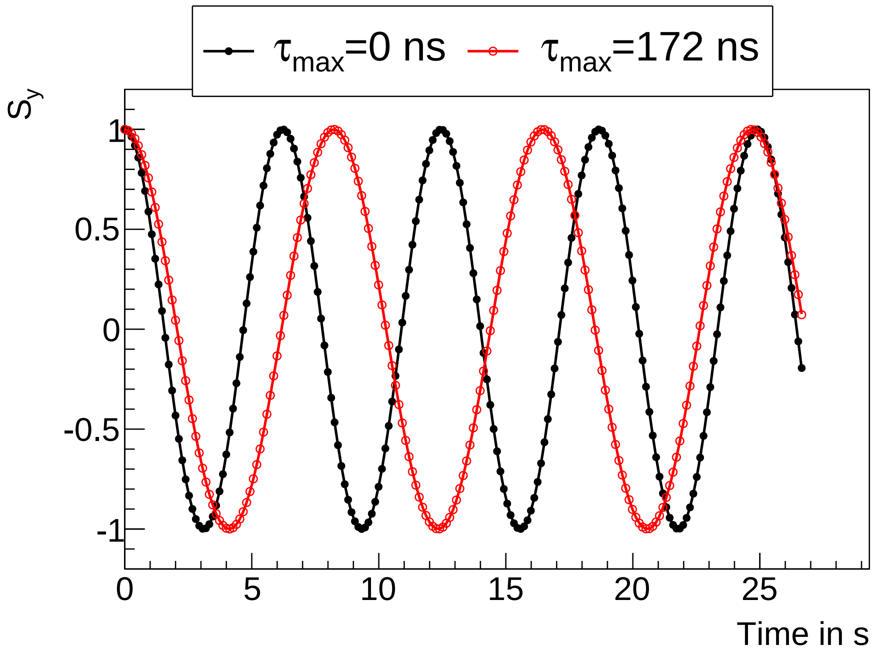

Figure 7.8: Comparison of the two implemented methods for the tracking simulation utilizing RF fields. The tracking results of the vertical spin component for deuterons with two different time deviation amplitudes τ_{max} in presence of an RF solenoid in the ring are illustrated. The setup of the tracking is based on the fit results obtained for the run at 871 kHz shown in Figure 7.4. The circles represent the tracking results for the simple kick approach, while the solid lines show the results obtained with a full map representation.

The circles represent the tracking results for the simple kick approach, while the solid lines show the results obtained with a full map representation. Both results are in excellent agreement with each other and reproduce the decreasing resonance strengths for particles with larger synchrotron oscillation amplitudes. Since the transverse phase space coordinates of these particles are initially set to zero, they can only be influenced by dispersive effects. Their influence on spin motion in this simulation configuration is negligible.

A second test utilizing the map method is performed comparing the analytical formula given in Equation 7.17 with tracking simulations for single particles. The fit results for the solenoid frequency of 630 kHz ($k = 1$) and the run shown in Figure 7.4 are applied in the model configuration. Additionally, different initial amplitudes $\tau_{\max}$ and an initially vertical spin vector are used. Figure 7.9 shows the results for $\tau_{\max} \in \{50\,\text{ns}, 150\,\text{ns}, 250\,\text{ns}\}$. For the smallest synchrotron amplitude, the tracking results reproduce the analytic formula very well. But, increasing initial amplitudes introduce significant deviations between the oscillation frequencies obtained in the tracking simulation and obtained by the analytic formula. The corresponding reason is a simplification introduced in the analytic formula: A harmonic oscillator behavior for the

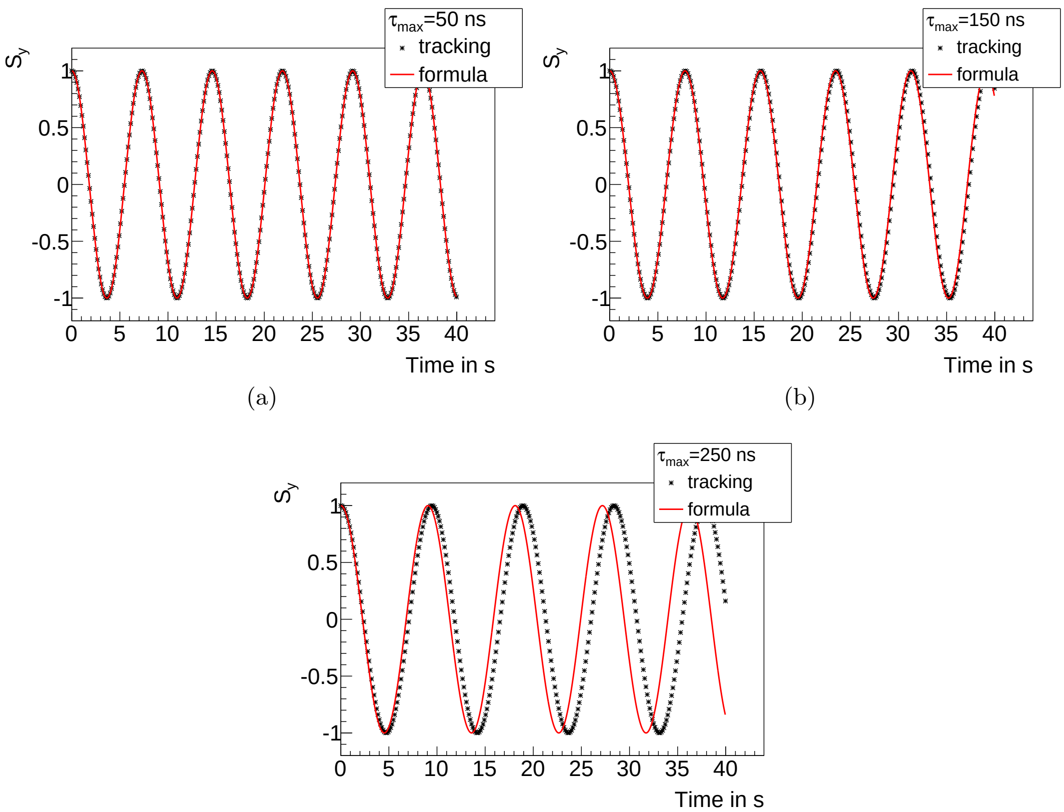

(a) (b) (c)

Figure 7.9: Vertical spin oscillation calculated by the analytical formula (lines) compared to tracking results (markers) obtained with a full map approach for a solenoid frequency of 630 kHz ($k = 1$). Different time deviation amplitudes $\tau_{\max}$ have been used. The deviations for larger $\tau_{\max}$ occur due to a simplification in the analytical formula.

synchrotron motion is assumed, which is equivalent to a restoring force depending linear on τ. The real restoring force of the RF cavity is defined by the sinusoidal oscillating electric field. Thus, it is only linear to first order. Large synchrotron amplitudes leave this linear regime, which leads to additional contributions. These effects are included in the tracking simulations and further reduce the resonance strength.

As a last test, the tracking results for a bunch of 1000 particles is compared to the analytical formula as well as the measurement results for the two settings presented in Figure 7.4. Here, the same $\tau_{\max}$ values as for the analytical calculation are used. Thus, the initial synchrotron phases of all particles in the tracking simulation are preset to zero. The comparison between the measured data, the tracking results and the analytic

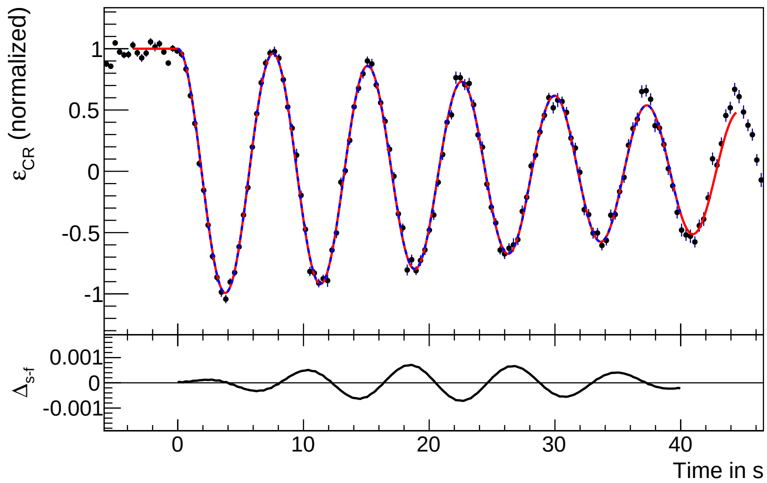

(a)

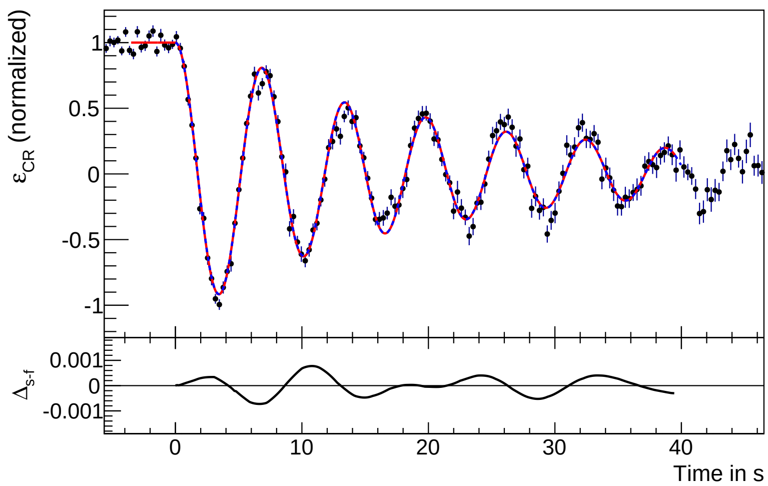

(b)

Figure 7.10: Normalized cross-ratios for two runs with different solenoid frequencies as already depicted in Figure 7.4. The blue line corresponds to tracking results based on the parameters (solenoid strength, width of particle distribution) obtained by the particular fit (red line). Both lines nearly cooincide with each other. For a direct comparison the deviation $\Delta_{\text{s-f}}$ between the tracking simulation and the analytical formula has been calculated.

formula is depicted in Figure 7.10. In addition to the normalized cross-ratio, also the difference $\Delta_{\text{s-f}}$ between the results of the tracking simulations and the analytic formula is calculated. In both cases, $\Delta_{\text{s-f}}$ keeps below 1‰ on the absolute scale and shows a beat hinting towards additional effects, which are present in the tracking simulations rather than a numerical issue. Overall, this validates the implementation of the new algorithms for RF fields.

7.5 Summary

In this chapter, the derivation of an analytical expression of the spin motion in presence of an RF solenoid has been presented. The different oscillation frequencies of the vertical polarization for the various particles in a bunch lead to a damping of the oscillating vertical polarization over time. The predicted dependence of this damping could be confirmed in measurements. Furthermore, the predicted spin behavior was used to benchmark the newly implemented methods for simulation of RF fields in COSY INFINITY. For small synchrotron amplitudes, they are in excellent agreement with the theory, while for larger amplitudes they reveal additional contributions with respect to the analytical formula. These contributions are not included in the analytic formalism due to a couple of assumptions and approximations, which have been used during its derivation. For example, the synchrotron motion was assumed to be harmonic, which is only valid for small synchrotron amplitudes. In summary, the new methods could be verified and are available to explore the systematic effects on the EDM measurement method using an RF Wien filter at COSY.

Chapter 8

EDM Measurement Method Using a Radiofrequency Wien Filter

8.1 Motivation

The algorithms recently developed for the simulation of RF fields have been benchmarked in the previous chapter. In this chapter, these algorithms are applied to study the systematic contributions to the EDM measurement method using an RF Wien filter. The fundamental details of this measurement method have been illustrated in Section 3.3.3. The currently mounted RF spin manipulators have been described in Section 4.1.2.2. For the EDM measurement a new type of RF Wien filter based on a stripline design is foreseen [161]. The orthogonal electric and magnetic fields of an electromagnetic wave provide the Wien filter condition. Due to an EDM related tilt of the spin closed orbit $\vec{n}_c$ a vertical polarization signal is produced. The corresponding theory of the polarization behavior in presence of an artificial spin resonance induced by an RF device has been discussed in Sections 3.2.7.3 and 3.2.8.2. The theoretically derived formula given in Equation 3.225 expresses the change of the spin component along the stable spin direction $\tilde{S}_3(\theta)$ for a particle circulating on the closed orbit. The projection onto the vertical axis $S_y(\theta) = -S_3(\theta) = -n_3(\theta) \cdot \tilde{S}_3(\theta) \approx -\tilde{S}_3(\theta)$ at the location of the polarimeter is used as measurement signal. This approximation is valid for small tilts of $\vec{n}_c$ with respect to the vertical axis. In the following calculations, an initial spin vector precessing in the plane perpendicular to $\vec{n}_c$ ($\tilde{S}_2(0) = 1$) is considered. Expecting a small change per turn, Equation 3.225 can be expanded. Up to first order, this yields:

$$\tilde{S}_3(\theta) \approx \frac{\alpha_0}{4\pi} \cdot [\tilde{m}_1 \cos(\phi) + \tilde{m}_2 \sin(\phi)] \cdot \theta \ . \tag{8.1}$$

The change is directly proportional to the maximum spin rotation angle α_0 induced by the RF device, which depends on the field strengths of the Wien filter. Furthermore a connection between the initial phase ϕ of the Wien filter with respect to the spin direction can be observed. This phase dependence couples differently to the parameters $\tilde{m}_1$ and $\tilde{m}_2$ defined in Equations 3.231 and 3.232. These parameters reflect the orientations of the spin closed orbit $\vec{n}_c$ and the spin rotation axis in the Wien filter $\vec{m}$ with respect to each other. A tilt of the spin closed orbit is induced by a non-vanishing EDM (Equation 3.227), but also by imperfections and misplacements of the magnets of the storage ring. The spin rotation axis in the Wien filter is defined by its field orientations and misplacement, respectively. The resulting values of $\tilde{m}_1$ and $\tilde{m}_2$ are calculated by the utilized simulation framework for different situations. Inserted in

Equation 8.1, the theoretically expected spin component change in all scenarios can be obtained. Finally, the results are directly compared to the spin tracking results for the same conditions. This allows for the benchmarking of the code and an estimation of the systematic limitations of the measurement method, simultaneously.

8.2 Simulation of the RF Wien Filter Method

In the following, the implementation of the Wien filter model into the simulation code is described. Afterwards different EDM magnitudes and imperfection conditions are defined and compared to each other in order to extract the systematic contributions. Intermediate results of the following simulation tasks have been published in [145, 158, 162]

8.2.1 Setup of the Wien Filter Model

Preliminary field calculations for the new RF Wien filter based on the stripline design are available [161]. Figure 8.1 depicts the evaluated field values at a specific grid for the maximum amplitudes of vertical magnetic and radial electric fields at a vanishing vertical coordinate $y = 0$. For further study, both field strengths are normalized to unity. In the simulation code COSY INFINITY customizable field models for electric and magnetic fields are available. Since the transfer map representation uses expansions up to an arbitrary order, multiple differentiable field descriptions are required, which need to satisfy Maxwell equations. The layout of the element often allows to exploit a symmetry with respect to the midplane. This allows one to calculate the three dimensional field information for static fields satisfying Maxwell equations based on known field magnitudes in the midplane. The fringe fields in longitudinal direction are often approximated by Enge functions (see Equation 5.10). In transverse direction, taylor expansions are commonly used. These simplifications have also been applied to construct a model for the RF Wien filter in COSY INFINITY. First, a superposition of the static electric and magnetic fields is generated. The fringe fields are described by Enge functions in longitudinal direction and polynomial functions in transversal

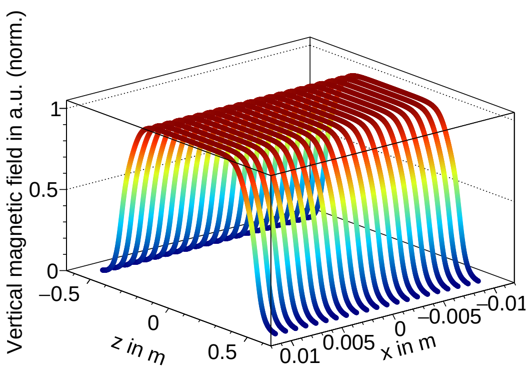

(a)

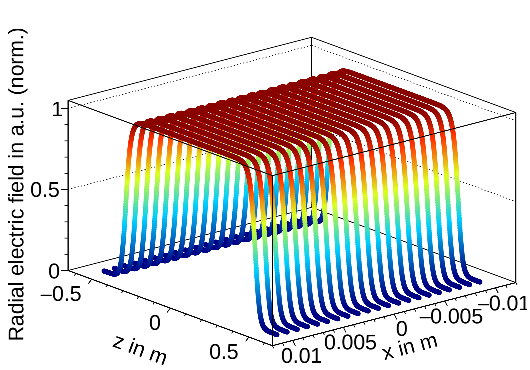

(b)

Figure 8.1: Field calculations for the vertical magnetic (a) and radial electric field (b) component of the RF Wien filter based on a stripline design. (data from [161, 163])

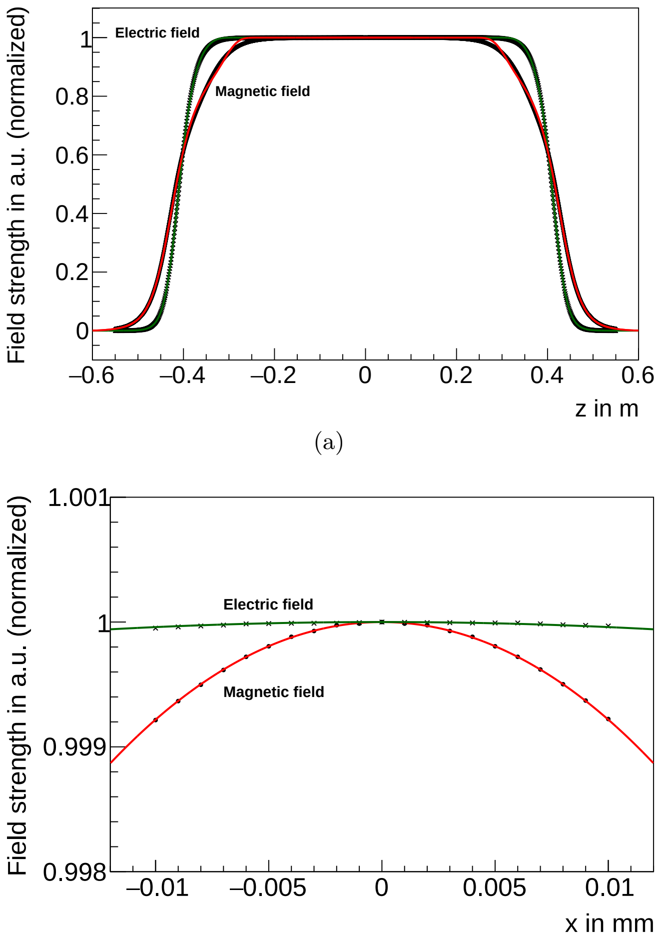

(a)

(b)

Figure 8.2: Calculated field profiles of the radial electric and vertical magnetic field of the Wien filter based on [161, 163]. The maximum field value is normalized to unity. Figure (a) shows the longitudinal profiles for $x = y = 0\,\mathrm{mm}$, Figure (b) depicts the transversal profiles for $y = z = 0\,\mathrm{mm}$. Fits of Enge functions and polynomial functions are used to describe the fringe fields.

direction, respectively. Second, the time dependency is included by assuming an oscillation of this fields according to a sine function with defined frequency and phase. The coefficients of the Enge and the polynomial functions for the magnetic and electric fields are determined by fits to the field calculations at $x = y = 0$ and $y = z = 0$, respectively. The fit results are shown in Figure 8.2. The calculations predict a steeper fall-off of the electric fields in longitudinal direction. A good representation of the calculated field values is achieved by different sets of coefficients for magnetic and electric fields. Only close to the maximum an increased discrepancy occurs in the magnetic case, but it is substantially smaller than the mismatch of the fringe fields for magnetic and electric fields. In transverse direction, the field fall-off is slightly larger for the magnetic field, but the reduction is still below one permille within $\pm 1\,\mathrm{cm}$. The extracted coefficients implemented into in the model are given in Table 8.1 and Table 8.2.

Table 8.1: Parameters of the Enge functions describing the vertical magnetic (a) and radial electric (b) field of the Wien filter, respectively. The effective length for the magnetic part (electric part) is $l_{\text{eff}} = 0.807\,\text{m}$ ($l_{\text{eff}} = 0.814\,\text{m}$).

(a)

	entrance	exit
a_1	-0.375	-0.376
a_2	2.923	2.924
a_3	1.490	1.491
a_4	-0.235	-0.232
a_5	-0.847	-0.854
a_6	0.381	0.383
D	0.1	0.1

(b)

	entrance	exit
a_1	-0.107	-0.109
a_2	5.839	5.832
a_3	1.635	1.626
a_4	0.632	0.772
a_5	-1.790	-2.010
a_6	0.705	0.803
D	0.1	0.1

Table 8.2: Parameters of the fitted polynomial $(f_0 \cdot (1 - \sum c_i \cdot x^i))$ to describe the transversal fall-off for vertical magnetic and radial electric field of the Wien filter, respectively.

	magnetic	electric
c_2	$-7.727\,\text{m}^{-2}$	$-0.404\,\text{m}^{-2}$
c_4	$-913.6\,\text{m}^{-4}$	$-0.003\,\text{m}^{-4}$

The different shapes of the magnetic and electric fringe fields prevent a precise local Lorentz force compensation. An accurate scaling of magnetic and electric field strengths is required to minimize the excitation of the beam. This is achieved by the following procedure in the model calculations. The central beam location is represented by a reference particle starting at zero initial coordinates. In an ideal ring without imperfections and disabled Wien filter, this particle does not change its beam coordinates, but turning on the RF Wien filter with local field mismatches excites betatron oscillations of this particle. If the oscillation frequencies of the Wien filter fields are close to a betatron sideband frequency, these excitations add up in subsequent turns, amplify the betatron oscillation amplitude and may lead to beam loss. Consequently, a matching procedure for electric and magnetic field strengths is most sensitive close to a betatron sideband frequency. This condition can be prepared by moving either the Wien filter frequency or the horizontal betatron tune. The former is already fixed, since it needs to fulfill the spin resonance condition in the EDM experiment. Thus, a variation of the horizontal betatron tune is used in the following. The simulations are performed using a deuteron beam momentum of 970 MeV/c. This corresponds to a spin tune of $\nu_s \approx -0.161$. The Wien filter frequency is set to 871 kHz ($k = -1$) (see also Chapter 7). To maximize the sensitivity to a field mismatch, the horizontal betatron tune is shifted to $Q_x = 4 + \nu_s \approx 3.839$ by variation of the arc quadrupoles. A nominal vertical betatron tune of $Q_y = 3.585$ is preserved, simultaneously. The expected magnetic field amplitude of the Wien filter depends on the particular power amplifier A field strength of about $\hat{B} = 0.1\,\text{mT}$ is expected.

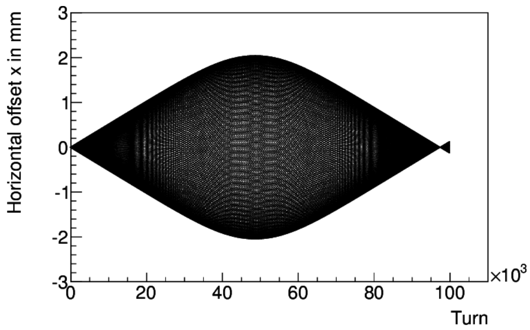

(a)

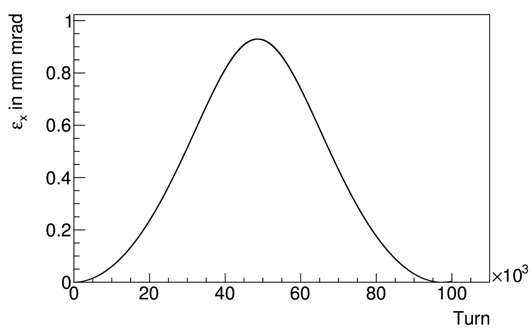

(b)

Figure 8.3: Tracking results for a reference deuteron with a momentum of 970 MeV/c. The horizontal tune is set to $Q_x = 4 - \nu_s$ and the Wien filter is operating at $\hat{B} = 0.1\,\mathrm{mT}$, $\hat{E} = -\beta c \cdot \hat{B}$ and $k = -1$ (871 kHz). Figure (a) shows the horizontal offset vs. turn number, in Figure (b) the calculated horizontal Courant-Snyder invariant vs. turn number is depicted.

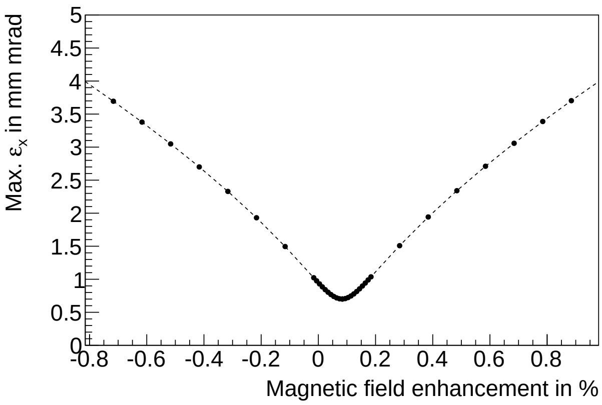

Figure 8.4: Simulated matching procedure of magnetic and electric field strengths to reduce the maximum Courant-Snyder invariant reached during the tracking simulation shown in Figure 8.3. The maximum value is plotted vs. an enhancement of the magnetic field while keeping the electric field constant. The horizontal tune is set to $Q_x = 4 + \nu_s \approx 3.839$.

To cancel the Lorentz force in simulations, a corresponding electric field amplitude of $\hat{E} = -\beta c \cdot \hat{B}$ is chosen as starting point for the matching procedure. Subsequently, the magnetic field is scaled iteratively and the reference particle is tracked for 100 000 turns, respectively. This is exemplarily shown in Figure 8.3 for the initial conditions. The initially vanishing horizontal offset is affected by the Wien filter excitation and the amplitude of the betatron oscillations increase. At some point the particle slips out of resonance with the Wien filter excitation, such that the amplitude decreases again. This can occur due a slight mismatch of betatron sideband frequency and the excitation frequency induced by an amplitude dependent betatron tune. In the particular scenario, the Courant-Snyder invariant reaches magnitudes close to 1 mm mrad. This value can be used as a measure for the field compensation quality. Figure 8.4 depicts the maxima for different enhancements of the magnetic field with respect to the initial conditions. The smallest excitation is observed at an enhancement of about 0.08 %. The

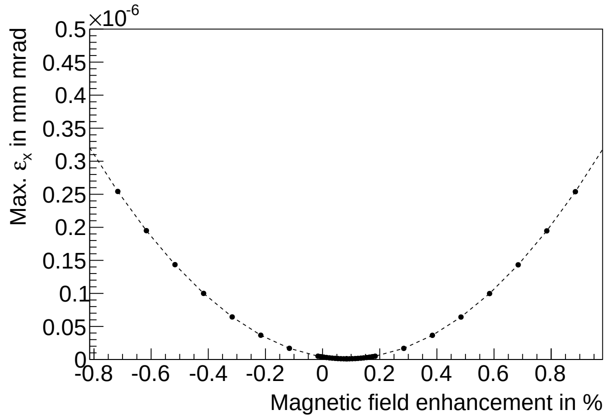

Figure 8.5: Simulated matching procedure of magnetic and electric field strength to reduce the maximum Courant-Snyder invariant reached during the tracking simulations. The maximum value is plotted vs. an enhancement of the magnetic field by keeping the electric field constant. The horizontal tune is set to $Q_x = 3.62$.

Courant-Snyder invariant at the minimum is about 0.7 mm mrad. A entirely vanishing excitation can not be achieved, because it requires a simultaneous minimization of the particle offset and angular deflection induced by the Wien filter, but the field scaling is the only free parameter. To further reduce the excitation a sufficient distance to the betatron sideband frequencies is mandatory. This is verified by a similar simulation at the nominal tune $Q_x = 3.62$ presented in Figure 8.5. Here, the betatron oscillation amplitude is reduced by several orders of magnitude. For the following investigation the enhancement factor providing a minimized excitation is selected and a setup based on the nominal betatron tunes $Q_x = 3.62$ and $Q_x = 3.585$ is used.

8.2.2 EDM Signal in the Wien Filter Measurement Method

A first reasonable test of the implemented Wien filter model is the benchmark against the theoretically expected spin interaction in case of an ideal model of the storage ring and an ideally oriented Wien filter with vertical magnetic and radial electric fields but a non-vanishing EDM. According to Equation 8.1, tilts of the spin closed orbit induce a slow variation of the vertical spin component. These tilts are introduced by imperfection resonances of the spin motion. In case of an ideal storage ring, there is no tilt due to misalignments and imperfections. The tilt due to a non-vanishing EDM has been discussed in Section 3.3.1 (Equation 3.227) and leads to a radial component of the spin closed orbit. The parameters $\tilde{m}_1$ and $\tilde{m}_2$ in Equation 8.1 are given by

$$\tilde{m}_1 = -n_x \approx \frac{\eta_{\mathrm{EDM}}\beta}{2G} , \tag{8.2}$$

$$\tilde{m}_2 = 0 . \tag{8.3}$$

Hence, Equation 8.1 simplifies to

$$\tilde{S}_3(\theta) \approx -\frac{\alpha_0}{4\pi} \cdot n_x \cos(\phi) \cdot \theta . \tag{8.4}$$

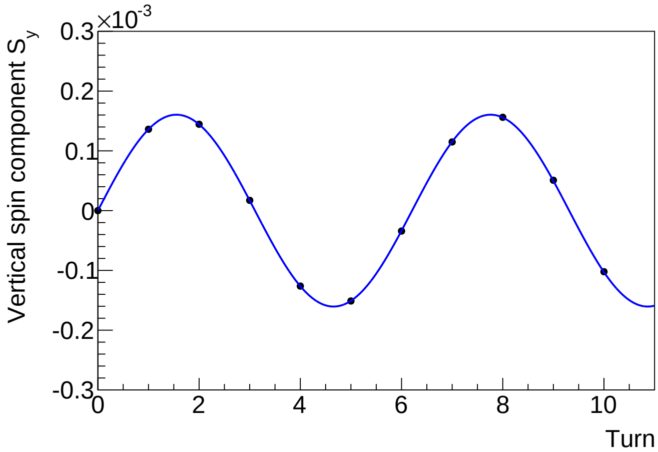

Figure 8.6: Fast oscillation of the vertical spin component of a reference deuteron. The initial spin vector is placed in the plane perpendicular to the spin closed orbit ($\tilde{S}_2(0) = 1$). An EDM of $\eta_{\text{EDM}} = 10^{-4}$ is assumed, which causes a tilt of the spin closed orbit. The solid line is a fit of a sinusoidal function.

According to this equation a strong connection of the phase of the Wien filter fields and the vertical spin component change is expected. To verify the theoretical formula, simulations based on tracking of the reference particle are conducted. An initial spin with $\tilde{S}_2 = 1$ is set up. Figure 8.6 illustrates the variation of the vertical spin component in the first ten turns assuming an EDM of $d_d \approx 5 \cdot 10^{-19}\, e\,\text{cm}$ corresponding to $\eta_{\text{EDM}} = 10^{-4}$. The tracking results are interpolated by the fit of a sine function. The fast oscillation of the vertical spin component corresponds to the precession around the tilted spin closed orbit of the static ring. This effect is also present without an additional RF Wien filter and is used in the parasitic method described in Section 3.3.1. The expected amplitude for the particular configuration of the model can be estimated by

$$A \approx \left| \frac{\eta_{\text{EDM}} \beta}{2G} \right| = 0.16 \cdot 10^{-3} \tag{8.5}$$

and agrees well with the tracking results. The fast oscillation not included in Equation 8.4 has been averaged out during the derivation (see Section 3.2.7.3). Instead a slow change of the average vertical spin component introduced by the RF Wien filter is predicted. For verification, the spin motion is also investigated for longer tracking periods as shown in Figure 8.7. Exemplarily, the tracking results for the two phases $\phi = 0°$ and $\phi = 90°$ of the Wien filter fields are depicted. The solid lines describe linear fits. The slopes of these fits corresponds to the average change of the vertical spin component ΔS_y per turn. As predicted by Equation 8.4 a slow rise occurs for $\phi = 0°$, while the averaged vertical spin component for a phase of $\phi = 90°$ is constant. Figure 8.8 illustrates the results for different EDM magnitudes and various initial phases of the Wien filter fields. The solid lines represent the theoretical expectation according to Equation 8.4. As previously described a Wien filter magnetic field amplitude of 0.1 mT (slightly increased in order to minimize the beam excitation) is utilized in these calculations. The buildup scales linearly with the EDM magnitude and disappears for a vanishing EDM. Furthermore, it scales linearly with the Wien filter field strengths. For $\eta_{\text{EDM}} = 10^{-4}$ the buildup is approximately $\Delta S_y = 1.6 \cdot 10^{-9}$ per turn. Thus, the average vertical spin component reaches the amplitude given in Equation 8.5 already after about 10^5 turns, which amounts to 0.1 s. In the next sections, various contributions, which could mimic the EDM signal, and their orders of magnitude are investigated.

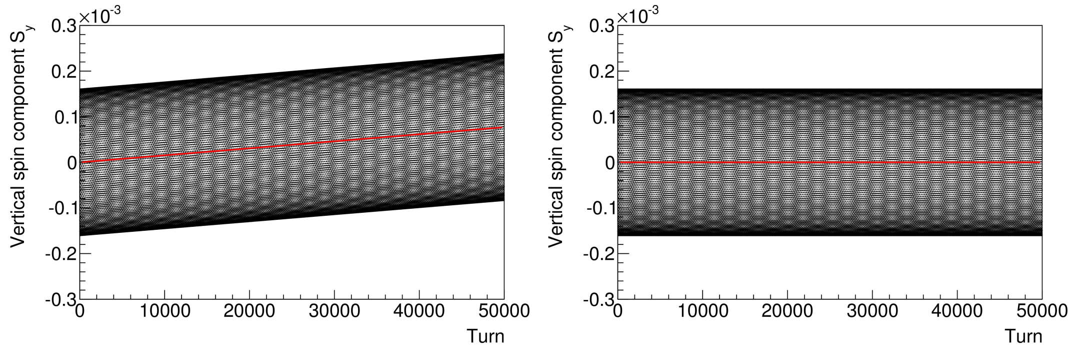

Figure 8.7: Tracking results of the vertical spin component in presence of an EDM ($\eta_{\text{EDM}} = 10^{-4}$) and the RF Wien filter with vertical magnetic field. In Figure (a) the initial phase of the Wien filter field oscillation is set to $\phi = 0°$, in Figure (b) it is set to $\phi = 90°$. The solid lines are linear fits used to extract the average change.

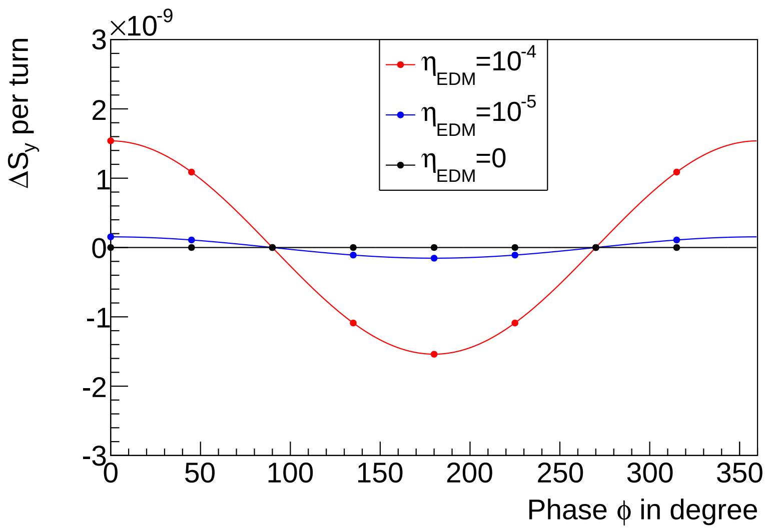

Figure 8.8: Average change of the vertical spin component for different initial phases of the Wien filter fields. Different magnitudes for an EDM are investigated. The solid lines correspond to the theoretical expectation given by Equation 8.4. A Wien filter magnetic field of $1 \cdot 10^4$ mT and the corresponding electric field are used. The Wien filter length is about 0.8 m.

8.2.3 Influence of Imperfections

The change of the vertical spin component depends on the tilt of the spin closed orbit, but also on a misaligned spin rotation axis within the Wien filter. Those tilts can be introduced by either misalignments and imperfections of the guiding magnets or the Wien filter itself. These effects are discussed in the following.

8.2.3.1 Wien Filter Rotations

Considering Equation 8.1, the change of the vertical spin component strongly depends on the parameters $\tilde{m}_1$ and $\tilde{m}_2$. A rotation of the Wien filter about the longitudinal axis will introduce radial magnetic and vertical electric field components on the reference trajectory. Thus, the spin rotation axis within the Wien filter is also tilted by the same amount. This can be parametrized by a rotation angle ζ of the Wien filter about the longitudinal axis. The parameters $\tilde{m}_1$ and $\tilde{m}_2$ can be expressed as

$$\tilde{m}_1 = \sin(\zeta) - \cos(\zeta) \cdot n_x \ , \tag{8.6}$$

$$\tilde{m}_2 = 0 \ , \tag{8.7}$$

in case one assumes that the only contribution to a tilt of the spin closed orbit of the static ring is a non-vanishing EDM. Thus, a rotation about the longitudinal axis modifies the parameter $\tilde{m}_1$, which also contains the EDM contribution. For that reason the same dependence on the phase of the Wien filter fields as for a pure EDM signal is expected. Figure 8.9 depicts the average change of the vertical spin component in case of a pure Wien filter rotation and a vanishing EDM. The solid lines represent the

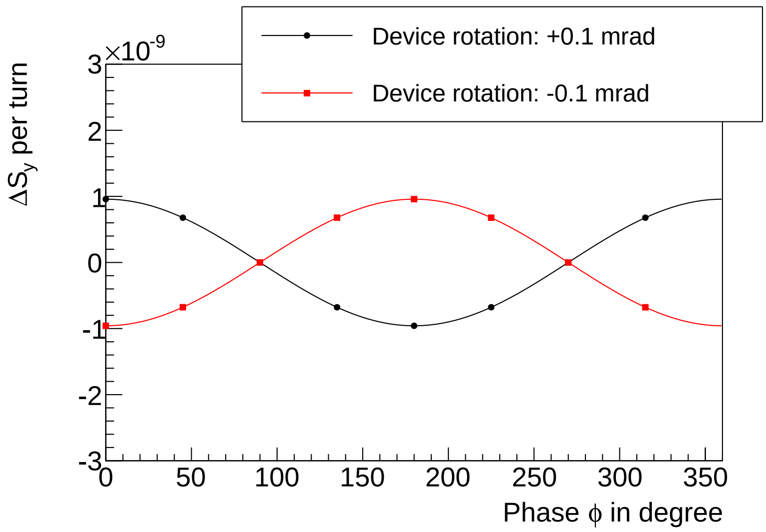

Figure 8.9: Average change of the vertical spin component for different initial phases of the Wien filter fields. The EDM is assumed to vanish, but the false signal for different rotation angles of the Wien filter about the longitudinal axis is investigated. The solid lines correspond to the theoretical expectation. A Wien filter magnetic field of $1 \cdot 10^4$ mT and corresponding electric field are used. The length of the Wien filter is about 0.8 m.

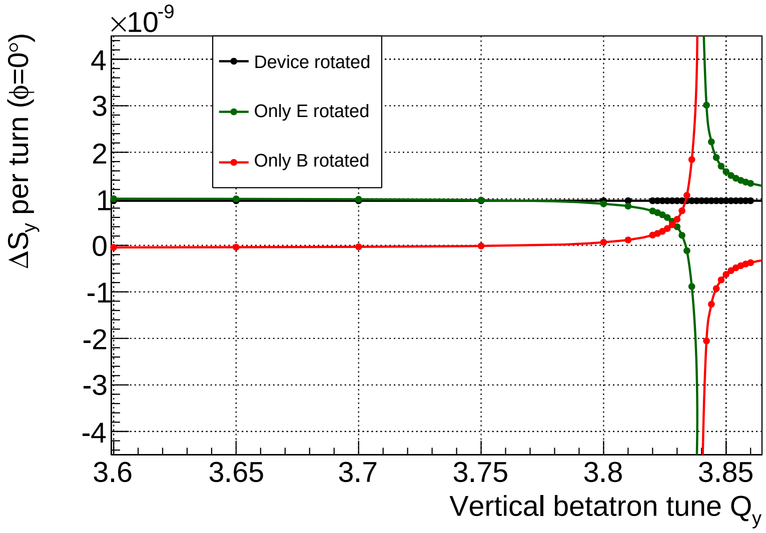

Figure 8.10: Average change of the vertical spin component for an initial Wien filter phase of $\phi = 0°$ and different vertical betatron tunes. The EDM is set to zero in simulations, but a rotation about the longitudinal axis of 0.1 mrad is implemented for either the whole device or magnetic / electric field, respectively. At $Q_y = 4 + \nu_s$ an enhancement due to betatron motion is observed, if one of the fields is rotated alone.

theoretical expectation. In fact, the phase dependence agrees with a pure EDM signal. For small rotation angles ζ the change of the vertical spin component scales linearly with the magnitude of ζ. Already for angles of 0.1 mrad this change is in the same order of magnitude as for the pure EDM contribution ($\eta_{\mathrm{EDM}} = 10^{-4}$), illustrated in the previous section. Thus, a precise alignment with respect to the ring plane would be absolutely mandatory to suppress this systematic effect for the EDM measurement method.

Besides a rotation of the device, also the rotation of only the magnetic or electric fields can be considered. This leads to a deviation from the Lorentz force compensation, which excites betatron oscillations and introduces secondary effects affecting the spin motion due to the spin interaction with the focusing fields of the storage ring. Theoretical calculations and measurement results show a strong connection to the vertical betatron tune [100, 101, 104]. In the following, this connection is studied in context of the Wien filter EDM measurement method. Figure 8.10 shows the average change of the vertical spin component for various vertical betatron tunes and a Wien filter phase $\phi = 0°$. Rotations of the whole device, only the magnetic or only the electric part are considered, respectively. The solid lines correspond to interpolations between the various tracking results, which are presented by the markers. In case of a rotation of the entire Wien filter, the minimization of the beam excitation is preserved. As a consequence no connection to the vertical betatron tune is observed. Investigating the effects of magnetic and electric field rotations separately, the sum of both effects always coincides with a rotation of the whole device. In case the betatron sideband frequencies are located sufficiently far away from the field oscillation frequency of the Wien filter, the direct contribution of the Wien filter dominates the change of the vertical spin component. While the magnetic field contribution nearly vanishes in this case, the electric field contribution possesses almost the same magnitude as in case of a whole device rotation. Moving a betatron sideband frequency close to the field oscillation frequency (i.e. $Q_y \approx 3.839$), the impact of betatron motion dominates and significantly enhances the average growth of the vertical spin component. This needs to be avoided in the experimental setup.

These results can be interpreted as an order of magnitude estimate of the influence of field imperfections of the Wien filter. In general, the total spin rotation within the Wien filter during one pass, can be characterized by a rotation axis and a rotation angle independent from the particular arrangement and shapes of the fields. In case this axis is tilted and any change of the vertical spin component constructively adds up in subsequent turns, a false EDM signal is produced.

8.2.3.2 Ring Imperfections

In this section, the additional tilts of the spin closed orbit due to misalignments and imperfections of the guiding and focusing magnets of the storage ring are examined. For this purpose, a perfectly aligned Wien filter is assumed. In this scenario, the parameters $\tilde{m}_1$ and $\tilde{m}_2$ are given by

$$\tilde{m}_1 = -n_x \ , \tag{8.8}$$
$$\tilde{m}_2 = -n_z \ . \tag{8.9}$$

Thus, tilts contributing to the radial component of $\vec{n_c}$ at the location of the Wien filter are critical and can influence the measured polarization signal related to an EDM. These tilts can be introduced by additional radial or longitudinal fields. Different sources of these fields are considered. Vertical shifts of the quadrupole magnets as well as rotations of the main bending dipoles about the longitudinal axis lead to radial magnetic fields on the reference trajectory. But also other shifts, tilts and rotations are possible sources of a false EDM measurement signal. In case of radial magnetic fields also the vertical beam motion is affected. Thus, a beam position measurement can be used to detect those field components. As shown in the following, this requires a high precision and accuracy of the beam position monitors. For that purpose, a new type of BPMs based on Rogowski coils is currently under investigation at COSY [164]. In the simulation study presented here, the misalignments are randomly generated according to Gaussian distributions assuming different widths, since the real values are not precisely known. The vertical orbit deviations evaluated at the quadrupole locations rather than the beam position monitor locations are used to investigate the correlation of a false EDM signal and the measured vertical beam offsets. This scheme provides an enhanced number of orbit samples, which are well distributed in the storage ring. For comparison, the vertical orbit RMS defined as

$$\Delta y_{\mathrm{RMS}} = \sqrt{\frac{1}{N}\sum_{i=1}^{N} y_i^2} \tag{8.10}$$

is calculated based on the results of the orbit simulations. Here, y_i denotes the vertical orbit position with respect to the reference coordinate system at the i-th quadrupole.

Figure 8.11 illustrates the variation of Δy_{RMS} for different widths of the Gaussian distribution σ_y, which are used for the randomization of the misplacements. In this

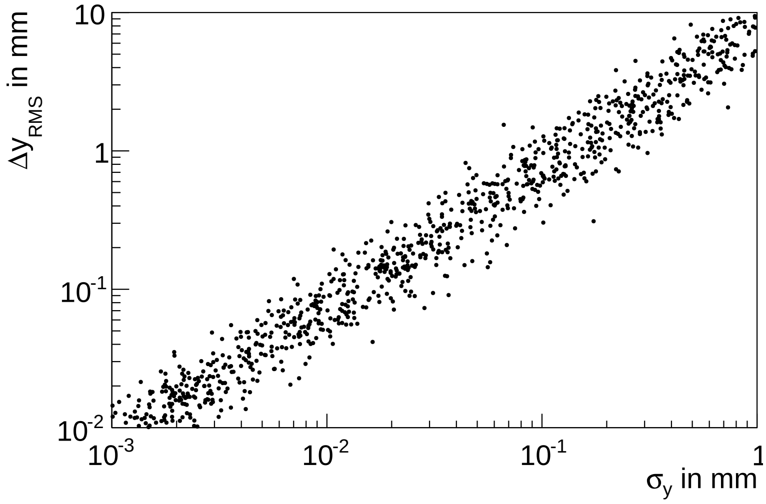

Figure 8.11: Simulated Δy_{RMS} as defined in Equation 8.10 in presence of misaligned quadrupole magnets. Distributed shifts of the quadrupoles in vertical direction are applied. These misalignments are randomly generated assuming different Gaussian widths σ_y.

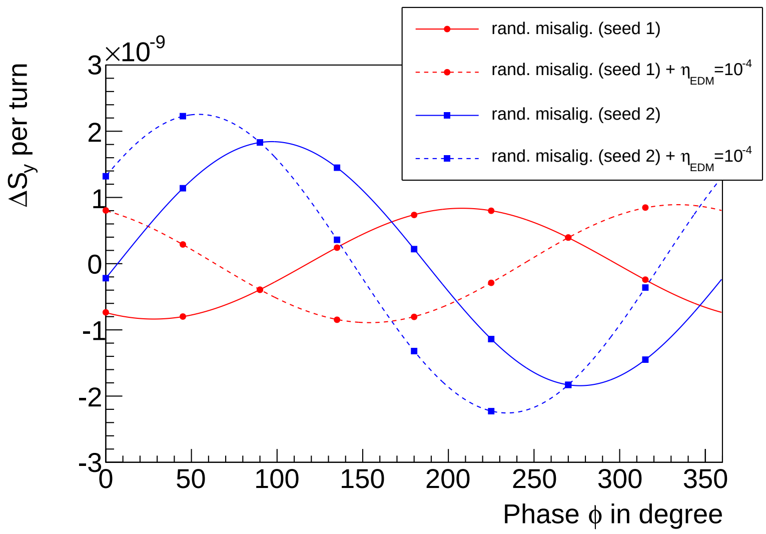

Figure 8.12: Average change of the vertical spin component for different initial phases of the Wien filter fields. The superposition of the false signal due to misaligned quadrupole magnets ($\sigma_y = 0.1\,\mathrm{mm}$) and different magnitudes of the EDM is investigated. Two different randomization seeds are illustrated. The solid and dashed lines correspond to the theoretical expectation. A Wien filter magnetic field of $1 \cdot 10^4\,\mathrm{mT}$ and the corresponding electric field are used. The length of the Wien filter is about 0.8 m.

particular scenario only the quadrupoles are misaligned in terms of shifts in vertical direction. A linear correlation between σ_y and Δy_{RMS} is observed as expected.

Besides the effects on the vertical orbit, the misalignments also lead to additional tilts of the spin closed orbit, which can introduce a buildup of the average vertical spin component in case the RF Wien filter is turned on. These induced tilts of the spin closed orbit are calculated by the simulation software. Figure 8.12 shows the simulated dependence of the buildup on the Wien filter phase for two different randomization seeds, both using $\sigma_y = 0.1\,\mathrm{mm}$. The EDM magnitude is varied to investigate the superposition of both contributions. The curves reflect the theoretical calculations based on the extracted tilts of the spin closed orbit. The Wien filter phase corresponding to the maximum buildup depends on the relation of the n_x and n_z components, which in general vary for different locations in the storage ring. Thus, in case of misalignments the maximum buildup is not necessarily observed at $\phi = 0°$. In contrast, the EDM related tilt of the spin precession in the guiding dipoles introduces only a radial component of the spin closed orbit. Thus, in case of a positive EDM the superposition of EDM signal and false signal due to misalignments always leads to a larger value at $\phi = 0°$. In the following, only the buildup at $\phi = 0°$ is considered, since it provides the highest sensitivity for an EDM measurement (together with $\phi = 180°$).

To characterize the buildup for a given value of Δy_{RMS}, the vertical misalignments are randomly generated for 1000 different randomization seeds. For each seed the Gaussian width of the misalignment error distribution is scaled to exactly produce a predefined value of Δy_{RMS}. In the next step, the absolute $|\Delta S_y|$ per turn is calculated for each configuration. For a $\Delta y_{\mathrm{RMS}} = 1\,\mathrm{mm}$, the results are shown in Figure 8.13. The retrieved buildup rates are sorted by magnitude and a 90 % upper confidence limit is calculated as depicted by the red line. It can be concluded, that 90 % of the randomized misalignments, which result in a $\Delta y_{\mathrm{RMS}} = 1\,\mathrm{mm}$, generate a buildup below $|\Delta S_y| \approx 0.95 \cdot 10^{-9}$ per turn. The same approach is repeated for different values of Δy_{RMS} and the corresponding confidence limit is determined. The simulated buildups of the average vertical spin component for different Δy_{RMS} are depicted in Figure 8.14. In the particular case, only randomly distributed vertical shifts of the quadrupoles are taken into account. The solid line corresponds to the 90 % upper confidence limit in case of a vanishing EDM. The average buildup of the vertical spin component tends to increase for larger vertical orbit deviations. The scattering reflects, that the buildup is

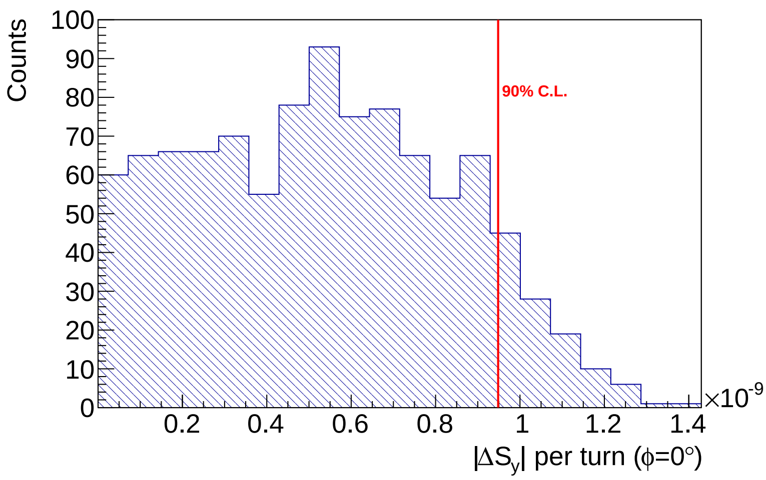

Figure 8.13: Absolute average change of the vertical spin component $|\Delta S_y|$ per turn caused by randomized vertical shifts of the quadrupole magnets. The shift magnitude is scaled to generate a $\Delta y_{\mathrm{RMS}} = 1\,\mathrm{mm}$ for each randomization seed. The simulated EDM is set to zero. The red line corresponds to a 90 % upper confidence limit obtained from the $|\Delta S_y|$ calculation.

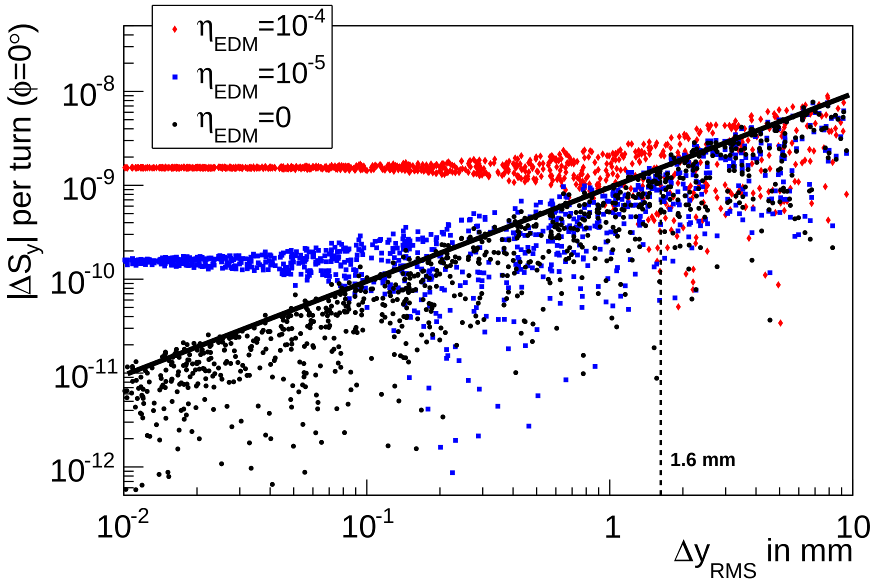

Figure 8.14: Absolute average change of the vertical spin component $|\Delta S_y|$ per turn with respect to different Δy_{RMS} and an initial Wien filter phase $\phi = 0°$ in the simulation. The different Δy_{RMS} are generated by randomized vertical quadrupole shifts assuming Gaussian distributed misalignments. Furthermore different EDM magnitudes are considered. The solid line shows the 90 % upper confidence limit for pure misalignments. The dashed line refers to the location for which the false signal by misalignments is equal to an EDM signal corresponding to $\eta_{\mathrm{EDM}} = 10^{-4}$.

not directly proportional to the orbit RMS, but limited below a certain level, which depends on the vertical orbit RMS. For larger buildup contributions connected to misalignments, the EDM related buildup becomes indistinguishable. Reducing the misalignments reveals a plateau in case of a non-vanishing EDM. In case the vertical quadrupole misalignments produce a $\Delta y_{\mathrm{RMS}} \approx 1.6\,\mathrm{mm}$, the 90 % upper confidence limit of the pure misalignment related buildup coincides with an EDM related buildup associated to $\eta_{\mathrm{EDM}} = 10^{-4}$. Similar simulations are performed taking only rotations of the bending dipoles or a superposition of shifts and rotations in all directions and around all axes for dipoles and quadrupoles into account. The results are shown in Figure 8.15. The 90 % upper confidence limits slightly change, but still the same order of magnitude is observed in these scenarios.

As last item of this section, the correlation between the vertical orbit RMS Δy_{RMS} either calculated at the locations of the quadrupoles or calculated at the locations of the beam position monitors $\Delta y^{\mathrm{BPM}}_{\mathrm{RMS}}$ is evaluated. Considering only vertical shifts of the quadrupoles, this is shown in Figure 8.16. A nearly perfect linear correlation and only a small spread can be observed. But, note that any influence connected to misalignments and measurement errors of the BPMs is not included, yet.

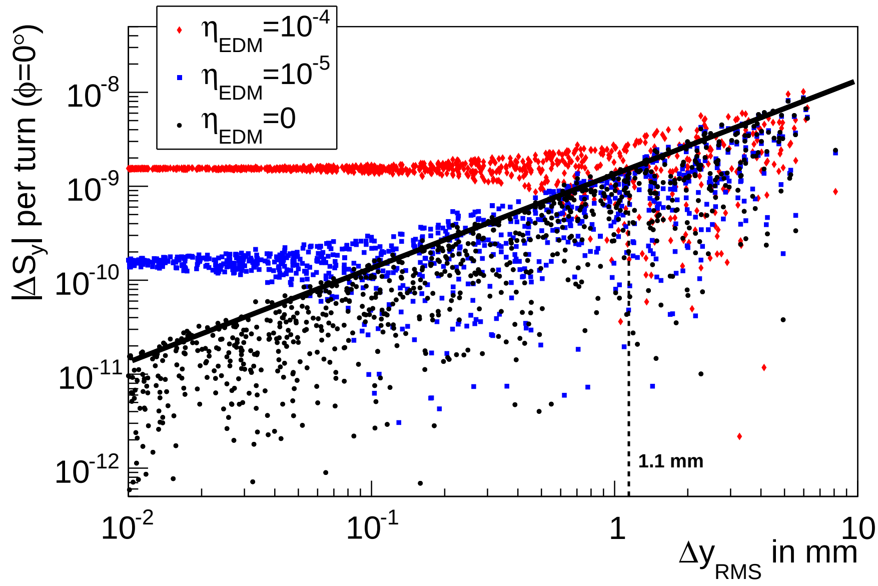

(a)

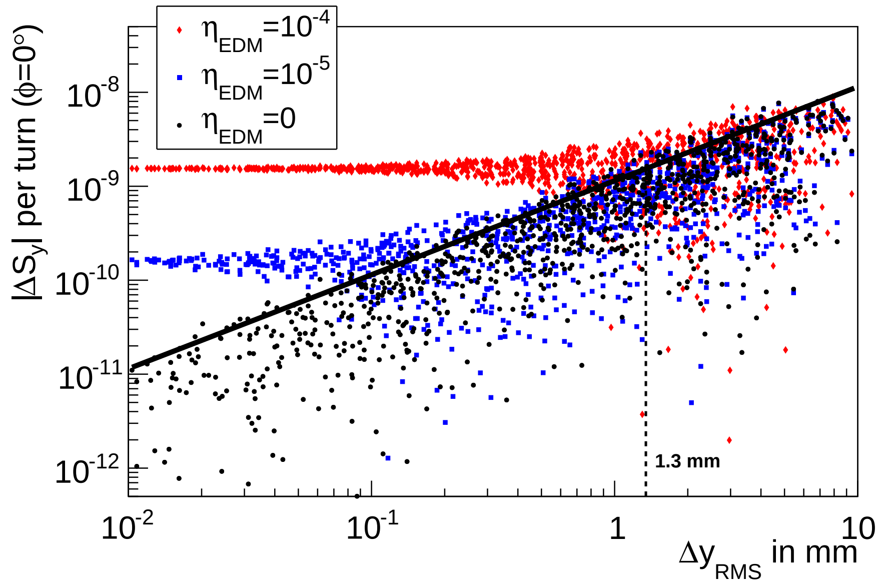

(b)

Figure 8.15: Absolute average change of the vertical spin component $|\Delta S_y|$ per turn with respect to different Δy_{RMS} and an initial Wien filter phase $\phi = 0°$ in the simulation. The different Δy_{RMS} are generated by randomized rotations about the longitudinal axis (a) or a full set of shifts and rotations of dipoles and quadrupoles assuming Gaussian distributed misalignments (b). Furthermore, different EDM magnitudes are considered. The solid line shows the 90 % upper confidence limit for pure misalignments. The dashed line refers to the location for which the false signal by misalignments is equal to an EDM signal corresponding to $\eta_{\mathrm{EDM}} = 10^{-4}$.

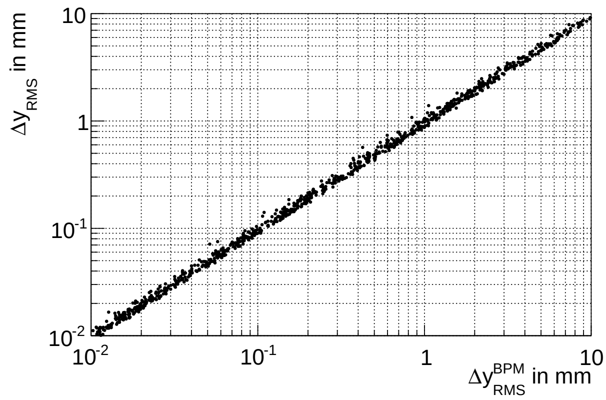

Figure 8.16: Correlation between the vertical orbit RMS simulated for the locations of the quadrupoles Δy_{RMS} and for the locations of the beam position monitors $\Delta y_{\mathrm{RMS}}^{\mathrm{BPM}}$. The orbit offsets are generated by randomized vertical shifts of the quadrupole magnets.

8.2.3.3 Orbit Correction

The results discussed in the previous chapter suggest that smaller vertical orbit deviations reduce the magnitude of false EDM signals introduced by misalignments.

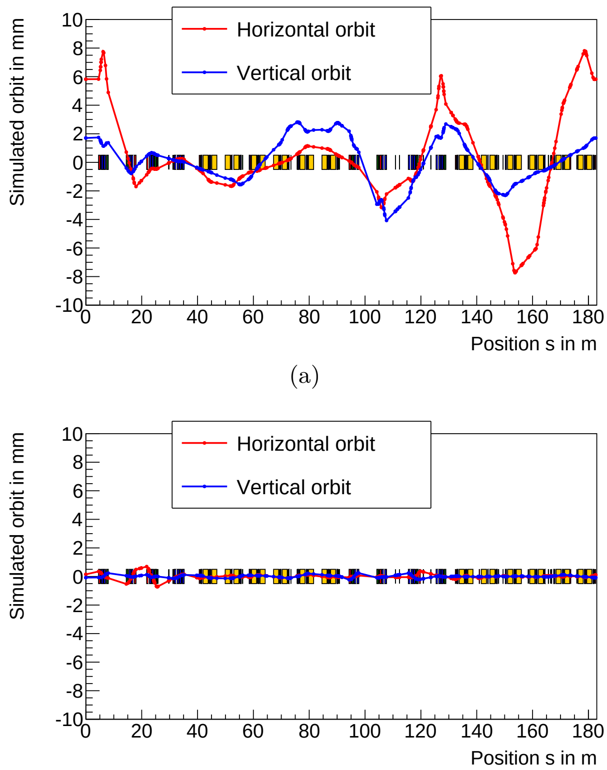

(b)

Figure 8.17: Simulated horizontal and vertical orbit before (a) and after (b) application of the orbit correction routine. An example with randomly generated shifts and rotations of dipoles and quadrupoles is shown. The colored boxes illustrate the locations of dipoles (yellow) and quadrupoles (blue)

Instead of correcting the a priori unknown misalignments and imperfections of each magnet, a global orbit correction can be considered to minimize those deviations by applying additional corrector magnetic fields. Routines for orbit correction are implemented into the COSY INFINITY framework as discussed in Section 5.2.4. In these routines, the orbit response matrix is calculated and (pseudo-)inverted to determine the required corrector strengths required for a minimization of the orbit. The (pseudo-)inversion is based on a singular value decomposition. In this particular study the correction algorithm is modified and aims for the minimization of the orbit deviations at the quadrupole locations instead of the beam position monitors. This allows for a correction at many locations well distributed in the whole storage ring and illustrates the optimum results, which is achievable by mounting new BPMs at each quadrupole. Furthermore, this study reveals, if the false signals can be reduced without correcting the actual misalignments but introducing additional fields of the corrector magnets. For that reason, the bias induced by a lack of beam position monitors and measurement errors is intentionally excluded.

Figure 8.17 exemplarily shows the simulated orbit for an arbitrary misalignment configuration before and after applying an orbit correction using all correctors. The orbit deviations are significantly reduced by an orbit correction. The evaluation of different sets and magnitudes of misalignments reveals that the RMS value can be reduced by about one order of magnitude using the described correction scheme.

This scheme is applied to investigate the impact on the buildup of the average vertical spin component. The results for only vertically shifted quadrupoles and a vanishing EDM magnitude are depicted in Figure 8.18 The reduction of Δy_{RMS} is accompanied by a reduction of the false EDM signal. Since no plateau in the distribution of the data

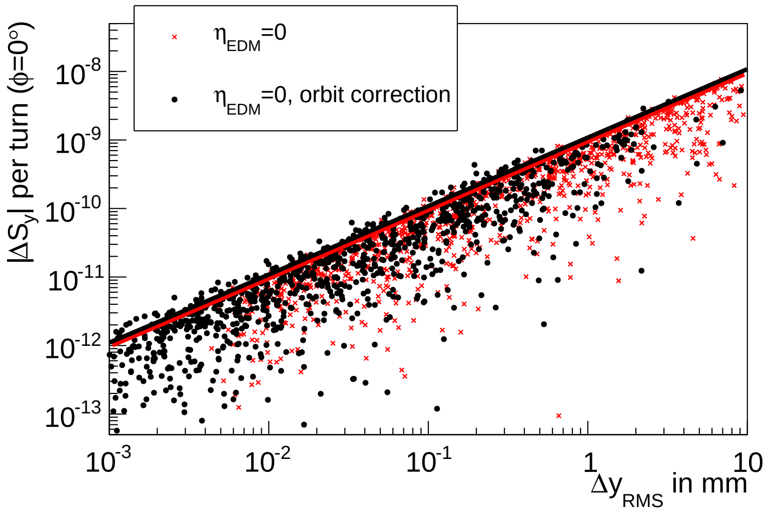

Figure 8.18: Absolute average change of the vertical spin component $|\Delta S_y|$ per turn with respect to different Δy_{RMS} and an initial Wien filter phase $\phi = 0°$ in the simulation. The different Δy_{RMS} are generated by randomized vertical quadrupole shifts assuming Gaussian distributed misalignment errors. Furthermore, an orbit correction is applied, which generally shifts the points to smaller RMS values. The EDM is set to zero. The solid lines show the 90 % upper confidence limit calculated for the corresponding sample.

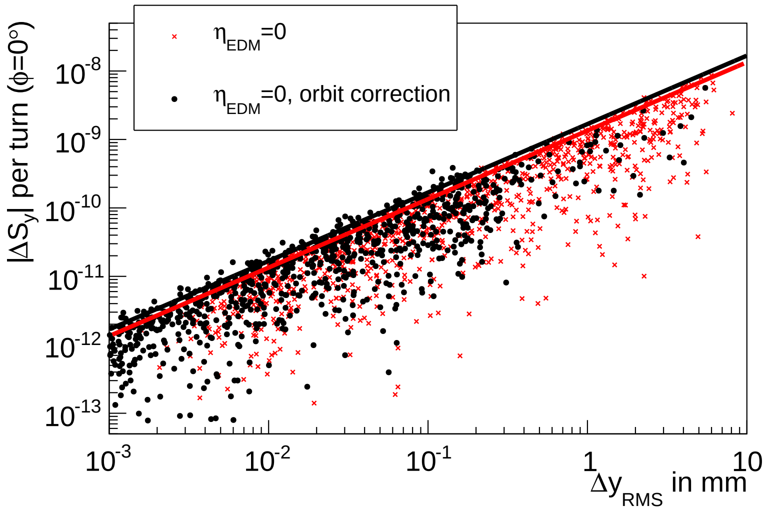

(a)

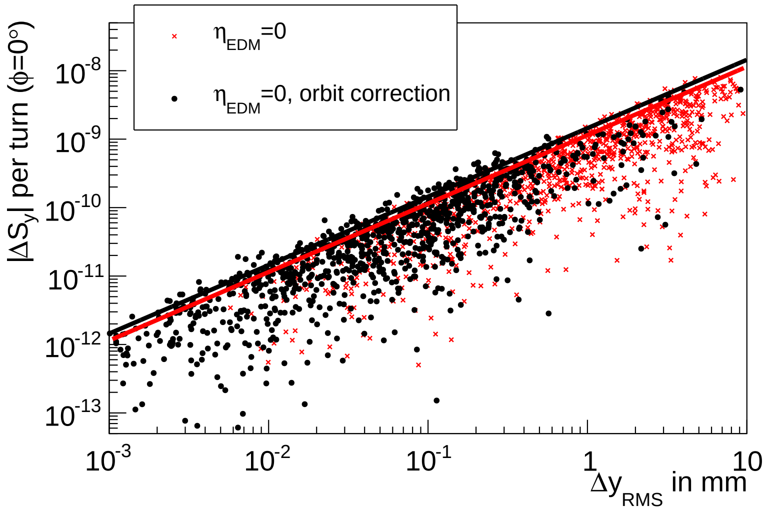

(b)

Figure 8.19: Absolute average change of the vertical spin component $|\Delta S_y|$ per turn with respect to different Δy_{RMS} and an initial Wien filter phase $\phi = 0°$ in the simulation. The different Δy_{RMS} are generated by randomized rotations about the longitudinal axis (a) or a full set of shifts and rotations of dipoles and quadrupoles assuming Gaussian distributed misalignment errors (b). Furthermore, an orbit correction is applied. The EDM is set to zero. The solid lines show the 90 % upper confidence limit calculated for the corresponding sample.

points is observed, a linear function with zero offset is used to also determine the 90 % upper confidence limit. For that purpose, the slope of the function is adjusted until 90 % of the simulated points are below the line.The resulting confidence limits before and after the correction are slightly different. The same effect can be observed for the other two misalignment scenarios illustrated in Figure 8.19. In all scenarios the confidence limit increases, but the expected order of magnitude with respect to the remaining Δy_{RMS} is preserved. For that reason, it can be concluded, that orbit correction provides an efficient tool to suppress false EDM signals arising from misalignments for the particular beam and machine configuration.

In reality the orbit is corrected with respect to the BPM measurements. Additional studies are conducted using an orbit correction scheme taking the BPM locations into account. In this case, a similar linear correlation between the vertical orbit RMS and the buildup of the vertical spin component is observed. Due to the limited number of BPMs, local regions with larger orbit deviations between the BPMs appear. This distortions are not detectable by the BPMs and tends to increase the orbit RMS associated to the quadrupole locations. In general, this leads to an increased $\Delta y_{\mathrm{RMS}} > \Delta y_{\mathrm{RMS}}^{\mathrm{BPM}}$, which deviates from the correlation shown in Figure 8.16. An associated increase of the vertical spin buildup by the same factor is not observed. Hence, localized vertical orbit distortions bias the vertical orbit RMS in quadrupoles as indicator for false EDM signals. Additional studies have to be carried out based on the currently available orbit correction abilities taking the limited precision and accuracy of the BPMs into account. In present experimental studies an optimization of these abilities is examined and executed [165].

8.2.3.4 Electron Cooler Environment

In the previous studies, the electron cooler magnetic environment has not been taken into account. The additional effects introduced by the magnetic elements in the electron cooler chicane are studied in the following. In the current test experiments, the beam is initially cooled in the first period of the cycle. Afterwards the electron beam is turned off, while the magnetic elements (solenoids, toroids and correctors) are kept on. The additional fields on the reference trajectory might also introduce a false EDM signal. An approximated model of the 100 keV-electron cooler chicane is implemented to study this effect. This model is shown schematically in Figure 8.20. Since currently no toroid model is available in the simulation framework, it is approximated by a radial magnetic dipole to model the beam deflection. The magnitude of the radial deflections are taken from [117] and linearly scaled considering a deuteron beam momentum of 970 MeV/c. The significantly smaller vertical deflection described in [117] is not converted in this model approximation. But due to an angular deviation with respect to the longitudinal axes of the compensation solenoids, the radial motion is also transferred into a vertical one. Four radial and four vertical corrector magnets are adjusted to minimize the orbit distortions in the rest of the storage ring. Due to a lack of space, those corrector magnets are partially exist as additional quadrupole windings or are even located in front or behind of an adjacent quadrupole triplet. Hence, a false EDM signal due to the non-commuting spin rotations is expected. Simultaneously, different misalignment magnitudes of the dipoles and quadrupoles are included into the simulations, but a vanishing EDM is assumed. The results are illustrated in Figure 8.21. At small values of the orbit RMS, a plateau of the average vertical spin component change with respect to the vertical orbit RMS Δy_{RMS} appears. This effect mimics an EDM signal corresponding to a value of η_{EDM} between 10^{-6} and 10^{-5} in the simulated setup of the experiment.

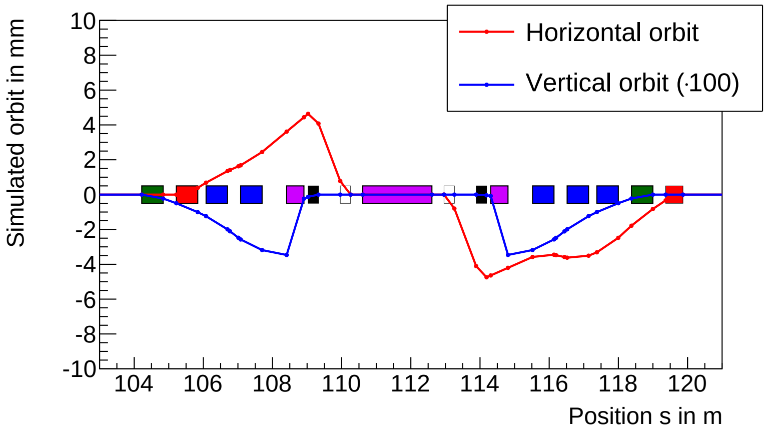

Figure 8.20: Simulated horizontal and vertical orbits in the electron cooler chicane. The vertical orbit is scaled by a factor 100. Four radial and four vertical corrector magnets are adjusted to compensate the orbit distortions due to the toroid magnets, such that the orbit deviations vanish in the rest of the storage ring. The main solenoid and the compensation solenoids are shown in pink, the toroids in white (approximated by small radial kicks), the electron cooler correctors in black, the quadrupoles without windings in blue and quadrupoles with windings for a radial (vertical) corrector in red (green). The last element in red depicts the corrector winding mounted on the ANKE-D1 dipole behind the quadrupole triplet.

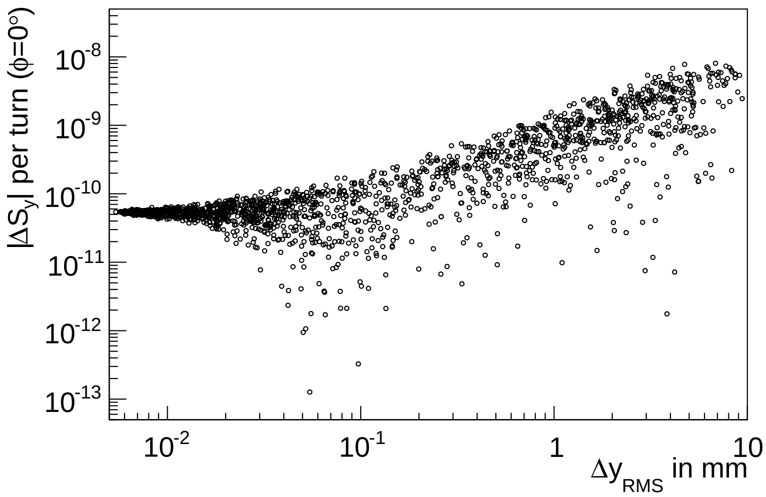

Figure 8.21: Absolute average change of the vertical spin component $|\Delta S_y|$ per turn with respect to different Δy_{RMS} and an initial Wien filter phase $\phi = 0°$ in the simulation. The different Δy_{RMS} are generated by randomized vertical quadrupole shifts assuming Gaussian distributed misalignment errors. Furthermore, a model of the 100 keV-electron cooler chicane is included into the simulation, while the EDM is set to zero.

8.2.3.5 Full Beam Simulations

Several systematic contributions have been pointed out by studying the spin motion of the reference particle. In this section, tracking simulations using a distribution of particles are presented. They aim to verify the numerical predictions in different scenarios. A sample beam of 1000 deuterons with initial spins $\tilde{S}_2(0) = 1$ are utilized. The initial particle coordinates are randomly generated according to Gaussian distributions in the uncoupled 2D-phase spaces. The following estimates obtained during the SCT studies are used:

$$\varepsilon_x^{1\sigma} = 0.2\,\mathrm{mm\,mrad}\ , \tag{8.11}$$

$$\varepsilon_y^{1\sigma} = 0.3\,\mathrm{mm\,mrad}\ , \tag{8.12}$$

$$\delta^{1\sigma} = 10^{-4}\ . \tag{8.13}$$

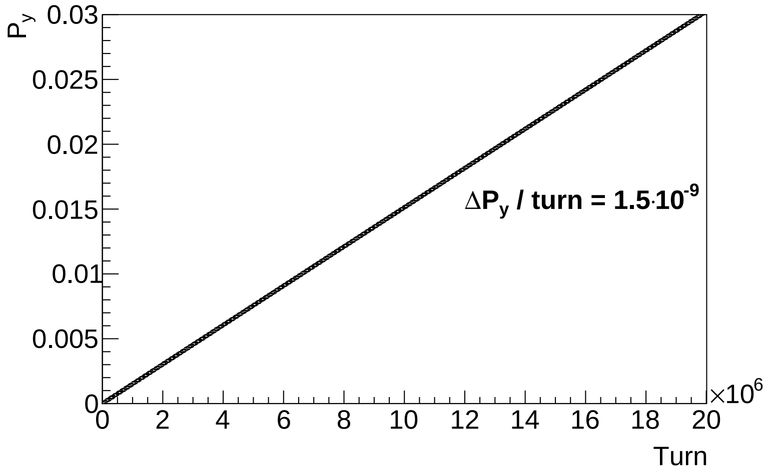

(a)

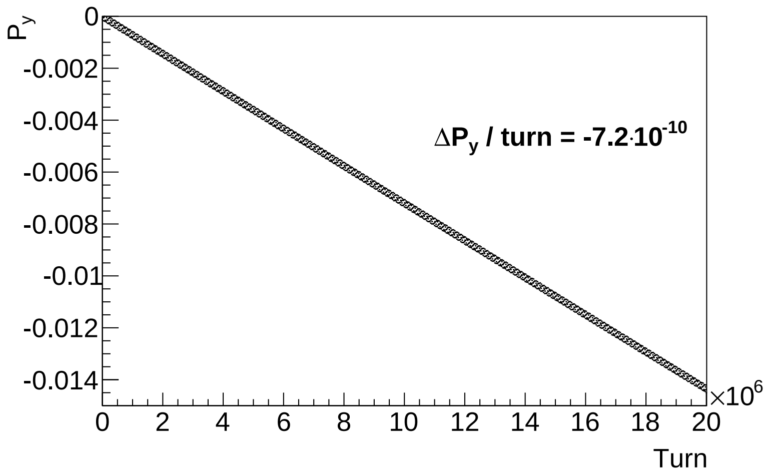

(b)

Figure 8.22: Change of the vertical polarization due to an EDM according to $\eta_{\mathrm{EDM}} = 10^{-4}$ (a) or due to vertically shifts of the quadrupoles (b) in presence of an RF Wien filter with vertical magnetic field at the "PAX location" of COSY.

The same machine setup at a reference momentum of 970 MeV/c as for the preceding studies is employed and the electron cooler magnet chicane is not included. Two different scenarios are simulated: The first scenario describes an ideal ring and no rotation of the Wien filter, but a deuteron EDM according to $\eta_{\mathrm{EDM}} = 10^{-4}$, in the second scenario the EDM vanishes, but the quadrupole magnets are randomly shifted in vertical direction. For comparison, the same conditions as for the reference particle simulations, as shown by red solid lines in Figure 8.8 and Figure 8.12, are used. Given an initial Wien filter phase $\phi = 0°$, the calculated buildup of the vertical spin component amounts to ΔS_y / turn $= 1.5 \cdot 10^{-9}$ (scenario 1) and ΔS_y / turn $= -7.2 \cdot 10^{-10}$ per turn (scenario 2). The corresponding results using the beam of 1000 particles are shown in Figure 8.22. The deuterons are tracked for 20 million revolutions, which corresponds to approximately 27 seconds. Linear fits confirm the same vertical polarization buildup rates as calculated for the vertical spin component of the reference particle. This verifies the estimates of the systematic effects obtained by the reference particle simulations in the previous sections.

8.3 Summary

In this chapter, the new algorithms for the simulation of RF devices could be successfully used to estimate systematic contributions of the Wien filter based EDM measurement method at COSY. The theoretical predictions are in very good agreement with the tracking results. The investigation reveals large systematic contributions arising from misalignments of the elements. Wien filter rotations of 0.1 mrad about the longitudinal axis lead to false EDM signals pretending an EDM magnitude of $d_d \approx 5 \cdot 10^{-19}\, e\,\mathrm{cm}$ ($\eta_{\mathrm{EDM}} = 10^{-4}$). The same order of magnitude is produced by vertical shifts of the quadrupoles, which are randomly distributed according to a Gaussian function with a width of 0.1 mm. Latter is caused by additional tilts of the spin closed orbit introduced by the additional field components. The vertical orbit RMS has been used to quantify the relation between the vertical orbit distortions and the false polarization buildup. Applying orbit correction routines, the false contributions from dipole and quadrupole misalignments could be partially suppressed. Furthermore, the connection between the

Table 8.3: Parameters used for the estimation of the statistical sensitivity of the RF Wien filter method.

Parameter	Value
Anomalous magnetic moment G	-0.14
Lorentz factor γ	1.13
Integrated field strength of RF Wien filter $\hat{B}_{\mathrm{wf}} l_{\mathrm{wf}}$	0.08 T mm
Number of stored particles N	10^9
Analyzing power A	0.4
Beam polarization P	0.6
Detection efficiency f	0.005
Revolution frequency f_{rev}	750 kHz
Spin coherence time τ	1000 s

magnetic chicane of the 100 keV-electron cooler and a false EDM signal was studied. A false signal mimicking an EDM between $d_d \approx 5 \cdot 10^{-20}\,e\,\mathrm{cm}$ and $d_d \approx 5 \cdot 10^{-21}\,e\,\mathrm{cm}$ was observed. These calculations revealed the systematic limitations of the proposed EDM measurement method using an RF Wien filter at COSY. These limitations can be compared to the statistical sensitivity of the RF Wien filter method. This calculation is based on [166], but the formula was slightly adapted. The statistical sensitivity for a deuteron measurement is approximately given by

$$\sigma_d = 2\hbar \left| \frac{G\gamma^2}{1+G} \right| \frac{1}{\hat{B}_{\mathrm{wf}} l_{\mathrm{wf}}} \frac{1}{\sqrt{N \cdot f} A P f_{\mathrm{rev}} \tau} \tag{8.14}$$

Assuming the parameter values given in Table 8.3, the approximated statistical sensitivity amounts to $\sigma_d \approx 10^{-21}\,e\,\mathrm{cm}$ in one cycle. For simplification, a polarization preserved during the entire measurement period was assumed.

Chapter 9

Conclusion and Outlook

The measurement of EDMs are considered to be one of the most promising ways to find CP violation beyond the presently known sources. EDMs of charged particles can be measured at storage rings. In the context of this thesis, several aspects of these measurements have been investigated. A new simulation framework was developed to study the proposed EDM measurements at COSY. The initial benchmarking of the COSY model provided a good agreement with experimental measurements. The calculated changes of storage ring parameters, i.e. betatron tunes, chromaticities and momentum compaction factor, mostly reproduced the measured quantities at a few percent level. Studies of the spin coherence time revealed a strong connection to these parameters, since they are related to path lengthening of individual particles and introduce a spin tune spread. Additionally, the relation between the spin coherence time and the locations and strengths of intrinsic spin resonances has been pointed out. Simulations confirmed the theoretical predictions. Since intrinsic resonances are associated to the vertical betatron tune, measurements at different tunes were conducted. In the various measurements, the longest spin coherence times were observed at measured chromaticities close to the model predictions. A conservative threshold of 60.6 % of the initial polarization was used to quantify the spin coherence time. During a measurement interval of 280 s, a spin coherence time of $\tau = 759^{+63}_{-51}\,\mathrm{s}$ could be achieved applying initial electron cooling for 75 s. This provided one important requirement for EDM measurements at COSY.

The study of systematic limitations of the RF Wien filter method demanded the implementation of time-varying fields into the simulation framework. New algorithms based on transfer map methods were developed. To verify these algorithms, the polarization evolution in presence of spin resonances induced by an RF solenoid were measured. The theoretically predicted dependence of the RF solenoid frequency on the damping of the vertical polarization oscillations was confirmed. Furthermore, the results based on the new algorithms agreed with the analytical estimates. Thus, the algorithms successfully benchmarked were applied to evaluate the systematic contributions providing fake EDM signals. Large systematic contributions due to misalignments and field imperfections were observed. Rotations of the RF Wien filter by 0.1 mrad or normally distributed vertical shifts of the quadrupoles with $\sigma_y = 0.1\,\mathrm{mm}$ introduced signals mimicking a deuteron EDM of about $5 \cdot 10^{-19}\,e\,\mathrm{cm}$. The contributions of quadrupole misalignments could be partially compensated by applying an orbit correction scheme. Since current experiments also rely on an initial electron cooling to reduce the beam emittances, a simplified model of the magnetic chicane of the electron cooler was investigated. It revealed systematic limitations of about $10^{-20}\,e\,\mathrm{cm}$. For the same RF Wien filter setup, the statistical sensitivity of a deuteron EDM measurement was estimated to $10^{-21}\,e\,\mathrm{cm}$ in only one cycle. For this calculation a polarization preserved in a measurement interval of 1000 s was assumed.

The EDM related polarization buildup in the RF Wien filter method depends on the relative phases between the oscillating fields and the orientation of the precessing polarization. This phase relation needs to be preserved by an active feedback utilizing the precise spin tune measurement. A first version of the feedback system was successfully tested recently and could preserve the spin tune by introducing small energy changes. Furthermore, the predicted phase dependence of the polarization buildup with respect to the oscillating field could be reproduced. For this purpose, a similar method using the RF solenoid was applied and the buildup was generated by coupling to the magnetic dipole moment. Further improvements of the feedback system are currently under investigation. Since the EDM related polarization buildup is expected to be small, additional studies improving the present polarimetry capabilities are ongoing. These aim for an increase of the statistical sensitivity and a simultaneous decrease of the systematic contributions of the polarization measurements.

The studies presented within this thesis strongly focused on the development of a precise storage ring model to prepare and evaluate the storage ring experiments. Several aspects can be considered to further improve this model. Additional contributions to spin motion, i.e. field gradients and the electric quadrupole moment, need to be included to investigate their systematic contributions to EDM measurements. Furthermore, the current implementation of the RF Wien filter is based on analytically approximated field descriptions. Simulations including more realistic three-dimensional field descriptions are required to verify the estimates of the systematic contributions connected to the Wien filter. In this context, also alignment routines of the RF Wien filter with respect to the ring plane needs to be studied. Concerning the misalignments of the storage ring elements, actual uncertainties of the beam position measurements need to be introduced to further quantify the present orbit correction abilities. This way, also the locations, at which BPMs are currently missing, can be identified. Furthermore, an improved orbit diagnosis system enables more precise measurements of the optical functions of COSY. Consequently, these measurements allow for a further benchmarking and improvement of the COSY accelerator model. This is mandatory to achieve a deeper understanding of the systematic effects towards a first direct EDM measurement of light charged hadrons.

Appendix A

COSY Layout

This chapter provides a short overview of the layout of the magnetic structure of COSY and the distribution of beam position monitors and corrector magnets used for the orbit correction schemes.

Figure A.1 illustrates the locations of the dipoles, quadrupoles and sextupole magnets of the storage ring. The labels on the inner side indicate the quadrupole families, while the sextupole families are denoted on the outer side. All dipoles belong to the same family. The beam injection point is located on the lower left side.

Figure A.2 depicts the locations of the beam position monitors and the corrector magnets. The corresponding labels of the BPMs are written on the outer side, while the labels on the inner side belong to the corrector magnets. The colors indicate, if the particular element measures or corrects in radial (red) or vertical (green) direction, respectively. Certain corrector windings are mounted on quadrupole magnets. They are displayed by a recoloring of the associated quadrupole magnet. The corrector magnets of the electron cooler and the winding of the ANKE-D3 dipole is not included in this figure.

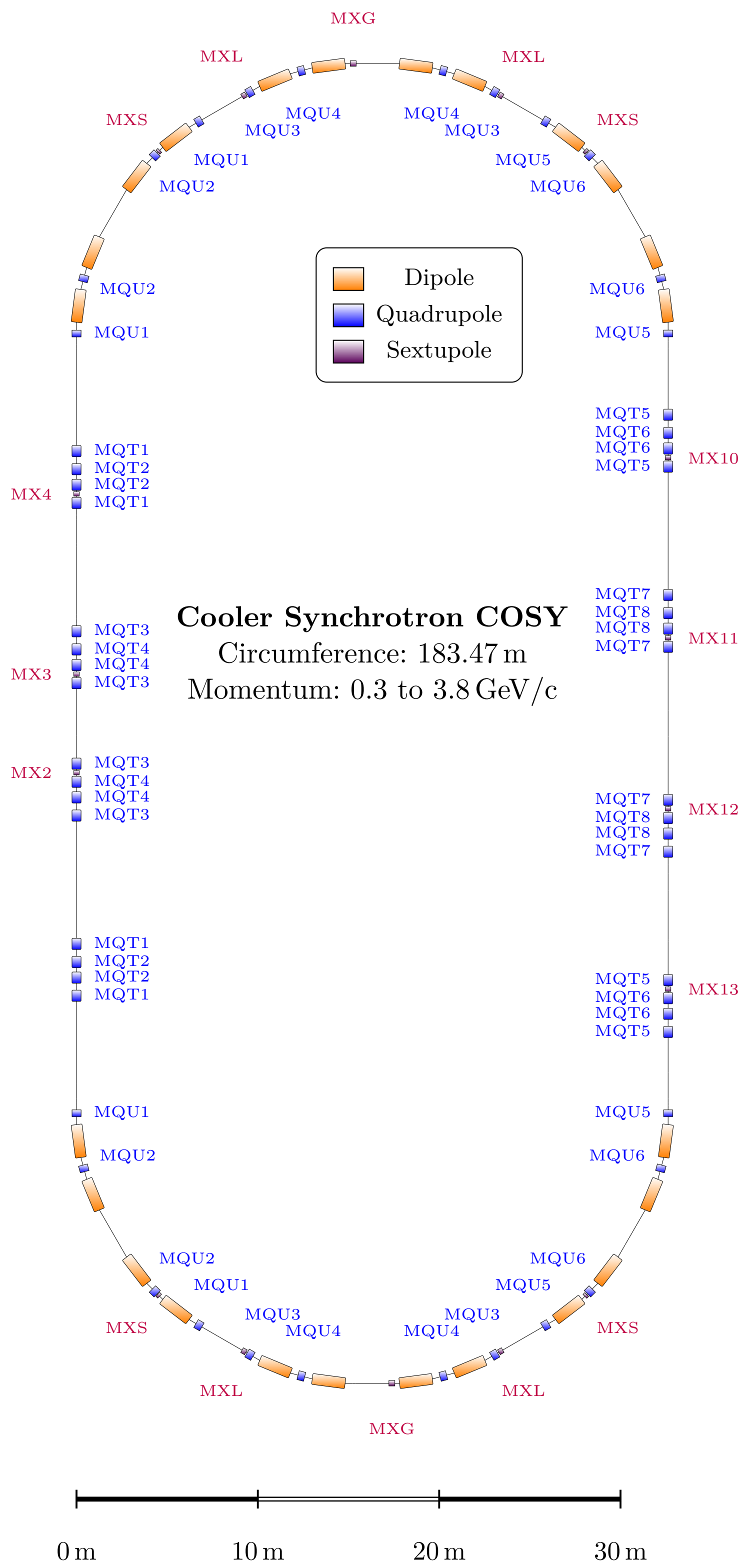

Figure A.1: The arrangement of dipole, quadrupole and sextupole families in the Cooler Synchrotron.

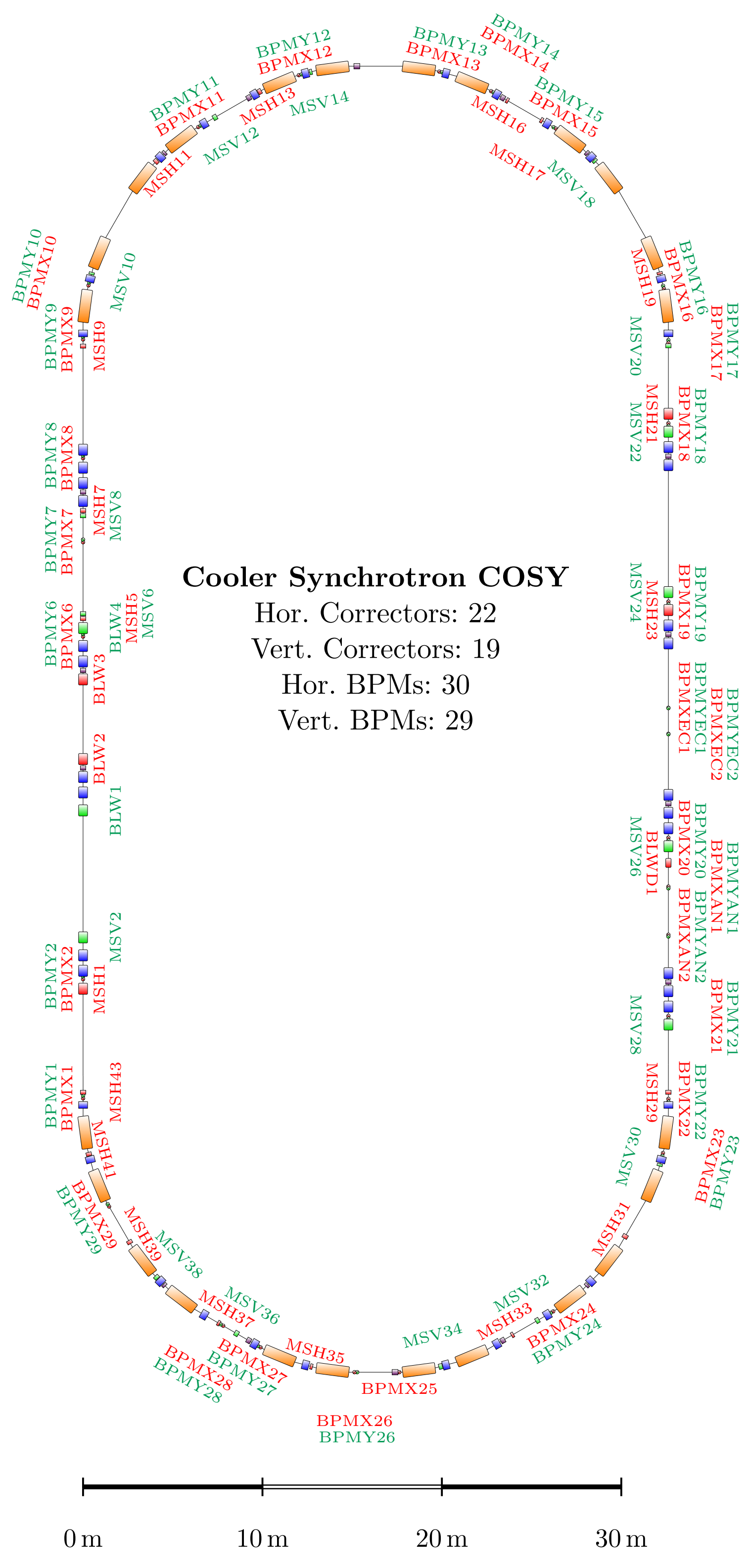

Figure A.2: Locations of the beam position monitors and the corrector magnets in the Cooler Synchrotron.

Appendix B

Results of Betatron Tune and Chromaticity Variations

Table B.1: Changes of the horizontal betatron tune Q_x due to quadrupole strength variations Δk. The results are given in $\frac{\Delta Q_x \cdot k}{\Delta k} \cdot 100$ for measurement and simulation.

Quadrupole family	Measurement	Simulation
MQT1	$-0.011\,12 \pm 0.000\,23$	$-0.012\,20$
MQT2	$0.020\,19 \pm 0.000\,36$	$0.020\,02$
MQT3	$0.008\,30 \pm 0.000\,52$	$0.008\,67$
MQT4	$-0.003\,78 \pm 0.000\,22$	$-0.004\,12$
MQT5	$-0.009\,33 \pm 0.000\,23$	$-0.008\,56$
MQT6	$0.019\,10 \pm 0.000\,92$	$0.015\,12$
MQT7	$-0.016\,97 \pm 0.000\,40$	$-0.016\,23$
MQT8	$0.028\,27 \pm 0.000\,88$	$0.028\,25$
MQU1	$-0.002\,25 \pm 0.000\,13$	$-0.002\,19$
MQU2	$0.006\,55 \pm 0.000\,20$	$0.006\,77$
MQU3	$-0.001\,69 \pm 0.000\,12$	$-0.001\,75$
MQU4	$0.006\,88 \pm 0.000\,04$	$0.007\,11$
MQU5	$-0.002\,67 \pm 0.000\,06$	$-0.002\,72$
MQU6	$0.009\,27 \pm 0.000\,17$	$0.009\,54$

Table B.2: Changes of the vertical betatron tune Q_y due to quadrupole strength variations Δk. The results are given in $\frac{\Delta Q_y \cdot k}{\Delta k} \cdot 100$ for measurement and simulation.

Quadrupole family	Measurement	Simulation
MQT1	$0.013\,81 \pm 0.000\,31$	$0.013\,19$
MQT2	$-0.009\,03 \pm 0.000\,32$	$-0.007\,71$
MQT3	$-0.007\,78 \pm 0.000\,09$	$-0.007\,49$
MQT4	$0.015\,67 \pm 0.000\,19$	$0.015\,30$
MQT5	$0.014\,73 \pm 0.000\,69$	$0.016\,88$
MQT6	$-0.008\,75 \pm 0.000\,63$	$-0.009\,06$
MQT7	$0.014\,08 \pm 0.000\,98$	$0.016\,64$
MQT8	$-0.008\,48 \pm 0.000\,47$	$-0.008\,78$
MQU1	$0.006\,66 \pm 0.000\,02$	$0.007\,26$
MQU2	$-0.003\,48 \pm 0.000\,13$	$-0.004\,25$
MQU3	$0.007\,49 \pm 0.000\,05$	$0.007\,50$
MQU4	$-0.005\,11 \pm 0.000\,09$	$-0.005\,01$
MQU5	$0.006\,71 \pm 0.000\,09$	$0.006\,93$
MQU6	$-0.004\,11 \pm 0.000\,03$	$-0.004\,12$

Table B.3: Changes of the horizontal chromaticity ξ_x due to sextupole strength variations Δk_2. The results are given in $\frac{\Delta \xi_x}{\Delta k_2}$ in m^3 for measurement and simulation.

Sextupole family	Measurement	Simulation
MXS	0.784 ± 0.007	0.763
MXL	0.783 ± 0.019	0.801
MXG	2.178 ± 0.035	2.349

Table B.4: Changes of the vertical chromaticity ξ_x due to sextupole strength variations Δk_2. The results are given in $\frac{\Delta \xi_y}{\Delta k_2}$ in m^3 for measurement and simulation.

Sextupole family	Measurement	Simulation
MXS	-0.574 ± 0.015	-0.535
MXL	-3.711 ± 0.023	-3.628
MXG	-1.665 ± 0.016	-1.568

List of Figures

List of Tables

List of Acronyms

AMS	Alpha Magnetic Spectrometer
ANKE	Apparatus for studies of Nucleon and Kaon Ejectiles
BAU	Baryon Asymmetry in the Universe
BBN	Big-Bang-Nucleosynthesis
BCT	Beam Current Transformer
BPM	Beam Position Monitor
BSM	Beyond the Standard Model
C	Charge conjugation transformation
CCD	Charge-Coupled Device
CKM	Cabibbo-Kobayashi-Maskawa
CMB	Cosmic Microwave Background
COSY	Cooler Synchrotron
CP	C + P transformation
EDDA	Excitation function Data acquisition Designed for Analysis of phase shifts
EDM	Electric Dipole Moment
ILL	Institut Laue-Langevin
IPM	Ionization Profile Monitor
JARA-FAME	Jülich Aachen Research Alliance - Forces And Matter Experiments
JEDI	Jülich Electric Dipole moment Investigations
MCP	Micro-Channel Plane
MDM	Magnetic Dipole Moment
ORM	Orbit Response Matrix
P	Parity transformation
PAX	Polarized Antiproton eXperiment
PDF	Probability Density Function
PMNS	Pontecorvo-Maki-Nakagawa-Sakata
PMT	PhotoMultiplier tube
QCD	Quantum Chromo Dynamics
RF	RadioFrequency

SCT	Spin Coherence Time
T	Time reversal transformation
TDC	Time-to-Digital Converter
UCN	Ultra Cold Neutron
WASA	Wide Angle Shower Apparatus

Bibliography

[1] I. B. Khriplovich and S. K. Lamoreaux. *CP Violation Without Strangeness: Electric Dipole Moments of Particles, Atoms, and Molecules*. 1997.

[2] W. Dekens, J. de Vries, J. Bsaisou, et al. Unraveling models of CP violation through electric dipole moments of light nuclei. *JHEP*, 07:069, 2014.

[3] G. W. Bennett, B. Bousquet, H. N. Brown, et al. Improved limit on the muon electric dipole moment. *Physical Review D*, 80(5):052008, 2009.

[4] W. C. Griffith, M. D. Swallows, T. H. Loftus, et al. Improved Limit on the Permanent Electric Dipole Moment of ^{199}Hg. *Phys. Rev. Lett.*, 102:101601, Mar 2009.

[5] Storage Ring EDM Collaboration, BNL. A Proposal to Measure the Proton Electric Dipole Moment with 10^{-29} e·cm Sensitivity. 2011.

[6] M Aoki66, M Bai, G Bennett, et al. Deuteron EDM Proposal: Search for a Permanent Deuteron Electric Dipole Moment at the 10^{-27} e·cm Level. 2004.

[7] JEDI Collaboration. JEDI Proposal: Search for Permanent Electric Dipole Moments at COSY - Step 1: Spin coherence and systematic error studies. 2012, 2014.

[8] R. Maier, U. Bechstedt, J. Dietrich, et al. Status of COSY. *Interner Bericht des Forschungszentrum Jülich GmbH*, Jül 1965:1–10, 1995.

[9] R. Maier. Cooler synchrotron COSY—Performance and perspectives. *Nuclear Instruments and Methods in Physics Research Section A: Accelerators, Spectrometers, Detectors and Associated Equipment*, 390(1):1–8, 1997.

[10] K. Makino and M. Berz. COSY INFINITY Version 9. *Nuclear Instruments and Methods in Physics Research Section A: Accelerators, Spectrometers, Detectors and Associated Equipment*, 558(1):346–350, 2006.

[11] D. Griffiths. *Introduction to Elementary Particles*. 2 edition, 2008.

[12] A. Riotto and M. Trodden. Recent progress in baryogenesis. *Ann. Rev. Nucl. Part. Sci.*, 49:35–75, 1999.

[13] M. S. Sozzi. *Discrete Symmetries and CP Violation*. 1 edition, 2008.

[14] B. D. Fields, P. Molaro, and S. Sarkar. Big-Bang Nucleosynthesis. *Chin. Phys.*, C38, 2014.

[15] P. A. R. Ade et al. Planck 2013 results. XVI. Cosmological parameters. *Astron.Astrophys.*, 571:A16, 2014.

[16] P. Chardonnet, J. Orloff, and P. Salati. The production of anti-matter in our galaxy. *Physics Letters B*, 409(1–4):313–320, 1997.

[17] B. Borgia. The alpha magnetic spectrometer on the International Space Station. *Nuclear Science, IEEE Transactions on*, 52(6):2786–2792, Dec 2005.

[18] A. D. Sakharov. Violation of CP Invariance, C Asymmetry, and Baryon Asymmetry of the Universe. *Soviet Journal of Experimental and Theoretical Physics Letters*, 5:24, January 1967.

[19] M. Pospelov and A. Ritz. Electric dipole moments as probes of new physics. *Annals of Physics*, 318(1):119–169, 2005. Special Issue.

[20] T. D. Lee and C. N. Yang. Question of Parity Conservation in Weak Interactions. *Phys. Rev.*, 104:254–258, Oct 1956.

[21] C. S. Wu, E. Ambler, R. W. Hayward, D. D. Hoppes, and R. P. Hudson. Experimental Test of Parity Conservation in Beta Decay. *Phys. Rev.*, 105:1413–1415, Feb 1957.

[22] M. Goldhaber, L. Grodzins, and A. W. Sunyar. Helicity of Neutrinos. *Phys. Rev.*, 109:1015–1017, Feb 1958.

[23] G. Backenstoss, B. D. Hyams, G. Knop, et al. Helicity of μ- Mesons from π-Meson Decay. *Physical Review Letters*, 6(8):415, 1961.

[24] M. Bardon, P. Franzini, and J. Lee. Helicity of μ- Mesons; Mott Scattering of Polarized Muons. *Physical Review Letters*, 7(1):23, 1961.

[25] A. Angelopoulos, A. Apostolakis, E. Aslanides, et al. First direct observation of time-reversal non-invariance in the neutral-kaon system. *Physics Letters B*, 444(1–2):43–51, 1998.

[26] J. Schwinger. The Theory of Quantized Fields. I. *Phys. Rev.*, 82:914–927, Jun 1951.

[27] M. Gell-Mann and A. Pais. Behavior of Neutral Particles under Charge Conjugation. *Phys. Rev.*, 97:1387–1389, Mar 1955.

[28] J. H. Christenson, J. W. Cronin, V. L. Fitch, et al. Evidence for the 2π Decay of the K_2^0 Meson. *Phys. Rev. Lett.*, 13:138–140, Jul 1964.

[29] N. Cabibbo. Unitary Symmetry and Leptonic Decays. *Phys. Rev. Lett.*, 10:531–533, Jun 1963.

[30] M. Kobayashi and T. Maskawa. CP-Violation in the Renormalizable Theory of Weak Interaction. *Progress of Theoretical Physics*, 49(2):652–657, 1973.

[31] B. Aubert, D. Boutigny, J-M. Gaillard, et al. Observation of CP violation in the B 0 meson system. *Physical Review Letters*, 87(9):091801, 2001.

[32] K. Abe, R. Abe, I. Adachi, et al. Observation of large CP violation in the neutral B meson system. *Physical Review Letters*, 87(9):091802, 2001.

[33] P. Huet and E. Sather. Electroweak baryogenesis and standard model *CP* violation. *Phys. Rev. D*, 51:379–394, Jan 1995.

[34] D. E. Morrissey and M. J. Ramsey-Musolf. Electroweak baryogenesis. *New J. Phys.*, 14:125003, 2012.

[35] T. Fukuyama and A. J. Silenko. Derivation of Generalized Thomas-Bargmann-Michel-Telegdi Equation for a Particle with Electric Dipole Moment. *Int. J. Mod. Phys.*, A28:1350147, 2013.

[36] B. Pontecorvo. Neutrino experiments and the problem of conservation of leptonic charge. *Sov. Phys. JETP*, 26(984):25, 1968.

[37] Z. Maki, M. Nakagawa, and S. Sakata. Remarks on the Unified Model of Elementary Particles. *Progress of Theoretical Physics*, 28(5):870–880, 1962.

[38] L. Wolfenstein. Parametrization of the Kobayashi-Maskawa Matrix. *Phys. Rev. Lett.*, 51:1945–1947, Nov 1983.

[39] K. A. (Particle Data Group) Olive et al. The Review of Particle Physics. *Chin. Phys. C*, 38(090001), 2014.

[40] C. Jarlskog. Commutator of the Quark Mass Matrices in the Standard Electroweak Model and a Measure of Maximal CP Nonconservation. *Phys. Rev. Lett.*, 55:1039–1042, Sep 1985.

[41] A. Czarnecki and B. Krause. Neutron electric dipole moment in the standard model: Complete three-loop calculation of the valence quark contributions. *Physical review letters*, 78(23):4339, 1997.

[42] E. D. Commins, J. D. Jackson, and D. P. DeMille. The electric dipole moment of the electron: An intuitive explanation for the evasion of Schiff's theorem. *American Journal of Physics*, 75(6):532–536, 2007.

[43] I. B. Khriplovich and A. R. Zhitnitsky. What is the value of the neutron electric dipole moment in the Kobayashi-Maskawa model? *Physics Letters B*, 109(6):490–492, 1982.

[44] F-K. Guo and U.-G. Meissner. Baryon electric dipole moments from strong CP violation. *JHEP*, 12:097, 2012.

[45] R. D. Peccei and H. R. Quinn. CP Conservation in the Presence of Pseudoparticles. *Phys. Rev. Lett.*, 38:1440–1443, Jun 1977.

[46] S. Weinberg. A New Light Boson? *Phys. Rev. Lett.*, 40:223–226, Jan 1978.

[47] F. Wilczek. Problem of Strong P and T Invariance in the Presence of Instantons. *Phys. Rev. Lett.*, 40:279–282, Jan 1978.

[48] J. S. M. Ginges and V. V. Flambaum. Violations of fundamental symmetries in atoms and tests of unification theories of elementary particles. *Physics Reports*, 397(2):63–154, 2004.

[49] M. da Silva. *Sensitive polarimetry in a search for the deuteron electric dipole moment.* PhD thesis, 2010.

[50] E. M. Purcell and N. F. Ramsey. On the Possibility of Electric Dipole Moments for Elementary Particles and Nuclei. *Phys. Rev.*, 78:807–807, Jun 1950.

[51] J. H. Smith, E. M. Purcell, and N. F. Ramsey. Experimental Limit to the Electric Dipole Moment of the Neutron. *Phys. Rev.*, 108:120–122, Oct 1957.

[52] C. A. Baker, D. D. Doyle, P. Geltenbort, et al. Improved Experimental Limit on the Electric Dipole Moment of the Neutron. *Phys. Rev. Lett.*, 97:131801, Sep 2006.

[53] L. I. Schiff. Measurability of Nuclear Electric Dipole Moments. *Phys. Rev.*, 132:2194–2200, Dec 1963.

[54] C. P. Liu, M. J. Ramsey-Musolf, W. C. Haxton, et al. Atomic Electric Dipole Moments: The Schiff Theorem and Its Corrections. *Phys. Rev.*, C76:035503, 2007.

[55] V. V. Flambaum and J. S. M. Ginges. The Nuclear Schiff moment and time invariance violation in atoms. *Phys. Rev.*, A65:032113, 2002.

[56] V. F. Dmitriev and R. A. Sen'kov. Schiff Moment of the Mercury Nucleus and the Proton Dipole Moment. *Phys. Rev. Lett.*, 91:212303, Nov 2003.

[57] P. G. H. Sandars. The electric dipole moment of an atom. *Physics Letters*, 14(3):194–196, 1965.

[58] E. D. Commins, J. D. Jackson, and D. P. DeMille. The electric dipole moment of the electron: An intuitive explanation for the evasion of Schiff's theorem. *American Journal of Physics*, 75(6):532–536, 2007.

[59] Z. W. Liu and H. P. Kelly. Analysis of atomic electric dipole moment in thallium by all-order calculations in many-body perturbation theory. *Phys. Rev. A*, 45:R4210, Apr 1992.

[60] The ACME Collaboration. Order of Magnitude Smaller Limit on the Electric Dipole Moment of the Electron. *Science*, 343(6168):269–272, 2014.

[61] J. P. Miller, E. De Rafael, and B. L. Roberts. Muon (g- 2): experiment and theory. *Reports on Progress in Physics*, 70(5):795, 2007.

[62] B. L. Roberts et al. Status of the Fermilab muon (g- 2) experiment. *Chinese Physics C*, 34(6):741, 2010.

[63] N. Saito et al. A novel precision measurement of muon g-2 and EDM at J-PARC. In *GUT2012*, volume 1467, pages 45–56. AIP Publishing, 2012.

[64] M. Berz, K. Makino, and W. Wan. *An Introduction to Beam Physics.* 1 edition, 2015.

[65] F. Hinterberger. *Physik der Teilchenbeschleuniger und Ionenoptik.* 1 edition, 1997.

[66] K. Wille. *Physik der Teilchenbeschleuniger und Synchrotronstrahlungsquellen.* 2 edition, 1996.

[67] H. Wiedemann. *Particle Accelerator Physics.* 1 edition, 1993.

[68] S. Y. Lee. *Accelerator Physics.* 3 edition, 2012.

[69] M. Berz. *Modern Map Methods in Particle Beam Physics.* 1 edition, 1999.

[70] G. W. Hill. On the part of the motion of the lunar perigee which is a function of the mean motions of the sun and moon. *Acta mathematica*, 8(1):1–36, 1886.

[71] E. D. Courant and H. S. Snyder. Theory of the alternating-gradient synchrotron. *Annals of physics*, 3(1):1–48, 1958.

[72] P. M. Lapostolle. Possible emittance increase through filamentation due to space charge in continuous beams. *Nuclear Science, IEEE Transactions on*, 18(3):1101–1104, 1971.

[73] J. Buon. Beam phase space and emittance. Technical report, Cern, 1992.

[74] K. Floettmann. Some basic features of the beam emittance. *Phys. Rev. ST Accel. Beams*, 6:034202, Mar 2003.

[75] http://uspas.fnal.gov/materials/10MIT/Emittance.pdf. Sep. 2015.

[76] J. Safranek. Experimental determination of storage ring optics using orbit response measurements. *Nuclear Instruments and Methods in Physics Research Section A: Accelerators, Spectrometers, Detectors and Associated Equipment*, 388(1):27–36, 1997.

[77] S. Y. Lee. *Spin Dynamics and Snakes in Synchrotrons*. 1 edition, 1997.

[78] D. Fick. *Einführung in die Kernphysik mit polarisierten Teilchen*. 1971.

[79] G. G. Ohlsen. Polarization transfer and spin correlation experiments in nuclear physics. *Reports on Progress in Physics*, 35(2):717, 1972.

[80] G. G. Ohlsen and P. W. Keaton. Techniques for measurement of spin-12 and spin-1 polarization analyzing tensors. *Nuclear Instruments and Methods*, 109(1):41–59, 1973.

[81] W. Pauli. Zur quantenmechanik des magnetischen elektrons. In *Wolfgang Pauli*. 1988.

[82] http://physics.nist.gov/cuu/Constants/index.html, Sep. 2015.

[83] P. A. M. Dirac. The quantum theory of the electron. In *Proceedings of the Royal Society of London A: Mathematical, Physical and Engineering Sciences*, volume 117, pages 610–624. The Royal Society, 1928.

[84] L. H. Thomas. I. The kinematics of an electron with an axis. *The London, Edinburgh, and Dublin Philosophical Magazine and Journal of Science*, 3(13):1–22, 1927.

[85] V. Bargmann, L. Michel, and V. L. Telegdi. Precession of the polarization of particles moving in a homogeneous electromagnetic field. *Physical Review Letters*, 2(10):435, 1959.

[86] E. M. Metodiev. Thomas-BMT equation generalized to electric dipole moments and field gradients. 2015.

[87] E. d. Courant and R. D. Ruth. The acceleration of polarized protons in circular accelerators. 1980.

[88] Y. S. Derbenev and A. M. Kondratenko. Polarization kinetics of particles in storage rings. *Sov. Phys. JETP*, 37:968, 1973.

[89] G. H. Hoffstaetter, M. Vogt, and D. P. Barber. Higher-order effects in polarized proton dynamics. *Physical Review Special Topics-Accelerators and Beams*, 2(11):114001, 1999.

[90] V. H. Ranjbar, S. Y. Lee, L. Ahrens, et al. Spin coupling resonance and suppression in the AGS. *Phys. Rev. ST Accel. Beams*, 7:051001, May 2004.

[91] W. Wien. Untersuchungen über die electrische Entladung in verdünnten Gasen. *Annalen der Physik*, 301(6):440–452, 1898.

[92] V. S. Morozov, A. D. Krisch, M. A. Leonova, et al. Spin manipulation of 1.94 GeV/c polarized protons stored in the COSY cooler synchrotron. *Phys. Rev. ST Accel. Beams*, 7:024002, Feb 2004.

[93] N. N. Nikolaev. Private communication.

[94] A. Saleev. Private communication.

[95] M. Froissart and R. Stora. Depolarisation d'un faisceau de protons polarises dans un synchrotron. *Nuclear Instruments and Methods*, 7(3):297–305, 1960.

[96] C. Steier and D. Husmann. Correction of depolarizing resonances in ELSA. In *Particle Accelerator Conference, 1997. Proceedings of the 1997*, volume 1, pages 1033–1035. IEEE, 1997.

[97] H. Huang, L. Ahrens, J. G. Alessi, et al. Preservation of Proton Polarization by a Partial Siberian Snake. *Phys. Rev. Lett.*, 73:2982–2985, Nov 1994.

[98] A. Lehrach. *Erarbeitung und Umsetzung eines Konzepts zur Beschleunigung polarisierter Protonen im Kuhlersynchrotron COSY*. PhD thesis, Universitat Bonn, 1998.

[99] M. Bai, L. Ahrens, J. Alessi, et al. Overcoming intrinsic spin resonances with an rf dipole. *Physical Review Letters*, 80(21):4673, 1998.

[100] S. Y. Lee. Spin resonance strength of a localized rf magnetic field. *Physical Review Special Topics-Accelerators and Beams*, 9(7):074001, 2006.

[101] A. D. Krisch, M. A. Leonova, V. S. Morozov, et al. Unexpected reduction of rf spin resonance strength for stored deuteron beams. *Phys. Rev. ST Accel. Beams*, 10:071001, Jul 2007.

[102] W. M. Morse, Y. F. Orlov, and Y. K. Semertzidis. rf Wien filter in an electric dipole moment storage ring: The "partially frozen spin" effect. *Physical Review Special Topics-Accelerators and Beams*, 16(11):114001, 2013.

[103] F. Rathmann, A. Saleev, and N. N. Nikolaev. Search for electric dipole moments of light ions in storage rings. *Physics of Particles and Nuclei*, 45(1):229–233, 2014.

[104] S. Mey and R. Gebel. Towards an RF Wien-Filter for EDM Experiment at COSY. *IPAC Proceedings*, 2015.

[105] R. Weidmann, A. Glombik, H. Meyer, et al. The polarized ion source for COSY. *Review of scientific instruments*, 67(3):1357–1358, 1996.

[106] S. Barsov, U. Bechstedt, W. Bothe, et al. ANKE, a new facility for medium energy hadron physics at COSY-Jülich. *Nuclear Instruments and Methods in Physics Research Section A: Accelerators, Spectrometers, Detectors and Associated Equipment*, 462(3):364–381, 2001.

[107] B. Hoistad, J. Ritman, et al. Proposal for the Wide Angle Shower Apparatus (WASA) at COSY-Juelich-" WASA at COSY". *arXiv preprint nucl-ex/0411038*, 2004.

[108] PAX Collaboration. Letter of Intent for Spin Filtering Studies at COSY. 2006.

[109] D. Prasuhn, J. Dietrich, R. Maier, et al. Electron and stochastic cooling at COSY. *Nuclear Instruments and Methods in Physics Research Section A: Accelerators, Spectrometers, Detectors and Associated Equipment*, 441(1):167–174, 2000.

[110] H. Poth. Electron cooling: theory, experiment, application. *Physics reports*, 196(3):135–297, 1990.

[111] V. Reva et al. COSY 2 MeV Cooler: Design, Diagnostic and Commissioning. In *Proceedings, 5th International Particle Accelerator Conference (IPAC 2014)*, 2014.

[112] A. Lehrach, U. Bechstedt, J. Dietrich, et al. Acceleration of Polarized Protons and Deuterons at COSY. In *AIP Conference Proceedings*, pages 153–165. IOP INSTITUTE OF PHYSICS PUBLISHING LTD, 2003.

[113] A. Lehrach, R. Gebel, R. Maier, et al. Suppressing intrinsic spin harmonics at the cooler synchrotron COSY. *Nuclear Instruments and Methods in Physics Research Section A: Accelerators, Spectrometers, Detectors and Associated Equipment*, 439(1):26–30, 2000.

[114] C. Weidemann. *Preparations for the spin-filtering experiments at COSY/Jülich.* PhD thesis, Universität zu Köln, 2011.

[115] M. A. Leonova. *Achieving High Spin-Flip Efficiency with an RF Magnet and Discovery of Spin-Resonance Strength Formulae Problem.* PhD thesis, 2008.

[116] V. Kamerdzhiev et al. *Untersuchung und Verbesserung des Stabilitätsverhaltens eines intensiven elektronengekühlten Teilchenstrahles in COSY.* PhD thesis, Universität Dortmund, 2004.

[117] H. Soltner, H. J. Stein, V. Kamerdzhiev, et al. Three-Dimensional Numerical Field Analysis for the Magnets of the 100-keV Electron Cooler at COSY-Jülich. *Applied Superconductivity, IEEE Transactions on*, 24(3):1–4, 2014.

[118] H. J. Stein, D. Prasuhn, H. Stockhorst, et al. Present Performance of Electron Cooling at Cosy-J\" ulich. *arXiv preprint arXiv:1101.5963*, 2011.

[119] C Böhme, M Bai, F Hinder, et al. Studies for a BPM Upgrade at COSY. In *Proceedings, IBIC 2015*. these proceedings, 2015.

[120] J. Biri, M. Blasovszky, J. Gigler, et al. Beam position monitor electronics at the cooler synchrotron COSY Julich. *Nuclear Science, IEEE Transactions on*, 41(1):221–224, 1994.

[121] C. Böhme, T. Weis, J. Dietrich, et al. Gas Scintillation Beam Profile Monitor at COSY Jülich. *Proceedings BIW10*, 2010.

[122] P. Forck et al. Minimal invasive Beam Profile Monitors for high intense hadron beams. *IPAC10*, page 1261, 2010.

[123] R. Maier, J. Bojowald, R. Danzglock, et al. Non-beam disturbing diagnostics at COSY-Julich. *Conf. Proc.*, C900612:800–802, 1990.

[124] J. Bisplinghoff, R. Bollmann, P. Cloth, et al. Position sensitivity by light splitting in scintillator arrays. *Nuclear Instruments and Methods in Physics Research Section A: Accelerators, Spectrometers, Detectors and Associated Equipment*, 329(1):151–162, 1993.

[125] Z. Bagdasarian et al. Measuring the Polarization of a Rapidly Precessing Deuteron Beam. *Phys. Rev. ST Accel. Beams*, 17(5):052803, 2014.

[126] M. Rosenthal. Development of a new control framework for lattice parameter calculations and particle tracking. *IKP Annual Report 2014*, 2015.

[127] R. Brun and F. Rademakers. ROOT—an object oriented data analysis framework. *Nuclear Instruments and Methods in Physics Research Section A: Accelerators, Spectrometers, Detectors and Associated Equipment*, 389(1):81–86, 1997.

[128] I. Antcheva, M. Ballintijn, B. Bellenot, et al. ROOT—A C++ framework for petabyte data storage, statistical analysis and visualization. *Computer Physics Communications*, 180(12):2499–2512, 2009.

[129] C. Sanderson. Armadillo: An open source C++ linear algebra library for fast prototyping and computationally intensive experiments. 2010.

[130] M. Berz. Computational aspects of optics design and simulation: COSY INFINITY. *Nuclear Instruments and Methods in Physics Research Section A: Accelerators, Spectrometers, Detectors and Associated Equipment*, 298(1):473–479, 1990.

[131] M. Berz, J. Hoefkens, and K. Makino. COSY INFINITY version 8.1 programming manual. *MSUHEP-20703, Department of Physics and Astronomy, Michigan State University*, 2002.

[132] M. Berz. Arbitrary order description of arbitrary particle optical systems. *Nuclear Instruments and Methods in Physics Research Section A: Accelerators, Spectrometers, Detectors and Associated Equipment*, 298(1):426–440, 1990.

[133] B. Hartmann, M. Berz, and H. Wollnik. The computation of aberrations of fringing fields of magnetic multipoles and sector magnets using differential algebra. *Nuclear Instruments and Methods in Physics Research Section A: Accelerators, Spectrometers, Detectors and Associated Equipment*, 297(3):343–353, 1990.

[134] K. Makino and M. Berz. Solenoid elements in COSY INFINITY. In *Computational Accelerator Physics 2003: Proceedings of the Seventh International Conference on Computational Accelerator Physics, Michigan, USA, 15-18 October 2003*, page 219. CRC Press, 2005.

[135] R. Hipple and M. Berz. A Comparison of Storage Ring Modeling with COSY INFINITY, ZGOUBI, and MAD8. *arXiv preprint arXiv:1503.02061*, 2015.

[136] M. Berz and K. Makino. Optics and nonlinear effects in repetitive systems. *Nuclear Instruments and Methods in Physics Research Section A: Accelerators, Spectrometers, Detectors and Associated Equipment*, 645(1):175–181, 2011.

[137] J. R. Rees. Symplecticity in beam dynamics: An introduction. Technical report, 2003.

[138] M. Berz. Private communication, 2015.

[139] H. Grote and F. C. Iselin. The MAD program (Methodical Accelerator Design) version 8.16, User's reference manual, CERN/SL/90-13 (AP),(rev. 4), 1995.

[140] L. H. A. Leunissen. *Non-linear transverse dynamics at the Cooler Synchrotron COSY*. PhD thesis, 1997.

[141] A. Pesce. *Spin Tracking Studies for EDM Search in Storage Rings*. PhD thesis, 2013.

[142] I. A. Koop and Ju. M. Shatunov. The spin precession tune spread in the storage ring. In *European particle accelerator conference*, 1988.

[143] Yu. Senichev, R. Maier, D. Zyuzin, et al. Spin tune decoherence effects in electro-and magnetostatic structures. *Momentum*, 2:11, 2013.

[144] M. Rosenthal. Polarisation Lifetime Studies for EDM Measurements at COSY. *IKP Annual Report 2013*, 2014.

[145] M. Rosenthal. Investigation of Beam and Spin Dynamics for EDM Measurements at COSY. 2015.

[146] Y. Shoji. Dependence of average path length betatron motion in a storage ring. *Phys. Rev. ST Accel. Beams*, 8:094001, Sep 2005.

[147] D. Eversmann, V. Hejny, F. Hinder, et al. New method for a continuous determination of the spin tune in storage rings and implications for precision experiments. *arXiv preprint arXiv:1504.00635*, 2015.

[148] D. Eversmann. *Spin Tune Determination in the COSY Storage Ring*. PhD thesis, to be published.

[149] F. C. Alegria. Bias of amplitude estimation using three-parameter sine fitting in the presence of additive noise. *Measurement*, 42(5):748–756, 2009.

[150] P. Händel. Amplitude estimation using IEEE-STD-1057 three-parameter sine wave fit: Statistical distribution, bias and variance. *Measurement*, 43(6):766–770, 2010.

[151] G. Guidoboni. *Spin Coherence Time studies for the storage ring EDM search*. PhD thesis, 2012.

[152] G. Guidoboni, E. Stephenson, et al. How to reach a thousand-second in-plane polarization lifetime with 0.97-GeV/c deuterons in a storage ring. *Submitted to Phys. Rev. Letters*, 2016.

[153] P. Benati, D. Chiladze, J. Dietrich, et al. Synchrotron oscillation effects on an rf-solenoid spin resonance. *Phys. Rev. ST Accel. Beams*, 15:124202, Dec 2012.

[154] P. Benati, D. Chiladze, J. Dietrich, et al. Erratum: Synchrotron oscillation effects on an rf-solenoid spin resonance [Phys. Rev. ST Accel. Beams **15** , 124202 (2012)]. *Phys. Rev. ST Accel. Beams*, 16:049901, Apr 2013.

[155] A. Lehrach, B. Lorentz, W. M. Morse, et al. Precursor Experiments to Search For Permanent Electric Dipole Moments (EDMs) of Protons and Deuterons at COSY. *Internal Note.*

[156] A. Lehrach, B. Lorentz, W. M. Morse, et al. Decoherence of Horizontal and Vertical Spins in a Magnetic Ring with Radiofrequency Spin Flipper. *Internal Note.*

[157] R. C. Hanna. Some experimental aspects of the use of polarized beams. In *Proceedings of the 2nd International Symposium on Polarization Phenomena of Nucleons*, page 280, 1965.

[158] M. Rosenthal et al. Spin Tracking Simulations towards Electric Dipole Moment Measurements at COSY. 2015.

[159] H. Stockhorst. Private communication.

[160] S. Mey. Private communication.

[161] J. S. Slim, D. Heberling, and D. Hölscher. Towards a High-Accuracy RF Wien Filter for Spin Manipulation at COSY Jülich. The International Workshop on Polarized Sources, Targets & Polarimetry, Bochum (Germany), 13 Sep 2015 - 18 Sep 2015, Sep 2015.

[162] M. Rosenthal. Systematic Limitations of EDM Measurements at COSY due to Magnet Misalignments. *IKP Annual Report 2015*, 2016.

[163] J. Slim. Private communication.

[164] F. Hinder et al. Development of new Beam Position Monitors at COSY. 2015.

[165] F. Hinder. Private communication.

[166] J. Pretz. Statistical Error of an EDM measurement with an RF- Wien filter. *JEDI Internal Note 2013/02*, 2013.

Acknowledgments

Finally, I would like to thank those persons who supported me during the last years and enabled these studies and experiments described within this thesis. First of all, I would like to thank my supervisors Prof. Dr. Jörg Pretz and Prof. Dr. Andreas Lehrach and also the directors of the IKP-4, Prof. Dr. Rudolf Maier and Prof. Dr, Mei Bai, for giving me the interesting opportunity to explore the spin dynamics and the experimental challenges of electric dipole moment measurements in storage rings. The theoretical investigations combined with the direct access to the near-by accelerator and storage ring COSY for experimental verification served as an excellent environment for these studies.

Further I would like to express my thanks to the contributing individual groups of and around the JEDI Collaboration for their help. I am grateful to the COSY accelerator group, especially to Dr. Dieter Prasuhn, Dr. Bernd Lorentz and Dr. Ralf Gebel, for their several hands-on tutorials during the machine setup periods at the COSY accelerator. This experience strengthens my knowledge of accelerator physics, which I could transfer to the spin dynamics simulations. Concerning simulations, I would like to thank the beam theory group of the Michigan State University (MSU) around Prof. Dr. Martin Berz and Prof. Dr. Kyoko Makino for providing me access to their simulation code COSY INFINITY. I appreciated their hospitality during my short visit in the United States and could strongly benefit from discussions about the code during international conferences and several phone meetings. For their efforts on the experimental setup, I would like to thank Dr. Volker Hejny and Dr. Peter Wüstner for taking care of the data acquisition in various beam times. The corresponding existing analysis framework fastly introduced me to the underlying methods, which I could partially adapt to develop my own algorithms. Furthermore, I am grateful to Dr. Ed Stephenson and Dr. Greta Guidoboni for several conversations and their work concerning the preparation and analysis of the experiments. For the theoretical discussions about the polarization oscillations induced by a radiofrequency solenoid, I would like to thank Dr. N. N. Nikolaev, who made the key contribution for proposing the associated experiments. Luckily, I also had the pleasure to collaborate with a nice group of doctoral candidates, especially Sebastian Mey, Fabian Hinder, Fabian Trinkel, Jan Hetzel, Dennis Eversmann, Paul Maanen, Nils Hempelmann, Artem Saleev and Stanislav Chekmenev. The conversations about theoretical considerations, simulation issues, accelerator and experimental setups as well as their efforts during the experimental periods made this thesis possible.

Last but not least, I also thank my parents Ursula and Bernd Rosenthal and my girlfriend Cindy Schiffer for all their support in the past years. Their help always cheered me up after some busy days, especially during the experimental run periods. The final words I spent in memory of my grandparents Christine and Alfred Rackow and Stefan Rosenthal, who unfortunately passed away during my physics studies and could not witness the award of my Ph.D degree.